UNIVERSITY OF LONDON THESIS

Degree PhD Year 2006 Name of Author MUNRO James Julian

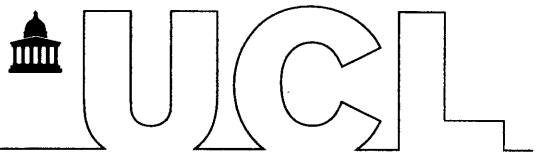

States Near Dissociation in H_3^+

James J. Munro

A thesis submitted to the University of London
for the degree of Doctor of Philosophy

Department of Physics and Astronomy
University College London

May 2006

ProQuest LLC
789 East Eisenhower Parkway
P.O. Box 1346
Ann Arbor, MI 48106-1346

I, James Julian Munro, confirm that the work presented in this thesis is my own. Where information has been derived from other sources, I confirm that this has been indicated in the thesis.

For Frances

Abstract

Ab initio calculations contributing to an understanding of the infra-red near-dissociation spectrum of H_3^+ are performed. All the bound vibrational nuclear-motion states and all the J=3 ro-vibrational states of H_3^+ are calculated using a discrete variable representation (DVR) of the Hamiltonian on a massively parallel computer.

The vibrational motion is evaluated in Jacobi and Radau coordinates. The rotational motion is evaluated using a z-perpendicular embedding of body-fixed coordinates. The vibrational band origins and ro-vibrational J=3 energy levels are calculated using an optimised basis set of effective size $696,960 \times 4(J+1)$. This results in ro-vibrational states which are converged to an unprecedented level of accuracy.

Preliminary resonance state calculations of a similar accuracy are also performed by extending the bound state calculations using a complex absorbing potential method.

The calculations performed are very large and therefore the algorithm has been extensively parallelised on a supercomputer. Several aspects of the DVR based algorithm are improved at every level of the calculation. An accurate and efficient system for performing resonance calculations based upon complex absorbing potentials is developed with an accuracy primarily dependant upon basis set completeness.

The calculated vibrational nuclear-motion states are examined near dissociation using a number of methods. A number of long range *van der Waals-like* states are found to exist near dissociation. These asymptotic vibrational states are studied, graphically, through classical motion calculations and expectation values of the wave functions.

Large basis 3D wave functions are also produced which are suitable for dipole transition calculations and could soon lead to a better understanding of the infra-red near-dissociation spectrum of H_3^+.

Contents

List of Figures

List of Tables

Acknowledgements

Many thanks to Jonathan Tennyson for being a great Supervisor and providing an expertise to which I have yet to find a limit.

During the early part of my PhD, Jayesh Ramanlal provided much intellectual and social support to which I owe thanks, thanks also to Hamse Mussa for useful conversations and a prolific legacy of work.

Best wishes and thanks to Paolo Barletta and Bruno Cesar Silva who joined the research project during the latter half of my PhD and helped with many aspects of it. I hope they will have great success in continuing the work on H_3^+ and other molecules.

Thanks to Tania Monteiro for useful discussions on the analysis of quantum systems and classical techniques and for being my second superviser.

Also thanks are due to many others from the TAMPA group at University College London for their support and advice.

Finally I would like to thank The Engineering and Physical Sciences Research Council for funding my PhD and for providing for the large amount of computer resources, without which these calculations would not have been possible.

Chapter 1

Introduction

H_3^+, three protons and two electrons, the three protons typically forming a triangle while the two electrons form a cloud around all three nuclei. As the simplest polyatomic molecule it was first discovered by Thomson in 1911 as an object with an atomic mass of three but a single positive charge [9; 10], long before a good understanding of quantum mechanics arose. Due to its simplicity, H_3^+ was the subject of many early theoretical studies [11], which predicted properties such as its equilibrium geometry [12]. This equilateral triangle geometry was confirmed by experiment in 1978 with a Coulomb explosion experiment [13]. However, it wasn't until after the development of useful lasers that the fundamental, infrared, spectrum of H_3^+ could be recorded by Oka in 1980 [14]. Not long after in 1982, Carrington, Buttenshaw and Kennedy recorded a very interesting spectrum of H_3^+ near dissociation [15]. The theory of this near dissociation spectrum forms a major motivation for this work, although general aspects of H_3^+ near dissociation and the accurate and efficient calculation of highly excited nuclear motion states are also considered.

1.1 The role of H_3^+ in the universe

H_3^+ is commonly formed from molecular hydrogen in the exothermic reaction,

$$H_2 + H_2^+ \rightarrow H_3^+ + H. \tag{1.1}$$

Hydrogen is the most common element in the universe and molecular hydrogen is the most common molecule. In light of this it is hardly surprising that H_3^+ is very important in physics and chemistry. However, the above reaction will only take place at temperatures low enough to allow for the formation of molecular hydrogen

and temperatures high enough to allow that same hydrogen to be ionized.

This rules H_3^+ out from being important in most stars. However, it is expected that H_3^+ will play an important part in cool 'zero-metallicity' stars [16].

Although the most obvious place that hydrogen would be dominant is in stars, there are two other important places, the interstellar medium and gas giants. In both of these places, molecular Hydrogen dominates. In the interstellar medium, this molecular Hydrogen is ionized by cosmic rays allowing the formation of H_3^+. H_3^+ then plays an important part in the chemistry of the interstellar medium, acting as a protonator in a whole host of possible reactions involving the major elements [17]. This is true for both dense and diffuse molecular clouds in the interstellar medium.

H_3^+ has been observed on most of our solar system's gas giants, including Jupiter where H_3^+ was recorded by instruments on the Voyager spacecraft [18] and by telescopes observing the emission spectrum of the Jovian atmosphere [19; 20], although it was a while before it was actually indentified as such. Subsequently, strong H_3^+ emmision was detected on Uranus [21] and surprisingly weak emission on Saturn [22]; H_3^+ is also expected to exist on Neptune.

1.2 Properties of the H_3^+ molecular ion.

The protons of H_3^+ form an equilateral triangle at equilibrium, the bondlength at equilibrium being $1.65a_0$. This equilateral triangle has three vibrational modes (figure 1.1). The first one is the symmetric breathing mode where all the internuclear distances grow and shrink simultaneously, the second two are the degenerate bending modes, v_{2x} and v_{2y}. Because of the Pauli principle, the A_1 ro-vibrational states (breathing modes for $J = 0$) are not physical. However, we still consider A_1 vibrational states in this work as they form band origins to $J > 0$ states that do not have A_1 symmetry and therefore can be populated. A consequence of the equilateral triangle configuration is that there is no permanent dipole moment at equilibrium and therefore there is no pure rotational spectrum for H_3^+. However, it has been predicted that there should be an observable 'forbidden' rotational spectrum [23; 24].

The ground electronic state of H_3^+ is a completely symmetric singlet state, labelled $1\ ^1A_1$ which has a dissociation limit of $H^+ + H_2(^1\Sigma_g^+)$. The first excited electronic state ($2\ ^1A_1$) dissociates to $H(1s) + H_2^+(^2\Sigma_g^+)$ instead. In this work we include a consideration of both of the states. The reason for considering both is because there is an avoided crossing between them and at some long range configurations of the molecule, the surface from the $2\ ^1A_1$ state actually has a lower energy than the surface for the $1\ ^1A_1$ state. Therefore a correct long range electronic

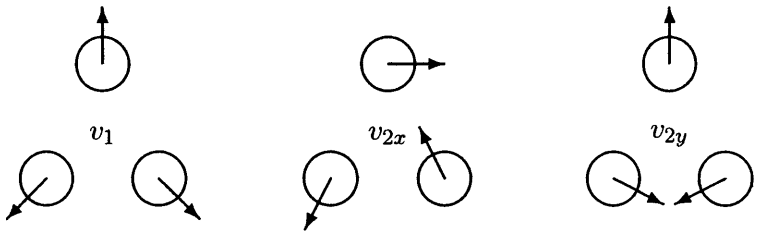

Figure 1.1: Vibrational modes of H_3^+, the v_1 breathing mode and the degenerate v_{2x} and v_{2y} bending modes.

Table 1.1: Allowed symmetries and spin statistical weights for H_3^+ (table from [7]).

Γ_{rve}	Γ_{ns}	Γ_{tot}	g_{ns}
A_1'	—	—	0
A_1''	—	—	0
A_2'	A_1'	A_2'	4
A_2''	A_1'	A_2''	4
E'	E'	A_2'	2
E''	E'	A_2''	2

potential must consider the effect of this avoided crossing in order to treat the near dissociation states correctly.

It is also often important to consider the symmetry effects of the protons. Formed from three fermions (spin-half protons) H_3^+ must obey Fermi-Dirac statistics. Under odd permutations of the protons the total wavefunction must change sign and under even permutations of the protons the total wavefunction must be invariant. In the molecular symmetry group of H_3^+ (D_{3h}^{MS}) the total wavefunctions must therefore have either A_2' or A_2'' symmetry. The molecular symmetry group of H_3^+ is discussed in more detail in section 2.4.

Because of this limitation there are forbidden levels in H_3^+. Ro-vibrational electronic wavefunctions with A_1' or A_1'' symmetry cannot exist as there is no way of forming total wavefunctions with A_2' or A_2'' symmetry. The allowed symmetries for the ro-vibrational electronic wavefunctions (Γ_{rve}), the nuclear-spin wavefunctions (Γ_{ns}) and the total wavefunctions (Γ_{tot}) are shown in table 1.1, along with the spin statistical weights g_{ns}.

1.3 The infra-red predissociation spectrum of H_3^+

The extremely complex spectrum of H_3^+ near dissociation recorded by Carrington *et al* has remained an enigma for decades. The initial observation by Carrington, Buttenshaw and Kennedy in 1982 was of a very unusual photo-dissociation spectrum of H_3^+ [15]. The physical structure of the experiment had consequences for this spectrum. A basic diagram of the experiment is shown in figure 1.2.

The incident photons were produced by a tunable infra-red CO_2 laser. The H_3^+ was produced by the electron impact ionisation of H_2. The positive potential of the electron impact ionisation source then accelerated the hot H_3^+ toward a bending magnet. This bending magnet then selected the ions by their mass-charge ratio, thereby only bringing the H_3^+ in line with the laser.

The H_3^+ then entered the drift tube where it could interact with the now collinear laser. The frequency of interaction between the infra-red photons and the H_3^+ was controlled by altering the ion-accelerating potential and thereby altering the ion velocity, Doppler shifting the ions with respect to the laser.

Any protons ejected from the drift tube were then measured using a combination of an electrostatic analyser (ESA) and a electron multiplier. The ESA voltage was varied to measure protons of different energies and the off-axis electron multiplier allowed them to measure the proton current at that energy. By giving the drift tube a different potential to the rest of the apparatus they were able to monitor just the protons resulting from interactions within the drift tube as they had a different energy.

Their first experiments revealed a very large number of transitions in the 872–1,094 cm^{-1} energy range. The dissociation energy of H_3^+ is large — approximately 35,000 cm^{-1} — therefore for the molecule to break, the initial and final states must all have been close to this dissociation energy and many will have been resonance states above dissociation.

In 1984, Carrington and Kennedy published their completed work on near-dissociation H_3^+ which included the recording of over 27,000 transitions and similar spectra for H_2D^+, D_2H^+ and D_3^+ [25]. The recorded lines also had a large range of widths, from the smallest width they could measure (≈ 0.0001 cm^{-1}) to as wide as they could discern. This range of widths can only come from resonances and so confirmed that they were looking at photo-dissociation of the molecule. Indeed, many of the states recorded had more energy than the photons from the CO_2 laser, suggesting that some of the initial states are also above dissociation.

The spectrum appeared to have very little structure with no hope of any as-

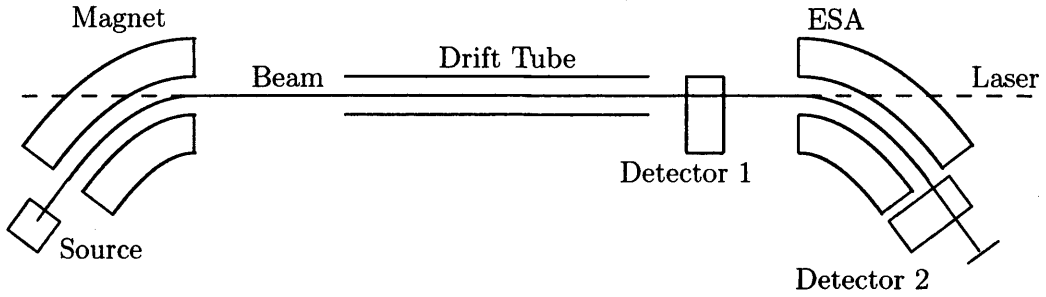

Figure 1.2: A holistic representation of the Carrington-Kennedy experiment. The molecular ions travel through the apparatus from left to right.

signment. The only structure found was that of four peaks formed from many lines when the spectrum is looked at a low resolution [26]. These four collections of peaks occur at 876, 928, 978 and 1,034 cm^{-1}.

As it was only the H_3^+-photon interactions that happened within the drift tube that were recorded, any resonance state of H_3^+ had to therefore survive long enough to enter the drift tube for it to form part of the recorded spectrum. The time it took to transport the ions into the drift tube therefore gave a lower limit to the lifetimes of the initial states involved in the predissociation. With a beam potential of 5kV the initial state lifetimes must have been greater than $3\mu s$.

The final states of H_3^+ then had to be short lived enough that dissociation could occur within the drift tube, otherwise the ejected protons would not have been recorded. At the same beam potential of 5kV the final state lifetime must have been less than $0.7\mu s$.

Ions which fragmented too quickly — quicker than about $7ns$ — resulted in lines that were too broad to discern against the background noise of the spectrum. The final state lifetimes in this range where directly measured as line-widths in the spectrum ($\tau = \hbar/\Gamma$) and so any theory of the spectrum must be able to explain it.

Further research was prompted by theoretical studies of the kinetic energy release of H^+ and D^+ from the isotopologue D_2H^+ [27; 28]. In 1993, Carrington, McNab and West repeated some of the earlier experiments at higher accuracy and extended them to include the recording of lines from products that had a much higher kinetic energy [29]. The recorded spectrum was still complicated but simpler than the earlier spectra of products with almost no kinetic energy (in the centre of mass frame of the molecule). As these lines must come from states with an energy considerably higher than the dissociation energy, the states in the narrower range generate a simpler spectrum.

This dependance of the spectrum on the kinetic energy of the fragements was found to be strong. The ESA used to record the spectrum was tuned to only allow H^+ fragements with a particular kinetic-energy to charge ratio into the detector. This window was varied over a range of kinetic energies from 0 cm^{-1} to 3000 cm^{-1}. When centered at 0 cm^{-1}, lines with a range of widths and intensities were detected. When centered at 500 cm^{-1}, a large number of weak lines were detected (*ca.* 60 per cm^{-1}). Finally at 3000 cm^{-1} a relatively clean spectrum was detected with few number of strong transitions, although no pattern was observed.

This further study also revealed that the four major clumps of lines could also be re-interpreted as four clumps of lines at 978 cm^{-1} and two clumps of lines at each of the other original clumps. Furthermore, this later study demonstrated that the results were truly reproducible. Previously, it was thought that details of the recorded spectra could be sensitive to the exact experimental conditions.

1.3.1 Explanations for the spectrum

Early analysis suggested that long-range $H_2 - H^+$ type complexes near dissociation [30] with significant rotational excitation could explain the near-dissociation spectrum [31]. This proposal has not been invalidated, but it now appears that a wider range of states, including close-coupling of all three nuclei, qualitatively fit the experimental data [32]. These *Horseshoe* states [33; 34] — displayed in section 6.4.4 — have been found to support strong dipole transitions [35] and with rotational excitation can form resonances with long lifetimes [32], trapped by the centrifugal potential barrier in the effective rotational potential energy surface. It should also be noted that these Horseshoe-like states will exist at higher rotational excitations than long range $H_2 - H^+$ type complexes because the effective centrifugal potential reduces the range of states involved. Figure 9 in the work of Berblinger *et al* [33] effectively portrays this for J greater than about 30.

1.4 Theoretical motivations

H_3^+ is theoretically interesting because it is a very simple molecule and yet a complete description is an enormous challenge to theory. Within the Born–Opeinheimer approximation, H_3^+ is also an example of the classic three body problem in physics, a problem that has been the subject of enormous amounts of study. Whilst in principle H_2^+ is the first molecule involving three bodies, two protons and an electron, it is not a particularly difficult version of the three body problem to solve. The vastly different masses of the protons and the electron allow for the separation of

electronic and nuclear motions, a very good initial step in the theory. However, the equal masses of the protons in H_3^+ provide a serious challenge when trying to obtain a complete description of its behaviour.

Secondly, H_3^+ supports a very large range of dynamics even at fairly low energies. For instance, at energies above linearity the classical behaviour is mostly chaotic [33], the quantum scars of this behaviour are therefore also very complicated. Related to this is the floppiness of H_3^+, the harmonic approximation fails particularly quickly in this case. Lastly, the strong Coriolis coupling between motions makes rotational calculations difficult.

1.5 Previous near-dissociation calculations

There have been a number previous attempts at a full quantum mechanical calculation on H_3^+ up to dissociation. With the aim of studying the high angular momentum limit variationally, Miller and Tennyson [36] calculated many states of H_3^+ and H_2D^+ at high J using a small basis set.

Carter and Meyer [37] calculated the vibrational states up to about 25,000 cm^{-1} above the ground state, the energy at which the potential [38] is still valid, some 10,000 cm^{-1} below the dissociation energy. Henderson and Tennyson [39] made the first attempt at calculating *all* the vibrational bound states using the same potential. A second attempt was made by Henderson *et al* [40] achieving a better convergence of ≈ 2 cm^{-1}.

Next, Bramley *et al* [41] used a novel approach based upon an efficient iterative diagonalisation of a sparse Hamiltonian to calculate all the bound states to a much higher accuracy of about 0.01 cm^{-1}. Their approach allowed for a very efficient calculation of the vibrational energies but not the wave functions which could only be produced at a considerable cost. Although the use of a potential that is not strictly valid at dissociation [38] make these results somewhat qualitative in nature and also easier to calculate than for a potential that behaves correctly at dissociation.

Later, Mandelshtam and Taylor [42] calculated all the bound states using a new filter diagonalisation technique [43; 44]. They also calculated a number of vibrational resonances — Feshbach resonances — using a complex absorbing potential method very simliar to the method used here in chapter 9. Again, as the behaviour of the potential of Meyer *et al* [38] used in this calculation is not correct at dissociation these results are somewhat qualitative and easier to calculate.

In 2003 Kostin *et al* [45] used a new surface [46] to calculate near-dissociation states. This new surface made calculations much more difficult, the dissociation

channels close to dissociation allowing for very long states and therefore requiring much larger basis sets. With this surface they did manage to calculate a large number of states up to dissociation, but with fairly poor convergence.

Calculations of rotational states are somewhat harder again. The number of states for a particular J scales at roughly $(2J + 1)$ and the basis set size required scales at a similar and perhaps worse rate. There have only been three attempts at calculating ro-vibrational states all the way up to dissociation. Henderson and Tennyson for $J = 1, 2$ [47], Kostin *et al* for $J = 2, 8$ [45] and those presented here for $J = 3$.

Chapter 2

Theoretical Background

The theory of di-atomics is well developed and has seen an accuracy of calculation that has approached that of experiment, even at energies close to dissociation [48] and at very long range [49]. However, for three atom molecules – the simplest of which is H_3^+ – this is not the case, although low and medium energy results are well understood and have been calculated to high accuracy [50]. Just as the step from two-body problems to three-body problems in classical physics is a difficult one, so it is in quantum mechanics. Here the situation is complicated slightly by the fact that H_3^+ contains five bodies. However, here we shall just be considering the nuclear motion behaviour. This means that within the Born–Oppenheimer approximation we have a three body problem, nuclei moving on a potential energy surface.

2.1 The molecular hamiltonian

The time-independent molecular Hamiltonian is the starting point for the bound state calculations. It describes the complete system and can, if desired, include relativistic or spin terms. Table 2.1 lists all the terms in the molecular Hamiltonian.

We start with the general time independent Schrödinger equation, $\hat{H}\Psi = E\Psi$ and we expand the molecular Hamiltonian $\hat{H}$,

$$\hat{H} = \hat{T}_n + \hat{H}_e \tag{2.1}$$

which is the sum of the nuclear kinetic energy,

$$\hat{T}_n = -\frac{\hbar^2}{2m_p}(\nabla^2_{\mathbf{x_1}} + \nabla^2_{\mathbf{x_2}} + \nabla^2_{\mathbf{x_3}}) \tag{2.2}$$

Table 2.1: Terms in the complete molecular Hamiltonian $\hat{H}$. Formalism due to Bunker and Jensen [8].

Term	Description
$\hat{T}$	Kinetic Energy ($\hat{T}_{\text{cm}} + \hat{T}^0 + \hat{T}'$)
$\hat{T}_{\text{cm}}$	Kinetic energy of the centre of mass
$\hat{T}^0$	Intra-molecular kinetic energy ($\hat{T}_n + \hat{T}_e$)
$\hat{T}'$	Cross terms in intra-molecular kinetic energy
$\hat{V}$	Electrostatic potential energy ($V_{ee} + V_{nn} + V_{ne}$)
$\hat{H}_{\text{es}}$	Interaction energy of the electron spin magnetic moments ($\hat{H}_{\text{so}} + \hat{H}_{\text{sr}} + \hat{H}_{\text{ss}}$)
$\hat{H}_{\text{so}}$	Electron spin–electron orbit interaction
$\hat{H}_{\text{sr}}$	Electron spin–nuclear motion interaction
$\hat{H}_{\text{ss}}$	Electron spin–electron spin interaction
$\hat{H}_{\text{hfs}}$	Interaction energy of the nuclear magnetic and electric moments ($\hat{H}_{\text{ns}} + \hat{H}_{\text{quad}}$)
$\hat{H}_{\text{ns}}$	Interaction energy of the nuclear spin magnetic moments ($\hat{H}_{\text{nso}} + \hat{H}_{\text{nsr}} + \hat{H}_{\text{nss}} + \hat{H}_{\text{nses}}$)
$\hat{H}_{\text{nso}}$	Nuclear spin-electron orbit interaction
$\hat{H}_{\text{nsr}}$	Nuclear spin-nuclear motion interaction
$\hat{H}_{\text{nss}}$	Nuclear spin-nuclear spin interaction
$\hat{H}_{\text{nses}}$	Nuclear spin-electron spin interaction
$\hat{H}_{\text{quad}}$	Interaction energy of the nuclear electric quadrupole moments with the electric field gradients

and the electronic Hamiltonian ($\hat{H}_e$). Here m_p is the mass of the proton and $\nabla^2_{\mathbf{x}}$ is the usual Laplacian for proton $\mathbf{j}$ at position $\mathbf{x_j}$ in some coordinate system (which includes a spin coordinate). The electronic Hamiltonian ($\hat{H}_e$) is itself the sum of the electronic kinetic energy ($\hat{T}_e$), the positive electron – electron potential energy (V_{ee}), the positive nuclei – nuclei potential energy (V_{nn}), and all the negative cross terms (V_{ne}),

$$\hat{H}_e = \hat{T}_e + V_{ee} + V_{nn} + V_{ne} \tag{2.3}$$

where, for H_3^+,

$$\hat{T}_e = -\frac{\hbar^2}{2m_e}(\nabla^2_{\chi_1} + \nabla^2_{\chi_2}) \tag{2.4}$$

$$V_{ee} = +\frac{e^2}{4\pi\epsilon_0}\left(\frac{1}{|\chi_1 - \chi_2|}\right) \tag{2.5}$$

$$V_{nn} = +\frac{e^2}{4\pi\epsilon_0}\left(\frac{1}{|\mathbf{x_1} - \mathbf{x_2}|} + \frac{1}{|\mathbf{x_2} - \mathbf{x_3}|} + \frac{1}{|\mathbf{x_3} - \mathbf{x_1}|}\right) \tag{2.6}$$

$$V_{ne} = -\frac{e^2}{4\pi\epsilon_0}\left(\sum_i^{1,2}\sum_j^{1,2,3}\frac{1}{|\chi_\mathbf{i} - \mathbf{x_j}|}\right), \tag{2.7}$$

here $\chi_\mathbf{i}$ is the position of electron $\mathbf{i}$.

Except for considering the effects of relativistic quantum mechanics (the small spin interaction terms) this provides a complete description of H_3^+. By constructing this Hamiltonian, or at least a good approximation to it, we can solve for all the bound state energies and wave functions. A description and method for solving the un-bound system will be discussed below.

2.1.1 Approximations

The full Schrödinger equation of the molecule is far too difficult to solve perfectly. In order to make this computationally possible a number of the terms are ignored. Additional approximations are also brought in during the calculation stage, such as quadrature approximations and finite basis sets, to make the solution of our approximate Hamiltonian possible.

In this work, the terms are treated as follows,

$\hat{\mathbf{T}}_{\mathbf{cm}}$ Calculations are performed in the molecules frame of reference, in internal coordinates. $\hat{T}_{\mathrm{cm}}$ is therefore zero.

$\hat{\mathbf{T}}^{\mathbf{0}}$ All terms are included in the calculation.

$\hat{\mathbf{T}}'$ Some of the cross terms are zero by construction. The nuclear cross terms are zero because of the orthogonal internal coordinates. The cross term between the two electrons is included in the electronic potential. The small nuclei–electron cross terms are not included as part of the Born–Oppenheimer approximation.

$\mathbf{V}$ The electrostatic potential energy is included, even including the electron – electron potential in the solution to the electron problem.

$\hat{\mathbf{H}}_{\mathbf{es}}$ Not included, apart from symmetry considerations.

$\hat{\mathbf{H}}_{\mathbf{hfs}}$ Not included, apart from symmetry considerations.

The problem therefore reduces to what is called the spin-free ro-vibronic Hamiltonian $(\hat{T}^0 + \hat{T}' + V)$.

2.2 The Born–Oppenheimer approximation

The first approximation made is the Born-Oppenheimer approximation. We note that the electron velocity is much greater than the proton velocity, because the electron is so much lighter. We can see that the state of the electrons will change (almost) instantaneously in response to any nuclear motion. Therefore it is reasonable to solve the electronic Schrödinger equation by keeping the terms parametric with respect to the proton positions $\mathbf{x_j}$,

$$H_e(\mathbf{x_j}; \chi_\mathbf{i})\psi_e(\mathbf{x_j}; \chi_\mathbf{i}) = E_e(\mathbf{x_j})\psi_e(\mathbf{x_j}; \chi_\mathbf{i}) \tag{2.8}$$

This results in a set of electronic states ψ_e and energies E_e which depend parametrically upon $\mathbf{x_j}$. Solving the ro-vibronic Hamiltonian for the nuclear motion states is then done by solving,

$$(T_n + V_e)\psi_{rv} = E_{rv}\psi_{rv}, \tag{2.9}$$

where the energies parametric in nuclei position (E_e) becomes the potential energy of the ro-vibrational hamiltonian (V_e) or the Born-Oppenheimer potential.

The calculation of Born–Oppenheimer potentials is a difficult problem in itself. For a floppy molecule, such as H_3^+, or when high energies are considered this involves solving the electron problem (H_e) for a wide range of nuclear configurations $\mathbf{x_i}$. For H_3^+ there have been several calculations of electronic surfaces [51; 52; 38; 53; 54; 46; 55], four of which have been constructed to work at high energy [52; 54; 46; 55]. However, only the surface of Polyansky *et al* (PPKT) [46] and the surface of Aguado *et al* [55] have the correct long range terms and can be considered to describe the

dissociative properties of the molecule accurately. A corrected version of the PPKT potential [56] is almost exclusively used in this work.

2.3 The variational principle

The variational principle underlies our calculation of the bound states of H_3^+ and for the ground state can be expressed as,

$$E_0^{\text{trial}} = \left\langle \Psi^{\text{trial}} \middle| \hat{H} \middle| \Psi^{\text{trial}} \right\rangle \geq E_0 \tag{2.10}$$

where the trial wave function (Ψ^{trial}) can only overestimate the ground state energy (E_0) of the Hamiltonian ($\hat{H}$) and therefore forms an upper bound (E_0^{trial}) for the ground state energy. This is the basis of the Rayleigh-Ritz variational method where Ψ^{trial} is chosen to be a function of a number of parameters which are then varied so as to minimise E^{trial}.

In the more general case where we want to calculate more than one bound state and use a basis set expansion, upper state trial functions can be constructed which each form upper bounds to the successive excited state energies (E_n) of the Hamiltonian. Increasing the basis set size (N) of an orthogonal basis (Φ) can only make the basis set more complete and the estimates better. Alternatively, this can be understood as the trial functions only becoming better by considering a trial wave function expanded in terms of an orthogonal basis Φ_n,

$$\Psi^{\text{trial}(N)} = \sum_{n=1}^{N} c_n \Phi_n, \tag{2.11}$$

increasing the basis to $N+1$ gives

$$\Psi^{\text{trial}(N+1)} = \left(\sum_{n=1}^{N} c_n \Phi_n \right) + c_{N+1} \Phi_{N+1}. \tag{2.12}$$

$\Psi^{\text{trial}(N)}$ has the extra parameter $c_{N+1}\Phi_{N+1}$, therefore the energy estimate will not increase but may decrease,

$$E_i^{\text{trial}(N)} \geq E_i^{\text{trial}(N+1)}. \tag{2.13}$$

We can actually be even more specific here because the Hylleraas-Undheim theorem [57] tells us that the energy estimates from the $N+1$ basis ($E_i^{\text{trial}(N+1)}$) will be

bounded by the old estimates of $E_{i-1}^{\text{trial}(N)}$ and $E_i^{\text{trial}(N)}$ giving

$$E_i^{\text{trial}(N)} \geq E_i^{\text{trial}(N+1)} \geq E_{i-1}^{\text{trial}(N)}. \tag{2.14}$$

2.4 Symmetry

The total wave function (Ψ) is the product of the electronic wave function (ψ_{e}), the ro-vibrational wave function (ψ_{rv}) and the nuclear spin wave function (ψ_{ns})

$$\Psi = \psi_{\text{e}}\psi_{\text{rv}}\psi_{\text{ns}}. \tag{2.15}$$

As H_3^+ is a fermionic system, Ψ must be anti-symmetric with respect to the permutation of two identical particles. The separation between Ψ_{rv} and Ψ_e exists because of the Born-Oppenheimer approximation. Ψ_e are solutions to the electronic problem and Ψ_{rv} are solutions to the subsequent ro-vibronic Hamiltonian. The separation of $\Psi_e\Psi_{rv}$ from Ψ_{ns} is because the interaction is very weak and in fact we only consider whether Ψ_{ns} has the correct symmetry.

When considering the ro-vibronic states of H_3^+, we refer to the symmetry of Ψ_{rv}, the molecular symmetry. There are two common ways of considering the molecular symmetry, one is to consider the geometry of the system under reflection and rotation, and the point group associated with that geometry, the other method used is to consider what happens under permutations of identical nuclei and/or inversion of the coordinates. As the geometric method is only correct at equilibrium geometries, here we consider the permutation and inversion symmetries instead. However, at equilibrium the molecular symmetry group (MS), formed from elements of the complete nuclear permutation and inversion group (CNPI), is isomorphic with the point group formed from elements of rotation and reflection.

If we let the permutation operations on the three identical nuclei of H_3^+ be represented by three numbers in brackets,

$$(ijk) \quad \text{with} \quad i,j,k = \{1,2,3\} \tag{2.16}$$

where atom 1 is replaced by atom i, atom 2 is replaced by atom j and atom 3 is replaced by atom k, then there are six possible permutations which form the complete nuclear permutation group,

$$\mathbf{G}^{\text{CNP}}(H_3^+) = \mathbf{S}_3 = \{(123),(213),(132),(321),(231),(312)\} \tag{2.17}$$

Table 2.2: The character table for the molecular symmetry group M_{3h}^{MS} and the point group D_{3h} [8].

D_{3h}^{MS}	E	(312) (231)	(213) (132) (321)	E^*	(312)* (213)*	(213)* (132)* (321)*
D_{3h}	E	$2C_3$	$3C_2$	σ_h	$2S_3$	$3\sigma_v$
A_1'	1	1	1	1	1	1
A_1''	1	1	1	-1	-1	-1
A_2'	1	1	-1	1	1	-1
A_2''	1	1	-1	-1	-1	1
E'	2	-1	0	2	-1	0
E''	2	-1	0	-2	1	0

and is a group with 6 elements where (123) is called the identity or null transform E. The inversion of the space fixed axis coordinates offers another energy conserving transformation of the molecule. This inversion group (ε) with elements E and E^* – where * signifies the inversion – allows us to form the complete nuclear permutation and inversion group,

$$\mathbf{G}^{\mathrm{CNPI}}(\mathrm{H}_3^+) = \mathbf{S}_3 \otimes \varepsilon = \left\{ \begin{array}{c} E, (213), (132), (321), (231), (312), \\ E^*, (213)^*, (132)^*, (321)^*, (231)^*, (312)^* \end{array} \right\} \tag{2.18}$$

with 12 elements.

This group $\mathbf{G}^{\mathrm{CNPI}}(\mathrm{H}_3^+)$ is called the Molecular Symmetry group [8] and gives the symmetry of the ro-vibronic wave functions ψ_{rv}. In this case the elements of $\mathbf{G}^{\mathrm{CNPI}}(\mathrm{H}_3^+)$ tell us that this is in fact the molecular symmetry group D_{3h}^{MS}. The character table for the group D_{3h}^{MS} in given in table 2.2. The table shows all 6 irreducible representations of the group. Also given in the table are the equivalent point group transformations for the point group D_{3h}.

It is no accident that at equilibrium the permutation and inversion operations match the rotation and reflection transformations in the near symmetry of a point group. The cyclic permutations (312) and (231) match the C_3 rotations. The pair permutations (213),(132) and (321) match the C_2 rotations. The inversion operation E^* matches the σ_h reflection. The cyclic permutation and inversion operations (312)* and (213)* match the S_3 improper rotations. Finally, the pair permutation and inversion operations (213)*,(132)* and (321)* match the σ_v reflections.

For H_3^+ the 6 representations of the full group D_{3h}^{MS} are often not referred to and as a shortcut the 3 representations of the sub-group C_{3v}, namely A_1,A_2 and E,

Table 2.3: The correlation table for the irreducible representations of D_{3h}, C_{3v} and C_{2v}.

D_{3h}	C_{3v}	C_{2v}
A_1'	A_1	A_1
A_1''	A_2	A_2
A_2'	A_2	B_1
A_2''	A_1	B_2
E'	E	$A_1 + B_2$
E''	E	$A_2 + B_1$

are referred to instead. However, the full symmetry D_{3h} is always implicit in these cases.

In chapter 6, the properties of these representations of D_{3h}^{MS} under permutation are used to determine symmetry of the vibrational bound states despite the fact that it was calculated in another sub-group with lower symmetry, namely C_{2v}^{MS}.

In order that we can move between representations of different groups referring to the same molecule, a table of correlations is given in table 2.3.

2.5 Coordinate systems

H_3^+ has 6 (3N-3) degrees of freedom in its centre of mass frame. By separating these 6 degrees into rotation and vibration degrees of freedom for the molecule we find that all the vibrational motion occurs in the plane of the molecule. The vibrational nuclear motion can then be described by three in-plane coordinates, for example by the three bond-length coordinates or the three normal coordinates.

There are a number of other coordinate systems that can be used for H_3^+. Perhaps the best choice for H_3^+ is hyper-spherical as it can exploit the full S_3 permutation symmetry of the molecule [58]. However, there already exists a suite of programs that work for H_3^+ and its isotopomers, DVR3D [59]. These programs work in both the Jacobi and Radau coordinate systems. In fact, internally they use a representation that generalises between Jacobi, Radau and bond-length bond-angle coordinates [1]. The Jacobi and Radau coordinate systems are both orthogonal coordinate systems that were originally used in astrophysical three body systems.

Jacobi (or scattering) coordinates are defined in terms of a diatomic distance between two of the three nuclei and a Jacobi coordinate that starts at the center of mass of the diatom and ends on the third nuclei, the angle between the diatomic distance and the Jacobi coordinate completing the description. By choosing the Jacobi distance to originate at the centre of mass of the diatom, the kinetic operator

becomes diagonal with respect to the coordinates. This is because this choice makes the off-diagonal reduced mass, μ_{12} equal to zero. Any S_2 permutation symmetry in the diatom can be exploited in Jacobi coordinates because the region with $\theta < 90°$ becomes identical to the region with $\theta > 90°$.

Radau coordinates [60] are slightly harder to visualise. As with Jacobi and bond-length bond-angle coordinates, two radial coordinates and an angle describe the configuration of the molecule. The angle is that between the two radial coordinates and both of those radial coordinates terminate on nuclei. However, just as with the Jacobi coordinates, the origin of the radial distances is a point chosen so as to make the kinetic energy operator diagonal in the coordinates. Here to, any S_2 permutation symmetry between a diatom can be exploited, but this time by permuting the coordinates R_1 and R_2.

The bond-length bond-angle coordinates are not used in this work but have been used before [61]. The Jacobi and Radau coordinate systems in the context of the Hamiltonian are discussed in more detail in section 3.3.

2.6 Nuclear motion resonances

The near dissociation spectrum of Carrington *et al* [15; 25] probes ro-vibrational states which are in the range $-1,100$ cm^{-1} to $2,000$ cm^{-1} with respect to the dissociation energy of H_3^+ into the fragments $H_2 + H^+$ (D_0) [62]. It appears that major features of the spectrum are formed from resonances above the dissociation energy but within this range. It is clear that in order to understand this spectrum we need to calculate states in the continuum above the dissociation energy. The most important states above dissociation are the ones which form the resonances, long-lived or meta-stable states.

The square integrable basis (L^2 in Hilbert space) of bound state Hamiltonian problems do not allow for the calculation of any states above the dissociation energy of a molecule. This is because the free wave functions are not normalisable, are therefore no longer in L^2 and are no longer accessible to basis set expansion. However a number of methods have been created to allow for the efficient calculation of these states in the continuum using a method which is still time-independent and extends the bound state calculations. These so called L^2 methods of calculating the energies and widths of resonances are discussed after a brief description of the different resonance types.

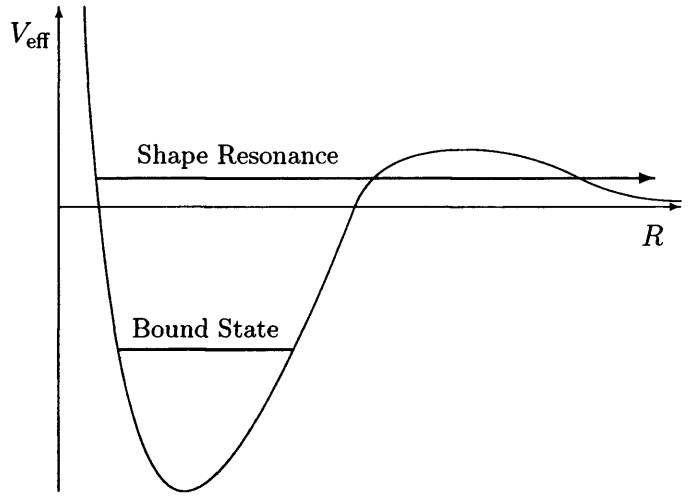

Figure 2.1: Effective potential energy (V_{eff}) formed from the molecular Morse-like potential and the centrifugal term ($1/r^2$)

2.6.1 Shape resonances

Shape resonances occur when the molecule rotates ($J > 0$) and a $V \propto 1/r^{-2}$ centrifugal term appears in the effective potential. Shape resonances are a purely quantal phenomenon as in the classical case with $\hbar \rightarrow 0$, there is no tunnelling and the state becomes bound by the centrifugal term. Figure 2.1 shows a schematic of how a shape resonance can be trapped by an effective barrier in a one-dimensional potential.

2.6.2 Feshbach resonances

A Feshbach resonance is a state which can form when a system has more than one degree of freedom, where the energy of the state is temporarily contained in degrees of freedom which do not dissociate. However, the system must couple these degrees of freedom to ones which do actually dissociate. Otherwise, the state would not be a resonance state but a bound state. The strongest Feshbach resonances form when the system only couples to degrees of freedom which dissociate weakly. This concept is valid for both classical and quantum systems and therefore, unlike the shape resonances, these occur in both classical and quantum systems and for vibrational states.

2.6.3 L^2 methods

Two common methods for calculating the positions and widths of resonances that use an L^2 basis and can extend bound state calculations are the Complex Scaling

method and the Complex Absorbing Potential method. In both of these methods the Hamiltonian becomes complex and resonances become associated with poles in the lower-half complex plane. The complex position of a pole (the Siegert energy) has real and imaginary parts,

$$E_{res} = E_R - i\frac{\Gamma}{2}, \tag{2.19}$$

where E_R is the energy of the maximum of the resonance and Γ is the width of the resonance. The width is related to the lifetime of a resonance by

$$\tau = \hbar/\Gamma. \tag{2.20}$$

2.6.3.1 The complex scaling method

An important L^2 method is the complex scaling method [63; 64; 65; 66]. By rotating the coordinates of a resonant wave function into the complex plane it becomes L^2 and therefore it can then be calculated using a basis set expansion.

The complex-scaling operator is normally given by

$$\hat{S} = e^{i\theta r\frac{\delta}{\delta r}}. \tag{2.21}$$

The complex scaling method is elegant but unfortunately its implementation is complicated as it requires the potential to be extended into the complex plane by analytic continuation. The global potential for H_3^+ [2] is complicated and so this step would prove difficult. An advantage of this method is that its solutions are strictly equivalent to the solutions of the original Hamiltonian and it does not include any un-physical perturbations. The Complex Absorbing Potential method (discussed below) does however include un-physical changes to the Hamiltonian, which is one of its weaknesses. A number of methods have been suggested so as to make complex scaling easier [67; 68; 69] notably smooth exterior scaling [70].

2.6.3.2 The complex absorbing potential method

The complex absorbing potential method (CAP method) also allows for the calculation of the Siegert energies using an L^2 basis. By perturbing the bound state Hamiltonian (H) with a complex potential on a dissociating coordinate ($U(R)$),

$$H'(\lambda) = H - i\lambda U(R) \tag{2.22}$$

and solving the complex symmetric (not Hermitian) matrix (H') for the complex eigenvalues. In the limit of $\lambda \rightarrow 0$ this reduces to the complex scaling method [71]. However, we can see that with a finite basis set the eigenvalues of H' become equal to the eigenvalues of H as $\lambda \rightarrow 0$. In this case we find that the basis set error and the error due to the complex absorbing potential cancel at some critical value, $\lambda = \lambda_c$. At this value (λ_c), the solutions to the eigen-equation of H',

$$H'\Psi_n = E_n\Psi_n = (\epsilon_n - i\frac{\Gamma_n}{2})\Psi_n \tag{2.23}$$

give the correct resonance position ϵ_n and width Γ_n for a particular state n. We can see that λ_c is different for each n as the basis set error and the effect of the CAP will change for each state.

The time-dependent interpretation of the CAP is that it removes un-physical reflections caused by the finite grid and instead absorbs the out going wave-packet. The wave-packet therefore behaves just as it would on an infinite grid within the region bounded by the CAP, for this reason the CAP is placed at long range where ideally the potential is close to its free-particle asymptote. However, construction of a perfect CAP with zero reflection and one hundred percent absorption is non trivial and may not even be possible. Fortunately we can get close, one of the CAPs used in this work [3] is completely absorbing by construction – with a vertical asymptote at R_{max} – and minimally reflective. In practice the CAP error proves to be smaller than the basis set error (see chapter 9). The fact that it absorbs a wave-packet completely would suggest that it cannot reflect, however this can be understood by realising that the CAP does not conserve the norm and some of the wave-packet is both reflected and absorbed.

Not all the solutions to H' are resonances. The solutions can be categorised because they behave in different ways, essentially responding to the presence of the CAP depending on their own character. The bound states of the molecule do not couple to the CAP (within the finite basis set error) as

$$\langle \Psi_n | U | \Psi'_m \rangle \approx 0 \quad \text{for} \quad E_{\{n,m\}} \leq D_0 \tag{2.24}$$

and so the eigenvalues (E_n) lie on the real axis, consistent with the idea that bound states have infinite lifetimes or infinitesimal widths. Diverging states are formed with λ trajectories ($E(\lambda)$), where the imaginary part of energy increases quickly with λ. These are not resonances but merely continuum states of the molecule, sometimes called rotating continua because the CAP's effect is similar to the effect of rotating states in the Complex Scaling method [72]. This again is consistent as the large

imaginary part gives a large width Γ and therefore a very short lifetime. The actual resonant states of the molecule form trajectories which do not move away from the real axis as quickly and instead form cusps or turning points in the complex plane.

In our problem the bound state calculations are carried out in the real number space, as that is all that is required for time-independent problems. The solutions from the bound state calculations are then used as both the basis for the resonance calculation and an estimate of the Hamiltonian

$$\langle \Psi_n | H' | \Psi_m \rangle = \epsilon_n \delta_{nm} - i\lambda \langle \Psi_n | U | \Psi_m \rangle . \tag{2.25}$$

This results in a complex symmetric Hamiltonian matrix instead of the usual Hermitian Hamiltonian. As the Hamiltonian matrix now gives,

$$\mathbf{H^T} = \mathbf{H} \tag{2.26}$$

we get left and right eigenvectors which are no longer the complex conjugate of each other but just the transpose of each other

$$(\mathbf{\Psi^L})^\mathbf{T} = \mathbf{\Psi^R}. \tag{2.27}$$

However, the norm is still usually defined as the Euclidean norm

$$\|\mathbf{\Psi}\| = \sqrt{\sum_i |\Psi_i|^2}. \tag{2.28}$$

There has been some previous work on the nuclear resonance states of triatomics using the Complex Absorbing Potential method. Mandelshtam and Taylor [42] calculated a number of vibrational Feshbach resonances for H_3^+ using an efficient filter diagonalisation technique. A number of calculations have been performed on HOCl [73; 74; 75], HCO [76; 77; 78; 79; 80] and HNO [81], which prove to be easier problems than H_3^+. A number of these calculations including rotational Feshbach resonances among their results.

The first calculation to identify shape resonances for a tri-atomic was performed by Mussa and Tennyson on HOCl [82; 83] using a method very similiar to that described here. They discovered four rotating resonances with no J=0 and therefore no Feshbach resonance counterpart. In chapter 9 the details of resonance calculations and the particulars of the CAPs are explored along with a set preliminary calculations.

Chapter 3

The DVR3D Program Suite

The DVR3D [59; 84; 85] program suite has been developed over many years to calculate a broad range of tri-atomic properties to high accuracy. The suite of programs is called DVR3D because it performs a full 3D calculation using a Discrete Variable Representation (DVR) method. It is composed of several parts, the major parts being DVR3DRJZ, ROTLEV3, ROTLEV3B, ROTLEV3Z, DIPOLE3 and SPECTRA. The first part DVR3DRJZ computes the vibrational nuclear motion states within the Born-Oppenheimer approximation with an electronic potential energy surface (PES). Although, in some cases the program includes small corrections to this, either through corrections to the single valued PES or through the correction and separation of masses into vibrational and rotational components. DVR3DRJZ also computes the first step vibrational basis which form an optimised basis under truncation for the full ro-vibrational calculations. ROTLEV3(B,Z) then combines the first step calculations with additional rotational and Coriolis terms to complete the calculation of the ro-vibrational states. DIPOLE3 then computes the dipole moments as an expectation value using a body-fixed dipole moment and the computed wave functions. Finally, SPECTRA produces synthetic spectra based on a number of parameters, such as temperature.

In this work we shall be focusing on DVR3DRJZ and ROTLEV3Z as, at this stage, we will be concerned with the calculation of the ro-vibrational states of H_3^+. The DVR3D program suite can perform the calculation in a number of ways. Firstly, there is the coordinate system, this can be either the Radau or Jacobi coordinate systems, in fact the program is based upon a generalisation between a number of three body coordinate systems [1]. Secondly, there is the choice of the body-fixed embedding of coordinates used for the rotational calculation in ROTLEV3(B,Z). ROTLEV3 embeds the z-axis along one of the vibrational coordinates, ROTLEV3B

embeds the z-axis in the plane of the molecule by bisecting the vibrational coordinates and ROTLEV3Z embeds the z-axis perpendicular to the plane of the molecule. The choice of which rotational embedding to use depends on the coordinate system used in the vibrational step (Jacobi or Radau) and a number of decisions can be made here to optimise the calculation. The calculations we will be presenting below use the Radau coordinates with a rotational embedding which has the z-axis perpendicular to the plane of the molecule. This embedding is likely the best choice for the K basis quantisation of rotational states in H_3^+ [86], where K is the projection of the rotational angular momentum J on the z axis.

The symmetry of C_{2v} molecules, such as D_2H^+ can also be exploited in the Radau and Jacobi coordinate systems, this is also taken full advantage of in DVR3D. Unfortunately the full D_{3h} symmetry of H_3^+ is not easily revealed in the Radau or Jacobi coordinate systems, whereas it could be exploited in, for instance, hyperspherical coordinates [58].

3.1 Finite basis representations

A finite basis representation (FBR) is variational technique for calculating bound states where the basis functions are a finite set of orthogonal polynomials. Typically polynomials that allow terms to be evaluated analytically or via a suitable Gaussian quadrature scheme is used. Wave functions are therefore linear combinations of these orthogonal polynomials and as the order of the polynomials is increased the representation becomes better.

3.2 Discrete variable representations

A Discrete Variable Representation (DVR) is an improvement in many ways to a FBR. It is a computational method that can be based on any Gaussian quadrature scheme appropriate for the basis being used. It provides a unitary transformation of that basis, that diagonalises a number of Hamiltonian terms with respect to the coordinates in question given some, N-point, Gaussian quadrature scheme for the basis polynomials. With abscissa η and weights w_η, we can transform the polynomial basis to a DVR basis,

$$T_\eta^t = \sqrt{w_\eta}|t(\eta)\rangle \tag{3.1}$$

where $|t\rangle$ is the polynomial basis function [87]. With this transform we find that terms in the Hamiltonian are partially or wholly diagonalised. For instance, the

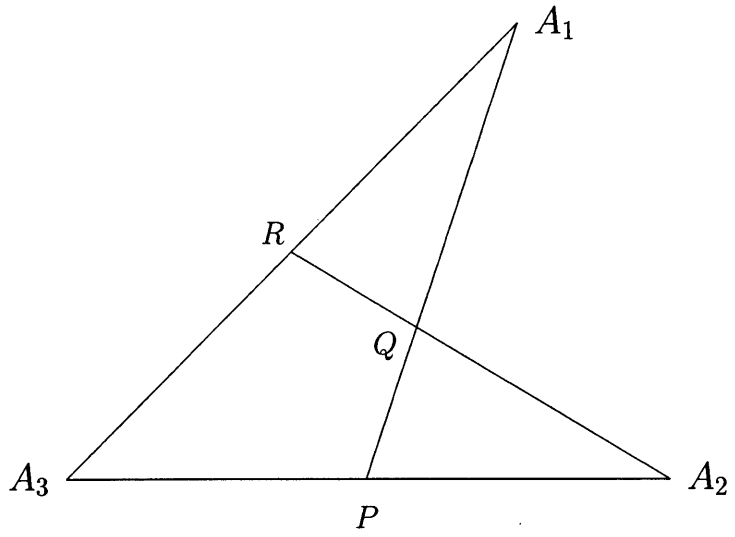

Figure 3.1: A generalised coordinate system for triatomic molecules. A_i represents the position of atom i with mass m_i and R, Q, P move so as to define a particular set of body-fixed coordinates [1].

potential is diagonalised because of the quadrature approximation

$$\sum_{mnj} \sum_{m'n'j'} T_m^\alpha T_n^\beta T_j^\gamma V_{m'n'j'}^{mnj} T_{\alpha'}^{m'} T_{\beta'}^{n'} T_{\gamma'}^{j'} = V_{\alpha\beta\gamma} \delta_{\alpha\alpha'} \delta_{\beta\beta'} \delta_{\gamma\gamma'}, \tag{3.2}$$

where m, n, j index the three FBR basis functions and α, β, γ index the DVR points, as demonstrated by Light *et al* in 1985 [87]. There have been many implimentations of DVR type schemes in the past, the method presented here is but one of many possible approaches [88].

3.3 Coordinate systems

The coordinate systems are defined using two parameters (g_1,g_2) that generalise between Jacobi, Radau, bondlength–bondangle and other coordinates. Figure 3.1, shows how the tri-atom is interpreted within this scheme by Sutcliffe and Tennyson [1].

The coordinates are defined as

$$R_1 = |\vec{A_2} - \vec{R}| \tag{3.3}$$

$$R_2 = |\vec{A_1} - \vec{P}| \tag{3.4}$$

$$\theta = \widehat{A_1 Q A_2} \tag{3.5}$$

with the geometric parameters

$$g_1 = \frac{|\vec{A_3} - \vec{P}|}{|\vec{A_3} - \vec{A_2}|} \tag{3.6}$$

$$g_2 = \frac{|\vec{A_3} - \vec{R}|}{|\vec{A_3} - \vec{A_1}|}. \tag{3.7}$$

The reduced masses in this representation are given by,

$$\mu_1^{-1} = g_2^2 m_1^{-1} + m_2^{-1} + (1 - g_2)^2 m_3^{-1} \tag{3.8}$$

$$\mu_2^{-1} = m_1^{-1} + g_1^2 m_2^{-1} + (1 - g_1)^2 m_3^{-1}. \tag{3.9}$$

where m_i is the mass of atom i [1].

3.3.1 Jacobi coordinates

For the Jacobi or scattering coordinates, the point R moves down to meet A_3 and the distance $R_1 = |\vec{A_2} - \vec{R}|$ becomes the inter-atomic distance (r) between atoms 3 and 2. Point P then moves to the centre of the inter-atomic mass giving,

$$g_1 = \frac{m_2}{m_2 + m_3} \tag{3.10}$$

$$g_2 = 0 \tag{3.11}$$

The distance $R_2 = |\vec{A_1} - \vec{P}|$ then becomes the Jacobi distance or the scattering coordinate. For a molecule with a homo-nuclear di-atomic with $m_2 = m_3$, such as H_3^+ and D_2H^+, $g_1 = 1/2$.

3.3.2 Radau coordinates

Within this system the Radau coordinates are not defined as is perhaps usual. Here the distances R_1 and R_2 do not end at the origin of θ (Q) but are instead defined to meet the opposite bondlength coordinate instead. This gives

$$g_1 = 1 - \frac{A}{A + B - AB} \tag{3.12}$$

$$g_2 = 1 - \frac{A}{1 - B + AB} \tag{3.13}$$

with

$$A = \sqrt{\frac{m_3}{m_1+m_2+m_3}} \tag{3.14}$$

$$B = \frac{m_2}{m_1+m_2}. \tag{3.15}$$

For a molecule with $m_1 = m_2$ such as H_3^+ and D_2H^+, this simplifies to become,

$$g_1 = 1 - \frac{2A}{A+1} \tag{3.16}$$

$$g_2 = 1 - \frac{2A}{A-1}. \tag{3.17}$$

3.4 Vibrational calculations

The problem is split into vibrational and rotational steps, for $J = 0$ only the vibrational step is necessary as the rotational (T^{rot}) and coriolis (T^{cor}) terms (defined later) are zero for $J = 0$. The vibrational Hamiltonian is therefore [1]

$$\begin{aligned}\hat{H}^{J=0} &= T^{\text{vib}} + V \\ &= -\frac{1}{2m_1}\frac{\partial^2}{\partial R_1^2} - \frac{1}{2m_2}\frac{\partial^2}{\partial R_2^2} - \left(\frac{1}{2m_1R_1^2} + \frac{1}{2m_2R_2^2}\right)\frac{\partial}{\partial c}(1-c^2)\frac{\partial}{\partial c} + V(R_1, R_2, c).\end{aligned} \tag{3.18}$$

where $c = cos(\theta)$ and V is the Born-Oppenheimer potential.

3.5 Basis sets

DVR3D supports a number of basis sets. For radial coordinates, Morse oscillators [89] or Spherical oscillators [90] can be used. In our calculations, the Jacobi basis was constructed from Morse Oscillators on r, Spherical Oscillators on R and normalised Legendre polynomials on $\cos\theta$. The reason for using spherical oscillators on R is because they can represent states with significant amplitude at linear configurations. For the Radau coordinate calculations, we tested both Morse oscillators and spherical oscillators in the radial coordinates. The angular basis on θ for the Radau calculations is the same as for the Jacobi calculations and are defined as $|j\rangle = P_j(\cos\theta)$ where P_j are the usual normalised Legendre polynomials.

3.5.1 Morse oscillators

The Morse oscillators are an efficient basis for the representation of diatomic nuclear motion. This is because they are derived from solutions to the Morse potential

$$V(r) = D_e[1 - e^{r-r_e}]^2 \tag{3.19}$$

with dissociation energy D_e and equilibrium bondlength r_e. This closely matches diatomic forces within the Born-Oppenheimer approximation. By extending the ground state solution to this we can construct a basis given by

$$H_n(r) = \sqrt{\beta} N_{n\alpha} e^{-\frac{y}{2}} y^{\frac{\alpha+1}{2}} L_n^{\alpha}(y) \tag{3.20}$$

where

$$y = Ae^{-\beta(r-r_e)} \tag{3.21}$$

$$A = \frac{4D_e}{\omega_e} \tag{3.22}$$

$$\beta = \omega_e \sqrt{\frac{\mu}{2D_e}} \tag{3.23}$$

$$\alpha = \text{int}(A) \tag{3.24}$$

with μ being the reduced mass and ω_e analogous to the fundamental frequency of the molecule. In actuality these parameters are not fixed by properties of the molecule but are variationally optimised for the particular problem.

However there is a problem when using high-order Morse oscillators, as these solutions are approximate and orthogonal over the unphysical range $(-\infty, \infty)$ instead of the physical $[0, \infty)$. This can be seen because here the Laguerre polynomials as functions of y are defined to be orthogonal over the range $[0, \infty)$ which gets transformed to the $(-\infty, \infty)$ range over r by equation 3.21. Therefore, when the zeros of $L_n^{\alpha}(y)$ become larger than

$$b = Ae^{\beta r_e} \tag{3.25}$$

r becomes less than zero. The high-N polynomials have negative zeros; the use a DVR basis with negative points in its abscissa is then problematic.

Solutions to the Morse potential over the r range of $[0, \infty)$ do exist [91] but are harder to calculate. The solutions are given by

$$\Phi_n(y) = C_n y^{(2D_e - n - \frac{1}{2})} e^{-\frac{y}{2}} {}_1F_1(-1; 4D_e - n + \frac{1}{2}; y) \tag{3.26}$$

where ${}_1F_1$ denotes the confluent hyper-geometric function and C_n is an appropriate normalisation. These solutions are orthogonal over the r interval $[0, \infty)$ or the y interval $[0, b]$ and will not give rise to unphysical DVR points. But here the problem would actually being able to construct a workable quadrature scheme from these functions.

Another alternative is to ignore Morse potential and instead construct a new basis from polynomials with the same weighting function as the Morse oscillators – the associated Laguerre weighting function ($e^{-y}x^{\alpha}$) – but orthogonal over the semi-infinite r range of $[0, \infty)$ instead of $(-\infty, \infty)$. The orthogonality condition for these new polynomials $M_n^{\alpha}(y)$ over the y range of $[0, b]$ is then given by

$$\int_0^b e^{-y}x^{\alpha}M_n^{\alpha}(y)M_m^{\alpha}(y)dy = h_n\delta_{nm}. \tag{3.27}$$

Often the Dirac notation is used in this context, the weighting function and limits are assumed:

$$\langle M_n^{\alpha}|M_m^{\alpha}\rangle = h_n\delta_{nm}. \tag{3.28}$$

If we use the Gram-Schmidt orthogonalisation technique we can generate these polynomials analytically. The Gram-Schmidt technique uses the following recurrence relation to generate a set of orthogonal polynomials,

$$M_n^{\alpha}(x) = \left(x - \frac{\langle xM_{n-1}^{\alpha}|M_{n-1}^{\alpha}\rangle}{\langle M_{n-1}^{\alpha}|M_{n-1}^{\alpha}\rangle}\right)M_{n-1}^{\alpha}(x) - \left(\frac{\langle M_{n-1}^{\alpha}|M_{n-1}^{\alpha}\rangle}{\langle M_{n-2}^{\alpha}|M_{n-2}^{\alpha}\rangle}\right)M_{n-1}^{\alpha}(x). \tag{3.29}$$

We start the recurrence relation off using $M_0^{\alpha}(x) = 1$ and $M_{-1}^{\alpha} = 0$, in order to create a set of monic polynomials, this leads to the following expressions for the polynomials of order 1 and 2,

$$M_1^{\alpha}(x) = x - \frac{\langle x|1\rangle}{\langle 1|1\rangle}, \tag{3.30}$$

$$M_2^{\alpha}(x) = \left(x - \frac{\langle xM_1^{\alpha}|M_1^{\alpha}\rangle}{\langle M_1^{\alpha}|M_1^{\alpha}\rangle}\right)M_1^{\alpha}(x) - \frac{\langle M_1^{\alpha}|M_1^{\alpha}\rangle}{\langle 1|1\rangle}. \tag{3.31}$$

The next step is to compute the integrals in equations (3.30), (3.31) and generally for any polynomial of the type M_n^{α}. This can done in terms of what are called incomplete Γ functions [92]. The usual Γ function is split into lower and upper parts using the limits,

$$\Gamma(\alpha + 1) = \int_0^b e^{-x}x^{\alpha}dx + \int_b^{\infty} e^{-x}x^{\alpha}dx \tag{3.32}$$

the lower part is labelled with γ and the upper part is labelled with Γ giving,

$$\Gamma(\alpha+1) = \gamma(\alpha+1,b) + \Gamma(\alpha+1,b). \tag{3.33}$$

The part that interests us here is the lower incomplete γ function as this covers the same finite interval $[0,b]$ as our integrals (equation 3.27). The usual recurrence relation for the complete Γ function,

$$\Gamma(\alpha+1) = \alpha\Gamma(\alpha) \tag{3.34}$$

becomes slightly more complicated,

$$\gamma(\alpha+1,b) = \alpha\gamma(\alpha,b) - b^{\alpha}e^{-b} \tag{3.35}$$

but is still useful for calculating terms of different powers.

Using this we can integrate over any of the polynomial terms ($C_p x^p$) with our desired limits and weighting function,

$$C_p\gamma(\alpha+p+1,b) = \int_0^b (C_p x^p)(e^{-x}x^{\alpha})dx. \tag{3.36}$$

The first polynomial generated is then given by,

$$M_1^{\alpha}(x) = x - \frac{\gamma(\alpha+2,b)}{\gamma(\alpha+1,b)}. \tag{3.37}$$

It is possible to create a workable numerical quadrature scheme using this result.

However, a bigger problem remains with all of these Morse-like bases, none of these bases allow for the good representation of wave functions with significant amplitude at $r = 0$. This is most obvious for the Jacobi R coordinate, as soon as the molecule can become linear – at about 14,000 cm^{-1} above the potential minimum for H_3^+ – the R coordinate can go to zero and states of H_3^+ may have significant amplitude at that geometry. One of the major benefits of the Radau coordinates is that the radial coordinates do not normally go to zero. But in fact for H_3^+ they can go to zero, just at a much higher energy, quite close to but below the dissociation energy for H_3^+. Therefore if we are to calculate all the states of H_3^+ up to dissociation and even beyond we must use another basis for the radial coordinates.

3.5.2 Spherical oscillators

We used spherical oscillators as a basis for both radial Radau coordinates. Spherical oscillators can adequately represent wave functions with significant amplitude at $r = 0$. Spherical oscillators do not tend to converge as quickly as the Morse oscillators at low energy but are required at high energy. They are defined as [90],

$$\begin{aligned} H_n(y) &= \sqrt{2}\sqrt[4]{\beta}N_{n\alpha+\frac{1}{2}}e^{-\frac{y}{2}}y^{\frac{\alpha+1}{2}}L_n^{\alpha+\frac{1}{2}}(y) \\ y &= \beta r^2 \\ \beta &= \sqrt{\mu\omega_e} \end{aligned} \tag{3.38}$$

where α and ω_e are adjustable parameters. L_n^α are the usual associated Laguerre polynomials, μ is the reduced mass in the direction of r and N is the normalisation constant for Laguerre polynomials. In order to represent the amplitude at $r = 0$, a particular value of α has to be chosen, $\alpha = 0$. This because only then can the term $r^{-1}H_n(y)$ take on non-zero values at $r = 0$. This is demonstrated in the section on basis set optimisation later (section 6.3.2.1).

3.5.3 Multidimensional basis functions

A direct-product multi-dimensional basis is formed from the spherical oscillators on R_1, R_2 and Legendre functions on θ.

$$|R_1, R_2, \theta\rangle = |R_1\rangle\,|R_2\rangle\,|\theta\rangle \tag{3.39}$$

In Radau coordinates, we can exploit a permutation symmetry in the radial coordinates if atom 1 and atom 2 are the same. In this case

$$|R_1, R_2\rangle = \pm\,|R_2, R_1\rangle\,. \tag{3.40}$$

This is represented in the 2D radial basis by taking either positive of negative linear combinations (labelled with a parity flag $s = 0, 1$),

$$|R_1, R_2, s\rangle = \frac{1}{\sqrt{2(1+\delta_{R_1,R_2})}}\left(|R_1, R_2\rangle + (-1)^s\,|R_2, R_1\rangle\right). \tag{3.41}$$

3.5.4 Hamiltonian in the DVR basis

The first step or vibrational step, uses a efficient diagonalisation and truncation scheme. Where, in Radau coordinates, solutions to a reduced dimension radial

problem with a frozen angular coordinate are treated as an optimised basis for the solution of the full $3D$ calculations.

Within the truncation scheme outlined above and when atom 1 and 2 are the same we get a symmetrised two dimensional Hamiltonian defined by

$$\begin{aligned} H^{2D}(\gamma)_{\alpha\alpha'\beta\beta'} = & \\ & (1+\delta_{\alpha\beta})^{-\frac{1}{2}}(1+\delta_{\alpha'\beta'})^{-\frac{1}{2}}\left(K_{\alpha\alpha'}\delta_{\beta\beta'} + (-1)^s K_{\alpha\beta'}\delta_{\beta\alpha'}\right. \\ & \left. + (-1)^s K_{\beta\alpha'}\delta_{\alpha\beta'} + K_{\beta\beta'}\delta_{\alpha\alpha'} + V(\alpha,\beta,\gamma)\delta_{\alpha\alpha'}\delta_{\beta\beta'}\right) \end{aligned} \tag{3.42}$$

where α, β and γ index the DVR basis points and $K_{\eta,\eta'}$ is part of the DVR transformed kinetic energy operator

$$K_{\eta,\eta'} = \sum_{i,i'} T_i^{\eta} \left\langle i \left| \frac{-\hbar^2}{2\mu}\frac{\partial^2}{\partial R^2} \right| i' \right\rangle T_{i'}^{\eta'} \tag{3.43}$$

with the FBR functions indexed by i. $V(\alpha,\beta,\gamma)$ is the potential at the DVR points.

The set of N_γ 2D Hamiltonians are then solved for their $l \times \gamma$ eigenvalues and eigenvectors,

$$H^{2D}(\gamma)C^{2D}_{\gamma l} = \epsilon^{2D}_{\gamma l} C^{2D}_{\gamma l}. \tag{3.44}$$

These solutions are used as an optimised 2D basis for the full 3-dimensional problem. In this basis the 3D DVR Hamiltonian is written as,

$$\begin{aligned} H^{3D}_{\gamma\gamma' ll'} = & \\ & \epsilon^{2D}_{\gamma l}\delta_{\gamma\gamma'}\delta_{ll'} + \sum_{\beta}^{\beta-s}\sum_{\alpha=1}\sum_{\beta'}^{\beta'-s}\sum_{\alpha'=1}(1+\delta_{\alpha\beta})^{-\frac{1}{2}}(1+\delta_{\alpha'\beta'})^{-\frac{1}{2}} C^{2D}_{\gamma\alpha\beta l} C^{2D}_{\gamma'\alpha'\beta' l'} \\ & \left(L_{\alpha\alpha'\gamma\gamma'}\delta_{\beta\beta'} + (-1)^s L_{\alpha\beta'\gamma\gamma'}\delta_{\beta\alpha'} + (-1)^s L_{\beta\alpha'\gamma\gamma'}\delta_{\alpha\beta'} + L_{\beta\beta'\gamma\gamma'}\delta_{\alpha\alpha'}\right) \end{aligned} \tag{3.45}$$

where $L_{\eta,\eta',\gamma,\gamma'}$ is the part of the kinetic energy that couples angular terms. $L_{\eta,\eta',\gamma,\gamma'}$ is given by

$$L_{\eta,\eta',\gamma,\gamma'} = J_{\gamma,\gamma'} \sum_{i,i'} T_i^{\eta} \left\langle i \left| \frac{\hbar^2}{2\mu R^2} \right| i' \right\rangle T_{i'}^{\eta'} \tag{3.46}$$

$J_{\gamma,\gamma'}$ is defined by

$$J_{\gamma,\gamma'} = \sum_j T_j^{\gamma} j(j+1) T_j^{\gamma'} \tag{3.47}$$

with j indexing the angular FBR functions. $L_{\eta,\eta',\gamma,\gamma'}$ can be evauluated using the

quadrature approximation,

$$L_{\eta,\eta',\gamma,\gamma'} \approx \frac{J_{\gamma,\gamma'}\hbar^2}{2\mu R^2}\delta_{\eta,\eta'} \tag{3.48}$$

however the $1/R^2$ term is not polynomial in nature and therefore the quadrature approximation leads to significant errors in the result [40]. Therefore, in this work we calculate the integral analytically despite the extra computational cost.

$$\left\langle i\left|\frac{\hbar^2}{2\mu R^2}\right|i'\right\rangle = \frac{\hbar^2\beta}{(2\alpha+1)\mu}\sqrt{\left(\frac{i!\Gamma(i'+\alpha+3/2)}{i'!\Gamma(i+\alpha+3/2)}\right)} \qquad (i \geq i') \tag{3.49}$$

This method uses the Sutcliffe-Tennyson Hamiltonian [1] in combination with what is called the DVR ray-eigenvector method (DVR-REV) by Bacic and Light [93; 94; 95]. The 3-dimensional Hamiltonian H^{3D} is then diagonalised to get the state energies ϵ and eigenvectors C^{3D} in the 2D basis,

$$H^{3D}C_n^{3D} = \epsilon_n C_n^{3D}. \tag{3.50}$$

In order to calculate the wave functions for states of H_3^+ we must transform these eigenvectors back onto the original basis,

$$\Psi^n_{\alpha,\beta,\gamma} = \sum_l C^{3D}_{\gamma,l,n} C^{2D}_{\alpha,\beta,\gamma,l}. \tag{3.51}$$

3.6 Diagonaliser performance

The solution of the eigen-system here is the primary computational step in calculating the energies and wave functions for our quantum system. However, this is a far from trivial step and achieving computational efficiency is a large subject of research in of itself. Here we utilise the fruits of the ongoing research into the solution of eigen-systems and examine the best algorithms, how they relate to our problem and the best ways of implementing them.

3.6.1 Techniques

The first usual distinction in eigen-solvers is between what is called dense and sparse algorithms. In our case this refers to the structure of the Hamiltonian matrix and in the simplest description whether it is mostly zero or not. Other factors affecting the choice of algorithm are how much working memory is required. What fraction of the solutions are wanted and whether eigenvectors are required and of course the

accuracy of the result. If you were to perform more than one diagonalisation then it would also be important to consider how they are related and whether any advantage can be obtained by chaining calculations together. This is a consideration for the resonance step calculation but not for DVR3D so it will not be discussed here.

LAPACK[96] is perhaps the best collection of linear algebra algorithms available. For symmetric matrix eigen-problems it has four primary routines DSYEV, DSYEVX, DSYEVD and DSYEVR.

DSYEV works by a process called QR factorisation and requires just $3N$ workspace in addition to the Hamiltonian matrix for a problem of size N.

DSYEVX uses an iterative technique to calculate a subset of the eigenvalues and eigenvectors and is efficient if only a very small number of solutions are required. In addition to the Hamiltonian it requires an extra $8N + M \times N$ workspace for M solutions.

DSYEVD uses a recursive divide and conquer method. Dividing the problem into smaller sub-problems which are either split again or solved. DSYEVD is very efficient, even for a very difficult problems, but does require an extra $2N^2+6N$ of workspace.

DSYEVR uses the *dqds algorithm* to compute a selected set of eigenvalues and various *Relatively Robust Representations* to calculate the eigenvectors. For a large range of problems it is perhaps the most efficient dense diagonaliser available. However its performance is very problem dependent. It requires and extra $M \times N + 26N$ workspace for M selected solutions.

3.6.2 Performance comparison

As we have seen the Divide and Conquer and Relatively Robust Representation methods both have their advantages over the QR factorisation. However, the important factor is how they actually perform in practice. Here we tested all three as implemented in LAPACK [96] on three modern processors with optimisation. This is shown in figure 3.2, where one can see that the UltraSPARC calculations did not perform as well. However, the important detail is that DSYEVR and DSYEVD both perform better for the Pentium and the PowerPC and DSYEVD performs better for the UltraSPARC. It may appear from the figure that the improvements are not particularly impressive, especially on the PowerPC where perhaps only a third of the time is saved. It should be remembered that this was a small benchmark job ($N_{3D} = 1500$) and that because of the way diagonalisers scale you see increasing

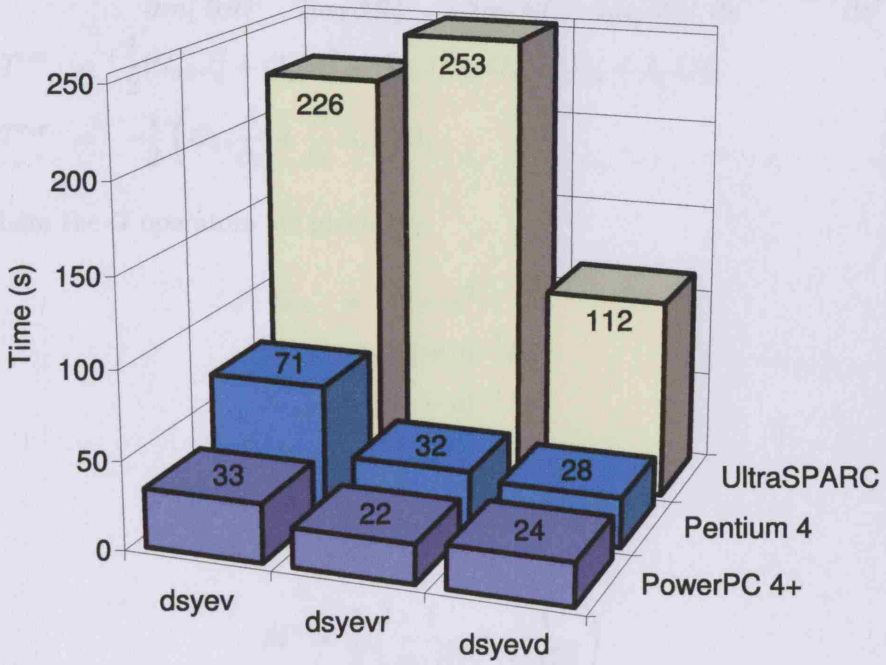

Figure 3.2: Comparison of diagonaliser performance on a number of different machines for a DVR3D job with a final Hamiltonian size of $N_{3D} = 1500$.

returns with increasing size. Also, the times quoted here are the complete DVR3D calculation time not just the diagonalisation time.

3.7 Rotational calculations

The z-perpendicular rotational axis embedding, was developed as part of the DVR3D program suite by Kostin *et al* [97], building on the work of Sarkar *et al* [98] that showed how singularities can be avoided when taking the z-axis perpendicular to the plane of the molecule. The z-perpendicular embedding is an advantage for H_3^+ as the natural quantisation axis for the rotations lies perpendicular to the plane of the molecule [86].

The Hamiltonian is closely related to the vibrational one but now includes extra terms, the potential energy surface remains the same but the kinetic energy operator gains rotational and Coriolis terms. In Radau coordinates we have

$$T = T^{\text{vib}} + T^{\text{rot}} + T^{\text{cor}}, \tag{3.52}$$

where

$$T^{\text{vib}} = -\frac{1}{2m_1}\frac{\partial^2}{\partial R_1^2} - \frac{1}{2m_2}\frac{\partial^2}{\partial R_2^2} - \left(\frac{1}{2m_1R_1^2} + \frac{1}{2m_2R_2^2}\right)\frac{\partial}{\partial c}(1-c^2)\frac{\partial}{\partial c}, \quad (3.53)$$

$$T^{\text{rot}} = \frac{1}{2}[G_{xx}J_x^2 + G_{yy}J_y^2 + G_{zz}J_z^2 + G_{xy}(J_xJ_y + J_yJ_x)], \quad (3.54)$$

$$T^{\text{cor}} = -\frac{i}{2}\left(G_{cz}\frac{\partial}{\partial c} + \frac{\partial}{\partial c}G_{cz}\right)J_z. \quad (3.55)$$

Where the G operators are given by,

$$G_{cz} = (1-c^2)^{1/2}M^- \quad (3.56)$$

$$G_{xx} = (1+c)^{-1}M^+ \quad (3.57)$$

$$G_{yy} = (1-c)^{-1}M^+ \quad (3.58)$$

$$G_{zz} = \frac{1}{2}M^+ \quad (3.59)$$

$$G_{xy} = -(1-c^2)^{-1/2}M^- \quad (3.60)$$

with

$$M^{\pm} = \frac{1}{2}\left(\frac{1}{m_1R_1^2} \pm \frac{1}{m_2R_2^2}\right). \quad (3.61)$$

J_x, J_y and J_z are the standard rotational angular momenta operators and $c = \cos(\theta)$. This is the same form as given by Kostin *et al* [97] and Sarkar *et al* [98].

The choice of the angular basis is important here, we must ensure all the matrix elements are strictly finite, despite the potentially infinite terms when $c = \pm 1$. Sarkar *et al* [98] showed that angular basis functions constructed from Jacobi functions

$$|j\rangle = \frac{1}{\sqrt{h_{jab}}}(1-c)^{\frac{a}{2}}(1+c)^{\frac{b}{2}}P_n^{ab}(c), \quad (3.62)$$

with

$$a = b = \sqrt{[J(J+1) - K^2]/2} \quad (3.63)$$

is just such a basis, where P_j^{ab} are the Jacobi polynomials and h_{abj} are the associated normalisation constants. We can see that equation (3.62) reduces to the Legendre polynomial basis used for the vibrational calculations when $J = 0$.

Building the real Hamiltonian matrix elements using the method of Huber [99]

we get the following rotational basis functions,

$$|JKq\rangle = \begin{cases} i^{-q}\frac{\sqrt{2J+1}}{4\pi}\left[D^{J*}_{K,M} + (-1)^{K+q}D^{J*}_{-K,M}\right] & : \quad K > 0, q = 0, 1 \\ \frac{\sqrt{2J+1}}{2\pi\sqrt{2}}D^{J*}_{K,M} & : \quad K = 0, q = 0 \end{cases} \tag{3.64}$$

where $D^{J}_{K,M}$ are rotation matrices [100].

This basis gives five non-zero terms in the Hamiltonian, the vibrational term is diagonal in all the basis parameters

$$\left\langle JKqj\middle|T^{vib}\middle|JK'q'j'\right\rangle = \tag{3.65}$$
$$\left[-\frac{1}{2m_1}\frac{\partial^2}{\partial R_1^2} - \frac{1}{2m_2}\frac{\partial^2}{\partial R_2^2} - M^+\left((j+a)(j+1+a) - \frac{K^2}{4}\right)\right]\delta_{K,K'}\delta_{q,q'}\delta_{j,j'}.$$

The rotational term couples K blocks differing by two

$$\langle JKqj|T^{\rm rot}|JK'q'j'\rangle = \tag{3.66}$$
$$-\frac{1}{2}M^+\left\langle j\middle|\frac{c}{1-c^2}\middle|j'\right\rangle A^{\pm}_{J,K'}\delta_{K,K'\pm 2}\delta_{q,q'} + \frac{1}{4}M^-\left\langle j\middle|(1-c^2)^{-\frac{1}{2}}\middle|j'\right\rangle A^{\pm}_{J,K'}\delta_{K,K'}\delta_{q,1-q'}$$

where

$$A^{\pm}_{J,K} = A^{\mp}_{J,-K} = \sqrt{[J(J+1) - K(K\pm 1)][J(J+1) - K(K\pm 3) - 2]}. \tag{3.67}$$

The coriolis terms are diagonal in K but have differing q,

$$\langle JKqj|T^{\rm cor}|JK'q'j'\rangle = \tag{3.68}$$
$$\frac{1}{2}(-1)^q K M^-\left[\left\langle j\middle|\frac{c(1+2a+2j')}{\sqrt{1-c^2}}\middle|j'\right\rangle + \left\langle j\middle|\frac{2(j'+a)}{\sqrt{1-c^2}}\frac{\sqrt{h^{ab}_{j'-1}}}{\sqrt{h^{ab}_{j'}}}\middle|j'\right\rangle\right]\delta_{K,K'}\delta_{q,1-q'}.$$

There are also two additional $T^{\rm rot}$ terms that need to be included seperately from the others because they augment the $T^{\rm vib}$ and the $T^{\rm cor}$ terms for $K = 1$. The diagonal $q = q'$ term augmenting $T^{\rm vib}$ is given by

$$\left\langle JKqj\middle|T^{\rm rot(1)}_{K=1}\middle|JK'q'j'\right\rangle = -\frac{1}{4}J(J+1)M^+\left\langle j\middle|\frac{c}{1-c^2}\middle|j'\right\rangle\delta_{K,1}\delta_{K',1}\delta_{q,q'} \tag{3.69}$$

and the off-diagonal $q = 1 - q'$ term augmenting the $T^{\rm cor}$ term is given by

$$\left\langle JKqj\middle|T^{\rm rot(2)}_{K=1}\middle|JK'q'j'\right\rangle = -\frac{(-1)^s}{4}J(J+1)M^-\left\langle j\middle|\frac{1}{\sqrt{1-c^2}}\middle|j'\right\rangle\delta_{K,1}\delta_{K',1}\delta_{q,1-q'} \tag{3.70}$$

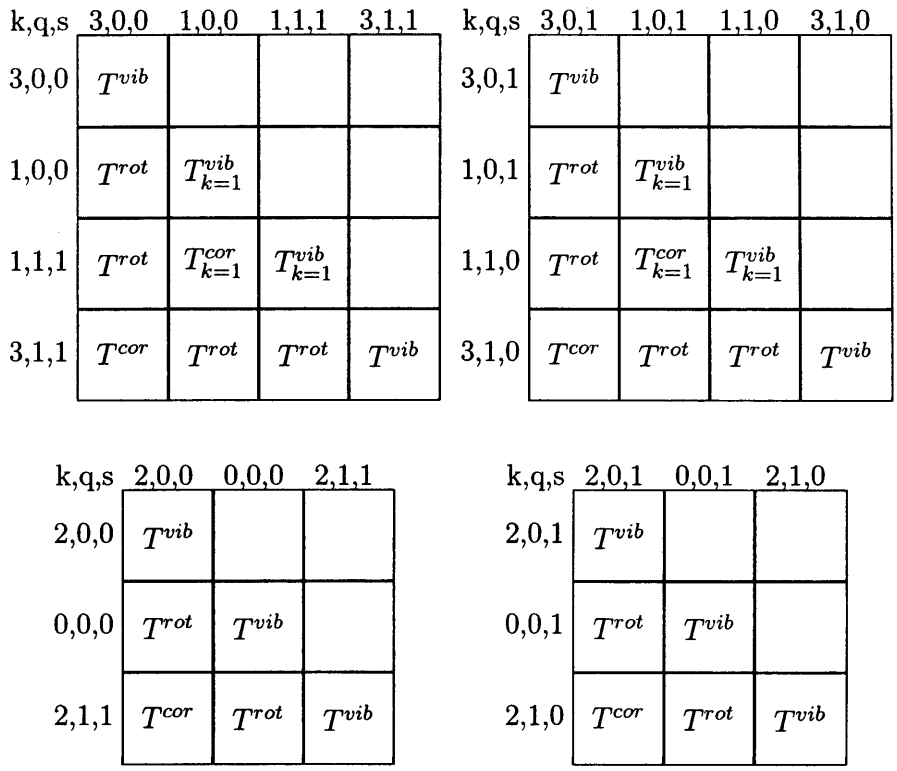

Figure 3.3: Structure of the ro-vibrational hamiltonian in the basis of the first step eigenvectors for $J = 3$ and for all four basis symmetries. Only the lower-half blocks in the symmetric Hamiltonian are shown.

These terms differ from those quoted by Kostin *et al* [97] as they include corrections as calculated by P. Barletta (unpublished,2005).

These terms result in a rather complicated Hamiltonian structure, as shown in figure 3.3 for $J = 3$.

3.7.1 Diagonaliser performance

The Hamiltonian in the rotational step is fairly sparse for high J. With up to four non-zero blocks per k in the high J limit, one of which is diagonal (T^{vib}). Therefore an efficient way of diagonalising the matrix is to use a sparse diagonaliser, which will save both on the memory and time requirements of the calculation.

Sparse matrix methods are usually performed in iterative ways, the most time critical part being the Hamiltonian vector product

$$\mathbf{y} = \mathbf{H}\mathbf{x}, \tag{3.71}$$

which for an unstructured matrix can take of the order of $\mathcal{O}(N^2)$ steps to perform and of course requires at least $\mathcal{O}(N^2+2N)$ memory to store. When the Hamiltonian is sparse and the time for each matrix-vector product decreases until it only takes of the order of $\mathcal{O}(N)$ steps to compute, as our Hamiltonian does here in the high J limit, sparse diagonalisers start to become preferable. A major advantage to the sparse approach is that the Hamiltonian structure can be taken advantage of and only the non-zero blocks need be stored.

A similar situation occurs when using the bisector embedding [59], instead of the z-perpendicular embedding described above. The code originally used a NAG routine called F02FJF [101] which uses the method of simultaneous (subspace) iteration to calculate k Ritz eigenvectors. However there have been several improvements to sparse matrix methods and the efficient ARPACK package implements a method known as the Implicitly Restarted Lanczos Method (IRLM). Therefore an implementation of ROTLEV3B now uses the ARPACK diagonaliser for its calculations. The system is several times faster, especially for large Hamiltonian sizes and large J.

Chapter 4

Parallel DVR Calculations

A number of calculations have been performed using DVR techniques on more than one processor for both the added capability and efficiency it provides. Mussa and Tennyson [82; 83] calculated both bound and quasi-bound states of HOCl in Jacobi coordinates on many processors. Also, Kostin *et al* [45] calculated some bound states of H_3^+ with $J = 0, 2$ and 8 on hundreds of processors using a technique similiar to the z-perpendicular Radau coordinate approach applied here.

In this chapter we explore how this technique has now been improved to work efficiently on well over a thousand processors. With this implimentation we are able to perform calculations with a vibrational basis set 12 times larger than that of Kostin *et al* [45]. As the problem difficulty increases with the square of the basis size – at best, the size of the computation has been increased by a factor of well over 144 times. These improvements have come about partly because of the increasing speed and capability of computers and partly because of improvements in the program that allow it to work more efficiently and with greater capability.

PDVR3DR is our acronym for the MPI parallelised program based upon DVR-3DRJZ [59], which is able to perform the vibrational bound state calculations on massively parallel computers, with over 1000 processors, in Radau coordinates. This is a necessary improvement to the code because benchmark problems, such as H_3^+ at dissociation, are difficult and require enormous basis sets to converge. This means that the corresponding Hamiltonian matrix, even when truncated, is very large and requires large amounts of computer memory to work with. In this work we shall see memory requirements of several hundred gigabytes. This size calculation is currently not possible on single processor machines and this is the overriding reason for parallelising the computer codes. A considerable amount of effort has now been put into creating an efficient parallel algorithm for PDVR3DR. Of course, an added

advantage and possibly a necessary one, is that the computation time is considerably reduced. Ideally this increase in speed would be directly proportional to the number of processors used. However, this is not always possible. In this chapter we will explore ways of actually realising these large basis set calculations and how we can approach the ideal of an efficient algorithm.

4.1 Algorithm separability

The fundamental problem in creating a parallel program is finding a way to implement the algorithm that minimises the communication between individual processors without noticeably increasing the number of steps required on each process or the amount or memory required for each process. The ideal is that a single process calculation requiring $\mathcal{O}(f(N))$ steps and $\mathcal{O}(g(N))$ storage for a calculation size of N, will, when run on p processors, require $\mathcal{O}(f(N)/p)$ steps and $\mathcal{O}(g(N)/p)$ storage on each processor.

To see how we can approach this goal, we will start with the single process implementation that has already been described and see how we can parallelise the different steps so as to minimise the storage of processing overheads. In the serial DVR3DRJZ the Radau coordinate calculation proceeds as follows:

1. Build a set of radial 2D Hamiltonians ($H^{2D}_{\alpha\beta}(\gamma)$), one for each angular DVR point. Where, α and β index the radial DVR grid points and γ indexes the angular DVR grid points.

2. Diagonalise each H^{2D} to produce l eigenvalues ($\epsilon^{2D}_{l\gamma}$) and eigenvectors ($C^{2D}_{\alpha\beta\gamma l}$).

3. Truncate the 2D solutions by energy ($\epsilon^{2D}_{l\gamma} < E^{2D}$) and use as an optimised 2D basis set for the next step.

4. Build the 3D Hamiltonian (H^{3D}) in the new basis.

5. Diagonalise the Hamiltonian to produce n eigenvalues (ϵ^{3D}_{n}) and eigenvectors ($C^{3D}_{l\gamma n}$).

6. Back transform the eigenvectors (C^{3D}) onto the original basis to produce the wave functions $\Psi_{\alpha\beta\gamma n}$.

The largest part of this calculation is step 5, the diagonalisation of the full 3D Hamiltonian. The most efficient parallel diagonalisers suiting our problem at the time of writing are implemented in the ScaLAPACK library [102] and below we investigate their relative merits and performance. However, the other steps are also

important and have to be implemented carefully otherwise they can quickly become very expensive. Also, because of the data dependence of a step on the previous steps, they can also strongly effect the implementation and efficiency of any following steps.

4.2 The two dimensional step

Steps 1, 2 and 3 enumerated above have a natural division scheme, the 2D Hamiltonians $H^{2D}(\gamma)$ can be solved at each angular grid point (γ) separately and this immediately provides a way to split the process into N_γ separate tasks. However, splitting the task further introduces complication. The ideal is probably to use a ScaLAPACK diagonaliser and perform each of the N_γ diagonalisations of H^{2D} in a parallel fashion. Though the step is not very expensive after performing the γ split and therefore we accept the minor performance penalty of performing the diagonalisation in serial but by only calculating the N_γ/N_p fraction of the solutions below our energy cut E^{2D} on each process of the N_p processes. The most important consideration at this point is to make sure that the C^{2D} vectors are evenly distributed as this strongly effects the performance and storage requirements of later steps. Our implementation is less than optimal in that the $l \times N_\gamma/N_p$ solutions per process can be different for each process as the number of solutions l depends on γ.

4.3 Truncation scheme

Previous implementations of PDVR3D [103; 82; 83; 45] took a constant number of basis N^{2D} functions from each reduced dimension calculation. This would appear to offer an easy route to parallelisation as each processor could compute the 2D radial basis of a single angular grid point. Each processor then only has to truncate according to size of basis required, no communication is required until the construction of the 3D Hamiltonian. Also the 2D calculations should take a similar amount of time because they require the same number of solutions; the code is therefore load levelled and will perform and scale better.

This previous truncation scheme,

$$1 \leq l \leq N^{2D}, \quad 1 \leq \gamma \leq N_\gamma \tag{4.1}$$

where $N^{2D} \times N_\gamma$ gives the final Hamiltonian size, is simple and works fairly well. However, there are advantages to using an energy truncation scheme and select only

those solutions with an eigenvalue less than E^{2D} instead,

$$\epsilon_{\gamma l}^{2D} \leq E^{2D} \tag{4.2}$$

where $\epsilon_{\gamma l}^{2D}$ are the eigenvalues from the 2D calculations and the final Hamiltonian size is not known *a priori* as the number of eigenvalues below E^{2D} will not be known in advance.

Energy is an important measure when considering the suitability of a basis function for inclusion. In our calculations we found that often an N^{2D} cut would perform no better than an energy cut with

$$E^{2D} = \min(\epsilon_{\gamma N^{2D}}^{2D}), \quad 1 \leq \gamma \leq N_\gamma \tag{4.3}$$

but at the sacrifice of a larger basis. We found that N^{3D} was often 20% larger with a number cut. So the final problem size increases and takes longer to compute but gives little return in terms of convergence or many savings in the earlier calculation steps.

As diagonalisers tend to scale with $\mathcal{O}(N^3)$ for large calculations, we find that the extra 20% in the order of the Hamiltonian can double the time it takes to perform the calculation and significantly increase the memory requirements. Therefore the energy selection scheme has been incorporated into PDVR3D.

4.4 Matrix construction

The next step (4) is to use the truncated vectors from the previous section as an optimised 2D basis for the 3D calculation. If we look again at the equation that describes this (3.45), this time simplifying so as to understand its role computationally. Replacing the indexes over the radial points (α, β) by a combined index η and bringing together terms,

$$H_{\gamma\gamma' ll'}^{3D} = \epsilon_{\gamma l}^{2D} \delta_{\gamma\gamma'} \delta_{ll'} + \sum_{\eta} \sum_{\eta'} M_{\eta\eta'\gamma\gamma'} C_{\gamma\eta l}^{2D} C_{\gamma'\eta' l'}^{2D} \tag{4.4}$$

where M is formed from the combined terms of equation (3.45). The sum over η and η' represents a calculation of $\mathcal{O}(N_R^4/4)$ steps. For a typical calculation ($N_R = 120$) this number is over 50 million. On a single *modern* processor this could be done fairly quickly. Therefore, the important consideration here is how to parallelise this so as to minimise the slow aspect, the communication. The M term does not need to be explicitly built and stored as it is highly structured, this saves us from

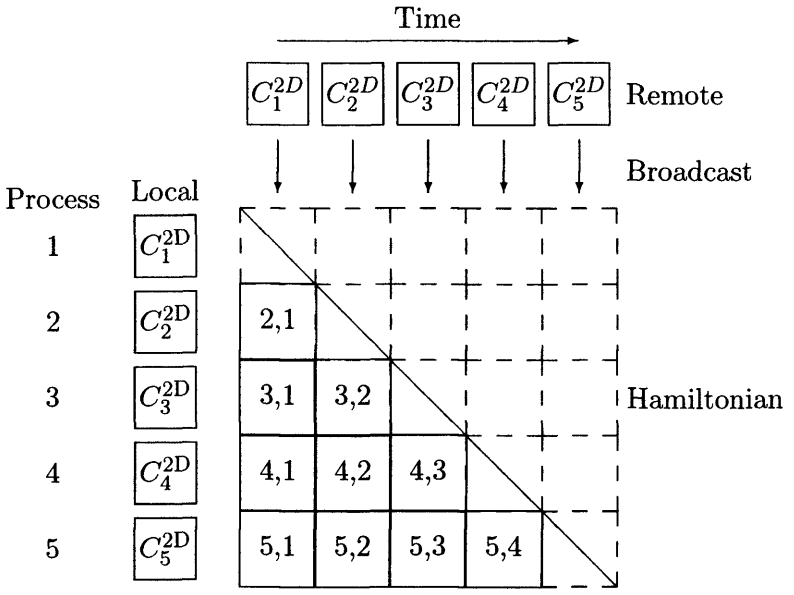

Figure 4.1: The Hamiltonian construction in parallel with $N_\theta = 5$ and $N_p = 5$. The build proceeds from left to right in parallel across the processors, which are depicted from top to bottom. The blocks of 2D vectors (C_γ^{2D}) are broadcast across the processors one at a time. Only the symmetric half of the Hamiltonian is built. Eigenvalues from the 2D step form the diagonal.

having to consider about $\mathcal{O}(N_R^2 N_\theta^2)$ of data. The 2D vectors (C^{2D}) are needed for the back transformation and must be saved, requiring $\mathcal{O}(N_\theta N_R^2 N^{2D}/2p)$ of memory on a processor. H^{3D} is also large and requires of $\mathcal{O}(N_\theta^2 (N^{2D})^2/p)$ storage on each processor.

Figure 4.1 shows how this matrix construction is implemented for a simple case of $N_\gamma = N_p = 5$. The matrix construction proceeds from left to right in the figure and only the symmetric lower half (γ, γ') blocks are built. As each C_γ^{2D} needs to be multiplied by every $C_{\gamma'}^{2D}$, the $C_{\gamma'}^{2D}$ are broadcast across the processes one at a time and the corresponding blocks are formed. The eigenvalues ϵ^{2D} are then cheaply added to the diagonal at the end.

4.4.1 Block cyclic distribution

ScaLAPACK [102] uses a block cyclic decomposition of the matrix. Here, block cyclic means that blocks of the matrix are mapped cyclically in both row and column directions across the processors. This block cyclic distribution provides two distinct advantages for dense matrix computations. The calculation, typically proceeding like a Gaussian elimination, is load levelled. This is because the Gaussian eliminations typically proceed from the top left to the bottom right of a matrix. If the matrix

was not cyclically distributed then as the elimination proceeded it would leave many processors with no part in the calculation. The blocked aspect of the distributed data takes advantage of the memory hierarchy and means that efficient routines can be used in each serial process to perform the matrix–matrix multiplications.

To map a matrix element i, j in block l, m onto a processor grid of size P_r, P_c with local matrix positions x, y on processors p_r, p_c we can use the following formula,

$$\begin{aligned} p_r &= \mathrm{mod}\left(\mathrm{floor}\left(\frac{i-1}{B}\right), P_r\right) \\ p_c &= \mathrm{mod}\left(\mathrm{floor}\left(\frac{j-1}{B}\right), P_c\right) \\ l &= \mathrm{floor}\left(\frac{i-1}{P_r B}\right) \\ m &= \mathrm{floor}\left(\frac{j-1}{P_c B}\right) \\ x &= \mathrm{mod}\left(i-1, B\right) + 1 \\ y &= \mathrm{mod}\left(j-1, B\right) + 1 \end{aligned} \tag{4.5}$$

where B is the block size and is chosen here to be the same in both the rows and columns of the matrix. However, there is no such restriction and the block sizes could be different if one so wished. The $\mathrm{mod}(x, y)$ function returns the remainder after the integer division of x by y and the $\mathrm{floor}(x)$ function is the largest integer below x. It is interesting to note that this map does not depend on the matrix size (N) and this is a useful feature that allows for a simple implementation and the ability to easily use sub-matrices in calculations.

An impractical but simple example of this matrix distribution is shown in figure 4.2, where a 5×5 matrix is mapped onto a grid of four processors with a block size of two. Notice that the remainder blocks at the end of the matrix rows and columns are still mapped cyclically into the distribution. Therefore, the block size does not have to be an integer fraction of the matrix size (N).

4.5 3D Hamiltonian diagonalisation

The largest component of the calculation is the final diagonalisation of the full 3D Hamiltonian matrix in the basis of the first step solutions. As we shall see, this truncated basis can still be very large, up to 80,000 for our H_3^+ calculations. A matrix of order 80,000 will require nearly 50 giga-bytes of RAM for a single copy. A typical diagonalisation will require two to three times this amount as workspace

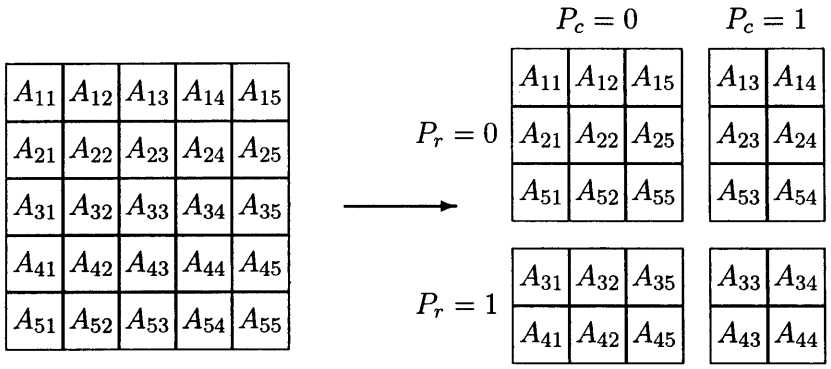

Figure 4.2: A block cyclic distribution of a 5 × 5 matrix onto a 2 × 2 process grid with a block size of 2 in both rows and columns.

and for storing the vectors of the required solutions.

4.5.1 ScaLAPACK diagonalisers

Within ScaLAPACK there are a number of real symmetric matrix diagonalisers to choose from [102]. They follow the linear algebra (LAPACK) library [96] naming scheme with the addition of a P- prefix signifying the parallel nature of the routine.

PDSYEV performs the diagonalisation using an implicit QL or QR method that is fairly efficient but does not parallelize particularly well and requires approximately $2N^2$ workspace in addition to the Hamiltonian matrix.

PDSYEVX uses a bisection and inverse iteration method and requires at least $N^2 + 10 * N$ extra workspace but may in fact use much more than this. PDSYEVX does not guarantee the correct answer with this $\mathcal{O}(N^2/p)$ memory per processor. The actual requirements depend on the eigenvalue spectrum. Specifically if the eigenvalues form tight clusters then the eigenvectors have to be calculated and then re-orthogonalised on the *same* processor and therefore the memory requirements can be as bad as $\mathcal{O}(N^2)$ per process. This is precisely the situation we encountered in the final diagonalisation for H_3^+. In some calculations all the M requested solutions formed a cluster and the algorithm effectively required $\mathcal{O}(M \times N)$ storage per processor making it inappropriate for our purposes.

PDSYEVD performs the diagonalisation using a divide and conquer technique [104]. The division of the matrix into sub-matrices that can be solved is difficult to do and keep numerical stability but has been achieved and proves to be an efficient way to parallelise the diagonalisation. It also provides explicitly orthogonal eigenvectors which do not require any expensive re-orthogonalisation. However the routine is

Table 4.1: Parallel diagonaliser performance comparison for the ScaLAPACK routines PDSYEV, PDSYEVX and PDSYEVD.

Diagonaliser	N	Eigenvalues	Eigenvectors?	Processors	Time (s)
PDSYEV	7013	700	no	128	25
PDSYEVX	7013	700	no	128	14
PDSYEVD	7013	7013	yes	128	31
PDSYEVX	62507	700	no	256	3967
PDSYEVD	62507	62507	yes	256	3217

limited in that there is very little saving if only a fraction of the solutions are desired.

4.5.2 Diagonaliser performance

Table 4.1 gives a summary of a few sample runs using PDSYEV, PDSYEVX and PDSYEVD. The efficiency of each diagonaliser depends on the problem size, indeed PDSYEVD does not beat PDSYEV(X) for small runs as it cannot take advantage of our need for only a fraction of the solutions. However, for large jobs ($N^{3D} = 62507$) the memory and efficiency advantages in PDSYEVD take over and it will calculate all the eigenvalues and eigenvectors faster than PDSYEVX can calculate just 1% of the eigenvalues.

4.5.3 Algorithm scaling

When performing large numbers of jobs we prefer to get things done as quickly and efficiently as possible. Ideally, when performed on twice as many processors a calculation will be twice as fast. However, we can see from figure 4.3 that this is not the case. The figure shows how the different parts of the calculation are performing. The two largest components of the calculation are the matrix construction step and the final diagonalisation. The matrix diagonalisation performs fairly well when working on very large matrices and the time shrinks significantly with increasing processor count. The matrix construction however is very communication dependent and becomes expensive for large calculations.

4.5.4 Multi-job harness

As we can see from the previous section, the program does not allow us to efficiently use more than 256 processors. However, there is a coarse grained parallelism we can take advantage of, as we run many of these jobs in the process of converging

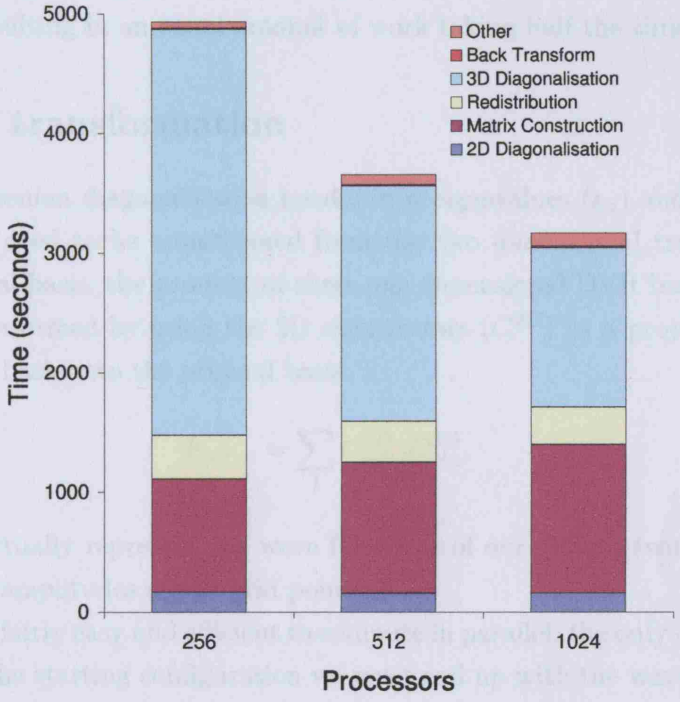

Figure 4.3: Parallel algorithm scaling to 1024 processors with a job size of $N^{3D} = 62507$. Different steps of the calculation are shown separately.

Table 4.2: Timings for calculations run with and without a job harness. The job harness provides perfect scaling.

Processors	BLACS grids	Time (seconds)
512	1	13935
1024	2 ($\times$ 512)	6822

results and also in the first step of a rotational calculation we group these jobs together at an efficient size ($N_p \approx 256$) and run them concurrently. This is often called a 'harness' and results in practically perfect scaling properties. This can be seen in table 4.2 where here we have run two 256-processor jobs concurrently on 512 processors. Resulting in an equal amount of work taking half the time.

4.6 Back transformation

The 3D Hamiltonian diagonalisation results in n eigenvalues (ϵ_n) and eigenvectors ($C^{3D}_{\gamma ln}$). These need to be transformed from the two dimensional truncated basis onto the original basis, the product of three one dimensional DVR basis. The back transform is performed by using the 2D eigenvectors (C^{2D}) as a projection matrix and projecting back onto the original basis,

$$\Psi_{\alpha\beta\gamma n} = \sum_l C^{2D}_{\alpha\beta\gamma l} C^{3D}_{\gamma ln}, \tag{4.6}$$

where the Ψ actually represent the wave functions of our system (within our basis set error) with amplitudes at the grid points.

This step is fairly easy and efficient to compute in parallel, the only complications are that from the starting configuration we must end up with the wave functions in the correct configuration for the rotational step as the Hamiltonian construction in the rotational step is expensive.

Our starting configuration has the 2D vectors (C^{2D}) split across processors by γ and then again by l, giving a N_θ/N_p fraction of $C^{2D}_{\alpha\beta l}$ on each processor. Also, the 3D vectors (C^{3D}) are split across the processors by n leaving a N_{eval}/N_p fraction of $C^{3D}_{\gamma ln}$ on each processor.

This is not an inherently expensive operation but can, if done wrongly, consume a large amount of memory and time, the solution is to perform the transform in two steps:

1. The sum is performed in parallel. If there is more than one processor per γ (as

is normal) then partial sums ($\Psi^{\text{partial}}_{\alpha\beta\gamma}$) are formed. The C^{3D} are communicated across each processor rather than the C^{2D} as C^{3D} is of $\mathcal{O}((N^{2D})^2 N_\theta N_e/2)$ and are almost certainly smaller than C^{2D} which are of $\mathcal{O}(N^{2D} N_\theta N_R^2/2)$. Each $\Psi^{partial}_{\alpha\beta\gamma n}$ is left split by γ across the processors.

2. $\Psi^{\text{partial}}_{\alpha\beta\gamma n}$ are summed across processors and re-distributed to form $\Psi_{\alpha\beta\gamma}$ so that the wave functions are split across processes by n instead of by γ.

The added advantage of this redistribution is that the wave functions become contiguous in memory and computing expectation values, norms and other variables becomes efficient and simple, for example the norm:

$$\sum_{\alpha\beta\gamma} \Psi_{\alpha\beta\gamma n} \Psi'_{\alpha\beta\gamma n'} = \delta_{nn'}. \tag{4.7}$$

4.7 Conclusion

In summary, PDVR3D has undergone a number of improvements and is able to perform very large basis set calculations efficiently on over 1000 processors. However the recent development of a diagonaliser algorithm based upon relatively robust representations [105] and the observation that an improved matrix construction is needed for larger calculations means that there a still a number of improvements that can be made.

Chapter 5

Rotational DVR calculations in parallel

The DVR3D algorithm has been extended to work on parallel computer systems before. Radau and Jacobi coordinate calculations were extended to parallel computers by Mussa *et al* [103] to calculate ro-vibrational states of water up to dissociation [106]. Extra work allowed the calculation of high energy ro-vibrational states of HOCl in Jacobi coordinates, including a number of quasi-bound states [82; 83]. More recently Kostin *et al* made the first attempt at calculating the $J = 2$ and $J = 8$ rotational bound states of H_3^+ all the way up to dissociation [45] by extending the z-perpendicular method [97] onto parallel computers.

In this chapter we describe what improvements are needed for Kostin *et al*'s parallel implimentation [45] of the z-perpendicular embedding in order that we may compute results for much larger basis sets. Kostin *et al* used a vibrational basis set of size 58,560 (including symmetry) with grid sizes of $N_R = 60$ and N_θ=32. While, as we shall see in chapter 6, in order to resolve long range states and correctly represent states at $R = 0$ we need a basis that is 12 times as large. The vibrational basis set size required is 696,960 (including symmetry), with grid sizes of $N_R = 120$ and $N_\theta = 96$.

In this large basis situation the construction of the rotational Hamiltonian in terms of the first-step vibrational basis becomes problematic. The construction step scales with the square of the vibrational basis size and the square of the number of included basis set vectors from the first step (truncated by energy). This creates a problem orders of magnitude larger than that tackled previously.

5.1 Parallelising the ROTLEV3Z algorithm

There are four main steps important to a computational implementation of the algorithm,

1. The first step vibrational calculations producing the 3D per k-block basis for the second step.
2. Build the rotational Hamiltonian in the first step basis, the diagonal terms being the eigenvalues.
3. Diagonalise the final Hamiltonian to produce the energies and vectors describing the states in the basis of the first step.
4. Back-transform the eigen-vectors onto the original basis, producing wave functions represented in terms of amplitudes at the DVR grid points.

5.2 Building the rotational Hamiltonian.

The rotational Hamiltonian, figure 3.3, has three terms that must be constructed by coupling wave functions from separate vibrational step calculations, T^{cor}, T^{rot} and $T^{\text{rot(2)}}_{k=1}$. The T^{vib} terms are completely diagonal in the basis only need to be included. Additionally the rotational term $T^{\text{rot(1)}}_{K=1}$ is also diagonal in the rotational basis and for this reason is calculated in the first step.

If you ignore the differences between the seperate off-diagonal rotational terms (T^{rot} and T^{cor}) and write them just in terms of how they are constructed from a radial coupling matrix M and an angular coupling matrix A. We find that a particular Hamiltonian block T that couples first-step eigen-vectors Ψ defined by K, q, s and K', q', s' is built from the elements n, n' with,

$$T^{k,q,s,k',q',s'}_{n,n'} = \sum_{\alpha,\beta}\sum_{\alpha',\beta'} M_{\alpha,\beta}\delta_{\alpha,\alpha'}\delta_{\beta,\beta'}\sum_{\gamma,\gamma'} A_{\gamma,\gamma'}\Psi^{k,q,s}_{\gamma,n,\alpha,\beta}\Psi^{k',q',s'}_{\gamma',n',\alpha',\beta'} \tag{5.1}$$

The difference between DVR and FBR representations is clear here, the Radial components of the Hamiltonian are diagonal whilst the angular components are not. The difficulty in constructing the ro-vibrational Hamiltonian is therefore linear with respect to the 2D radial basis size (N_R^2), varies with the square of the angular basis size (N_θ) and the square of the truncated vibrational basis size (N_{vib}). Overall this creates a very large construction step given the vibrational basis used for our calculations. With $N_\theta = 96$, $N_R = 120$ and $N_{\text{vib}} = 4000$ the sums in equation 5.1 iterate

over 10^{15} combinations of elements for just one block of the Hamiltonian. The computation time is about two orders of magnitude larger than for the diagonalisation step in this case.

In order to make this construction scale efficiently to many processors it is best to split the calculation along the diagonal components, in this case splitting the calculation with respect to α and β. This saves having to communicate elements of matrices between processors when computing the sums in equation 5.1. What results is an algorithm where partial sums are computed for each α and β on separate processors, these are then combined in a relatively small parallel global sum giving,

$$T_{n,n'} = \sum_{\alpha,\beta} T^{\text{partial}}_{n,n'}(\alpha,\beta) \tag{5.2}$$

5.3 Diagonalising the Hamiltonian

The diagonlisation of the ro-vibrational hamiltonian proves simpler than in previous calculations because the truncation between the vibrational and rotational steps is very efficient. Of the 2,090,880 basis functions in the complete ro-vibrational basis only 12,000 are needed to produce a reasonable convergence for all states with $J = 3$, in the symmetry block with K=even and $q = s$. This is just 0.6% of the basis, much more efficient that the $2D \rightarrow 3D$ truncation used in vibrational calculation where over 10% of the $2D$ basis was required before achieving sub-wavenumber convergence.

Here we implimented the ScaLAPACK diagonaliser PDSYEVD[104], just the same diagonaliser used in the vibrational calculations. For high values of J the Hamiltonian becomes sparse as the number of non-zero blocks in the Hamiltonian scales linearly with J,

$$N_{\text{BLOCKS}} = \begin{cases} 4(J+1) & : \quad J+K = \text{even} \\ 4J & : \quad J+K = \text{odd} \end{cases} . \tag{5.3}$$

This suggests that for large values of J a diagonaliser appropriate to sparse matrices would be better. But with anything below $J = 5$ the Hamiltonian has no zero blocks so its sparsity is only important for much higher values of J.

5.4 Back-transform onto the original basis

The eigenvectors from the diagonalisation of the rotational Hamiltonian are in the basis of the first step eigen-vectors. Therefore we have to back-transform these

vectors onto our original basis to form the H_3^+ ro-vibrational wave functions.

Chapter 6

Vibrational bound states of H_3^+

6.1 Introduction

Accurate nuclear motion calculations were performed on H_3^+ using fit 2 of the global, *ab initio*, electronic ground state potential energy surface developed by Polyansky *et al* (PPKT) [2]. This potential, with corrections, is plotted in Jacobi coordinates at an angle of 90° and also at $r = 1.4a_0$ (figure 6.1). This potential correctly considers the charge – polarisability interaction between H^+ and H_2 at long range. This leads to a long, shallow well in the dissociation coordinate (R). A previous study of rotation – vibration states using this potential attempted to calculate all the states [45] but had insufficient computational power to converge the near-dissociation states. This chapter deals with the calculation and convergence of these bound states and some of their properties. There were a number of criteria which needed to be satisfied in order to make this calculation useful,

- The calculation should be performed on the best electronic surface possible, at the time of writing this is PPKT.
- The radial grid should extend out far enough that it would be possible to perform resonance calculations using the complex absorbing potential method.
- The near-dissociation states should be converged as much as possible, here this meant sacrificing some convergence in lower states.
- The calculation should also be able to be extended to perform rotational calculations using PROTLEV3Z.

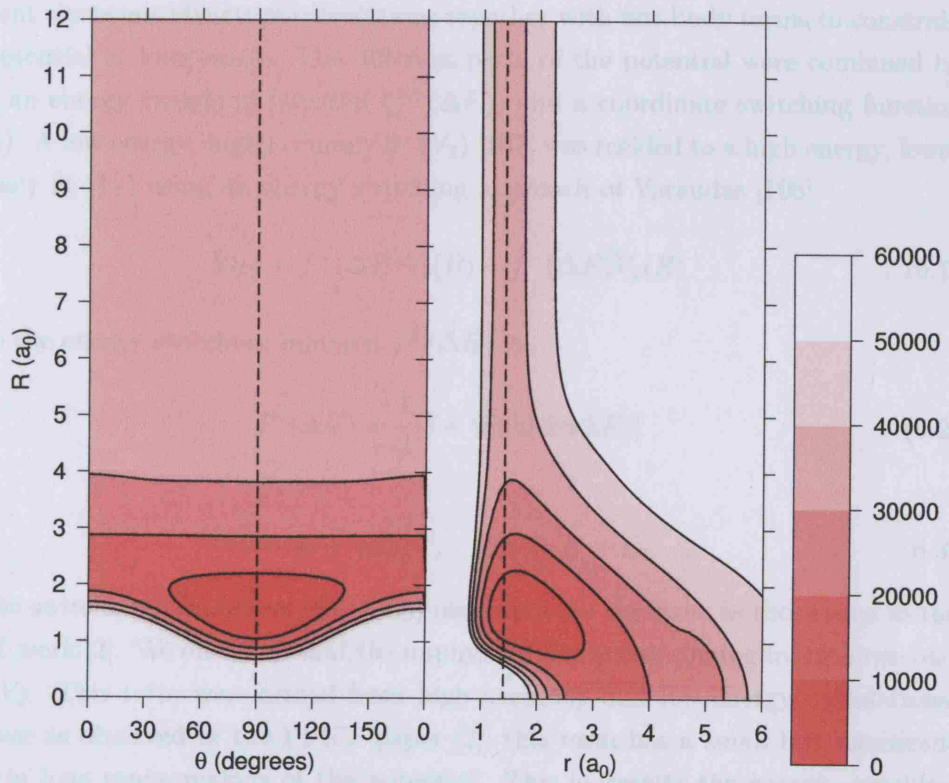

Figure 6.1: The contours of the PPKT2 potential energy surface in Jacobi coordinates. The left hand plot is at fixed diatomic distance $r = 1.4a_0$. The right hand plot is at a fixed angle $\theta = 90°$. The minimum of the potential has zero energy and the contours are plotted every $10,000$ cm^{-1} from $10,000$ cm^{-1} to $50,000$ cm^{-1}.

6.2 The potential energy surface

The PPKT potential energy surface was constructed to have the correct dissociative behaviour. However closer inspection revealed that at large Jacobi R the potential exhibits an apparently un-physical hump of about 500 cm^{-1}. This hump happens to support a number of long range states with associated classical trajectories. These states are very similar to the asymptotic vibrational states discussed later, but trapped by this barrier. Therefore for the purposes of this work we made slight adjustments to the potential. The PPKT potential was constructed from a number of different electronic structure calculations together with few body terms to constrain the potential at long range. The different parts of the potential were combined by using an energy switching function ($f^{\pm}(\Delta E)$) and a coordinate switching function ($g(R)$). A low energy, high accuracy fit (V_2) [107] was melded to a high energy, lower accuracy fit (V_1) using an energy switching approach of Varandas [108],

$$V_{ES} = f^{+}(\Delta E)V_1(R) + f^{-}(\Delta E)V_2(R) \tag{6.1}$$

where the energy switching function $f^{\pm}(\Delta E)$ is,

$$f^{\pm}(\Delta E) = \frac{1}{2}[1 + \tanh(\pm\gamma\Delta E)] \tag{6.2}$$

with

$$\gamma = \gamma_0 + \gamma_1\Delta E^2, \quad \Delta E = E - E_0. \tag{6.3}$$

The switching parameters (γ_0,γ_1,E_0) used here are the same as those used in the PPKT work [2]. We observed that the unphysical hump was coming from the second term V_2. This term was formed from high accuracy and low energy calculations. However as observed in the PPKT paper [2], this term has a small but significant effect in long range regions of the potential. This is despite the energy switching approach of equation 6.1. Therefore long range terms were also included in V_2,

$$V_2 = g(R)V_{SR} + [1 - g(R)]V_{LR} \tag{6.4}$$

where $g(R)$ switches between the long range (V_{LR}) and short range (V_{SR}) terms,

$$g(R) = \begin{cases} 1 & R < R_{LIM} \\ \cos^2\left[\frac{\pi(R-R_{LIM})}{2(R_M-R_{LIM})}\right] & R_{LIM} \leq R \leq R_M \\ 0 & R > R_M \end{cases} \tag{6.5}$$

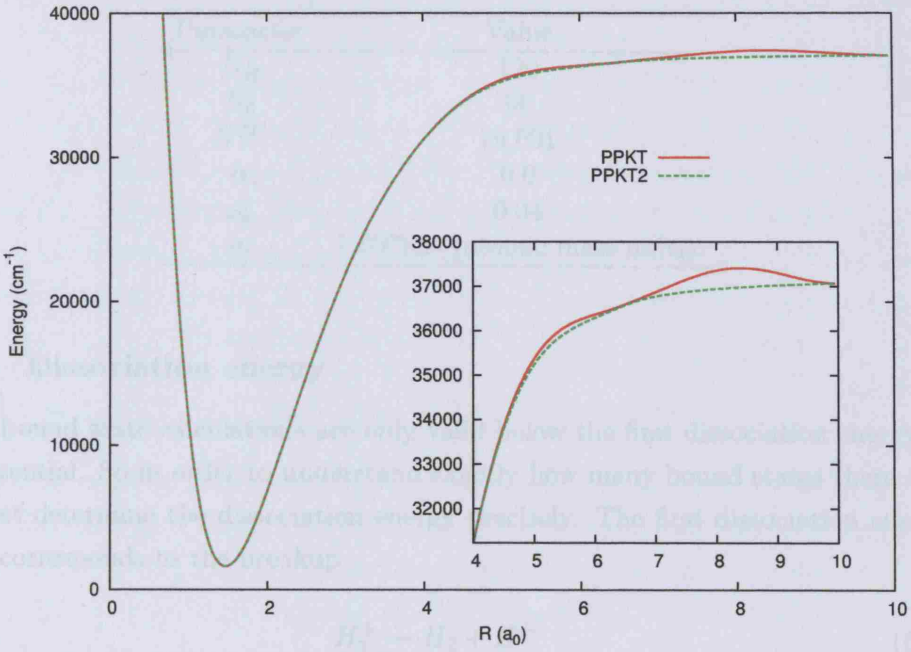

Figure 6.2: Comparison of PPKT and PPKT2 along the dissociation channel where $r = 1.4a_0$ and $\theta = 90°$.

with $g(R)$ turning on at R_{LIM} and turning off at R_M. After a number of tests we modified just the end of the switching function R_M from the value of $R_M = 10.0a_0$ to $R_M = 7.0a_0$ and the hump disappeared. This new potential is referred to as PPKT2 in this work. We note that PPKT and PPKT2 are equal up to an energy of 30,800 cm^{-1} (above the potential minimum) and a number of the calculations presented below for energies lower than this actually used the original PPKT implementation. Figure 6.2 shows the difference between the PPKT and PPKT2 potentials along the H_2 — H^+ dissociation channel at a fixed r=1.4a_0; notice the disappearance of the unphysical hump between 6.5a_0 and 10a_0.

6.3 Calculation

The calculations used the adapted version of the PDVR3D code described earlier to perform large basis set calculations efficiently in parallel. The fully converged Radau coordinate calculations (table 6.1) used 384 IBM Power4+ processors for 2 hours and 25 minutes. Calculations were performed on the HPCx supercomputer at the Daresbury Laboratory, UK.

Table 6.1: Radau coordinate calculation parameters used for the converged results.

Parameter	Value
N_R	120
N_θ	96
N^{3D}	79,091
α	0.0
ω_e	0.04
m	1.007825 (atomic mass units)

6.3.1 Dissociation energy

These bound state calculations are only valid below the first dissociation energy of the potential. So in order to understand exactly how many bound states there are, we must determine the dissociation energy precisely. The first dissociation energy of H_3^+ corresponds to the breakup

$$H_3^+ \rightarrow H_2 + H^+ \tag{6.6}$$

and therefore the dissociation energy (D_0) corresponds to H_2 with its zero point energy. D_0 therefore differs from the classical dissociation energy D_e as any classical system would not have to achieve the zero point energy of H_2. In order to calculate the D_0 supported by the potential, we performed a diatomic calculation using the one dimensional potential generated by PPKT for large values of the Jacobi coordinate R and for fixed Jacobi angle θ. Using the diatomic code LEVEL 7.5 [109] with this one dimensional potential we calculated the vibrational states of H_2. A number of cuts of the potential for various values of R and for various values of θ were tested, we found a stable value of $D_0 = 34,911.6$ cm^{-1} relative to the ground state of H_3^+. This value is correct for both PPKT and PPKT2 as it only relies on long range terms in the potential beyond the range of the switching function.

6.3.2 Convergence

Numerical convergence of our results depends on five parameters. Three parameters control the size of the basis within our truncation scheme; N_R, N_θ and E^{2D}. Here we also refer to the final basis size (N^{3D}) calculated by using an energy cut of E^{2D}. N_R, N_θ and N^{3D} offer monotonic but not necessarily variational convergence. Two other parameters control the character of the spherical oscillators; α and ω_e effect the rate of convergence.

The main results were calculated in Radau coordinates using the PPKT2 potential energy surface. However a number of calculations were also performed in Jacobi on the PPKT potential energy surface (some of these results are referred to below) for which we achieved good agreement up to energy where PPKT and PPKT2 differ.

We find that with the Radau calculation all states below D_e converge to better than 0.7 cm^{-1} and all but one state below D_0 converge to better than 1.0 cm^{-1}, when using the parameters given in table 6.1. It is possible to converge lower energy states to much better than this, but here we intentionally tried to resolve very long range states. This required a much more extended radial grid and sacrificing some of the convergence in lower energy states.

6.3.2.1 Basis set optimisation

The angular basis over the interval $[-\pi, \pi]$ set does not require any optimisation and are just formed from Legendre polynomials. However, the radial basis set is complete over the interval $[0, \infty)$ and requires some optimisation to efficiently represent the states of H_3^+ with its rather modest span of a several a_0. Quoting the formula for spherical oscillators (equation 3.38) again, for convenience,

$$\begin{aligned} |n\rangle &= \sqrt{2}\sqrt[4]{\beta} N_{n\alpha+\frac{1}{2}} e^{-\frac{y}{2}} y^{\frac{\alpha+1}{2}} L_n^{\alpha+\frac{1}{2}}(y) \\ y &= \beta r^2 \\ \beta &= \sqrt{\mu\omega_e}. \end{aligned} \tag{6.7}$$

The only two parameters that control the character of the basis set are α and ω_e. The ω_e value sustains the correct normalisation of $|n\rangle$ (with $\sqrt[4]{\beta}$) and also pre-multiplies the transformed distance y (with $\sqrt{\mu\omega_e}$). Therefore increasing ω_e, increases the range of the basis set and conversely decreasing ω_e, decreases the range. Therefore, when optimising ω_e it is important to consider how it effects the very high energy states, right up to dissociation. As these states, will undoubtedly be of a longer range and probably have pre-dissociative properties. So, while a short range basis will converge low energy states very well, when looking at the complete energy range, it is the worst case convergence that is more important and this requires a very long range basis.

The other parameter to optimise is α, which tends to shift the basis function out to longer ranges, as it increases. For low values of α, ($\alpha \approx 0, 1$) the behaviour at $R = 0$ is effected. This is important in these calculations as, even in Radau coordinates, H_3^+ can access configurations with $R = 0$ before dissociation. This is because of the nature of the potential in this region. Table 6.2 shows how the

Table 6.2: Comparison of the last 5 even (N_e) and odd (N_o) bound states of H_3^+ with respect to changing α. Energies are given in cm^{-1} from the bottom of the potential energy surface.

N_e	$\alpha = 0$	$\alpha = 1$	Δ	N_o	$\alpha = 0$	$\alpha = 1$	Δ
683	39227.029	39228.537	1.508	595	39219.535	39219.920	0.385
684	39244.581	39246.788	2.207	596	39226.975	39227.877	0.902
685	39252.952	39253.113	0.161	597	39244.584	39246.492	1.908
686	39259.603	39261.798	2.195	598	39258.708	39259.153	0.445
687	39262.627	39262.732	0.105	599	39266.228	39266.551	0.323

energies change for the even and odd parity calculations when selecting $\alpha = 0, 1$. In both cases the $\alpha = 0$ calculations produce lower energies and therefore in our variational method are better converged.

6.3.2.2 Basis set size

Table 6.3 shows the last twenty bound states converging with respect to the number of radial grid points (N_R). We can see that the convergence improves and that the states converge from above as expected. The biggest final change being $\Delta E(115) = -0.544\ cm^{-1}$.

Table 6.4 shows the last twenty bound states converging with respect to the number of angular grid points (N_θ). Here the convergence is clearly better than with N_R for all but the very last states. This makes sense as the high energy states have a much longer range (as we shall see in detail later) and as the spacing of the angular grid is much greater at long range we therefore need larger grids. It is also important to note that the convergence is from below, obviously this is not variational behaviour. A DVR system can behave in a non-variational way when it is no longer isomorphic to the FBR, the isomorphism fails when the quadrature approximation fails [87; 110; 111]. Hence, we can assume that the integrals are being poorly evaluated here. Some effort was made to correct but with no success. However because the integration is improving with increasing basis size and the numbers are converging to agree with the Jacobi result we can safely continue the calculation.

Table 6.5 shows the last twenty bound states converging with respect to the final Hamiltonian size (N^{3D}). Here the convergence is completely monotonic and is from above, also the convergence is better than in the cases of N_θ and N_R.

Table 6.3: Convergence of even parity band origins ($E(N_R)$) with respect to changes in N_R for the last 20 bound states of H_3^+. $\Delta E(N_R) = E(120) - E(N_R)$

N_e	$E(120)$	$\Delta E(100)$	$\Delta E(105)$	$\Delta E(110)$	$\Delta E(115)$
668	34716.850	-0.285	-0.264	-0.121	-0.040
669	34726.958	-0.537	-0.390	-0.158	-0.082
670	34744.139	-0.384	-0.270	-0.125	-0.028
671	34745.815	-0.497	-0.457	-0.274	-0.098
672	34750.744	-0.573	-0.370	-0.233	-0.084
673	34763.433	-1.068	-0.603	-0.424	-0.170
674	34769.659	-0.370	-0.208	-0.207	-0.060
675	34790.860	-0.435	-0.307	-0.194	-0.081
676	34795.457	-0.390	-0.449	-0.260	-0.092
677	34811.712	-0.556	-0.341	-0.200	-0.090
678	34823.961	-0.436	-0.222	-0.155	-0.082
679	34825.222	-0.805	-0.538	-0.304	-0.114
680	34836.529	-0.565	-0.313	-0.134	-0.027
681	34852.006	-0.414	-0.211	-0.099	-0.051
682	34858.105	-0.555	-0.307	-0.143	-0.094
683	34865.425	-0.549	-0.281	-0.113	-0.014
684	34882.977	-0.801	-0.432	-0.261	-0.126
685	34891.348	-2.044	-1.323	-0.775	-0.270
686	34897.999	-0.555	-0.331	-0.138	-0.142
687	34901.023	-3.238	-2.052	-1.214	-0.544

Table 6.4: Convergence of even parity band origins ($E(N_\theta)$) with respect to changes in N_θ for the last 20 bound states of H_3^+. $\Delta E(N_\theta) = E(96) - E(N_\theta)$

N_e	$E(96)$	$\Delta E(72)$	$\Delta E(80)$	$\Delta E(88)$
668	34716.850	0.119	0.157	0.016
669	34726.958	0.025	0.045	0.004
670	34744.139	0.068	0.057	0.002
671	34745.815	0.027	0.058	0.007
672	34750.744	2.605	0.046	0.005
673	34763.433	12.716	0.085	0.003
674	34769.659	6.242	0.054	0.003
675	34790.860	21.217	0.039	0.002
676	34795.457	4.616	0.058	0.001
677	34811.712	16.275	0.058	0.001
678	34823.961	12.258	0.031	0.003
679	34825.222	1.243	0.064	0.008
680	34836.529	11.338	0.033	0.006
681	34852.006	15.499	0.035	0.007
682	34858.105	6.100	0.033	0.005
683	34865.425	7.316	0.077	0.017
684	34882.977	17.718	0.143	0.026
685	34891.348	8.864	1.770	0.381
686	34897.999	10.031	2.119	0.291
687	34901.023	4.689	2.944	2.569

Table 6.5: Convergence of even parity band origins ($E(N^{3D})$) with respect to changes in N^{3D} for the last 20 bound states of H_3^+. $\Delta E(N^{3D}) = E(79091) - E(N^{3D})$.

N_e	$E(79091)$	$\Delta E(59091)$	$\Delta E(64091)$	$\Delta E(69091)$	$\Delta E(74091)$
668	34716.850	-0.284	-0.217	-0.103	-0.033
669	34726.958	-0.485	-0.351	-0.190	-0.078
670	34744.139	-0.169	-0.230	-0.078	-0.056
671	34745.815	-0.616	-0.379	-0.202	-0.098
672	34750.744	-0.534	-0.320	-0.160	-0.092
673	34763.433	-0.811	-0.586	-0.349	-0.141
674	34769.659	-0.312	-0.178	-0.147	-0.052
675	34790.860	-0.446	-0.302	-0.116	-0.089
676	34795.457	-0.610	-0.334	-0.243	-0.101
677	34811.712	-0.394	-0.302	-0.149	-0.081
678	34823.961	-0.332	-0.232	-0.117	-0.057
679	34825.222	-0.771	-0.471	-0.280	-0.129
680	34836.529	-0.518	-0.299	-0.120	-0.074
681	34852.006	-0.232	-0.196	-0.090	-0.053
682	34858.105	-0.436	-0.285	-0.152	-0.073
683	34865.425	-0.370	-0.273	-0.129	-0.054
684	34882.977	-0.579	-0.404	-0.244	-0.100
685	34891.348	-0.202	-0.142	-0.070	-0.024
686	34897.999	-0.512	-0.340	-0.182	-0.064
687	34901.023	-0.308	-0.190	-0.107	-0.045

6.4 Symmetry assignment

In Radau coordinates the radial basis parity ('s' here) cleanly splits the Hamiltonian into separate blocks. However, in our problem this is a reduced symmetry, in fact H_3^+ is in the D_{3h} point group, while the calculation is performed in the C_{2v} point group. We can see from the D_{3h} - C_{2v} correlation table (table 2.3) that the even parity ($s = 0$) states, usually states with A_1 or A_2 symmetry in the C_{2v} point group, are now of A_1 or E symmetry in the D_{3h} point group. Also, the odd parity states, usually states with B_1 or B_2 symmetry in the C_{2v} point group, are now of A_2 or E symmetry in the D_{3h} point group. This means that the E symmetry states, formed from linear combinations of $A_1 + B_2$ or $A_2 + B_1$ appear in both blocks of the Hamiltonian.

Usually the E states are paired together by comparing the energies of the states (for example see Henderson [112]). However, this poses some difficulties. States with different symmetries can often be very close together in energy, therefore it is often unclear which state should be paired with which.

6.4.1 Cyclic transformation method

Convergence was also tested by examining how the energies of states degenerate between the radial parity blocks compared. Each state was labelled with an irreducible representation (A_1, A_2, E) by examining the dot products of a wave function with itself under the three possible cyclic coordinate transformations. Taking $\hat{T}$ to be the cyclic transformation operator we have,

$$\hat{T}\phi(r_1, r_2, \theta) = \phi'(r_1', r_2', \theta') \tag{6.8}$$

$$\hat{T}^2\phi(r_1, r_2, \theta) = \phi''(r_1'', r_2'', \theta'') \tag{6.9}$$

$$\hat{T}^3\phi(r_1, r_2, \theta) = \phi(r_1, r_2, \theta) \tag{6.10}$$

where r_1,r_2 and θ are the Radau coordinates. We then computed the overlap integral

$$\langle \hat{T}\phi | \hat{T}^2\phi \rangle = \langle \phi' | \phi'' \rangle \tag{6.11}$$

Even parity states have the property that $\langle \hat{T}\phi | \hat{T}^2\phi \rangle \approx 1$ for A_1 states and $\langle \hat{T}\phi | \hat{T}^2\phi \rangle \approx -0.5$ for E states. Combined with energy comparisons this gives a reliable method for discerning the symmetry of all the bound states. At equilibrium this permutation symmetry matches that of the D_{3h} point group. An advantage of this technique is that the difference between one symmetry and another is clear and is not overly dependant on convergence. The disadvantage is that in doing the coordinate per-

mutations the grid representation of the wave function is lost and one has to fit it back onto the original grid in three dimensions. The PSPLINE package [113] proved useful for this as it can perform a tri-cubic spline fit and provided a good enough fit to the wave function. Using this technique it was possible to clearly identify the symmetry of all but 2 states. States $N_e = 664$ and $N_e = 665$ differ by only 0.177 cm^{-1} and they appear to be of a mixed A_1,E symmetry. This is an accuracy problem. Whilst the potential is invariant to D_{3h} operations, the complete Hamiltonian used in Radau coordinates is not. The *perfect* result, where only A_1,A_2 and E states are calculated, only occurs in the complete basis set limit.

6.4.2 Symmetric operator method

Another way to determine the symmetry of a state is to use an appropriate operator (one with a symmetry matching that of the molecule) and examine the overlap of the states you are studying with respect to this operator. An easy operator to pick is the potential energy because we know it has the full D_{3h} point group of the Hamiltonian, this gives us,

$$\langle\phi|V|\psi\rangle = \begin{cases} 0 & \Gamma_\phi \neq \Gamma_\psi \\ > 0 & \Gamma_\phi = \Gamma_\psi \end{cases} \tag{6.12}$$

where ϕ and ψ are two arbitrary nuclear motion states of the molecule. Of course, this means that you need to know the symmetry of at least one of the states in order to determine the others, the ground state is useful here because we know it has A_1 symmetry. An advantage of this method is that it does not destroy the grid representation of the wave functions and therefore does not rely on our ability to fit the wave function onto the original grid. A disadvantage is that it depends strongly upon the convergence of the states as we need to be able to tell the difference between a small overlap for states with the same symmetry ($\langle\phi_{A_1}|V|\psi_{A_1}\rangle \approx 0$) and the overlap of states which are not perfectly converged ($\langle\phi_{A_1}|V|\psi_E\rangle \approx 0$).

The states from each parity block were then combined to give a unified list of bound states. Each state was numbered in order of energy and states degenerate across parity block were treated as a single state. The degenerate states have their energy as an average of the separate energies. This new state numbering is referred to as N_s.

Having unified the calculations from separate radial parity blocks we observe that the separation in energies of degenerate states from each parity block also provides a measure of convergence. Figure 6.3 plots these differences on a logarithmic scale against the band origin of the same state. For all except one state, the last state ($N_s = 859$) with a difference of 3.6 cm^{-1}, the energy difference is better than 1 cm^{-1}.

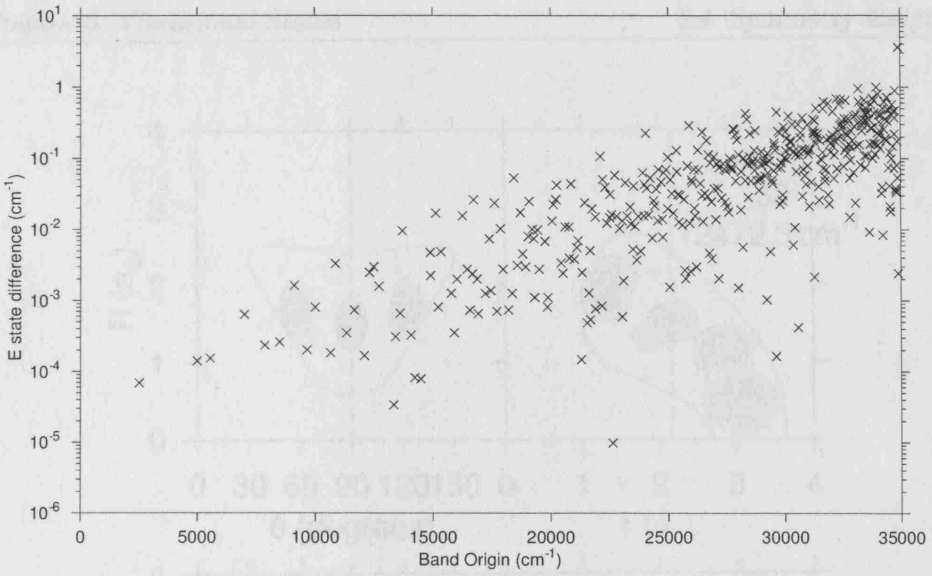

Figure 6.3: Comparison of energy for states degenerate across parity block. Energy difference is plotted on a logarithmic scale against the band origin of the same state.

6.4.3 Assignment results

With the PPKT2 potential energy surface and the convergence parameters given in table 6.1, results we find 687 even parity bound states, 599 odd parity bound states. In terms of the irreducible representations we find 260 A_1 states, 172 A_2 states and 427 E states, where here we have counted the degenerate E states as a single state just as with our symmetry numbering (N_s). The complete list of assignments is given in appendix A along with the energies and observables of the vibrational bound states.

6.4.4 Horseshoe states

Horseshoe states are characterised as states of H_3^+ where the proton passes through the diatom, this is an extension of the v_{2y} bending mode (described in chapter 1) above the barrier to linearity [34; 32]. A selection of horseshoe states are shown in figure 6.4. There are many more states which could be described as horse shoes, all the bound states are plotted and displayed in appendix B.

Berblinger *et al* showed that these rotating hosrseshoe states could satisfy the requirements of the near-dissociation spectrum [33]. Also, Le Sueur *et al* [35] showed that horseshoe states have strong dipole couplings to low lying states. They may therefore play an important part in the spectra of H_3^+.

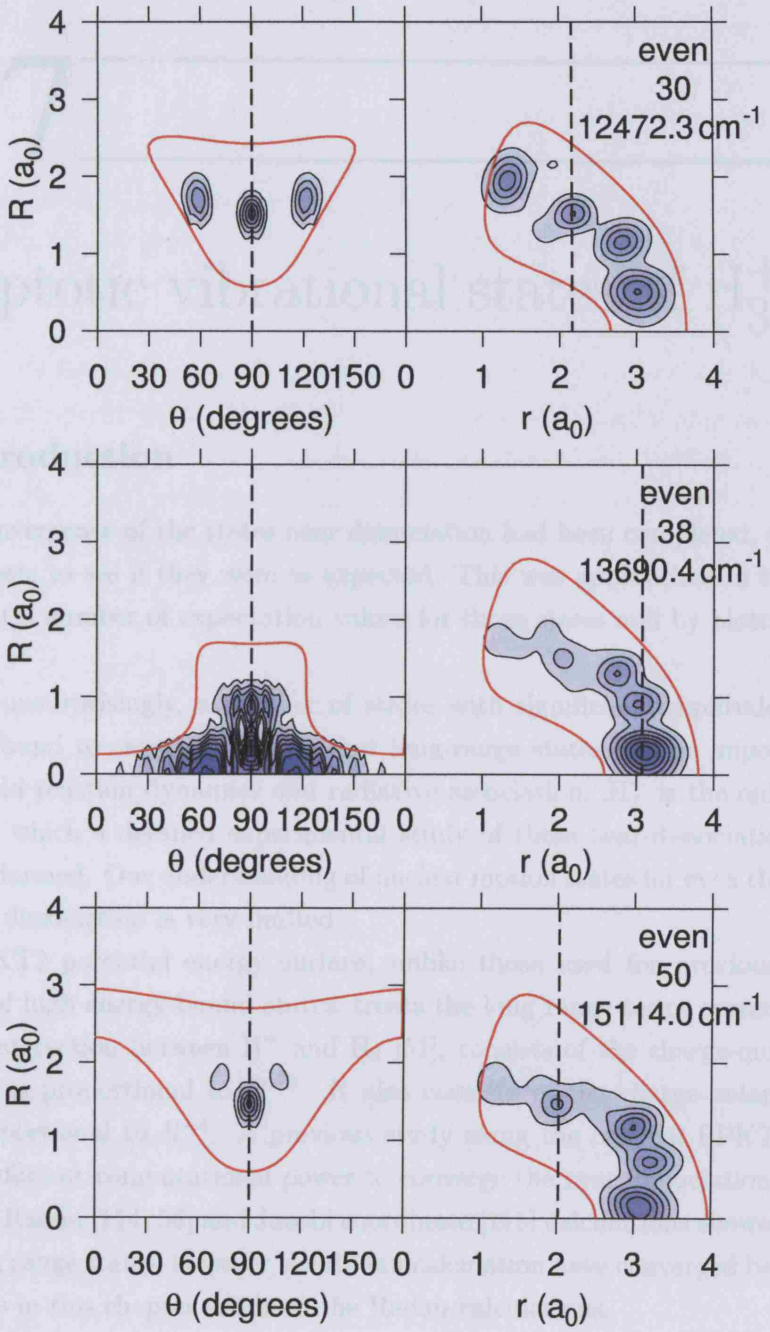

Figure 6.4: Three Horseshoe states of H_3^+. Two cuts of the three dimensional wave function ($|\psi|^2$), one in R and θ at constant r and the other in R and r at constant θ. The dashed lines show the position of the cuts (which always passes through the maximum of $|\psi|^2$). The red outer contour depicts the classical turning point.

Chapter 7

Asymptotic vibrational states of H_3^+

7.1 Introduction

Once the convergence of the states near dissociation had been completed, we began a series of tests to see if they were as expected. This was approached in two ways, by looking at a number of expectation values for those states and by plotting them graphically.

Perhaps unsurprisingly, a number of states with significant amplitude at long range were found to exist. It is clear that long-range states will be important for near-threshold reaction dynamics and radiative association. H_3^+ is the only bound molecule for which a detailed experimental study of these near-dissociation states has been performed. Our understanding of nuclear motion states for even this simple system near dissociation is very limited.

The PPKT2 potential energy surface, unlike those used for previous studies [39; 41; 42] of high energy bound states, treats the long range terms correctly. The long range interaction between H^+ and H_2 [51], consists of the charge-quadrupole term, which is proportional to R^{-3}. It also consists of the charge-polarisability, which is proportional to R^{-4}. A previous study using the original PPKT surface [45] had insufficient computational power to converge the near dissociation states.

Both the Radau [114; 56] and Jacobi coordinate [115] calculations showed a clear signal of long range states, however the Radau calculation have converged better and so the results in this chapter are from the Radau calculations.

7.2 Graphical analysis

By taking two-dimensional cuts of the DVR wave functions along the plane (r, R) and (θ, R) (in Jacobi coordinates), we were able to construct a picture of what was happening at long range.

Graphical analysis of the wave functions of all our bound states was performed by taking a variety of 2D cuts through the wave functions for several coordinate positions (for both Radau and Jacobi coordinate calculations), paying particular attention to states lying above D_e. These cuts revealed a number of states whose amplitude can be regarded as lying substantially in the asymptotic region of the potential.

We also examined the wave functions by cutting along R and θ for fixed r (the H_2 equilibrium bond length). We found that there are a series of long range states with excitations in both the radial R coordinate and the angular θ coordinate. These states retain the complicated short-range behaviour which ensures orthogonality to the other high energy states and do not have any excitations in the H–H distance, r. This is to be expected because of the almost one dimensional nature of the potential at long range.

Graphical analysis was performed for all the bound states, with particular emphasis on states with energy greater than D_e. The plots in figure 7.1 and 7.2 are DVR wave functions from the Radau coordinate calculation but plotted in Jacobi coordinates. Each Radau point was converted to Jacobi and any points lying between 89° and 91° of the Jacobi angle was included in the plot of R against r. Any Jacobi point lying between 1.3 and 1.4 of the inter-atomic r coordinate was included in the plot of R against θ. The first three plots (N_s=801, 824, 834) have a similar structure and all show no structure at all at $\theta = 90°$, this is because they are all from the odd radial parity calculation and have nodes at 90°. In other states, clear nodes are visible on both the radial and angular coordinates.

We can see that the wave functions, plotted in figure 7.1 and 7.2, all have significant amplitudes at longe range. This is why they were selected for display over the other states. We can also see that these long-range states continue to have a complicated chaotic type behaviour at short range and therefore their structure can not be wholly attributed to one-dimensional H_2—H^+ type motions. Finally the structure at long-range is, in contrast to the structure at short range, quite simple and exists at a relatively low order of excitation. This can be expected from the one-dimensional nature of the potential at long-range along the dissociation channel. These states close to dissociation are not clearly distinct from other bound states because of their

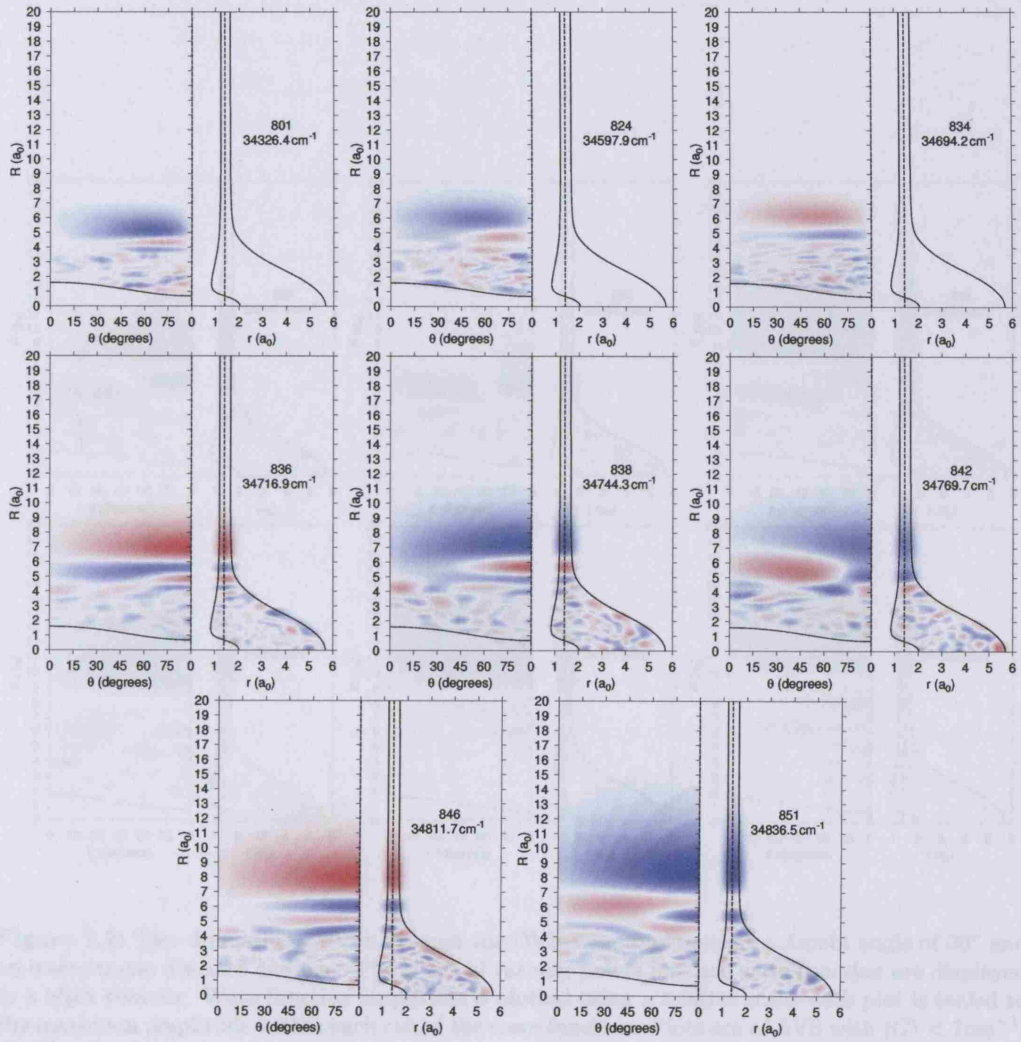

Figure 7.1: Two dimensional slices through the DVR wave functions at a Jacobi angle of 90° and an inter-atomic distance of $1.4a_0$. The classical turning points for each wave function are displayed as a black contour. Wave function amplitude is plotted using a relative scale; each plot is scaled to the maximum amplitude within each cut of the wave function. Plots are of AVS with $\langle C \rangle < 7\text{cm}^{-1}$. The fan-shaped lines at long range are a fitting artifact.

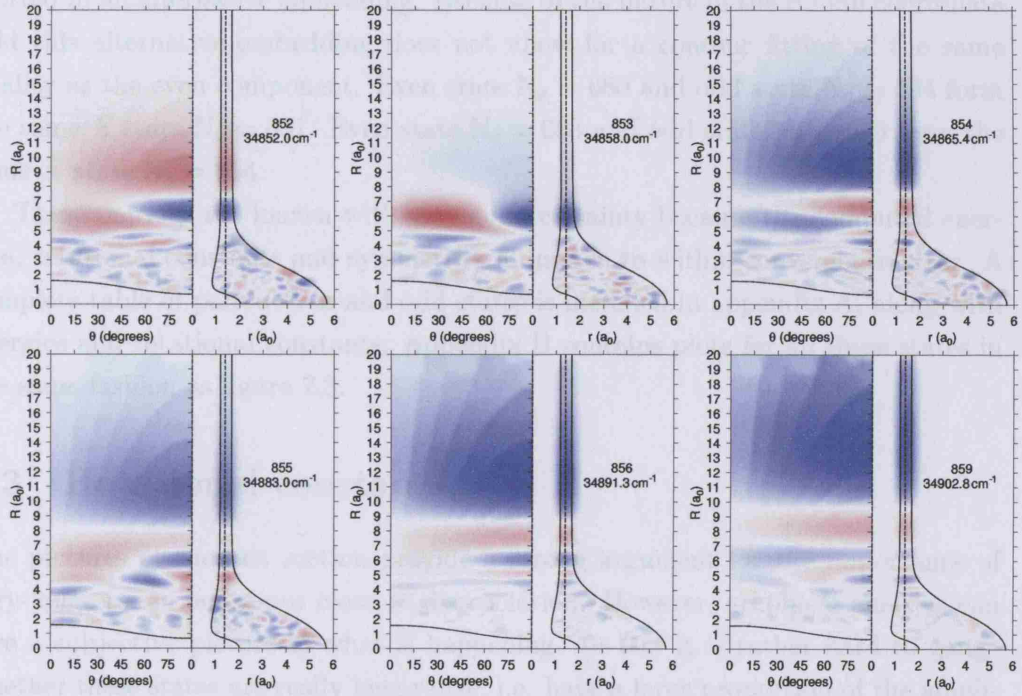

Figure 7.2: Two dimensional slices through the DVR wave functions at a Jacobi angle of 90° and an inter-atomic distance of $1.4a_0$. The classical turning points for each wave function are displayed as a black contour. Wave function amplitude is plotted using a relative scale; each plot is scaled to the maximum amplitude within each cut of the wave function. Plots are of AVS with $\langle C \rangle < 7\text{cm}^{-1}$. The fan-shaped lines at long range are a fitting artifact.

mixed type behaviour and the smooth way in which this behaviour emerges. However, the simple long range behaviour is new and only emerges close to dissociation. We have labelled states with this type of structure asymptotic vibrational states (AVS).

The E symmetry states have even and odd components calculated separately because of the radial basis parity. The long range nature of the E symmetry AVS states can therefore be seen in both even and odd parity wavefunctions. Figure 7.3 shows two such pairs of wavefunctions. In the symmetric embedding of Jacobi coordinates, odd states have a node at 90°. The odd components are therefore plotted in an alternative embedding. Because of the nature of the Radau coordinate grid this alternative embedding does not allow for a contour fitting of the same quality as the even component. Even state $N_e = 680$ and odd state $N_o = 594$ form the same E state $N_s = 851$. Even state $N_e = 683$ and odd state $N_o = 596$ form the same E state $N_s = 854$.

These pairings are known with very good certainty because the computed energies, rotational constants and symmetries all match to within convergence error. A complete table of paired even and odd states is included in appendix A, along with energies and rotational constants. Appendix B contains plots for all these states in the same fashion as figure 7.3.

7.3 Rotational constants

The pictures of the last section provide a strong argument for the importance of very-longe range behaviour close to disscociation. However, graphical analysis can give a subjective picture of what is happening. In fact it is rather hard to gauge whether these states are really long range, i.e. have a large proportion of the amplitude at long range, or whether these pictures are only showing us long-range tails which contribute little to the state. In order to develop a more objective and quantitative picture of these states, we calculated a number of expectation values of the wavefunction. One of the most informative of these was an expectation value for the rotational constant of the state in the spirit of the rigid rotor approximation.

The rigid rotor approximation tells us that (for H_3^+) the energy of the molecule is related to its angular momentum by the formula for an oblate symmetric top,

$$\Delta E(J,K) = BJ(J+1) + (C-B)K^2 \tag{7.1}$$

where $\Delta E(J,K)$ is the difference from the band origin as a function of the total angular momentum (J) and its projection on the z axis (K). Here the rotational

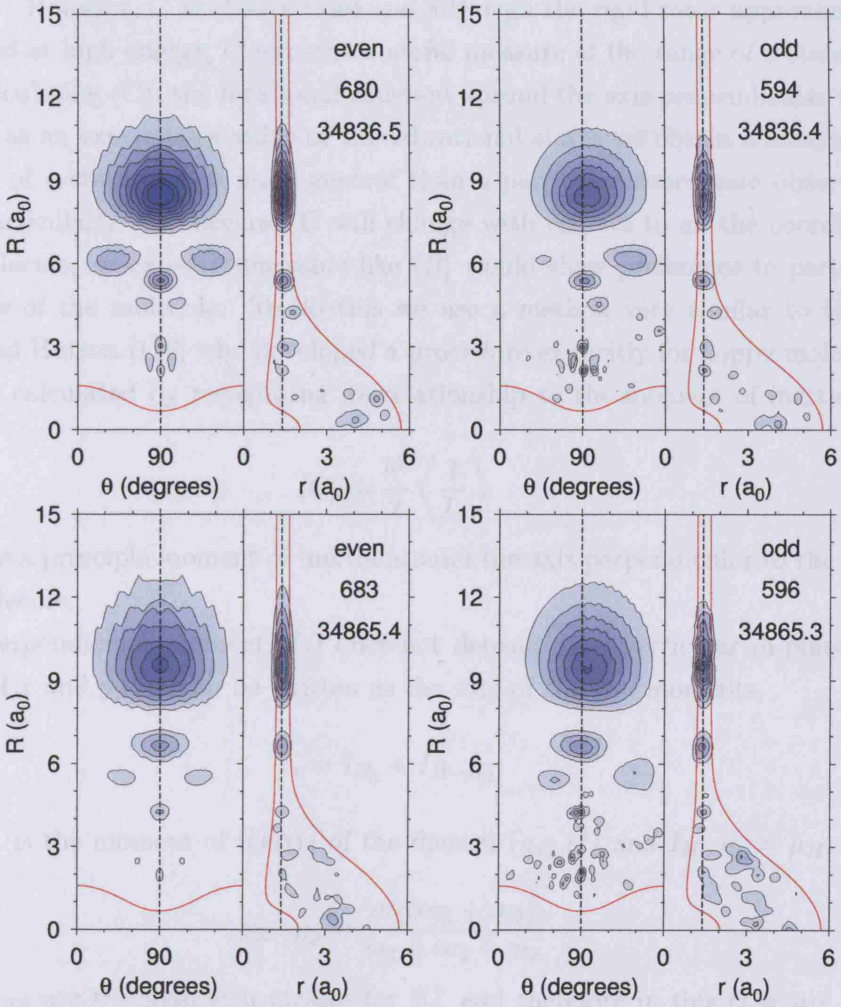

Figure 7.3: Two dimensional slices through the DVR wave functions at a Jacobi angle of 90° and an inter-atomic distance of $1.4a_0$. The classical turning points for each wave function are displayed as a red contour. Probability amplitude is plotted in 10% increments up to the maximum of the wavefunction. Plots are of even and odd components of AVS with E symmetry.

constants A,B and C are taken to be with respect to the x, y and z axes respectively. In our formulation, A and B are therefore rotational constants for motion in the plane of the molecule and they quickly become very large at the low energy for which H_3^+ begins to access linear configurations. The classical approach to calculating A and B from the moment of inertia would lead to infinities as $R \to 0$. Here however A and B remain well defined because the DVR basis does not include the values $R = 0$ or $\theta = n\pi$. However, C is always valid and although the rigid rotor approximation is not valid at high energy, C remains a useful measure of the range of a state.

By calculating $\langle C \rangle$, the rotational constant around the axis perpendicular to the molecule, as an expectation value of the vibrational states we obtain a measure for the range of a state that is more general than a particular coordinate observable. This is particularly true because C will change with respect to all the coordinates of the molecule, an expectation value like $\langle R \rangle$ would show preference to particular geometries of the molecule. To do this we use a method very similar to that of Ernesti and Hutson [116] who developed a procedure explicitly for floppy molecules. Here C is calculated by recognising its relationship to the moment of inertia of a molecule,

$$\langle C \rangle = \frac{\hbar^2}{2} \left\langle \frac{1}{I_z} \right\rangle \tag{7.2}$$

where I_z is a principle moment of inertia around the axis perpendicular to the plane of the molecule.

The perpendicular moment (I_z) does not depend on a particular in-plane embedding of x and y and can be written as the sum of the two moments,

$$I_z = I_{H_2} + I_{H-H_2}, \tag{7.3}$$

where I_{H_2} is the moment of inertia of the diatom ($\mu_{H_2} r^2$) and $I_{H-H_2} = \mu_{H-H_2} R^2$ with

$$\mu_{H-H_2} = \frac{m_1(m_2 + m_3)}{m_1 + m_2 + m_3} \tag{7.4}$$

where $m_{1,2,3}$ are the hydrogen masses for H_3^+ and therefore in this case μ_{H-H_2} is just $(2/3)m_H$.

The DVR wave functions are initially in Radau coordinates and therefore have to be converted into Jacobi coordinates so that the rotational constants can be computed, just as with the graphical plots of the previous section. This is combined with the symmetry assignments from section 6.4. Each E symmetry state therefore has two rotational constants computed and the results quoted are the average of these.

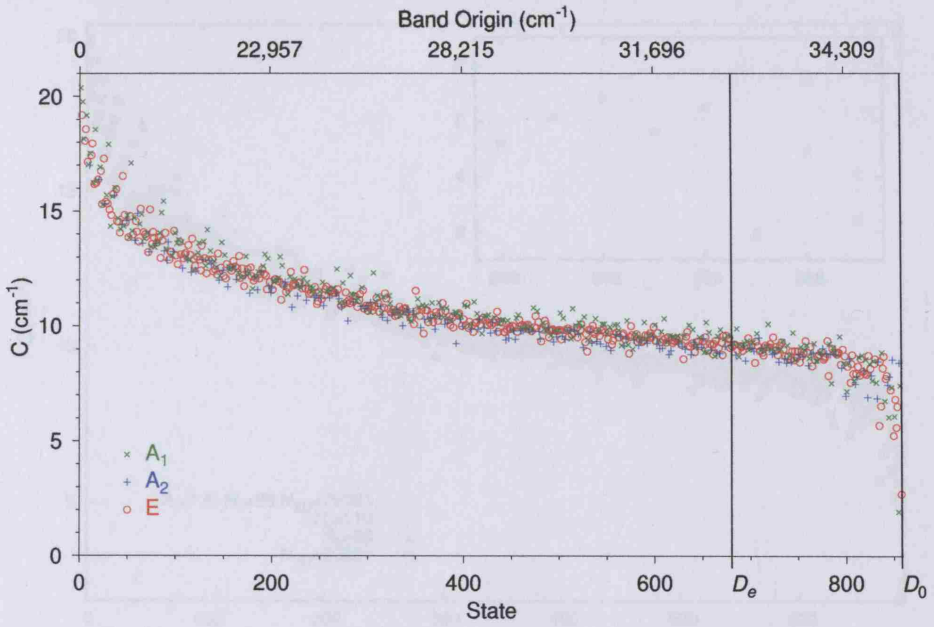

Figure 7.4: Plot of rotational constant C against state number. The classical dissociation energy (D_e) is after state 681 and the first dissociation energy (D_0) allowed in our calculation is after state 859. The state number is not linear in energy, however representative values for band origins are given on the top axis.

Figure 7.4 plots the rotational constant C for all the bound vibrational states of H_3^+. For low lying states $C \approx 20$ cm^{-1}, but this drops to $10 \leq C \leq 14$ cm^{-1} as states soon possess energy sufficient to sample linear geometries. Above D_e there are 14 states for which C is less than 7 cm^{-1}. Furthermore, there is a close and unsurprising correlation between the extent of the AVS and a low value of C. Thus, for example, state 856, a very extended state, has the lowest value of C, 1.94 cm^{-1}.

We must consider the convergence for these expectation values. This is because, although we have computed these states using a variational method and can be confident in the error of the energy of these states, this does not guarantee the convergence of the computed expectation value.

The C rotational constant was computed for a number of pre-converged calculations. This was done for a calculation with $N_r = 110$, $N_\theta = 88$ and $N_{3D} = 69,091$, seperately. Figure 7.5 shows in detail how C changes with the differences. As we can see, the values are well converged and closely overlap with each other. The only large differences are detailed in the zoom-out which shows that the last two states have rotational constants changing with respect to the number of angular grid points N_θ. This is consistent with what can be expected from the energy convergence.

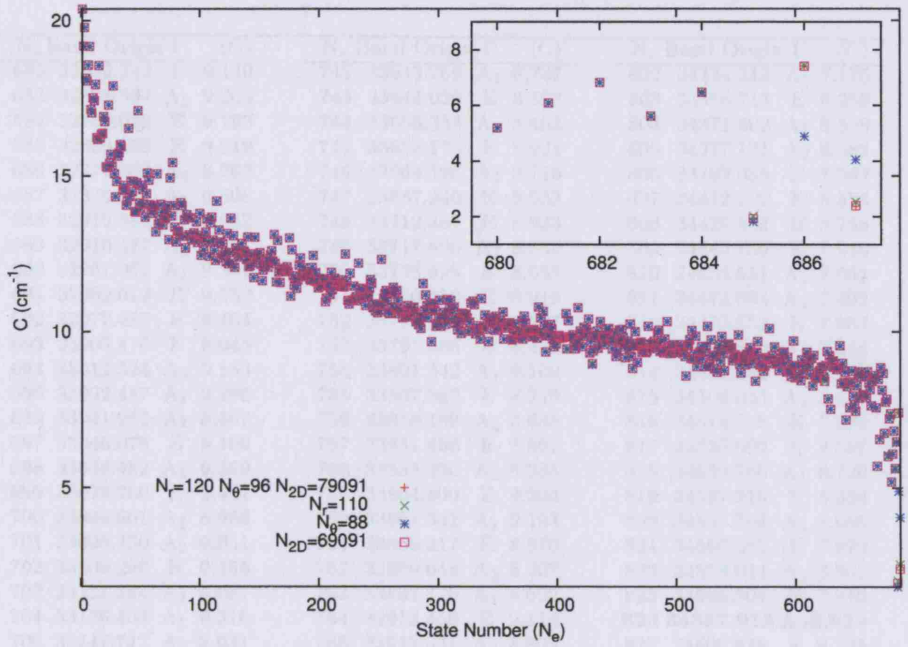

Figure 7.5: The convergence of rotational constant C for each state (N_e) with respect to the basis set sizes, N_R, N_θ and N_{2D}.

Table 7.1 gives the calculated rotational constants for all states above the classical dissociation energy D_e and below the quantum dissociation energy D_0. Toward the end of this table we observe a number of states for which the rotational constant is less than expected. Here we identify 14 states with $\langle C \rangle < 7$ cm^{-1} as asymptotic vibrational states (AVS), although calculations with even more extended radial basis sets would undoubtedly lead to further such states. These 14 states with low $\langle C \rangle$ are precisely the same 14 states plotted earlier in figure 7.1 and 7.2.

7.4 The ubiquity of AVS states

These AVS states are interesting because they show how a pre-dissociative molecule can have a completely different behaviour and structure to any lower energy states, undoubtedly because of the nature of the potential near dissociation. However, this is not really surprising, indeed as we shall see when we look at the classical trajectories, these states can be understood in just one or two dimensions. One dimension, in the sense that in fact the behaviour is essentially one dimensional, it is behaviour that is asymptotic to the zero-point behaviour where only the diatom distance is important. However, we will need to think in terms of two or three

Table 7.1: Rotational constants for all states above the classical dissociation energy (D_e). The 14 AVS states are marked in bold (identified here as states with $\langle C \rangle < 7.0 cm^{-1}$).

N_s	Band Origin	Γ	$\langle C \rangle$	N_s	Band Origin	Γ	$\langle C \rangle$	N_s	Band Origin	Γ	$\langle C \rangle$
682	32832.743	E	9.139	742	33643.759	A_1	8.737	802	34334.312	A_1	7.175
683	32838.584	A_1	9.263	743	33644.020	E	8.573	803	34356.713	E	8.256
684	32857.022	E	9.193	744	33656.333	A_2	8.463	804	34371.402	A_1	8.398
685	32859.159	E	9.219	745	33659.176	E	8.921	805	34377.121	A_2	8.583
686	32874.409	A_2	8.763	746	33669.196	A_1	9.716	806	34383.058	E	7.563
687	32876.224	A_1	9.898	747	33687.240	E	8.533	807	34412.222	E	8.376
688	32915.384	E	8.962	748	33712.387	E	8.933	808	34425.456	E	8.758
689	32916.477	A_1	8.681	749	33717.896	A_1	8.550	809	34440.739	E	7.940
690	32961.061	A_1	9.207	750	33738.596	E	8.653	810	34458.531	A_1	7.661
691	32962.012	E	9.152	751	33766.310	E	8.919	811	34473.004	A_2	7.492
692	32977.487	E	9.104	752	33774.187	A_2	8.787	812	34473.552	E	7.953
693	33005.470	E	8.948	753	33791.886	E	8.441	813	34479.869	A_2	7.818
694	33012.324	A_2	9.163	754	33801.342	A_1	9.100	814	34487.882	E	8.257
695	33022.487	A_1	9.289	755	33807.867	E	8.719	815	34509.045	A_1	8.657
696	33041.952	A_2	8.507	756	33818.189	A_2	8.688	816	34514.278	E	7.876
697	33046.078	E	9.166	757	33831.466	E	8.867	817	34530.009	E	8.587
698	33048.482	A_1	9.369	758	33833.300	A_1	8.985	818	34530.760	A_1	8.730
699	33078.760	E	9.491	759	33854.800	E	9.364	819	34537.215	E	8.034
700	33094.601	A_1	8.986	760	33861.541	A_1	9.193	820	34537.704	A_2	8.085
701	33098.350	A_2	9.051	761	33866.317	E	8.870	821	34560.585	E	7.973
702	33100.299	E	9.155	762	33889.648	A_2	8.307	822	34578.624	A_1	8.561
703	33121.584	A_2	9.081	763	33892.770	A_1	8.622	823	34595.804	E	7.910
704	33136.403	A_1	9.316	764	33913.458	E	9.114	**824**	**34597.913**	**A_2**	**6.924**
705	33147.742	A_2	8.931	765	33913.631	A_2	8.803	825	34606.838	E	8.728
706	33162.403	E	8.421	766	33931.202	E	8.274	826	34619.147	A_1	8.365
707	33174.989	E	9.340	767	33954.829	A_2	8.857	827	34633.976	E	8.167
708	33186.704	A_1	9.692	768	33956.829	A_1	9.248	828	34645.934	A_2	7.864
709	33192.039	E	9.156	769	33961.768	E	8.556	829	34646.539	A_1	7.650
710	33201.243	A_2	9.493	770	33992.400	A_1	8.509	830	34667.981	A_1	8.498
711	33226.285	E	8.937	771	34009.164	A_1	8.508	831	34668.083	E	8.384
712	33234.119	A_1	8.970	772	34016.768	E	8.700	832	34677.439	E	8.581
713	33246.551	A_2	9.043	773	34029.107	E	8.767	833	34685.077	A_1	7.562
714	33275.107	E	8.875	774	34033.467	A_1	8.880	**834**	**34694.164**	**A_2**	**6.875**
715	33284.878	E	8.746	775	34038.754	A_2	8.773	835	34711.831	A_2	8.461
716	33315.650	A_1	8.905	776	34042.648	E	8.892	**836**	**34716.886**	**E**	**5.694**
717	33329.792	E	9.172	777	34058.184	A_2	9.044	837	34727.068	E	8.474
718	33347.108	A_1	9.132	778	34066.149	E	8.561	**838**	**34744.326**	**E**	**6.538**
719	33352.410	E	9.110	779	34078.049	E	8.640	839	34745.815	A_1	8.858
720	33361.203	A_1	10.099	780	34079.101	E	8.699	840	34750.977	E	8.180
721	33370.986	E	9.104	781	34082.293	A_2	8.832	841	34762.988	E	8.689
722	33386.455	E	9.231	782	34103.762	E	9.369	**842**	**34769.659**	**A_1**	**6.759**
723	33408.141	A_1	8.981	783	34121.110	E	7.856	843	34790.841	E	7.728
724	33423.080	A_2	8.791	784	34126.874	A_1	9.234	844	34795.439	E	7.857
725	33435.645	E	9.529	785	34129.533	A_2	8.789	845	34808.455	A_2	7.461
726	33439.955	A_2	8.852	786	34148.197	A_1	7.527	**846**	**34811.712**	**A_1**	**6.048**
727	33451.474	E	9.109	787	34158.178	E	9.043	847	34812.020	A_2	7.816
728	33453.888	E	8.956	788	34159.421	A_1	9.082	848	34823.944	E	7.233
729	33465.606	A_1	9.016	789	34172.314	A_1	8.889	849	34825.222	A_1	7.343
730	33480.188	E	8.759	790	34176.888	E	8.859	850	34834.888	A_2	8.548
731	33493.204	A_2	8.457	791	34189.886	A_2	8.767	**851**	**34836.489**	**E**	**5.250**
732	33507.168	E	9.173	792	34201.917	E	8.789	**852**	**34852.006**	**A_1**	**6.085**
733	33513.046	A_1	9.017	793	34227.369	E	8.869	**853**	**34858.018**	**E**	**6.828**
734	33520.245	E	9.309	794	34239.662	E	8.859	**854**	**34865.398**	**E**	**5.603**
735	33536.546	A_1	9.354	795	34263.257	A_1	9.554	**855**	**34882.978**	**E**	**6.512**
736	33548.716	E	9.004	796	34274.747	E	8.341	**856**	**34891.348**	**A_1**	**1.941**
737	33578.056	A_2	8.601	797	34294.720	A_2	8.199	857	34897.104	A_2	8.405
738	33585.915	E	8.712	798	34300.868	E	8.997	858	34897.999	A_1	7.423
739	33590.436	A_2	8.413	799	34313.672	A_1	8.385	**859**	**34902.824**	**E**	**2.706**
740	33596.613	A_1	9.177	800	34321.463	E	8.709				
741	33610.523	E	8.714	**801**	**34326.376**	**A_2**	**6.976**				

dimensions and the complete three-body system in order to understand how these states actually arise in our poly-atomic.

The natural question to ask is whether these states, or similar states have been seen before and in what context. Also what can we learn from these previous works and how do they relate to our system?

Quasi-Landau states [117; 118] appear to be the simplest quantum states that show an analogous behaviour. They occur in the comparatively simple system of a hydrogen atom in a strong magnetic field. The radial r^{-1} Coulomb field is intersected by a x^2 magnetic field. The r^{-1} term being radial, the electrostatic force between the proton and the electron. The x^2 term being uni-directional with parallel field lines from a macroscopic magnetic field.

This system generates a simple potential,

$$V(x,y) = \frac{\alpha}{r} + \beta x^2 \tag{7.5}$$

so that the usual hydrogen dissociation,

$$H + \gamma \rightarrow H^+ + e^- \tag{7.6}$$

now includes a dissociation channel that supports zero-point energies for the escaping proton and electron.

$$E_H + E_\gamma \rightarrow E_{H^+} + E_{e^-} \tag{7.7}$$

where E_{H^+} and E_{e^-} must both be greater than or equal to their respective zero-point energies.

This system generates a complicated spectrum [117] and previous studies [118] have shown that long range pre-dissociative states exist that explain this spectrum and possess interesting dynamics that are closely analogous to the behaviour of H_3^+ near dissociation.

We can try and relate what is happening to simple diatomic systems such as H_2. This system has been extensively studied before and is well understood near dissociation [48]. However, here the comparison breaks down as di-atomics do not normally support a zero-point energy at break up. In the case of H_2, the released hydrogen atoms can have a continuum of energies. Without this zero-point constraint there would appear to be no way to support this kind of long-range behaviour.

There have also been a few studies involving other tri-atomics with lower dimension calculations that have alluded to the existence of AVS type states. Similar van der Waals states were found for ozone near its dissociation limit [119]. Also,

Jost *et al* [120] observed an unexplained increase in the density of states for NO_2 near its dissociation limit, for low values of angular momentum. Further analysis revealed that this could be explained in terms of loosely bound states [121]. This relates directly back to our calculation of the rotational constant C, as, if NO_2 also supports an appreciable amount of AVS type behaviour then we can expect that the associated low rotational constants will mean that many rotational states exist for these AVS, before they reach dissociation. We can therefore expect to also see an increase in the rotational density of states near dissociation in further calculations.

There is perhaps one other comparison that appears to be worth drawing, that is to *Efimov* states [122]. Efimov states also exist at long range and between D_e and D_0 but are different to AVS in that they are a true three-body effect. They occur in weakly bound tri-atomics such as $^4He_3$ [123; 124]. However, even though there can, theoretically, be infinitely many of these states, in practise this requires very special conditions and only a few have been observed (e.g. 1 or 2 for $^4He_3$ [124]). Here we can see that the exact nature of the potential strongly effect the exact nature of these Efimov states. We can also, therefore, expect the exact nature of the AVS to be critically dependant of nature of the potential at long-range.

We know from the Quasi-Landau case that states such as these can exist for the strongest of dissociative potential curves R^{-1}, but what about the weakest, such as the van der Waals R^{-6} type behaviour? We can test this by modifying our potential so that its strongest term is R^{-6} while keeping the end points in the potential fixed to the original fit. In figure 7.6 we can see how this change affects the potential along the dissociation channel.

By running our converged calculation on this new *weaker* potential we find less bound states (681 even states). This can be expected as we can see from figure 7.6 that we have reduced the phase space that states can occupy and therefore the density of states must go down. However, calculating the rotational constant C of the new states (figure 7.7) demonstrates that the AVS survive as there is still a clear drop in the rotational constant before dissociation.

7.5 Conclusions

An early hypothesis to explain the near dissociation results of Carrington *et al*, was that H_3^+ forms a series of $H_2 - H^+$ type complexes, essentially vibrational bending modes at high energy [30]. The existence of the AVS which contain this mode of behaviour would seem to lend credence to this idea. However it was suggested that it is the rotating forms of these complexes behind an effective centrifugal-barrier

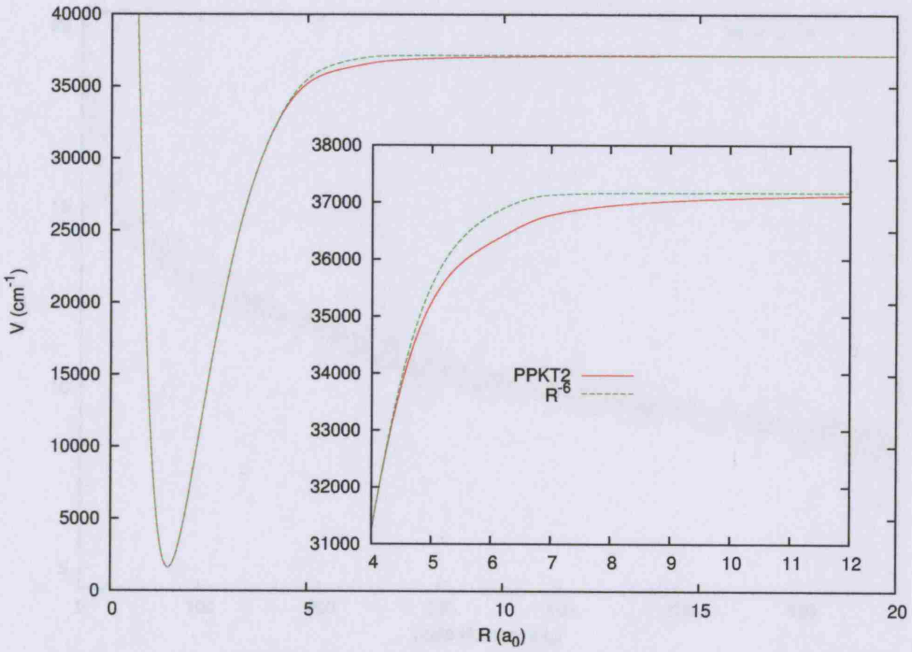

Figure 7.6: Plot comparing the PPKT2 potential [2] with the R^{-6} potential. The R^{-6} potential only differs as it approaches dissociation, an R^{-6} term being used but with boundary values that match the original potential.

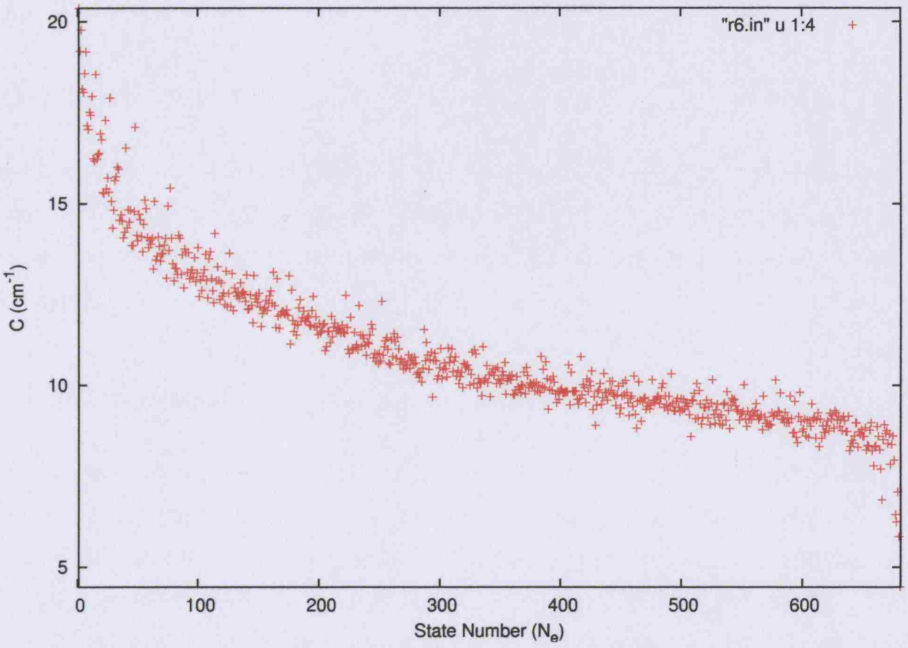

Figure 7.7: Plot of rotational constant C against state number (N_e) for vibrational states calculated on a R^{-6} potential surface. Here N_e counts just the even parity states from the calculation ($A_1 + E$).

that could explain the near dissociation spectrum [31].

$H_2 + H^+$ is also a simple and typical collisional system. The long range nature of AVS means that they will probably play an important role in this type of process. The many short-range states of H_3^+ have been shown to play an important role in inelastic collisions [125] and it is known that collisions are very sensitive to the nature of the potential at long range [126].

Chapter 8

Classical study of states

8.1 Introduction

In order to understand what is giving rise to these AVS and to see whether they can be understood as quantum scars of periodic classical orbits we performed a series of classical trajectory calculations including the calculation of a number of Poincaré surfaces of section.

8.2 The classical approximation

Two dimensional classical trajectory calculations were performed on the Jacobi coordinates r and R (at a fixed $\theta = 90°$) This is because the dissociation channel of $H_3^+ \rightarrow H_2 + H^+$ is essentially one dimensional near the dissociation energy, with a rapidly changing derivative in the r direction, but slowly changing in the R and θ directions. Therefore in order to understand the dissociative trajectories available to the system we choose to vary r (the inter-atomic distance) and R (the dissociative coordinate) but freeze θ. Using the simplified classical Hamiltonian,

$$H = \frac{P_r^2}{2\mu_r} + \frac{P_R^2}{2\mu_R} + V(r, R) \tag{8.1}$$

where P is the momentum along a radial coordinate and μ is the reduced mass along the same coordinate.

$$\mu_r^{-1} = m_2^{-1} + m_3^{-1} \tag{8.2}$$

$$\mu_R^{-1} = m_1^{-1} + \frac{\mu_r^{-1}}{4} \tag{8.3}$$

By using *Hamilton's equations*,

$$\dot{r} = \frac{\partial H}{\partial P_r} = \frac{P_r}{\mu_r} \tag{8.4}$$

$$\dot{P}_r = -\frac{\partial H}{\partial r} = -\frac{\partial V}{\partial r} \tag{8.5}$$

$$\dot{R} = \frac{\partial H}{\partial P_R} = \frac{P_R}{\mu_R} \tag{8.6}$$

$$\dot{P}_R = -\frac{\partial H}{\partial R} = -\frac{\partial V}{\partial R} \tag{8.7}$$

we get a system of first order differential equations. This then forms the basis of an initial value problem, which can be solved using one of the many FORTRAN integrators available.

Here we tested RKSUITE [127], ODEPACK [128] and a selection of FORTRAN routines from *Numerical Recipes* [129]. RKSUITE proved to be fast and accurate over a wide range of conditions and so was used for all the calculations quoted here.

Here we use precisely the same potential (V) as for the quantum calculations (PPKT2) and the FORTRAN Runge-Kutta integrator, RKSUITE [127], to compute the time evolution of a trajectory.

8.3 Low energy

At low energy we see typical, molecular behaviour, figure 8.1 shows a classical breathing behaviour at low energy.

8.4 Medium energy

At medium energies we find the expected trajectories for H_3^+, now showing very floppy behaviour, including the so called Horseshoe trajectories. Horseshoe trajectories are named as such because of the shape of the trajectory as plotted in figure 8.2. The Horseshoe trajectories are very stable at low energy, the motion is that of a proton moving toward the centre of the di-atom, the molecule becoming linear and then moving through equilibrium and up the potential on the other side of the di-atom [34]. It is possible that resonance versions of these states trapped behind an effective centrifugal barrier in the rotating molecule form the basis of the near dissociation spectrum [32].

We also plotted Poincaré surfaces of section at low energy and dissociative en-

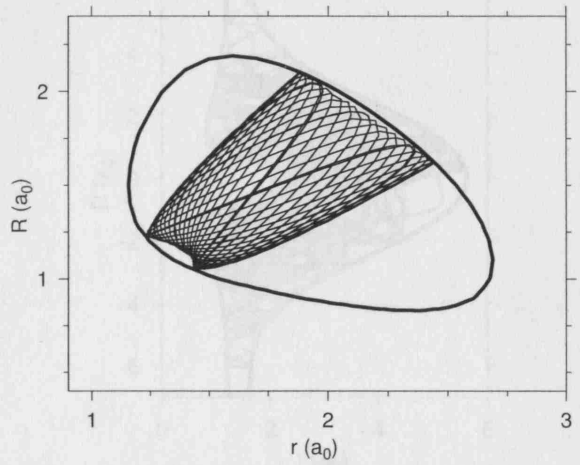

Figure 8.1: Plot of a classical trajectory close in behaviour to an H_3^+ breathing mode at an energy of 8,500 cm^{-1} (above the potential minimum). The classical turning point for the potential at the same energy is shown as a thick black contour.

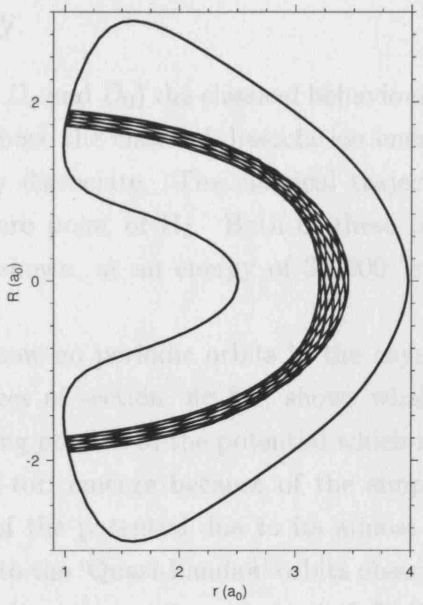

Figure 8.2: Plot of a classical trajectory from a stable periodic horseshoe state at an energy of 19,600 cm^{-1} (above the potential minimum). The classical turning point for the potential at the same energy is shown as a thick black contour.

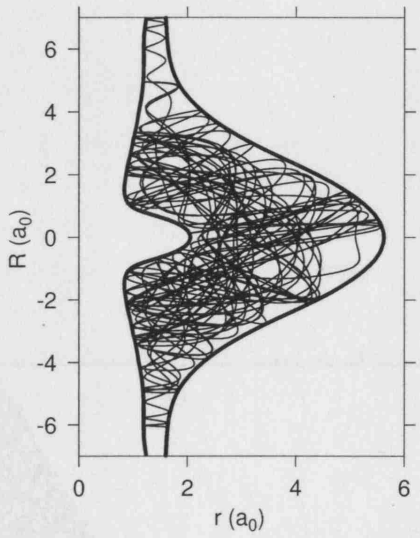

Figure 8.3: Plot of a typical classical trajectory at an energy of $38{,}000^{-1}$ (above the potential minimum). The classical turning point of the potential is plotted as a thick black contour.

ergies in order to characterise the behaviours of the system.

8.5 High energy

At high energy (between D_e and D_0) the classical behaviour of the molecule becomes unstable and chaotic. Above the classical dissociation energy D_e the system is also open and can classically dissociate. The classical trajectories are not bound by having to achieve the zero point of H_2. Both of these properties can be seen in a typical trajectory, as shown, at an energy of $38,000$ cm^{-1} above the potential minimum, see figure 8.3.

These calculations show no periodic orbits in the asymptotic (large R) region. However Poincaré surfaces of section, fig 8.4, shows what appears to be half-tori trapped in the dissociating portion of the potential which merge with chaotic orbits at small R. These half-tori emerge because of the simple nature of trajectories in the long range part of the potential due to its almost one dimensional nature. This situation is similar to the 'Quasi-Landau' orbits observed in another classically unbound system, the Hydrogen atom in a magnetic field [118].

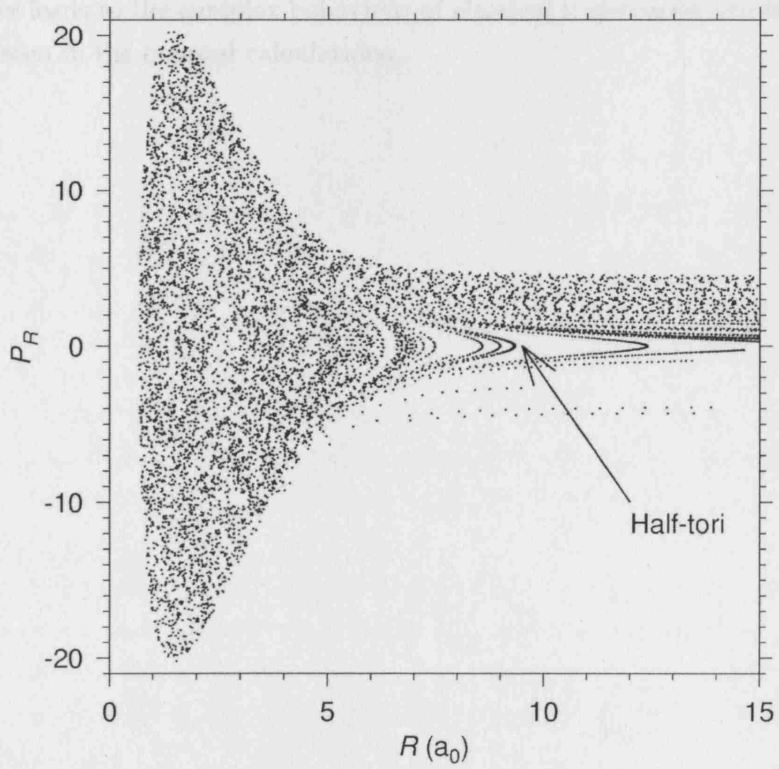

Figure 8.4: Poincaré surface of section for classical trajectories intersecting the R and P_R plane where P_R is the momentum along R. The plane lies along $r = 1.4a_0$ (the equilibrium H_2 bond length). Trajectories have an energy of 39,000 cm^{-1} above the potential minimum.

8.6 Conclusion

It can be seen that the AVS discussed in the previous chapter (chapter 7) may be understood in terms of these long-range classical trajectories. At long range the potential is almost one-dimensional in nature, it is relatively flat in the Jacobi R and θ coordinates, whilst in the H_2 distance (r) the potential is much stronger. At long range this results in both the simple classical trajectories and the simple nodal structure of the AVS states. At short range the stronger coupling between Jacobi coordinates leads to the complex behaviour of classical trajectories and the complex structure seen in the quantal calculations.

Chapter 9

The resonance states of H_3^+

As described in chapter 2, we use a system where the bound state calculations are extended with a complex absorbing potential (CAP),

$$H'(\lambda) = H - i\lambda U(R) \tag{9.1}$$

where H is the bound state Hamiltonian , $U(R)$ is the CAP defined in terms of a dissociating coordinate R and λ is the CAP strength. For H_3^+ we can see that using the Jacobi coordinate R is a good choice as it always grows large as the molecule dissociates.

A complex Siegert energy, E, is found for a resonance state by finding an optimal $\lambda = \lambda_{\text{op}}$ for each state. There are a number of strategies for locating the optimal value of λ_{op}, all of which are based on finding stabilities in the complex $E(\lambda)$ trajectory. A common technique is to locate the minimum of $|dE(\lambda)/d\lambda|$ [72]. Either, by finite differences,

$$\frac{dE(\lambda_i)}{d\lambda} \approx \frac{E(\lambda_{i+1}) - E(\lambda_i)}{\lambda_{i+1} - \lambda_i} \tag{9.2}$$

or by using the Hellman-Feynman theorem [130],

$$\frac{dE(\lambda)}{d\lambda} = -i \langle \Psi(\lambda) | U | \Psi(\lambda) \rangle . \tag{9.3}$$

In this work we have used two forms for the CAPs. One has a simple polynomial form of order n scaled to the range $[R_{\text{min}}, R_{\text{max}}]$

$$U_n(R) = \left(\frac{R - R_{\text{min}}}{R_{\text{max}} - R_{\text{min}}} \right)^n . \tag{9.4}$$

The other has a more complicated form, as suggested by Gonzalez-Lezana *et al* [4] building on work by Manolopoulos [3],

$$U_m(R) = \frac{\hbar^2}{2\mu}\left(\frac{2\pi}{R_{\max} - R_{\min}}\right)^2 y(x), \tag{9.5}$$

with μ being the reduced mass and $y(x)$ is an elliptic function but is approximated closely by,

$$y(x) = \frac{4}{(c-x)^2} + \frac{4}{(c+x)^2} - \frac{8}{c^2} \tag{9.6}$$

where x is a scaled coordinate, scaling the CAP to the appropriate range $[R_{\min}, R_{\max}]$,

$$x = c\frac{R - R_{\min}}{R_{\max} - R_{\min}}, \tag{9.7}$$

c is given by a definite elliptic integral,

$$c = \sqrt{2}K(1/\sqrt{2}) \approx 2.62206. \tag{9.8}$$

Specifically, K is a complete elliptic integral of the first kind [92].

Figure 9.1 compares three choices for the CAP, quadratic and cubic CAPs based on equation 9.4 and the CAP of Manolopoulos *et al* [3; 4]. As we can see, these CAPs are very different in character and if the results are sensitive to the detailed shape of a CAP then we would expect to see this.

In the basis of the bound state calculations, the perturbed Hamiltonian (H') can be written as

$$\langle \Psi_l | H' | \Psi_m \rangle = \langle \Psi_l | H | \Psi_m \rangle - i\lambda \langle \Psi_l | U | \Psi_m \rangle, \tag{9.9}$$

of course $\langle \Psi_l | H | \Psi_m \rangle$ is just the diagonal eigenvalue matrix of the bound state problem ($\epsilon_{lm}\delta_{lm}$) and the basis is defined on a grid of points in a DVR. Writing the matrix elements of the perturbed Hamiltonian in these terms we get,

$$H'_{lm} = \epsilon_{lm}\delta_{lm} - i\lambda \sum_{\alpha\beta\gamma} \Psi_{l\alpha\beta\gamma}\Psi_{m\alpha\beta\gamma}U(\alpha,\beta,\gamma) \tag{9.10}$$

where α, β and γ index the DVR points.

9.1 Calculations on HOCl

As mentioned in section 2.6.3.2, there have been a number of previous results for resonances of HOCl [73; 74; 75; 82; 83]. HOCl is also a somewhat easier problem

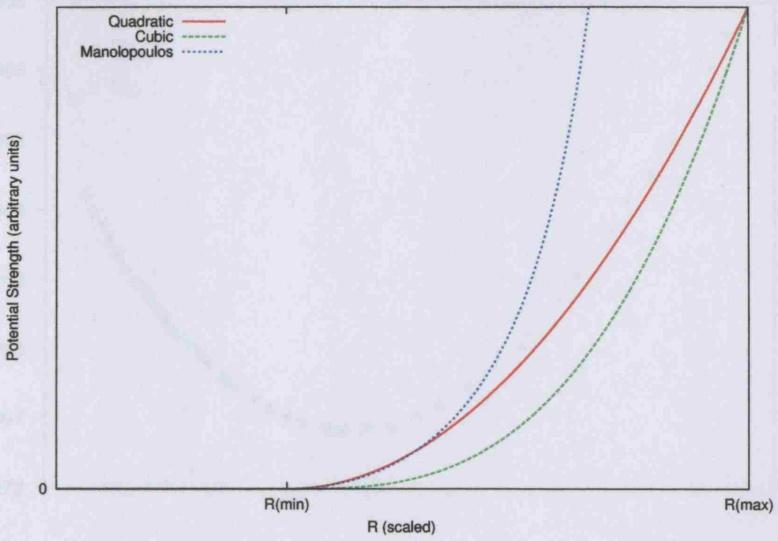

Figure 9.1: A comparison of the shapes of quadratic, cubic and the Manolopoulos *et al* [3; 4] complex absorbing potentials.

than H_3^+, requiring a vibrational Hamiltonian size of just 14,400 to converge many resonance states to better than 0.01 cm^{-1}. These previous works, in combination with the relative ease of the problem – as compared to H_3^+ — make HOCl a useful benchmark and test system for this method.

Mussa *et al*'s work [83] included a study of the best range for the CAP, $[R_{\min}, R_{\max}]$, and the convergence of their basis set, but not the best shape of the CAP. Here we have repeated a number of Mussa *et al*'s calculations with a cubic CAP, but have extended them by using the CAP of equation 9.5 to study the importance of CAP shape to the result.

The Jacobi vibrational basis of Mussa *et al* consisted of Morse oscillator-like functions on R and r, and Legendre polynomials on θ. The same sequential diagonalisation and truncation approach described earlier was used to solve the Hamiltonian. A truncated basis set of size 14,400 was constructed from one dimensional basis sets of size $N_R = 96$, $N_r = 45$ and $N_\theta = 60$. The variational parameters that define these are detailed in Mussa *et al*'s work [83].

As with Mussa *et al*, we did not include the first 480 bound states in the resonance Hamiltonian (H') because these states do not couple to a CAP with long enough range,

$$\langle \Psi_{n\leq 480} | U | \Psi_{m\leq 480} \rangle \cong 0 \tag{9.11}$$

and therefore do not effect the result. The next 1920 eigen-vectors were then used

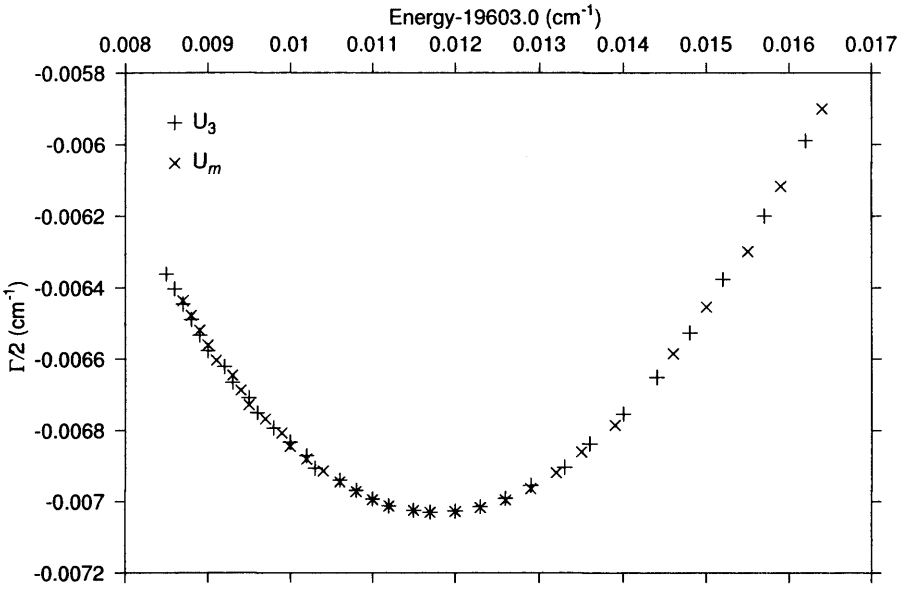

Figure 9.2: Comparison of complex trajectories for a $J = 0$ resonance of HOCl with $E = 19,603.01$ cm^{-1} and $\Gamma = 0.013$ cm^{-1}. Using the U_3 CAP (+) and the more accurate U_m CAP (×) with λ taking 32 values from 0.016 E_h to 0.078 E_h.

as a basis for the solution of $H'(\lambda)$.

The eigenvalues form the complex $E(\lambda)$ trajectories and were plotted for a series of λs. Figures 9.2, 9.3 and 9.4 are three such trajectories and show how closely the two CAPs agree on resonance positions for HOCl. The trajectories almost perfectly sit on top of each other, demonstrating that any errors due to the nature of the CAP are in fact very small. Mussa *et al* [83] concluded that the largest error was due to basis set incompleteness and that this is the reason for difference between their results and those of Skokov *et al* [73].

9.2 Calculations on H_3^+

The only previous fully quantum mechanical result for resonances of H_3^+ is that of Mandelshtam and Taylor [42]. In which they used a quadratic CAP (U_2) in the range $R_{\text{min}} = 12a_0$ to $R_{\text{max}} = 17a_0$ to calculate $J = 0$ states or Feshbach states, of H_3^+ using the potential of Meyer *et al* [38].

Our preliminary calculations on the $J = 0$ resonances of H_3^+ [5] have revealed that the insensitivity to details or parameters of the CAP in HOCl is also true for H_3^+. Thus, the remaining basis set error is the dominant error. Figure 9.5 compares the complex-trajectories for a resonance of H_3^+ calculated using two different CAPs.

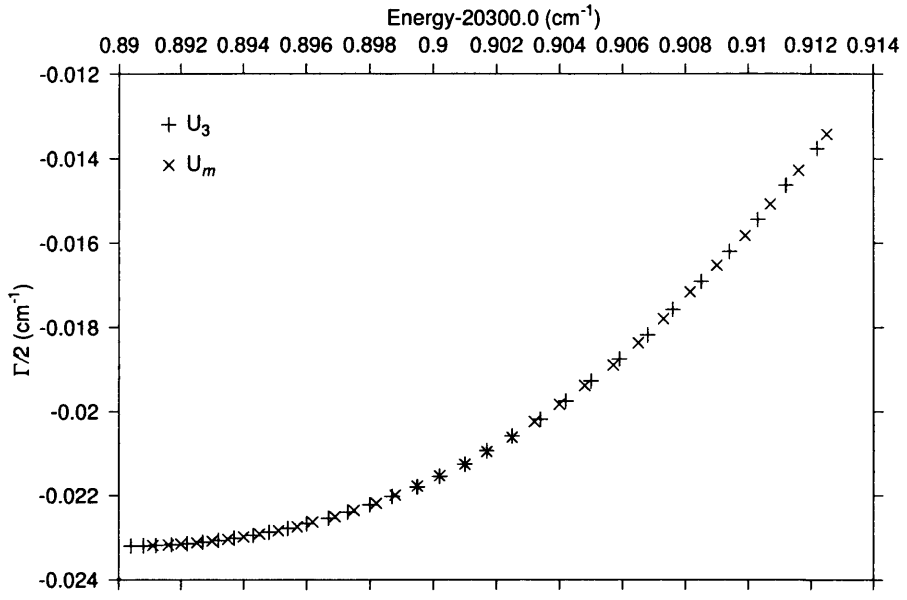

Figure 9.3: Comparison of complex trajectories for a $J = 0$ resonance of HOCl with $E = 20,300.90$ cm^{-1} and $\Gamma = 0.046$ cm^{-1}. Using the U_3 CAP (+) and the more accurate U_m CAP (×) with λ taking 32 values from 0.016 E_h to 0.078 E_h.

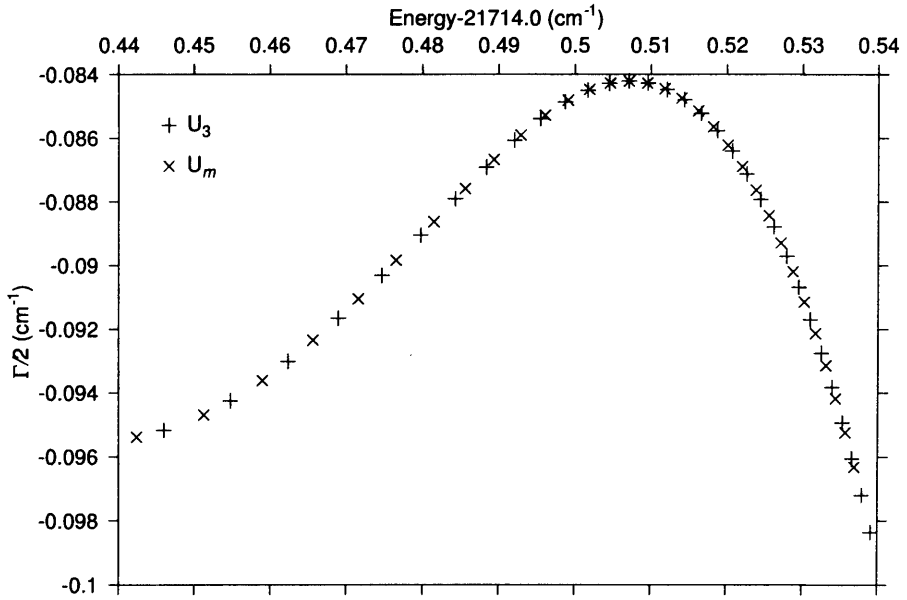

Figure 9.4: Comparison of complex trajectories for a $J = 0$ resonance of HOCl with $E = 21,71453$ cm^{-1} and $\Gamma = 0.0080$ cm^{-1}. Using the U_3 CAP (+) and the more accurate U_m CAP (×) with λ taking 32 values from 0.016 E_h to 0.078 E_h.

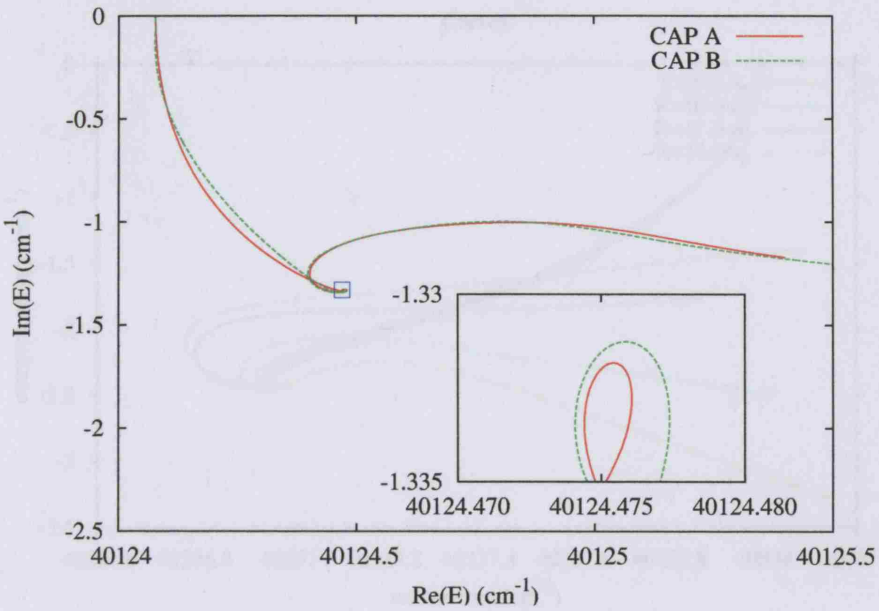

Figure 9.5: Comparison of the effect of the quadratic (CAP A, equation 9.4) and the Manolopoulos (CAP B, equation 9.5) complex absorbing potentials on a resonance state of H_3^+ [5].

Figure 9.6 compares the complex-trajectories for a quadratic CAP (U_2) with changing R_{min}. Both of these figures show that although the trajectories may deviate from each other, the turning points are still very close together and therefore the resonance position is only changing very slightly.

Using this method a number of preliminary results for H_3^+ were calculated to check for correctness. Table 9.1 lists five states calculated using this method, extending the same vibrational basis used for the bound state calculations. These five states are shown because of there strong invariance to a change in the CAP. The energy and lifetimes of these states are in close agreement for both CAPs (U_2 and U_m) and for a range of values of R_{min} from 9 a_0 to 12 a_0.

These calculations have shown that the $J = 0$ H_3^+ resonances are rather broad with widths often greater than 1 cm^{-1} and therefore they have very short lifetimes — as displayed in table 9.1. These results agree with previous semi-classical [131] and quantum results [42], although, the calculations of Mandelshtam and Taylor [42] are based upon a potential that does not dissociate correctly.

States this short-lived clearly do not contribute much to the near-dissociation spectrum. This is because the spectrum was formed from transitions between initial states with lifetimes greater than $3 \times 10^{-6} s$ and final states as short-lived as those calculated here are too broad to be discernible against the background noise of the

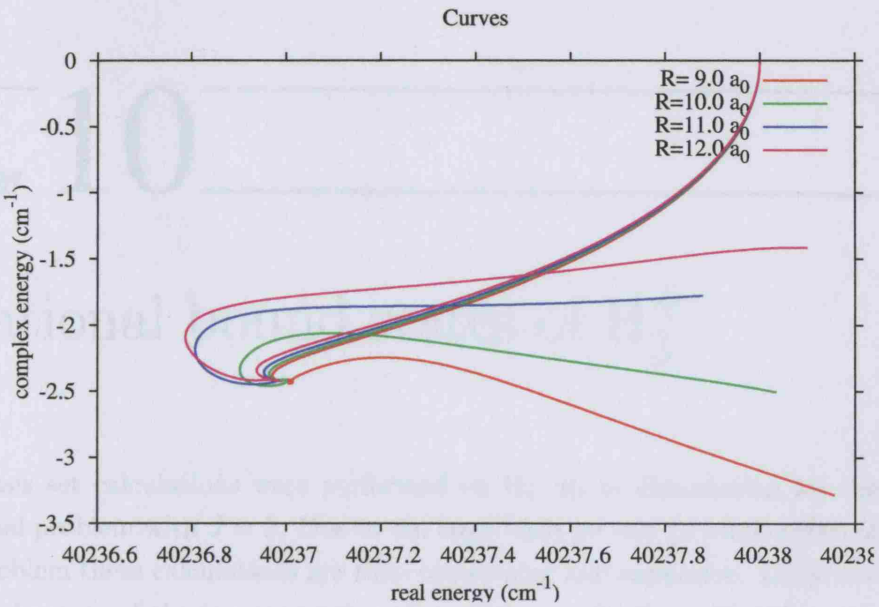

Figure 9.6: Comparison of the effect of the quadratic (U_2,equation 9.4) complex absobing potential on a resonance state of H_3^+ [6].

Table 9.1: Five $J = 0$ H_3^+ resonances calculated with the same $N_R = 120$ basis set of the bound state calculations.

Energy (cm^{-1})	Lifetime (s)
39,436.1	3.6×10^{-11}
39,511.2	1.9×10^{-10}
39,975.0	9.5×10^{-13}
40,237.0	2.6×10^{-13}
40,595.4	3.0×10^{-13}

experiment. This reinforces the idea that the spectrum is a product of rotating resonances behind a centrifugal barrier.

Chapter 10

Rotational bound states of H_3^+

Large basis set calculations were performed on H_3^+ up to dissociation for the rovibrational problem with $J = 3$. Due to the large basis set size (N=6,912,000) of the $J = 3$ problem these calculations are time comsuming and expensive. Large savings are made because of the two truncation steps with cut-offs $E_{2d} = 70,577$ cm^{-1} and $N_{\text{vib}} = 4000$, which makes the vibrational step possible and reduces the rotational basis set size to N=40,000.

Complete calculations of all the $J = 3$ bound states were performed with $N_{\text{vib}} = 3000$, requiring approximately 45,000 processor hours to complete. One symmetry block (K=even,q=s) was computed with a larger vibrational basis cut-off of $N_{\text{vib}} = 4000$, requiring approximately 20,000 processor hours of computer time to complete. These calculations were performed on 1024 proccessors of the HPCx supercomputer, at the Daresbury laboratory, UK.

10.1 Results

Table 10.1 shows the number of rotational states of $J = 3$ below the dissociation energy D_0. A slightly more accurate calculation with $N_{\text{vib}} = 4000$, K =even and $q = s$ yielded 1678 bound states, one more than with $N_{\text{vib}} = 3000$. Therefore, there will be a different, more accurate number of states if larger basis sets are used. As the convergence with respect to N_{vib} is variational, we know that there will be more than 7777 states for $J = 3$.

A first order approximation to the number of states that exist with angular momentum J is given by

$$N_J = (2J + 1) \times N_{J=0}. \tag{10.1}$$

Table 10.1: The number of bound states calculated for each of the four ro-vibrational symmetry blocks of $J = 3$, including the total and a first order approximation for the total number of states expected.

K	q,s	Number
even	$q = s$	1677
even	$q \neq s$	1600
odd	$q = s$	2249
odd	$q \neq s$	2251
	total =	7777

It is important here that we count the $J = 0$ states in the same way that we count the $J = 3$ states. As we are not attempting to assign the rotational states with their correct symmetries, we will not be able to single count any degenerate states as we did earlier with the vibrational E states. Therefore, here $N_{J=0}$ refers to the number of vibrational states without any consideration of degeneracies, just the sum of even and odd parity states $N_{J=0} = N_{\text{even}} + N_{\text{odd}}$.

With this count there are $N_{J=0} = 1286$ vibrational states, giving 9002 states for $N_{J=3}$. This is very different from 7777 but is not an accurate number because a number of high energy vibrational bands will have rotational states that go above the dissociation energy even if it has a band origin below.

A slightly better estimate for the number of bound states with $J = 3$ can be obtained by using the rigid rotor approximation for the rotational energy,

$$E(J, K) = BJ(J + 1) + (C - B)K^2 \tag{10.2}$$

By using the rotational constants calculated from the vibrational states we can compute the rigid rotor energy of each state and obtain an estimate for how many are below D_0 for $J = 3$. Using this method we obtain $N_{J=3} = 4767$. However, this number is an under-estimate because the rotational constant in the plane of the molecule (B) ceases to become meaningful when H_3^+ reaches energies that allow linearity. As explained in section 7.3 with a DVR basis that does not include $R = 0$ in the abscissa we still get a well defined number of the rotational constant computed as an expectation value. However, B becomes very large for these higher energy states and leads to many of the estimates for the rotational energies being too large. Therefore the estimate for $N_{J=3}$ of 4767 is clearly an underestimate.

By using the low energy rigid rotor approximation of $B = 2C$ instead of the inappropriate values computed earlier we get another approximation, $N_{J=3} = 8798$.

This is closer still to the computed number of 7777 states. Further improvements to this estimate would require other methods, such as the phase space integration of Berblinger *et al* [132; 133].

10.2 Basis set convergence

All the parameters that effect the convergence of the vibrational calculations are also a part of the full ro-vibrational basis and effect its convergence. The ro-vibrational basis also includes the extra parameter N_{vib}, the number of vibrational vectors for each k-block that are used to build the full $3D$ ro-vibrational basis. The rotational Hamiltonian is then constructed in this basis, the size of the Hamiltonian depending upon the symmetry block being used,

$$N_{\text{ham}} = \begin{cases} (J+1)N_{\text{vib}} & : \quad J+K = \text{even} \\ JN_{\text{vib}} & : \quad J+K = \text{odd} \end{cases} . \tag{10.3}$$

Therefore all the parameters N_R, N_θ, E_{2D} and N_{nvib} should be tested for convergence at this stage. It is generally not sufficient to consider the vibrational basis as well adapted to the rotational problem, only approximately so. Ideally one would converge a separate basis for each angular momentum quantum number J. In this work we only consider the convergence of the $J = 3$ states with respect to N_R,N_θ and N_{nvib}. We do not consider the first truncation energy E_{2D} as it does not strongly change the convergence with changing J.

Table 10.2 shows how the energies change with respect to the number of radial points used in the basis. At low energy the states are extremely well converged, the Born-Oppenheimer approximation producing an error much larger than the convergence error in these cases. For higher energies the differences are sub-wavenumber and support the conclusion that the states are converged to within a wavenumber. Near dissociation the differences approach a wavenumber, the ultimate difference between the energy in this basis and in the complete basis set limit may therefore be larger than a wavenumber but are consistent and still show good convergence.

Table 10.3 is similiar but show the differences in energy for states computed using different angular basis sizes (N_θ). The results here are perhaps an order of magnitude better than in the case of convergence with respect to N_R, even though the basis fraction is identical,

$$\frac{88}{96} = \frac{110}{120}. \tag{10.4}$$

Of course, one should consider the square of the radial basis as it is two-dimensional,

Table 10.2: The energies of $J = 3$ ro-vibrational states relative to the bottom of the electronic potential with $p = q$ and K =even. Every hundredth energy and the last five energies are given for 110 and 120 grid points on R. More significant figures are given for the first state to demonstrate the excellent convergence at low energy.

N	$E(N_R = 110)$	$E(N_R = 120)$	ΔE
1	4789.601430789	4789.601430781	-0.000000008
101	18840.763	18840.828	0.065
201	22598.719	22598.725	0.006
301	25340.031	25340.110	0.079
401	27363.238	27363.282	0.044
501	28992.285	28992.384	0.099
601	30390.915	30391.174	0.259
701	31664.911	31665.182	0.271
801	32709.761	32710.051	0.290
901	33679.818	33680.035	0.217
1001	34602.565	34602.875	0.310
1101	35421.199	35421.483	0.284
1201	36204.767	36205.140	0.373
1301	36924.197	36924.694	0.497
1401	37615.322	37615.693	0.371
1501	38247.667	38248.024	0.357
1601	38839.504	38840.166	0.662
1673	39255.476	39256.047	0.571
1674	39260.141	39260.945	0.804
1675	39262.905	39263.624	0.719
1676	39268.046	39268.959	0.913
1677	39268.510	39269.312	0.802

Table 10.3: The energies of $J = 3$ ro-vibrational states relative to the bottom of the electronic potential with $p = q$ and K =even. Every hundredth energy and the last five energies are given for 88 and 96 grid points on θ. More significant figures are given for the first state to demonstrate the excellent convergence at low energy.

N	$E(N_\theta = 88)$	$E(N_\theta = 96)$	ΔE
1	4789.6014305	4789.6014307	0.0000002
101	18840.822	18840.828	0.006
201	22598.725	22598.725	0.000
301	25340.108	25340.110	0.002
401	27363.281	27363.282	0.001
501	28992.378	28992.384	0.006
601	30391.156	30391.174	0.018
701	31665.177	31665.182	0.005
801	32710.041	32710.051	0.010
901	33680.026	33680.035	0.009
1001	34602.866	34602.875	0.009
1101	35421.435	35421.483	0.048
1201	36205.112	36205.140	0.028
1301	36924.633	36924.694	0.061
1401	37615.678	37615.693	0.015
1501	38248.005	38248.024	0.019
1601	38840.151	38840.166	0.015
1673	39256.016	39256.047	0.031
1674	39260.914	39260.945	0.031
1675	39263.587	39263.624	0.037
1676	39268.858	39268.959	0.101
1677	39269.281	39269.312	0.031

but this produces less than 10% difference in ratio. It is not generally important that an angular basis should out perform a radial basis in a particular situation and converge quicker. In this case however, we can see a change from the vibrational case to the $J = 3$ case.

In the vibrational case the radial and angular DVR's performed almost as well, the sizes of $N_\theta = 96$ and $N_R = 120$ were chosen for this reason, to balance the convergence error from the different parameters of the basis. In going from $J = 0 \rightarrow 3$ that rate of convergence with respect to N_θ has dramatically increased while the rate with respect to N_R has only changed slightly and has perhaps become slower.

The final convergence parameter tested was N_{vib}. The convergence with respect to N_{vib} is easy to test in detail because the the diagonalisation step is cheap compared to the cost of building the ro-vibrational Hamiltonian. Therefore the largest Hamil-

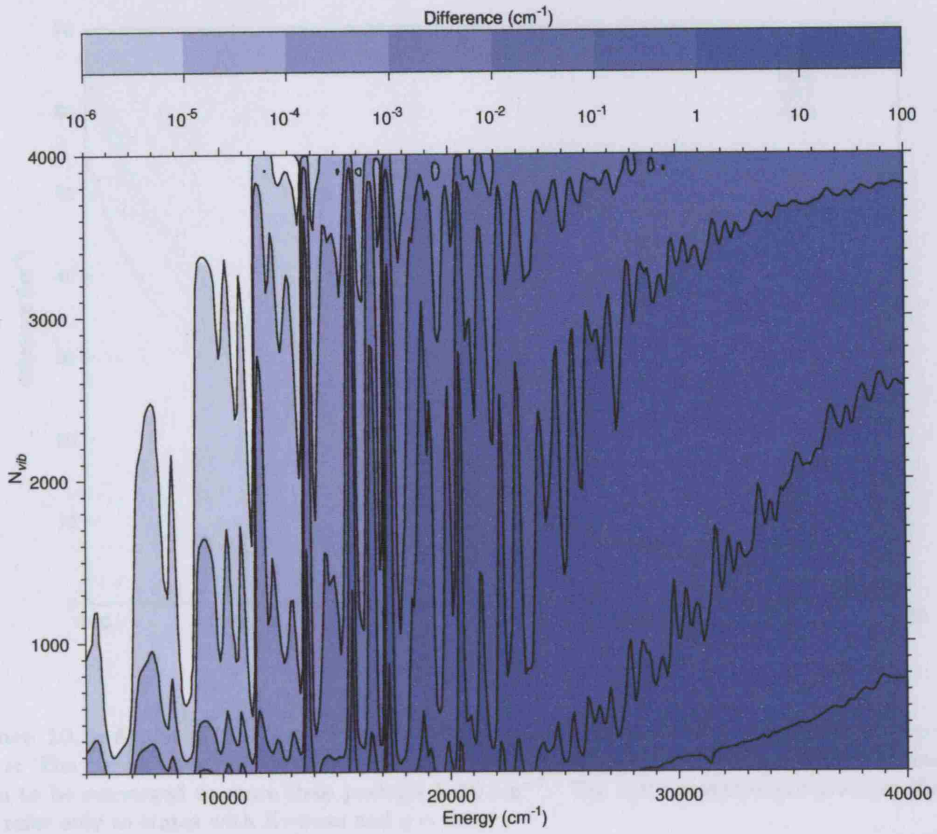

Figure 10.1: A contour plot showing the way in which states at each energy converge with respect to the number of vibrational vectors included in each k-block (N_{vib}). The states included are for the symmetry block with K=even and $q = s$. Contours are plotted logarithmically for differences in energy between $E(N_{\text{vib}})$ and $E(4000)$ from 10^{-6}cm^{-1} to 100cm^{-1}.

tonian is built and a number of truncations of that Hamiltonian are used with N_{vib} less than the maximum. Results were calculated from $N_{\text{vib}} = 200$ to $N_{\text{vib}} = 4000$ for K=even and $q = s$ providing a very smooth measure of convergence.

Figure 10.1 is a plot of logarithmic contours showing the difference between the states energy and the energy at $N_{vib} = 4000$. The contours map out an unsurprising convergence pattern. The low energy states converge quickly and well, while the high energy states are much slower to converge even though the differences all drop below a wavenumber before $N_{\text{vib}} = 4000$. Also the speed in which a state converges depends on that particular state, resulting in the jagged appearence of the contours.

Using the $N_{\text{vib}} = 4000$ result as the end result in figure 10.1 gives an optimistic picture of the convergence. A more accurate picture for how well converged high energy states are can be obtained by looking at a few of the near-dissociation states

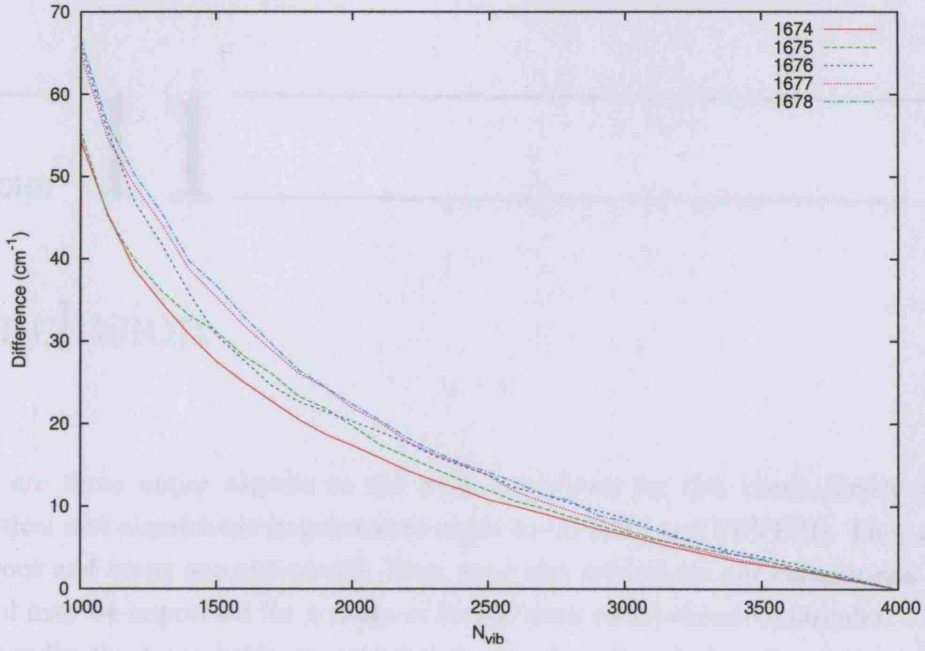

Figure 10.2: A plot of $E(N_{\text{nvib}}) - E(4000)$ for the last five states with symmetry K=even and $q = s$. The curves have not yet become asymptotic and therefore it is not reasonable to consider them to be converged to more than perhaps 5–10 cm^{-1}. The state numbers are given in the key and refer only to states with K=even and $q = s$.

in detail. Figure 10.2 shows the differences between the energy with N_{vib} and $N_{\text{vib}} = 4000$ for the last 5 states with K=even and $q = s$. The initial convergence is almost exponential in nature but as $N_{\text{vib}} = 4000$ is approached becomes more linear in form. Unfortunately this means we cannot assume that the states are better converged than about 5 cm^{-1} or 10 cm^{-1}.

10.3 Conclusions

The results quoted in this chapter are the most accurate high energy ro-vibrational calculations that have been performed on H_3^+ to date. However, they are probably also the most expensive calculations to be performed on H_3^+. The largest calculation performed required over 20,000 CPU hours to compute the results of just the cheapest of four symmetry blocks with $J = 3$. A calculation large enough to calculate all the bound states for a large range of J is therefore beyond the capability of computers for a few years to come. If the z-perpendicular vibrational – rotational splitting is truly optimal for H_3^+, as suggested by Watson [86], then it would appear we need to look elsewhere for ways to improve the algorithm.

Chapter 11

Conclusion

There are three major aspects to the work completed for this thesis, firstly the theoretical and algorithmic improvments made to DVR3D and PDVR3D. They are numerous and many are non-trivial. They were also critical for our calculations on H_3^+ and may be important for a range of future work on tri-atomic molecules.

Secondly the large basis set calculations for $J = 0$ and $J = 3$ are the most accurate yet, but are also the most difficult. The improvement in accuracy mainly stems from the use of a potential energy surface that is correct at dissociation. The extra cost emerges because the basis must cover very extended states.

Thirdly, the results and analysis for vibrational states has revealed a theoretically interesting mode of behaviour and set of states. This long range behaviour is asymptotic to the behaviour at dissociation, hence their name, asymptotic vibrational states (AVS). It also appears that these AVS or van der Waals like states will likely exist for most if not all poly-atomic molecules, as long as one of the dissociating species has a significant zero-point energy.

The vibrational calculation of all the bound states of H_3^+ presented in this work is probably the most computationally demanding nuclear-motion calculation ever to be performed on a tri-atomic. Another calculation of all the vibrational bound states using a global potential was attempted [45], but with questionable convergence.

The rotational $J = 3$ results up to dissociation were very difficult to achieve, only just possible on the 1280 node HPCx supercomputer, and it was not possible to achieve a convergence of better than 10 cm^{-1}. However, these are the most accurate to date and further analysis of these results are expected to reveal that rotational forms of AVS do exist. These Asymptotic Rotational States (ARS) could prove very interesting, especially if resonance states analagous to them are discovered, trapped by an effective centrifugal barriers in the potential.

It appears that these AVS or ARS could easily contribute to the near dissociation spectrum, although, it is also clear that the possible range and strength of the transitions between horseshoe states means they will likely form the dominant part of the spectrum. Especially when you consider that the AVS may only exist for J less than about 30, because the effective potential formed from the centrifugal term will limit the range of H_3^+ for high J's.

Either way, the next generation of machines may make this type of direct approach at the calculation finally possible, but at a tremendous cost. Perhaps a better path to take is either to develop better non-direct diagonalisation techniques or to approach the problem in a way which could explain features of the spectrum quantitatively but at the cost of predicting actual states and transitions.

Bibliography

[1] B. T. Sutcliffe and J. Tennyson. A general treatment of vibration-rotation coordinates for triatomic molecules. *Intern. J. Quantum Chem.*, 39:183–196, 1991.

[2] O. L. Polyansky, R. Prosmiti, W. Klopper, and J. Tennyson. An accurate, global, *ab initio* potential energy surface for the H_3^+ molecule. *Mol. Phys.*, 98:261–273, 2000.

[3] D. E. Manolopoulos. Derivation and reflection properties of a transmission-free absorbing potential. *J. Chem. Phys.*, 117(21):9552–9559, 2002.

[4] T. Gonzalez-Lezana, E. J. Rackham, and D. E. Manolopoulos. Quantum reactive scattering with a transmission-free absorbing potential. *J. Chem. Phys.*, 120(5):2247–2254, 2004.

[5] J. Tennyson, P. Barletta, J. J. Munro, and B. C. Silva. The role of asymptotic vibrational states in H_3^+. *Mol. Phys. (submitted)*, 2006.

[6] B. C. Silva, P. Barletta, J. J. Munro, and J. Tennyson. Theoretical spectroscopy of H_3^+ near dissociation. In *Nineteenth Colloquium on High Resolution Molecular Spectroscopy*, number P18 in Salamanca 2005, Universidad de Salamanca, September 2005. Sociedad Española de Óptica.

[7] P. R. Bunker and P. Jensen. *Fundamentals of Molecular Symmetry.* First edition, 2005.

[8] P. R. Bunker and P. Jensen. *Molecular Symmetry and Spectroscopy.* NRC Research Press, second edition, 1998.

[9] J. J. Thomson. *Philos. Mag.*, 21:225, 1911.

[10] J. J. Thomson. *Philos. Mag.*, 24:209, 1912.

[11] J. Tennyson. Spectroscopy of H_3^+: planets, chaos and the universe. *Rep. Prog. Phys.*, 57:421–476, 1995.

[12] J. O. Hirschfelder. The energy of the triatomic hydrogen molecule and ion, v. *J. Chem. Phys.*, 6(12):795–806, 1938.

[13] M. J. Gaillard, D. S. Gemmell, G. Goldring, I. Levine, W. J. Pietsch, J. C. Poizat, A. J. Ratkowski, J. Remillieux, Z. Vager, and B. J. Zabransky. Experimental determination of the structure of H_3^+. *Phys. Rev. A*, 17:1797, 1978.

[14] T. Oka. Observation of the infrared spectrum of H_+^3. *Phys. Rev. Lett.*, 45:531–534, 1980.

[15] A. Carrington, J. Buttenshaw, and R. A Kenedy. Observation of the infrared spectrum of H_3^+ ion at its near dissciation limit. *Mol. Phys.*, 45:753, 1982.

[16] G. J. Harris, A. E. Lynas-Gray, S. Miller, and J. Tennyson. The effect of the electron donor H_3^+ on the pre–main-sequence and main-sequence evolution of low-mass, zero-metallicity stars. *Astrophys. J.*, 600:1025–1034, January 2004.

[17] E. F. Van Dishoeck. Interstellar chemistry and submillimetre observations. *Proceedings of an ESA Workshop on a 'Space-Borne Sub-Millimetre Astronomy Mission'*, pages 107–117, August 1986.

[18] D. C. Hamilton, G. Gloeckler, S. M. Krimigis, C. O. Bostrom, T. P. Armstrong, W. I. Axford, C. Y. Fan, L. J. Lanzerotti, and D. M. Hunten. Detection of energetic hydrogen molecules in Jupiter's magnetosphere by Voyager 2: evidence for an ionospheric plasma source. *Geophys. Res. Lett.*, 7(10):813–816, 1980.

[19] P. Drossart, J.-P. Maillard, J. Caldwell, S. J. Kim, J. K. G. Watson, W. A. Majewski, J. Tennyson, S. Miller, S. K. Atreya, J. T. Clarke, J. H. Waite Jr., and R. Wagener. Detection of H_3^+ on Jupiter. *Nature*, 340:539–541, August 1989.

[20] L. M. Trafton, D.F. Lester, and K.L. Thompson. Unidentified emission lines in Jupiter's northern and southern 2mm aurorae. *Astrophys. J.*, 343:L73–L76, 1989.

[21] L. M. Trafton, T.R. Geballe, S. Miller, J. Tennyson, and G.E. Ballester. Detection of H_3^+ from Uranus. *Astrophys. J.*, 405:761–766, 1993.

[22] T. R. Geballe, M. F. Jagod, and T. Oka. Detection of H_3^+ infrared-emission lines in Saturn. *Astrophys. J.*, 408(2):L109–L112, May 1993.

[23] F.-S. Pan and T. Oka. Calculated forbidden rotational spectra of H_3^+. *Astrophys. J.*, 305:518–525, June 1986.

[24] S. Miller and J. Tennyson. Calculated rotational and ro-vibrational transitions in the spectrum of H_3^+. *Astrophys. J.*, 335:486–490, 1988.

[25] A. Carrington and R. A. Kennedy. Infrared predissociation limit of the H_3^+ ion. *J. Chem. Phys.*, 81:91, 1984.

[26] I. R. McNab. The spectroscopy of H_3^+. *Adv. Chem. Phys.*, 89:1–87, 1995.

[27] M. Berblinger, J. M. Gomez Llorente, E. Pollak, and C. Schlier. Photodissociation dynamics of the D_2H^+ molecular ion. *Chem. Phys. Lett.*, 146:353–357, 1988.

[28] A. V. Chambers and M. S. Child. Barrier effects on the vibrational predissociation of D_2H^+. *Mol. Phys.*, 65:1337–1344, 1987.

[29] A. Carrington, I. R. McNab, and Y. D. West. Infrared predissociation spectrum of the H_3^+ ion. II. *J. Chem. Phys.*, 98(2):1073, 1993.

[30] M. S. Child. The estimation of vibrational predissociation lifetimes. *J. Chem. Soc. Faraday Trans. 2, Molec. Chem. Phys.*, 82:1143–1149, 1986.

[31] R. Pfeiffer and M. S. Child. Towards an understanding of the predissociation excitation spectrum of H_3^+. *Mol. Phys.*, 60:1367–1378, 1987.

[32] E. Pollak and C. Schlier. Theory of unimolecular dissociation of small metastable molecules and ions as exemplified by H_3^+. *Acc. Chem. Res.*, 22(6):223–229, 1989.

[33] M. Berblinger, E. Pollak, and Ch. Schlier. Bound states embedded in the continuum of H_3^+. *J. Chem. Phys.*, 88(9):5643–5656, 1988.

[34] J.M. Gomez Llorente and E. Pollak. A classical trajectory study of the photodissociation spectrum of H_3^+. *J. Chem. Phys.*, 90:5406, 1989.

[35] C. R. Le Sueur, J. R. Henderson, and J. Tennyson. Gateway states and bath states in the vibrational spectrum of H_3^+. *Chem. Phys. Lett.*, 206:429–436, 1993.

[36] S. Miller and J. Tennyson. Calculation of the high angular momentum dissociation limit for H_3^+ and H_2D^+. *Chem. Phys. Lett.*, 145:117–120, 1988.

[37] S. Carter and W. Meyer. A variational method for the calculation of vibrational energy levels of triatomic molecules using a Hamiltonian in hyperspherical coordinates. *J. Chem. Phys.*, 93(12):8902–8914, 1990.

[38] W. Meyer, P. Botscwina, and P. Burton. *Ab initio* calculation of near-equilibrium potential and multipole moment surfaces and vibrational frequencies of H_3^+ and its isotopomers. *J. Chem. Phys.*, 84(2):891–900, 1986.

[39] J. R. Henderson and J. Tennyson. All the vibrational bound states of H_3^+. *Chem. Phys. Lett.*, 173:133–138, 1990.

[40] J. R. Henderson, J. Tennyson, and B. T. Sutcliffe. All the bound vibrational states of H_3^+: a reappraisal. *J. Chem. Phys.*, 98:7191–7203, 1993.

[41] M. J. Bramley, J. W. Tromp, T. Carrington Jr., and G C Corey. Efficient calculation of highly excited vibrational-energy levels of floppy molecules - the band origins of H_3^+ up to 35,000 cm^{-1}. *J. Chem. Phys.*, 100(9):6175–6194, 1994.

[42] V. A. Mandelshtam and H. S. Taylor. The quantum resonance spectrum of the H_3^+ molecular ion for J=0. An accurate calculation using filter diagonalization. *J. Chem. Soc. Faraday Trans.*, 93(5):847–860, 1997.

[43] D. J. Kouri, W. Zhu, G. A. Parker, and D. K. Hoffman. Acceleration of convergence in the polynomial-expanded spectral density approach to bound and resonance state calculations. *Chem. Phys. Lett.*, 238(4-6):395–403, June 1995.

[44] R. Chen and H. Guo. A general and efficient filter-diagonalization method without time propagation. *J. Chem. Phys.*, 105(4):1311–1317, 1996.

[45] M. A. Kostin, O. L. Polyansky, J. Tennyson, and H. Y. Mussa. Rotation-vibration states of H_3^+ at dissociation. *J. Chem. Phys.*, 118:3538–3542, 2003.

[46] O. L. Polyansky, R. Prosmiti, W. Klopper, and J. Tennyson. An accurate, global, *ab initio* potential energy surface for the H_3^+ molecule. *Mol. Phys.*, 98:261–273, 2000.

[47] J. R. Henderson and J. Tennyson. Calculated spectrum for near-dissociation H_3^+: a first attempt. *Mol. Phys.*, 89:953–963, 1996.

[48] R. J. LeRoy and R. B. Bernstein. Dissociation energy and long–range potential of diatomic molecules from vibrational spacings of higher levels. *J. Chem. Phys.*, 52(8):3869–3879, 1970.

[49] F. Luo, C. F. Giese, and W. R. Gentry. Direct measurement of the size of the helium dimer. *J. Chem. Phys.*, 104(3):1151–1154, 1996.

[50] O. L. Polyansky and J. Tennyson. *Ab initio* calculation of the rotation-vibration energy levels of H_3^+ and its isotopomers to spectroscopic accuracy. *J. Chem. Phys.*, 110:5056–5064, 1999.

[51] C. F. Giese and W. R. Gentry. Classical trajectory treatment of inelastic scattering in collisions of H^+ with H_2, HD, and D_2. *Phys. Rev. A*, 10:2156–2173, 1974.

[52] R. Schinke, M. Dupuis, and Jr. W. A. Lester. Proton–H_2 scattering on an *ab initio* CI potential energy surface. I. vibrational excitation at 10 eV. *J. Chem. Phys.*, 72(7):3909–3915, 1980.

[53] M. J. Bramley, J. R. Henderson, J. Tennyson, and B. T. Sutcliffe. On the MBB potential energy surface of H_3^+. *J. Chem. Phys.*, 98:10104–10105, 1993.

[54] R. Prosmiti, O. L. Polyansky, and J. Tennyson. A global potential energy surface for the H_3^+ molecule. *Chem. Phys. Lett.*, 273:107–114, 1997.

[55] A. Aguado, O. Roncero, C. Tablero, C. Sanz, and M. Paniagua. Global potential energy surfaces for the H_3^+ system. analytical representation of the adiabatic ground-state 1 $_1A'$ potential. *J. Chem. Phys.*, 112(3):1240–1254, 2000.

[56] J.J. Munro, J. Ramanlal, J. Tennyson, and H.Y. Mussa. Properties of high-lying vibrational states of the H_3^+ molecular ion. *Mol. Phys.*, 104:115, 2005.

[57] E. A. Hylleraas and B. Undheim. Numerische berechnung der 2 s-terme von ortho- und par-. helium. *Z. Phys.*, 65:759–772, 1930.

[58] A. Alijah, J. Hinze, and L. Wolniewicz. Rotation-vibrational states of H_3^+ using hyperspherical coordinates and harmonics. *Ber. Bunsen-Ges. Phys. Chem.*, 99(3):251, 1995.

[59] J. Tennyson, M. A. Kostin, P. Barletta, G. J. Harris, O. L. Polyansky, J. Ramanlal, and N. F. Zobov. DVR3D: a program suite for the calculation of

rotation-vibration spectra of triatomic molecules. *Computer Phys. Comms.*, 163:85–116, 2004.

[60] B. R. Johnson and W. P. Reinhardt. Adiabatic separations of stretching and bending vibrations - application to H_2O. *J. Chem. Phys.*, 85(8):4538–4556, October 1986.

[61] S. Carter, N. C. Handy, and B. T. Sutcliffe. A variational method for the calculation of rovibrational levels of any triatomic molecule. *Mol. Phys.*, 49(3):745–748, 1983.

[62] F. Kemp, C. Euan Kirk, and I.R. McNab. The infrared predissociation spectrum of H_3^+. *Phil. Trans. R. Soc. Lond. A*, 358:2403, 2000.

[63] J. Aguilar and J. M. Combes. Class of analytic perturbations for one-body Schrödinger hamiltonians. *Communications in Mathematical Physics*, 22(4):269–279, 1971.

[64] E. Balslev and J. M. Combes. Spectral properties of many-body Schrödinger operators with dilatation-analytic interactions. *Communications In Mathematical Physics*, 22(4):280–294, 1971.

[65] B. Simon. Resonances in body quantum systems with dilatation analytic potentials and foundations of time-dependent perturbation-theory. *Ann. Mathematics*, 97(2):247–274, 1973.

[66] N. Moiseyev. Quantum theory of resonances: calculating energies, widths and cross-sections by complex scaling. *Physics Reports*, 302:211–293, 1998.

[67] C. W. McCurdy and T. N. Rescigno. Extension of the method of complex basis functions to molecular resonances. *Phys. Rev. Lett.*, 41(20):1364–1368, 1978.

[68] B. Simon. The definition of molecular resonance curves by the method of exterior complex scaling. *Phys. Lett. A*, 71:211–214, April 1979.

[69] J. D. Morgan and B. Simon. The calculation of molecular resonances by complex scaling. *J. Phys. B: At. Mol. Phys.*, 14:L167–L171, March 1981.

[70] N. Lipkin, N. Moiseyev, and E. Brändas. Resonances by the exterior-scaling method within the framework of the finite-basis-set approximation. *Phys. Rev. A*, 40:549–553, July 1989.

[71] N. Rom, N. Lipkin, and N. Moiseyev. Optical potentials by the complex coordinate method. *Chem. Phys.*, 151(2):199–204, 1991.

[72] J. G. Muga, J. P. Palao, B. Navarro, and I. L. Egusquiza. Complex absorbing potentials. *Physics Reports*, 395:357–426, 2004.

[73] S. Skokov, J. M. Bowman, and V. A. Mandelshtam. Calculation of resonance states of non-rotating HOCl using an accurate *ab initio* potential. *Phys. Chem. Chem. Phys.*, 1:1279, 1999.

[74] S. Skokov and J. M. Bowman. Complex L^2 calculation of the variation of resonance widths of HOCl with total angular momentum. *J. Chem. Phys.*, 111(11):4933–4941, 1999.

[75] J. Weiss, J. Hauschildt, R. Schinke, O. Haan, S. Skokov, J. M. Bowman, V. A. Mandelshtam, and K. A. Peterson. The unimolecular dissociation of the OH stretching states of HOCl: Comparison with experimental data. *J. Chem. Phys.*, 115(19):8880–8887, 2001.

[76] G. S. Whittier and J. C. Light. Calculation of resonances of HCO by the artificial boundary inhomogeneity method. *J. Chem. Phys.*, 107(6):1816–1823, 1997.

[77] H.-M. Keller and R. Schinke. Unimolecular dissociation of HCO part III. comparison of calculated and measured CO rotational-state distributions. *J. Chem. Soc. Faraday Trans.*, 93:879–884, 1997.

[78] C.-Y. Yang and S. K. Gray. The effect of angular momentum on the unimolecular dissociation HCO $\rightarrow$ H + CO. *J. Chem. Phys.*, 107(19):7773–7786, 1997.

[79] J. Weiss, R. Schinke, and V. A. Mandelshtam. Renner–Teller induced photodissociation of HCO in the first absorption band: Determination of linewidths for the $\tilde{A}^2A''$ K = 0,1 states by filter-diagonalization. *J. Chem. Phys.*, 113(11):4588–4597, 2000.

[80] U. Brandt-Pollmann, J. Weiss, and R. Schinke. The unimolecular dissociation of HCO. V. mixings between resonance states. *J. Chem. Phys.*, 115(19):8876–8879, 2001.

[81] J. Weiss and R. Schinke. Renner–Teller induced predissociation of HNO($\tilde{A}^1$ A''): Rotational-state dependent linewidths of quasibound states. *J. Chem. Phys.*, 115(7):3173–3183, 2001.

[82] H. Y. Mussa and J. Tennyson. Bound and quasi-bound rotation-vibrational states using massively parallel computers. *Computer Phys. Comms.*, 128:434–445, 2000.

[83] H. Y. Mussa and J. Tennyson. Calculating quasi-bound rotation-vibrational states of HOCl using massively parallel computers. *Chem. Phys. Lett.*, 366:449–457, 2002.

[84] J. Tennyson, J. R. Henderson, and N. G. Fulton. DVR3D: programs for fully pointwise calculation of ro-vibrational spectra of triatomic molecules. *Computer Phys. Comms.*, 86:175–198, 1995.

[85] J. R. Henderson, C. R. Le Sueur, and J. Tennyson. DVR3D: programs for fully pointwise calculation of vibrational spectra. *Computer Phys. Comms.*, 75:379–395, 1993.

[86] J. K. G. Watson. Higher-order vibration-rotation energies of the X_3 molecule. *J. Mol. Spectrosc.*, 103:350–363, 1984.

[87] J. C. Light, I. P. Hamilton, and J. V. Lill. Generalized discrete variable approximation in quantum mechanics. *J. Chem. Phys.*, 82(3):1400–1409, 1985.

[88] J. C. Light and T. Carrington. Discrete-variable representations and their utilization. *Adv. Chem. Phys.*, 114:263–310, 2000.

[89] J. Tennyson and B. T. Sutcliffe. The *ab initio* calculation of the vibration-rotation spectrum of triatomic systems in the close-coupling approach with KCN and H_2Ne as examples. *J. Chem. Phys.*, 77:4061–4072, 1982.

[90] J. Tennyson and B. T. Sutcliffe. Variationally exact ro-vibrational levels of the floppy CH_2^+ molecule. *J. Mol. Spectrosc.*, 101:71–82, 1983.

[91] H. Taseli. Exact solutions for vibrational levels of the Morse potential. *J. Phys. A: Math. Gen.*, 31(2):779–788, 1998.

[92] M. Abramowitz and I. A. Stegun. *Handbook of Mathematical Functions with Formulas, Graphs, and Mathematical Tables.* Dover, New York, ninth Dover printing, tenth GPO printing edition, 1964.

[93] Z. Bacic and J. C. Light. Highly excited vibrational levels of "floppy" triatomic molecules: A discrete variable representation—distributed Gaussian basis approach. *J. Chem. Phys.*, 85(8):4594–4604, 1986.

[94] Z. Bacic and J. C. Light. Accurate localized and delocalized vibrational states of HCN/HNC. *J. Chem. Phys.*, 86(6):3065–3077, 1987.

[95] J. C. Light and Z. Bacic. Adiabatic approximation and nonadiabatic corrections in the discrete variable representation: Highly excited vibrational states of triatomic molecules. *J. Chem. Phys.*, 87(7):4008–4019, 1987.

[96] E. Anderson, Z. Bai, C. Bischof, S. Blackford, J. Demmel, J. Dongarra, J. Du Croz, A. Greenbaum, S. Hammarling, A. McKenney, and D. Sorensen. *LAPACK Users' Guide*, 3 edition, August 1999.

[97] M. A. Kostin, O. L. Polyansky, J. Tennyson, and H. Y. Mussa. Calculations of rotation-vibration states with the z axis perpendicular to the plane: High accuracy results for H_3^+. *J. Chem. Phys.*, 116:7564–7573, 2002.

[98] P. Sarkar, N. Poulin, and T. Carrington Jr. Calculating rovibrational energy levels of a triatomic molecule with a simple Lanczos method. *J. Chem. Phys.*, 110(21):10269–10274, 1999.

[99] D. Huber. Energies of vibrating and rotating molecules by ladder operators. *International Journal Of Quantum Chemistry*, 28(2):245–267, 1985.

[100] D. M. Brink and G. R. Satchler. *Angular Momentum.* Clarendon Press, Oxford, second edition, 1968.

[101] Numerical Algorithms Group Ltd, Oxford UK. *The NAG Fortran Library Manual*, mark 21 edition, 2004.

[102] L. S. Blackford, J. Choi, A. Cleary, E. D'Azevedo, J. Demmel, I. Dhillon, J. Dongarra, S. Hammarling, G. Henry, A. Petitet, K. Stanley, D. Walker, and R. C. Whaley. *ScaLAPACK Users' Guide*, May 1997.

[103] H. Y. Mussa, J. Tennyson, C. J. Noble, and R. J. Allan. Rotation-vibration calculations using massively parallel computers. *Computer Phys. Comms.*, 108:29–37, 1998.

[104] F. Tisseur and J. Dongarra. Parallelizing the divide and conquer algorithm for the symmetric tridiagonal eigenvalue problem on distributed memory architectures. *LAPACK Working Notes*, 132:UT–CS–98–382, March 1998.

[105] D. Antonelli and C. Vömel. PDSYEVR. ScaLAPACK's parallel MRRR algorithm for the symmetric eigenvalue problem. *LAPACK Working Notes*, 168:Technical Report UCB/CSD–05–1399, August 2005.

[106] H. Y. Mussa and J. Tennyson. Calculation of rotation-vibration states of water at dissociation. *J. Chem. Phys.*, 109:10885–10892, 1998.

[107] W. Cencek, J. Rychlewski, R. Jaquet, and W. Kutzelnigg. Sub-microhartree accuracy potential energy surface for H_3^+ including adiabatic and relativistic effects. I. calculation of the potential points. *J. Chem. Phys.*, 108(7):2831–2836, 1998.

[108] A. J. C. Varandas. Energy switching approach to potential surfaces: An accurate single-valued function for the water molecule. *J. Chem. Phys.*, 105:3524–3531, 1996.

[109] R. J. Le Roy. LEVEL 7.5: A computer program for solving the radial Schrödinger equation for bound and quasibound levels. Chemical Physics Research Report CP-655, University of Waterloo, 2002.

[110] M. Lombardi, P. Barletta, and A. Kievsky. Variational estimates using a discrete variable representation. *Phys. Rev. A*, 70(3):032503, 2004.

[111] P. Barletta, M. Lombardi, and A. Kievsky. Variational DVR calculations. *Few-Body Systems*, 34:11–14, May 2004.

[112] J. R. Henderson. *Highly Excited Ro-vibrational States of Small Molecules using Discrete Variable Representations.* PhD thesis, University of London, September 1990.

[113] D. McCune. PSPLINE. Technical report, Princeton Plasma Physics Laboratory, 2004.

[114] J. J. Munro, J. Ramanlal, and J. Tennyson. Asymptotic vibrational states of the H_3^+ molecular ion. *New Journal of Physics*, 7:196, 2005.

[115] J. Ramanlal. *The Spectroscopy of H_3^+: Low Energy to Dissociation.* PhD thesis, University of London, November 2004.

[116] A. Ernesti and J. M. Hutson. On the rotational constants of floppy molecules. *Chem. Phys. Lett.*, 222:257, 1994.

[117] J. Main, G. Wiebusch, A. Holle, and K. H. Welge. New quasi-Landau structure of highly excited atoms: The hydrogen atom. *Phys. Rev. Lett.*, 57(22):2789–2792, 1986.

[118] A. Holle, J. Main, G. Weisbuch, H. Rottke, and K. H. Welge. Quasi-Landau spectrum of the chaotic diagmagnetic hydrogen atom. *Phys. Rev. Lett.*, 61(2):161–164, 1988.

[119] S. Y. Grebenshcikov, R. Schinke, P. Fleurat-Lessard, and M. Joyeux. Van der Waals states in ozone and their influence on the threshold spectrum of $O_3(X^1A_1)$. i. bound states. *J. Chem. Phys.*, 119(13):6512–6523, 2003.

[120] R. Jost, J. Nygard, A. Pasinski, and A. Delon. The photodissociation threshold of NO_2 : Precise determination of its energy and density of states. *J. Chem. Phys.*, 105(3):1287, 1996.

[121] S. Heilliette, A. Delon, R. Jost, S. Yu. Grebenshchikov, R. Schinke, B. Abel, and J. C. Rayez. Density of loosely bound states in a triatomic molecule: The role of long range interactions. *Z. Phys. Chem.*, 215(8):1069–1086, 2001.

[122] V. Efimov. Weakly-bound states of 3 resonantly-interacting particles. *Journal of Nuclear Physics USSR*, 12(5):589–1971, 1971.

[123] T. Cornelius and W. Glockle. Efimov states for three ^{4}He atoms? *J. Chem. Phys.*, 85(7):3906–3912, 1986.

[124] T. González-Lezana, J. Rubayo-Soneira, S. Miret-Artés, F. A. Gianturco, G. Delgado-Barrio, and P. Villarreal. Efimov states for ^{4}He trimers? *Phys. Rev. Lett.*, 82(8):1648–1651, 1999.

[125] P. S. Krstic and R. K. Janev. Inelastic processses from vibrationally excited states in slow $H^+ + H_2$ and $H + H_2^+$ collisions. II. dissociation. *Phys. Rev. A*, 67(2):022708, 2003.

[126] P. Barragan, L. F. Errea, A. Macias, L. Mendez, I. Rabadan, A. Riera, J. M. Lucas, and A. Aguilar. Study of *ab initio* molecular data for inelastic and reactive collisions involving the H_3^+ quasimolecule. *J. Chem. Phys.*, 121(23):11629–11638, 2004.

[127] R. W. Brankin, I. Gladwell, and L. F. Shampine. RKSUITE: a suite of Runge-Kutta codes for the initial value problem for ODE's. Technical Report Softreport 92-S1, Department of Mathematics, Southern Methodist University, 1992.

[128] A. C. Hindmarsh. ODEPACK, a systematized collection of ODE solvers. *IMACS Transactions on Scientific Computation*, 1:55–64, 1983.

[129] W. H. Press, S. A. Teukolsky, W. T. Vetterling, and B. P. Flannery. *Numerical Recipes in Fortran 90.* Cambridge University Press, second edition, 1996.

[130] G. Jolicard, C. Leforestier, and E. J. Austin. Resonance states using the optical potential model. study of Feshbach resonances and broad shape resonances. *J. Chem. Phys.*, 88(2):1026–1031, 1988.

[131] C. Schlier and U. Vix. Lifetimes of triatomic collision complexes. *Chem. Phys.*, 95(3):401–409, May 1985.

[132] M. Berblinger and C. Schlier. Accurate specific molecular state densities by phase space integration. I. computational method. *J. Chem. Phys.*, 96:6834–6841, 1992.

[133] M. Berblinger, C. Schlier, J. Tennyson, and S. Miller. Accurate specific molecular state densities by phase space integration. II. comparison with quantum calculations on H_3^+ and HD_2^+. *J. Chem. Phys.*, 96:6842–6849, 1992.

Appendix A

States of H_3^+

Table A.1: Table of the vibrational bound states of H_3^+, the symmetric state number (N_s) is given along with the irreducible representation Γ and the state numbers from the even and odd basis parity calculations (N_e,N_o). The band origins are also given for the even (E_e) and the odd (E_o) calculations along with the rotational constants (C_e,C_o).

N_s	Γ	N_e	N_o	E_e	E_o	$E_e - E_o$	C_e	C_o	$C_e - C_o$
1	A_1	1		0.000			20.375		
2	E	2	1	2520.864	2520.864	0.000	19.186	19.186	0.000
3	A_1	3		3178.779			19.776		
4	A_1	4		4777.046			18.148		
5	E	5	2	4996.964	4996.964	0.000	18.061	18.061	0.000
6	E	6	3	5554.111	5554.111	0.000	18.575	18.575	0.000
7	A_1	7		6263.045			19.174		
8	E	8	4	7004.172	7004.172	0.001	17.152	17.152	0.000
9	A_1	9		7283.734			17.042		
10	A_2		5		7491.572			17.001	
11	A_1	10		7768.693			17.522		
12	E	11	6	7869.467	7869.467	0.000	17.435	17.435	0.000
13	E	12	7	8488.208	8488.208	0.000	17.950	17.950	0.000
14	A_1	13		8999.016			16.240		
15	E	14	8	9110.418	9110.416	0.002	16.182	16.182	0.000
16	A_1	15		9253.137			18.560		
17	E	16	9	9651.777	9651.778	0.000	16.232	16.232	0.000
18	A_1	17		9967.252			16.352		
19	E	18	10	9995.992	9995.991	0.001	16.383	16.383	0.000
20	A_2		11		10209.053			16.372	
21	A_1	19		10592.758			16.920		
22	E	20	12	10644.612	10644.611	0.000	16.756	16.756	0.000
23	E	21	13	10859.183	10859.180	0.003	15.311	15.311	0.000
24	A_1	22		10919.822			15.289		
25	E	23	14	11323.366	11323.366	0.000	17.292	17.292	0.000
26	A_2		15		11526.425			15.326	
27	E	24	16	11655.646	11655.645	0.001	15.412	15.412	0.000
28	A_1	25		11812.540			15.708		
29	E	26	17	12076.832	12076.833	0.000	15.326	15.326	0.000
30	A_1	27		12147.868			17.911		
31	E	28	18	12299.182	12299.180	0.002	15.070	15.070	0.000
32	A_1	29		12374.313			14.339		
33	E	30	19	12472.378	12472.375	0.003	14.831	14.831	0.000
34	A_1	31		12588.410			15.645		
35	E	32	20	12695.800	12695.799	0.002	15.748	15.748	0.000
36	A_2		21		12830.710			15.701	
37	A_1	33		13287.333			16.017		
38	E	34	22	13316.822	13316.822	0.000	15.957	15.957	0.000
39	E	35	23	13389.385	13389.385	0.000	14.555	14.555	0.000

continued...

Table A.1: *...continued*

N_s	Γ	N_e	N_o	E_e	E_o	$E_e - E_o$	C_e	C_o	$C_e - C_o$
40	A_1	36		13397.026			14.695		
41	E	37	24	13585.907	13585.906	0.001	14.539	14.539	0.000
42	E	38	25	13690.406	13690.397	0.010	14.064	14.064	0.000
43	A_1	39		13715.877			14.218		
44	A_2		26		13753.064			14.447	
45	E	40	27	14054.875	14054.875	0.000	16.531	16.531	0.000
46	A_1	41		14189.407			14.349		
47	E	42	28	14215.352	14215.352	0.000	14.837	14.837	0.000
48	E	43	29	14471.982	14471.982	0.000	14.498	14.498	0.000
49	A_2		30		14563.861			14.582	
50	A_1	44		14664.198			14.826		
51	E	45	31	14878.091	14878.086	0.005	13.862	13.862	0.000
52	A_1	46		14888.335			13.847		
53	E	47	32	14888.939	14888.937	0.002	14.791	14.791	0.000
54	A_1	48		14941.211			17.104		
55	A_1	49		15068.515			14.134		
56	E	50	33	15114.050	15114.033	0.017	13.989	13.989	0.000
57	A_1	51		15163.812			14.714		
58	A_2		34		15185.502			13.724	
59	E	52	35	15210.758	15210.757	0.001	14.567	14.567	0.000
60	E	53	36	15328.536	15328.541	-0.005	14.101	14.101	0.000
61	A_2		37		15371.667			14.908	
62	E	54	38	15769.882	15769.881	0.001	13.682	13.682	0.000
63	A_1	55		15868.510			14.440		
64	E	56	39	15886.136	15886.136	0.000	15.105	15.105	0.000
65	A_1	57		15908.696			14.870		
66	A_2		40		15962.723			13.615	
67	E	58	41	16007.440	16007.438	0.002	14.081	14.081	0.000
68	A_1	59		16192.425			13.802		
69	E	60	42	16246.011	16245.995	0.016	13.999	13.999	0.000
70	E	61	43	16449.962	16449.965	-0.003	13.898	13.898	0.000
71	A_1	62		16452.965			14.052		
72	E	63	44	16556.733	16556.733	-0.001	13.211	13.211	0.000
73	A_2		45		16588.658			13.222	
74	E	64	46	16672.482	16672.480	0.002	15.072	15.072	0.000
75	A_1	65		16702.873			13.455		
76	E	66	47	16718.323	16718.297	0.026	13.570	13.571	0.000
77	E	67	48	16860.662	16860.660	0.002	14.091	14.091	0.000
78	E	68	49	16910.668	16910.668	0.001	13.834	13.834	0.000
79	A_1	69		17056.774			13.430		
80	A_2		50		17081.657			13.595	
81	E	70	51	17213.965	17213.963	0.001	13.623	13.623	0.000
82	A_1	71		17263.531			13.645		
83	E	72	52	17381.294	17381.287	0.007	13.872	13.872	0.000
84	A_1	73		17436.063			14.051		
85	E	74	53	17445.991	17445.990	0.001	12.958	12.958	0.000
86	A_1	75		17591.884			14.940		
87	E	76	54	17606.158	17606.134	0.024	13.722	13.722	0.000
88	A_1	77		17683.233			15.439		
89	A_2		55		17686.686			13.259	
90	E	78	56	17698.310	17698.310	0.001	14.056	14.056	0.000
91	A_1	79		17744.342			13.355		
92	A_2		57		17809.261			12.854	
93	A_2		58		17850.462			13.658	
94	E	80	59	17856.634	17856.644	-0.010	12.884	12.884	0.000
95	E	81	60	17967.780	17967.778	0.003	13.240	13.240	0.000
96	E	82	61	18194.787	18194.787	0.001	13.221	13.221	0.000
97	A_1	83		18214.263			13.064		
98	A_2		62		18328.289			13.244	
99	E	84	63	18353.010	18353.009	0.001	14.141	14.141	0.000
100	A_1	85		18364.443			14.056		
101	E	86	64	18435.177	18435.123	0.053	13.069	13.069	0.000
102	A_1	87		18451.737			13.598		
103	E	88	65	18575.557	18575.554	0.003	12.690	12.690	0.000
104	A_1	89		18588.840			13.762		
105	E	90	66	18707.713	18707.696	0.017	13.666	13.666	0.000
106	E	91	67	18795.653	18795.657	-0.005	13.118	13.118	0.000
107	A_1	92		18808.540			13.657		
108	A_2		68		18865.820			12.514	
109	E	93	69	18924.867	18924.865	0.003	12.947	12.947	0.000
110	E	94	70	19043.631	19043.623	0.008	13.117	13.117	0.000
111	E	95	71	19082.078	19082.053	0.025	13.181	13.181	0.000
112	A_1	96		19103.912			12.981		
113	A_2		72		19178.707			12.893	
114	E	97	73	19213.069	19213.079	-0.010	13.525	13.526	0.000

continued...

Table A.1: *...continued*

N_s	Γ	N_e	N_o	E_e	E_o	$E_e - E_o$	C_e	C_o	$C_e - C_o$
115	A_1	98		19240.288			12.868		
116	E	99	74	19272.341	19272.348	-0.007	13.099	13.098	0.000
117	A_2		75		19274.063			12.337	
118	E	100	76	19300.718	19300.716	0.001	13.801	13.801	0.000
119	A_1	101		19420.130			12.452		
120	E	102	77	19427.401	19427.392	0.010	12.918	12.919	0.000
121	E	103	78	19495.783	19495.780	0.003	12.623	12.623	0.000
122	A_2		79		19710.896			12.393	
123	E	104	80	19740.904	19740.897	0.007	13.013	13.013	0.000
124	A_1	105		19772.009			13.193		
125	A_1	106		19791.404			13.619		
126	E	107	81	19837.709	19837.708	0.001	12.888	12.888	0.000
127	E	108	82	19870.597	19870.596	0.001	12.417	12.418	0.000
128	E	109	83	20048.966	20048.953	0.013	13.500	13.500	0.000
129	A_2		84		20073.621			12.893	
130	A_1	110		20077.858			13.684		
131	E	111	85	20100.320	20100.297	0.023	12.947	12.947	0.000
132	A_1	112		20177.086			12.614		
133	E	113	86	20206.592	20206.565	0.026	12.287	12.288	0.000
134	A_1	114		20211.416			14.191		
135	E	115	87	20243.962	20243.919	0.042	12.888	12.888	0.000
136	A_2		88		20275.841			12.858	
137	A_1	116		20315.523			13.270		
138	A_2		89		20371.239			12.690	
139	E	117	90	20423.919	20423.923	-0.003	12.888	12.888	0.000
140	E	118	91	20499.494	20499.491	0.002	12.373	12.372	0.000
141	A_1	119		20509.063			12.832		
142	E	120	92	20599.537	20599.526	0.011	12.463	12.463	0.000
143	A_1	121		20615.520			12.554		
144	E	122	93	20768.888	20768.899	-0.011	12.237	12.237	-0.001
145	E	123	94	20777.067	20777.063	0.004	13.153	13.153	0.000
146	A_2		95		20796.801			11.992	
147	A_1	124		20837.030			12.183		
148	E	125	96	20848.146	20848.102	0.044	12.538	12.538	0.000
149	A_1	126		20917.921			13.645		
150	A_2		97		20935.311			12.416	
151	E	127	98	20986.846	20986.850	-0.004	12.187	12.187	0.000
152	A_1	128		21032.948			13.087		
153	E	129	99	21101.107	21101.102	0.006	12.066	12.066	0.000
154	E	130	100	21152.002	21151.996	0.007	12.695	12.696	0.000
155	A_2		101		21179.284			11.714	
156	A_1	131		21202.124			12.582		
157	A_1	132		21224.099			12.464		
158	E	133	102	21280.958	21280.958	0.000	12.561	12.561	0.000
159	E	134	103	21317.184	21317.187	-0.002	12.405	12.405	0.000
160	A_2		104		21334.171			12.567	
161	E	135	105	21436.542	21436.518	0.024	12.828	12.829	0.000
162	A_1	136		21463.052			12.559		
163	E	137	106	21536.800	21536.799	0.000	12.591	12.591	0.000
164	A_2		107		21587.893			12.028	
165	E	138	108	21607.496	21607.497	-0.001	12.516	12.516	0.000
166	A_1	139		21626.389			12.320		
167	E	140	109	21664.292	21664.287	0.005	13.050	13.049	0.001
168	E	141	110	21674.990	21674.991	-0.001	12.093	12.094	-0.001
169	A_1	142		21740.612			12.118		
170	E	143	111	21755.734	21755.714	0.020	12.505	12.505	0.000
171	E	144	112	21887.218	21887.219	-0.001	12.206	12.205	0.001
172	E	145	113	21889.202	21889.217	-0.015	11.734	11.734	-0.001
173	A_2		114		21889.659			12.198	
174	A_1	146		21992.106			13.034		
175	A_1	147		22075.433			12.390		
176	E	148	115	22106.001	22105.894	0.107	12.479	12.480	0.000
177	A_1	149		22160.728			12.301		
178	A_2		116		22164.619			11.424	
179	E	150	117	22170.100	22170.101	-0.001	12.546	12.546	0.000
180	E	151	118	22202.145	22202.094	0.051	12.164	12.165	0.000
181	A_1	152		22289.593			11.633		
182	E	153	119	22306.029	22305.990	0.039	11.980	11.981	0.000
183	A_2		120		22331.433			12.145	
184	E	154	121	22380.966	22380.978	-0.012	12.088	12.088	0.000
185	A_1	155		22413.003			12.138		
186	A_2		122		22424.205			11.571	
187	A_1	156		22471.080			12.348		
188	E	157	123	22508.231	22508.216	0.015	12.068	12.069	-0.001
189	E	158	124	22518.403	22518.434	-0.031	12.277	12.277	0.000

continued...

Table A.1: *...continued*

N_s	Γ	N_e	N_o	E_e	E_o	$E_e - E_o$	C_e	C_o	$C_e - C_o$
190	A_2		125		22551.672			12.377	
191	E	159	126	22594.954	22594.938	0.016	12.477	12.476	0.000
192	A_1	160		22618.612			12.606		
193	E	161	127	22626.893	22626.893	0.000	12.272	12.272	0.000
194	A_1	162		22693.079			13.130		
195	E	163	128	22716.526	22716.468	0.058	12.195	12.196	0.000
196	E	164	129	22797.215	22797.231	-0.016	11.599	11.599	0.000
197	A_1	165		22845.918			12.940		
198	A_2		130		22872.120			11.736	
199	E	166	131	22918.810	22918.800	0.010	11.914	11.914	0.000
200	A_2		132		22957.048			11.457	
201	A_2		133		23005.206			11.665	
202	E	167	134	23023.557	23023.556	0.001	11.577	11.577	0.000
203	A_1	168		23035.907			11.965		
204	E	169	135	23036.799	23036.813	-0.013	12.032	12.032	0.000
205	E	170	136	23081.423	23081.422	0.002	12.041	12.041	0.000
206	A_1	171		23141.591			11.993		
207	E	172	137	23164.740	23164.695	0.046	11.968	11.968	0.000
208	A_1	173		23207.181			12.085		
209	E	174	138	23245.569	23245.553	0.016	11.929	11.929	0.000
210	A_1	175		23307.490			13.018		
211	E	176	139	23369.222	23369.201	0.021	11.142	11.142	0.000
212	A_1	177		23396.355			12.633		
213	E	178	140	23398.128	23398.116	0.012	11.793	11.793	0.000
214	A_2		141		23425.581			11.738	
215	A_2		142		23480.564			11.910	
216	E	179	143	23485.333	23485.338	-0.005	11.487	11.487	0.000
217	E	180	144	23515.019	23514.978	0.041	11.687	11.687	0.000
218	A_1	181		23538.449			11.396		
219	E	182	145	23579.856	23579.845	0.011	11.663	11.663	0.000
220	A_1	183		23610.341			12.137		
221	E	184	146	23652.601	23652.597	0.004	12.366	12.366	0.000
222	A_2		147		23692.579			10.817	
223	E	185	148	23727.733	23727.748	-0.015	11.762	11.762	0.000
224	E	186	149	23811.892	23811.887	0.005	11.872	11.872	0.000
225	A_1	187		23891.618			12.055		
226	E	188	150	23904.983	23904.920	0.063	11.796	11.796	0.000
227	A_1	189		23924.182			11.764		
228	A_2		151		23948.886			11.311	
229	E	190	152	23949.688	23949.704	-0.016	11.861	11.861	0.000
230	E	191	153	23974.420	23974.377	0.043	11.915	11.916	-0.001
231	A_1	192		24009.747			11.670		
232	A_2		154		24022.368			11.762	
233	E	193	155	24038.132	24037.906	0.225	11.642	11.643	-0.001
234	A_1	194		24051.372			12.072		
235	E	195	156	24075.054	24075.015	0.038	12.449	12.448	0.001
236	E	196	157	24157.623	24157.607	0.016	11.631	11.631	0.000
237	A_2		158		24161.713			11.118	
238	A_1	197		24166.155			11.895		
239	E	198	159	24221.672	24221.726	-0.053	11.597	11.597	0.000
240	E	199	160	24312.696	24312.689	0.008	11.405	11.405	0.000
241	A_1	200		24325.841			11.713		
242	E	201	161	24368.099	24368.074	0.025	11.456	11.456	0.000
243	A_1	202		24371.851			11.507		
244	A_1	203		24382.374			11.669		
245	A_2		162		24399.554			11.244	
246	E	204	163	24421.491	24421.469	0.022	11.704	11.705	-0.001
247	A_2		164		24457.492			11.319	
248	E	205	165	24486.406	24486.369	0.037	10.963	10.963	0.000
249	E	206	166	24546.538	24546.525	0.013	11.076	11.076	0.000
250	E	207	167	24579.327	24579.257	0.070	11.487	11.486	0.000
251	A_1	208		24589.954			11.504		
252	A_2		168		24642.460			11.228	
253	E	209	169	24688.745	24688.698	0.047	11.188	11.188	0.000
254	A_1	210		24700.229			11.905		
255	A_2		170		24717.239			10.895	
256	E	211	171	24736.847	24736.833	0.014	11.342	11.342	0.000
257	E	212	172	24759.050	24759.042	0.008	11.610	11.610	0.000
258	E	213	173	24801.821	24801.758	0.063	11.719	11.720	-0.001
259	A_1	214		24840.547			11.497		
260	A_1	215		24872.838			11.583		
261	A_2		174		24906.635			11.233	
262	E	216	175	24907.983	24907.914	0.069	11.518	11.519	0.000
263	E	217	176	24964.935	24964.916	0.020	11.557	11.558	0.000
264	E	218	177	24980.844	24980.741	0.103	11.448	11.448	0.000

continued...

Table A.1: *...continued*

N_s	Γ	N_e	N_o	E_e	E_o	$E_e - E_o$	C_e	C_o	$C_e - C_o$
265	A_1	219		24997.414			11.665		
266	E	220	178	25053.101	25053.103	-0.002	11.468	11.468	0.000
267	E	221	179	25086.676	25086.727	-0.050	11.435	11.435	0.000
268	A_2		180		25137.623			11.432	
269	A_1	222		25147.229			12.487		
270	E	223	181	25148.465	25148.497	-0.032	11.607	11.607	0.000
271	A_2		182		25152.150			11.191	
272	A_1	224		25190.975			10.997		
273	E	225	183	25222.503	25222.520	-0.017	10.888	10.888	0.000
274	A_2		184		25302.393			10.823	
275	A_1	226		25317.411			11.878		
276	E	227	185	25349.982	25349.853	0.129	10.988	10.988	0.000
277	A_1	228		25370.046			11.020		
278	E	229	186	25370.552	25370.487	0.065	11.468	11.468	0.000
279	E	230	187	25414.354	25414.323	0.031	11.045	11.046	0.000
280	A_2		188		25428.558			10.229	
281	E	231	189	25451.517	25451.504	0.013	11.123	11.123	0.000
282	E	232	190	25506.638	25506.608	0.030	10.992	10.991	0.000
283	A_1	233		25528.293			12.195		
284	A_1	234		25567.956			11.395		
285	E	235	191	25595.581	25595.593	-0.012	11.082	11.082	0.000
286	A_2		192		25602.635			11.055	
287	A_1	236		25663.625			11.372		
288	E	237	193	25679.398	25679.371	0.027	11.303	11.303	0.000
289	A_1	238		25703.288			11.112		
290	E	239	194	25706.702	25706.700	0.003	10.834	10.834	0.000
291	A_1	240		25731.639			11.190		
292	E	241	195	25741.676	25741.674	0.002	11.149	11.149	0.000
293	E	242	196	25822.604	25822.526	0.078	11.393	11.393	-0.001
294	A_2		197		25860.557			10.863	
295	A_1	243		25899.515			11.677		
296	E	244	198	25903.668	25903.379	0.288	11.559	11.562	-0.004
297	E	245	199	25918.424	25918.412	0.012	10.766	10.765	0.001
298	A_2		200		25924.860			10.750	
299	E	246	201	25956.711	25956.709	0.003	10.887	10.886	0.001
300	A_2		202		25975.956			10.877	
301	E	247	203	26003.715	26003.765	-0.050	10.669	10.668	0.001
302	E	248	204	26027.204	26027.158	0.046	10.861	10.860	0.001
303	A_1	249		26068.476			10.611		
304	A_2		205		26089.677			11.039	
305	E	250	206	26107.239	26107.169	0.070	10.880	10.880	0.000
306	E	251	207	26126.230	26126.210	0.020	10.681	10.680	0.001
307	A_1	252		26135.785			12.319		
308	E	253	208	26151.424	26151.409	0.016	10.841	10.842	-0.001
309	A_1	254		26185.512			11.070		
310	E	255	209	26206.842	26206.845	-0.003	11.225	11.225	0.000
311	A_1	256		26231.410			11.321		
312	E	257	210	26263.983	26263.851	0.131	10.999	10.999	0.000
313	E	258	211	26295.759	26295.690	0.069	10.617	10.617	-0.001
314	A_2		212		26301.935			10.871	
315	A_1	259		26327.984			10.575		
316	A_2		213		26334.591			10.394	
317	A_1	260		26375.644			11.266		
318	E	261	214	26378.374	26378.418	-0.044	10.801	10.802	-0.001
319	E	262	215	26440.960	26440.930	0.030	11.425	11.425	0.000
320	E	263	216	26461.637	26461.403	0.235	11.205	11.204	0.000
321	A_2		217		26476.475			10.256	
322	E	264	218	26495.091	26495.104	-0.013	10.754	10.753	0.000
323	A_1	265		26514.807			11.324		
324	A_1	266		26530.514			11.000		
325	E	267	219	26580.348	26580.315	0.032	10.579	10.579	0.000
326	A_2		220		26583.220			10.515	
327	E	268	221	26645.909	26645.731	0.178	10.720	10.720	0.000
328	A_1	269		26655.693			10.656		
329	E	270	222	26680.851	26680.880	-0.029	10.444	10.445	-0.001
330	E	271	223	26728.521	26728.633	-0.112	10.640	10.639	0.001
331	A_2		224		26745.644			10.723	
332	E	272	225	26762.590	26762.585	0.005	10.484	10.484	0.001
333	A_1	273		26778.269			10.567		
334	E	274	226	26803.061	26802.975	0.086	10.842	10.843	0.000
335	A_1	275		26826.336			10.465		
336	E	276	227	26853.360	26853.335	0.025	10.699	10.699	-0.001
337	A_2		228		26869.775			10.022	
338	E	277	229	26870.486	26870.482	0.004	10.767	10.764	0.002
339	A_1	278		26955.984			10.583		

continued...

Table A.1: *...continued*

N_s	Γ	N_e	N_o	E_e	E_o	$E_e - E_o$	C_e	C_o	$C_e - C_o$
340	E	279	230	26960.132	26960.027	0.105	10.785	10.784	0.001
341	E	280	231	26980.629	26980.667	-0.037	10.620	10.621	-0.001
342	A_2		232		26982.027			10.756	
343	A_2		233		27028.288			10.596	
344	A_1	281		27030.604			10.317		
345	E	282	234	27037.947	27037.934	0.014	10.366	10.367	-0.001
346	A_1	283		27066.025			10.226		
347	E	284	235	27104.408	27104.324	0.084	10.366	10.366	0.000
348	A_2		236		27107.582			10.660	
349	E	285	237	27141.718	27141.680	0.038	10.092	10.077	0.015
350	A_1	286		27142.096			10.485		
351	E	287	238	27163.338	27163.336	0.002	11.543	11.544	-0.001
352	E	288	239	27188.164	27188.090	0.074	10.674	10.673	0.002
353	A_1	289		27197.742			11.184		
354	A_1	290		27210.555			10.837		
355	E	291	240	27284.704	27284.677	0.028	10.444	10.444	0.000
356	A_2		241		27291.243			9.941	
357	E	292	242	27338.763	27338.847	-0.084	10.712	10.713	0.000
358	A_1	293		27379.863			10.921		
359	E	294	243	27400.339	27400.410	-0.071	9.679	9.681	-0.002
360	A_2		244		27404.153			10.300	
361	E	295	245	27434.369	27434.393	-0.024	10.695	10.695	0.001
362	A_1	296		27461.497			10.884		
363	E	297	246	27470.515	27470.447	0.067	10.680	10.679	0.001
364	E	298	247	27511.561	27511.582	-0.021	10.176	10.177	0.000
365	A_1	299		27562.698			10.265		
366	A_2		248		27573.032			10.386	
367	E	300	249	27579.536	27579.518	0.018	10.481	10.481	0.000
368	A_1	301		27587.682			11.015		
369	E	302	250	27632.963	27632.863	0.099	10.178	10.177	0.000
370	A_1	303		27662.810			10.430		
371	A_2		251		27667.360			9.876	
372	E	304	252	27669.220	27669.148	0.072	10.614	10.614	0.000
373	E	305	253	27695.270	27695.176	0.095	10.458	10.458	0.000
374	E	306	254	27723.826	27723.901	-0.075	10.236	10.236	0.000
375	A_1	307		27726.568			11.024		
376	A_2		255		27755.107			10.436	
377	E	308	256	27758.619	27758.549	0.070	10.628	10.631	-0.002
378	A_1	309		27765.592			10.781		
379	E	310	257	27784.537	27784.278	0.258	11.002	11.009	-0.008
380	A_1	311		27797.924			10.381		
381	A_2		258		27825.714			10.086	
382	E	312	259	27826.935	27826.680	0.255	10.669	10.663	0.005
383	A_1	313		27856.169			10.792		
384	A_2		260		27863.517			10.259	
385	E	314	261	27868.405	27868.190	0.215	10.257	10.256	0.001
386	E	315	262	27893.519	27893.568	-0.048	10.413	10.413	0.000
387	E	316	263	27950.992	27951.174	-0.182	10.050	10.050	-0.001
388	A_1	317		27983.212			10.242		
389	E	318	264	27999.444	27999.445	-0.002	10.366	10.367	-0.001
390	E	319	265	28026.038	28026.151	-0.113	9.942	9.941	0.002
391	A_2		266		28026.976			10.575	
392	A_1	320		28056.108			10.601		
393	A_2		267		28089.416			9.247	
394	A_1	321		28106.489			10.562		
395	E	322	268	28109.236	28109.217	0.019	10.499	10.498	0.000
396	E	323	269	28128.826	28128.761	0.065	10.563	10.564	-0.001
397	A_2		270		28137.195			10.306	
398	A_1	324		28177.409			10.445		
399	E	325	271	28199.164	28199.169	-0.006	10.010	10.011	0.000
400	A_2		272		28215.565			9.989	
401	E	326	273	28234.041	28234.142	-0.101	10.301	10.301	0.001
402	A_1	327		28291.198			10.921		
403	E	328	274	28300.902	28300.951	-0.049	10.052	10.057	-0.005
404	E	329	275	28314.336	28313.911	0.426	10.978	10.974	0.005
405	A_1	330		28349.547			10.867		
406	E	331	276	28373.746	28373.392	0.354	9.933	9.931	0.002
407	E	332	277	28394.244	28394.161	0.083	10.192	10.197	-0.005
408	A_1	333		28416.203			10.063		
409	A_2		278		28418.346			9.865	
410	E	334	279	28425.191	28425.276	-0.085	10.042	10.048	-0.006
411	E	335	280	28427.976	28428.005	-0.028	9.757	9.750	0.007
412	A_1	336		28447.464			11.064		
413	E	337	281	28487.531	28487.636	-0.105	10.142	10.150	-0.008
414	E	338	282	28492.333	28492.554	-0.221	10.172	10.157	0.014

continued...

Table A.1: *...continued*

N_s	Γ	N_e	N_o	E_e	E_o	$E_e - E_o$	C_e	C_o	$C_e - C_o$
415	A_1	339		28492.743			10.544		
416	A_2		283		28508.667			9.875	
417	A_2		284		28546.812			10.309	
418	E	340	285	28550.992	28551.040	-0.048	10.070	10.070	0.000
419	E	341	286	28597.617	28597.532	0.086	10.295	10.292	0.002
420	A_1	342		28612.605			9.685		
421	E	343	287	28631.506	28631.597	-0.091	10.359	10.360	-0.001
422	A_2		288		28644.971			9.931	
423	A_1	344		28674.153			10.449		
424	E	345	289	28686.219	28686.089	0.130	10.276	10.276	0.000
425	A_1	346		28705.684			10.440		
426	E	347	290	28706.747	28706.814	-0.068	10.048	10.049	-0.001
427	A_1	348		28722.907			10.497		
428	E	349	291	28723.804	28723.559	0.245	10.163	10.158	0.005
429	A_2		292		28736.799			9.707	
430	E	350	293	28808.297	28808.248	0.049	10.054	10.053	0.001
431	A_2		294		28821.622			10.175	
432	E	351	295	28838.666	28838.758	-0.092	10.142	10.142	0.000
433	A_1	352		28877.281			10.377		
434	E	353	296	28899.614	28899.579	0.036	10.282	10.282	0.000
435	A_2		297		28907.443			9.799	
436	E	354	298	28933.160	28933.110	0.050	10.631	10.632	-0.001
437	E	355	299	28956.660	28956.606	0.054	9.755	9.753	0.002
438	A_1	356		28976.028			10.119		
439	E	357	300	28987.085	28986.961	0.124	10.190	10.191	-0.001
440	A_1	358		28995.553			10.257		
441	E	359	301	29023.060	29022.980	0.081	10.161	10.159	0.002
442	A_1	360		29064.244			10.287		
443	E	361	302	29080.410	29080.320	0.090	9.753	9.754	-0.001
444	E	362	303	29116.336	29116.436	-0.100	9.734	9.734	0.000
445	A_2		304		29123.318			9.401	
446	E	363	305	29158.585	29158.529	0.056	9.874	9.874	0.000
447	A_1	364		29187.011			10.242		
448	A_2		306		29193.511			9.484	
449	E	365	307	29198.297	29198.212	0.086	9.964	9.965	-0.001
450	E	366	308	29219.842	29219.843	-0.001	9.887	9.887	0.001
451	A_1	367		29240.814			9.800		
452	E	368	309	29255.916	29255.798	0.118	10.021	10.022	0.000
453	A_2		310		29272.484			9.795	
454	E	369	311	29275.558	29275.621	-0.063	9.984	9.984	0.000
455	A_2		312		29313.095			9.430	
456	A_1	370		29315.215			10.358		
457	E	371	313	29349.541	29349.633	-0.092	9.764	9.767	-0.003
458	A_1	372		29356.726			10.492		
459	E	373	314	29376.406	29376.411	-0.005	10.274	10.273	0.001
460	A_1	374		29426.607			9.928		
461	A_2		315		29428.727			9.796	
462	E	375	316	29449.753	29449.802	-0.049	10.065	10.063	0.002
463	A_2		317		29457.516			9.808	
464	E	376	318	29481.508	29481.464	0.045	10.009	10.008	0.000
465	A_1	377		29501.750			9.998		
466	E	378	319	29525.843	29525.776	0.067	10.043	10.050	-0.006
467	A_1	379		29534.642			9.834		
468	E	380	320	29542.983	29543.148	-0.165	10.078	10.068	0.010
469	E	381	321	29552.018	29551.867	0.151	9.866	9.869	-0.003
470	A_2		322		29554.222			9.851	
471	A_1	382		29584.597			10.001		
472	E	383	323	29585.362	29585.493	-0.131	9.790	9.793	-0.003
473	A_2		324		29610.251			9.777	
474	A_1	384		29616.986			10.796		
475	E	385	325	29618.628	29618.628	0.000	9.966	9.965	0.001
476	E	386	326	29648.159	29647.715	0.444	10.442	10.439	0.003
477	E	387	327	29690.910	29690.984	-0.075	9.928	9.928	0.000
478	A_1	388		29694.176			10.653		
479	E	389	328	29715.552	29715.314	0.238	10.184	10.185	-0.001
480	A_2		329		29726.602			9.769	
481	A_2		330		29744.219			9.449	
482	E	390	331	29786.134	29786.360	-0.226	9.347	9.348	0.000
483	E	391	332	29793.623	29793.600	0.023	9.864	9.859	0.005
484	A_1	392		29796.669			10.132		
485	A_1	393		29809.294			9.876		
486	E	394	333	29840.514	29840.441	0.074	10.238	10.248	-0.010
487	E	395	334	29845.839	29845.926	-0.087	10.090	10.082	0.008
488	A_1	396		29867.844			9.767		
489	A_2		335		29876.393			9.939	

continued...

Table A.1: *...continued*

N_s	Γ	N_e	N_o	E_e	E_o	$E_e - E_o$	C_e	C_o	$C_e - C_o$
490	E	397	336	29892.150	29892.176	-0.026	9.522	9.520	0.002
491	E	398	337	29905.565	29905.595	-0.031	9.829	9.831	-0.002
492	A_1	399		29908.022			9.608		
493	E	400	338	29951.351	29951.074	0.277	9.847	9.851	-0.004
494	E	401	339	29972.037	29972.138	-0.101	9.878	9.877	0.001
495	A_2		340		30001.031			9.321	
496	A_1	402		30017.492			9.789		
497	E	403	341	30032.005	30031.768	0.236	9.806	9.804	0.002
498	A_2		342		30038.594			9.547	
499	E	404	343	30047.099	30046.972	0.127	9.799	9.805	-0.006
500	A_1	405		30059.839			9.822		
501	E	406	344	30080.582	30080.393	0.189	9.841	9.855	-0.015
502	A_1	407		30085.184			10.580		
503	E	408	345	30089.703	30089.801	-0.098	9.444	9.425	0.019
504	A_2		346		30095.868			9.566	
505	A_1	409		30143.069			10.354		
506	E	410	347	30155.319	30155.709	-0.390	9.841	9.840	0.000
507	A_2		348		30193.449			9.427	
508	A_1	411		30211.351			9.833		
509	E	412	349	30212.462	30212.327	0.135	9.831	9.831	0.000
510	E	413	350	30251.300	30251.123	0.177	9.904	9.920	-0.016
511	E	414	351	30254.276	30254.443	-0.167	9.561	9.543	0.018
512	A_2		352		30263.813			9.838	
513	A_1	415		30294.627			9.451		
514	E	416	353	30324.380	30324.081	0.299	9.644	9.642	0.001
515	A_1	417		30336.460			10.767		
516	E	418	354	30355.007	30355.001	0.006	9.722	9.723	-0.001
517	A_2		355		30367.835			9.800	
518	A_1	419		30373.943			10.026		
519	E	420	356	30400.909	30400.783	0.126	9.940	9.938	0.001
520	E	421	357	30429.735	30429.724	0.011	9.520	9.521	-0.002
521	A_2		358		30443.304			9.660	
522	A_1	422		30451.241			10.149		
523	E	423	359	30466.807	30466.695	0.112	9.850	9.851	-0.001
524	E	424	360	30488.411	30488.346	0.065	10.092	10.092	0.000
525	A_1	425		30506.662			9.988		
526	A_2		361		30507.398			9.079	
527	A_1	426		30555.728			10.405		
528	E	427	362	30566.177	30566.177	0.000	9.314	9.312	0.003
529	E	428	363	30576.798	30576.498	0.300	9.679	9.679	0.000
530	E	429	364	30604.825	30604.950	-0.125	8.941	8.859	0.082
531	A_1	430		30605.343			9.417		
532	E	431	365	30619.091	30618.982	0.109	9.850	9.853	-0.003
533	A_2		366		30635.931			9.779	
534	E	432	367	30659.837	30659.642	0.195	9.869	9.870	-0.001
535	A_2		368		30663.560			9.276	
536	E	433	369	30675.558	30675.329	0.229	10.025	10.027	-0.002
537	E	434	370	30732.419	30732.284	0.135	9.471	9.471	0.000
538	E	435	371	30740.832	30741.203	-0.371	9.667	9.670	-0.003
539	A_1	436		30742.055			10.327		
540	A_2		372		30749.467			9.330	
541	E	437	373	30757.155	30757.126	0.030	9.805	9.803	0.003
542	A_1	438		30792.690			9.798		
543	E	439	374	30793.456	30793.385	0.070	9.591	9.594	-0.003
544	A_2		375		30813.156			9.241	
545	E	440	376	30853.204	30853.261	-0.057	9.814	9.812	0.001
546	A_1	441		30857.271			10.101		
547	E	442	377	30864.495	30864.362	0.133	9.872	9.873	-0.001
548	A_1	443		30903.498			10.099		
549	E	444	378	30917.339	30917.383	-0.043	9.747	9.746	0.000
550	A_2		379		30923.564			9.138	
551	A_1	445		30932.285			9.706		
552	E	446	380	30968.947	30968.653	0.294	9.445	9.437	0.008
553	E	447	381	30982.761	30982.683	0.079	9.749	9.752	-0.003
554	A_1	448		31005.209			9.971		
555	A_2		382		31018.573			8.953	
556	E	449	383	31020.517	31020.632	-0.115	9.207	9.205	0.003
557	E	450	384	31024.566	31024.437	0.129	9.378	9.379	-0.001
558	E	451	385	31056.360	31056.382	-0.021	9.686	9.689	-0.003
559	A_1	452		31073.935			10.064		
560	A_2		386		31082.090			9.649	
561	E	453	387	31113.230	31113.097	0.132	9.726	9.728	-0.002
562	A_1	454		31115.204			10.075		
563	A_1	455		31132.915			9.823		
564	E	456	388	31147.517	31147.563	-0.046	9.520	9.518	0.002

continued...

Table A.1: *...continued*

N_s	Γ	N_e	N_o	E_e	E_o	$E_e - E_o$	C_e	C_o	$C_e - C_o$
565	A_2		389		31150.697			9.569	
566	A_1	457		31188.854			9.169		
567	E	458	390	31195.750	31196.102	-0.353	9.633	9.626	0.006
568	E	459	391	31208.293	31208.070	0.223	9.698	9.704	-0.006
569	A_2		392		31219.327			9.166	
570	E	460	393	31220.439	31220.683	-0.244	9.435	9.427	0.007
571	A_2		394		31223.385			9.464	
572	A_1	461		31244.184			10.244		
573	A_1	462		31259.381			9.202		
574	E	463	395	31261.835	31261.833	0.002	8.820	8.820	-0.001
575	E	464	396	31282.456	31282.117	0.339	9.540	9.539	0.001
576	E	465	397	31299.738	31299.512	0.225	10.003	10.021	-0.018
577	E	466	398	31312.275	31312.110	0.165	9.627	9.617	0.010
578	A_1	467		31328.077			9.009		
579	A_2		399		31331.948			9.407	
580	E	468	400	31341.444	31340.942	0.501	9.572	9.565	0.007
581	A_1	469		31359.321			9.641		
582	E	470	401	31384.700	31384.509	0.191	9.666	9.666	0.000
583	E	471	402	31415.070	31415.290	-0.219	9.338	9.341	-0.003
584	A_2		403		31443.746			9.168	
585	E	472	404	31454.764	31454.804	-0.040	9.431	9.429	0.002
586	A_1	473		31466.606			9.494		
587	A_2		405		31467.833			9.401	
588	E	474	406	31484.052	31484.078	-0.026	9.328	9.327	0.001
589	E	475	407	31519.664	31519.840	-0.176	9.381	9.386	-0.005
590	A_1	476		31541.449			10.178		
591	E	477	408	31542.145	31542.243	-0.099	9.613	9.609	0.004
592	A_1	478		31568.245			9.458		
593	A_2		409		31574.894			9.271	
594	E	479	410	31583.675	31583.770	-0.095	9.608	9.613	-0.006
595	A_1	480		31589.025			9.638		
596	E	481	411	31621.362	31621.241	0.121	9.696	9.694	0.002
597	E	482	412	31633.375	31632.881	0.494	9.497	9.496	0.001
598	E	483	413	31655.715	31655.787	-0.072	9.560	9.572	-0.012
599	A_2		414		31665.168			9.565	
600	E	484	415	31670.094	31669.475	0.619	9.978	9.968	0.010
601	A_1	485		31696.849			10.055		
602	E	486	416	31714.914	31714.969	-0.055	9.373	9.373	0.000
603	A_2		417		31721.242			9.241	
604	E	487	418	31728.446	31728.398	0.048	9.709	9.707	0.002
605	A_1	488		31743.604			9.384		
606	A_2		419		31749.903			9.035	
607	E	489	420	31775.396	31775.465	-0.069	9.314	9.315	-0.001
608	A_1	490		31777.323			9.772		
609	A_2		421		31791.131			9.049	
610	E	491	422	31798.540	31798.356	0.184	9.420	9.413	0.007
611	A_1	492		31822.491			10.327		
612	E	493	423	31858.137	31857.546	0.592	9.478	9.478	-0.001
613	E	494	424	31865.451	31865.482	-0.031	9.291	9.297	-0.006
614	A_1	495		31875.883			9.302		
615	E	496	425	31913.363	31913.386	-0.023	9.533	9.530	0.003
616	A_2		426		31917.508			8.774	
617	A_1	497		31924.586			9.589		
618	A_2		427		31930.368			8.949	
619	E	498	428	31952.323	31952.131	0.192	9.395	9.394	0.002
620	E	499	429	31971.606	31971.483	0.123	9.293	9.251	0.042
621	A_1	500		31971.919			9.539		
622	E	501	430	31993.873	31993.707	0.166	9.352	9.356	-0.004
623	E	502	431	32045.598	32045.383	0.216	9.484	9.490	-0.007
624	E	503	432	32062.053	32061.602	0.451	9.467	9.465	0.003
625	A_1	504		32070.007			9.586		
626	A_2		433		32073.793			9.242	
627	E	505	434	32079.319	32079.467	-0.148	9.498	9.490	0.009
628	A_1	506		32093.779			9.342		
629	E	507	435	32115.025	32115.077	-0.052	9.207	9.208	-0.001
630	A_2		436		32135.386			9.148	
631	E	508	437	32142.202	32142.091	0.112	8.578	8.580	-0.002
632	A_1	509		32154.720			9.591		
633	A_2		438		32162.187			9.009	
634	E	510	439	32181.720	32181.544	0.176	9.558	9.558	0.000
635	E	511	440	32235.603	32234.917	0.686	9.751	9.754	-0.003
636	E	512	441	32251.406	32251.478	-0.072	9.146	9.153	-0.006
637	A_1	513		32260.185			10.048		
638	E	514	442	32280.866	32281.110	-0.244	9.121	9.127	-0.006
639	A_2		443		32286.507			8.779	

continued...

Table A.1: *...continued*

N_s	Γ	N_e	N_o	E_e	E_o	$E_e - E_o$	C_e	C_o	$C_e - C_o$
640	E	515	444	32287.555	32287.747	-0.191	9.272	9.258	0.014
641	A_1	516		32298.382			9.860		
642	A_2		445		32323.869			9.322	
643	E	517	446	32340.481	32341.055	-0.574	8.886	8.883	0.003
644	A_1	518		32344.887			9.115		
645	A_2		447		32379.804			9.112	
646	E	519	448	32381.954	32381.664	0.289	9.334	9.345	-0.012
647	E	520	449	32397.082	32397.282	-0.200	9.368	9.357	0.011
648	A_1	521		32406.708			9.532		
649	E	522	450	32411.359	32410.693	0.666	9.146	9.150	-0.004
650	A_2		451		32412.801			9.092	
651	E	523	452	32455.063	32454.757	0.306	9.348	9.350	-0.002
652	A_2		453		32457.944			9.481	
653	A_1	524		32462.034			8.879		
654	E	525	454	32476.318	32476.650	-0.332	9.533	9.530	0.003
655	A_1	526		32493.943			10.173		
656	A_1	527		32520.771			8.889		
657	E	528	455	32527.911	32527.635	0.276	8.953	8.967	-0.014
658	A_1	529		32535.324			9.740		
659	E	530	456	32540.043	32540.120	-0.077	9.247	9.240	0.006
660	A_2		457		32561.185			8.985	
661	E	531	458	32581.236	32580.874	0.363	9.199	9.199	0.000
662	E	532	459	32586.488	32586.618	-0.130	8.808	8.800	0.008
663	E	533	460	32616.366	32617.016	-0.651	9.242	9.245	-0.003
664	A_1	534		32622.934			8.704		
665	E	535	461	32634.724	32634.504	0.220	9.387	9.388	-0.001
666	A_2		462		32649.322			8.856	
667	A_1	536		32662.545			9.578		
668	E	537	463	32665.424	32665.568	-0.145	9.057	9.055	0.003
669	A_2		464		32681.295			8.818	
670	A_1	538		32687.428			9.854		
671	E	539	465	32690.785	32690.471	0.314	9.300	9.296	0.004
672	E	540	466	32711.716	32711.833	-0.117	8.759	8.761	-0.003
673	E	541	467	32723.223	32723.011	0.213	9.589	9.588	0.001
674	A_1	542		32727.646			9.457		
675	A_2		468		32729.368			9.120	
676	E	543	469	32738.255	32737.894	0.361	9.606	9.605	0.002
677	A_1	544		32765.224			9.612		
678	E	545	470	32777.732	32777.571	0.160	9.453	9.454	-0.001
679	E	546	471	32795.345	32795.360	-0.015	9.497	9.504	-0.007
680	E	547	472	32804.901	32804.848	0.053	9.071	9.068	0.003
681	A_2		473		32805.672			9.175	
682	E	548	474	32832.696	32832.790	-0.094	9.141	9.137	0.004
683	A_1	549		32838.584			9.263		
684	E	550	475	32857.143	32856.900	0.243	9.192	9.195	-0.003
685	E	551	476	32859.087	32859.231	-0.144	9.220	9.218	0.001
686	A_2		477		32874.409			8.763	
687	A_1	552		32876.224			9.898		
688	E	553	478	32915.296	32915.473	-0.176	8.950	8.973	-0.023
689	A_1	554		32916.477			8.681		
690	A_1	555		32961.061			9.207		
691	E	556	479	32961.980	32962.043	-0.063	9.150	9.154	-0.004
692	E	557	480	32977.682	32977.292	0.390	9.107	9.100	0.007
693	E	558	481	33005.330	33005.611	-0.281	8.948	8.948	-0.001
694	A_2		482		33012.324			9.163	
695	A_1	559		33022.487			9.289		
696	A_2		483		33041.952			8.507	
697	E	560	484	33046.090	33046.066	0.024	9.165	9.166	-0.001
698	A_1	561		33048.482			9.369		
699	E	562	485	33078.556	33078.964	-0.408	9.493	9.488	0.005
700	A_1	563		33094.601			8.986		
701	A_2		486		33098.350			9.051	
702	E	564	487	33100.373	33100.225	0.148	9.155	9.156	-0.001
703	A_2		488		33121.584			9.081	
704	A_1	565		33136.403			9.316		
705	A_2		489		33147.742			8.931	
706	E	566	490	33162.249	33162.556	-0.307	8.420	8.423	-0.003
707	E	567	491	33174.517	33175.460	-0.944	9.342	9.339	0.002
708	A_1	568		33186.704			9.692		
709	E	569	492	33192.348	33191.730	0.618	9.157	9.156	0.001
710	A_2		493		33201.243			9.493	
711	E	570	494	33226.208	33226.363	-0.155	8.938	8.936	0.002
712	A_1	571		33234.119			8.970		
713	A_2		495		33246.551			9.043	
714	E	572	496	33275.067	33275.148	-0.081	8.874	8.877	-0.003

continued...

Table A.1: *...continued*

N_s	Γ	N_e	N_o	E_e	E_o	$E_e - E_o$	C_e	C_o	$C_e - C_o$
715	E	573	497	33285.138	33284.619	0.518	8.746	8.745	0.000
716	A_1	574		33315.650			8.905		
717	E	575	498	33329.914	33329.670	0.244	9.171	9.173	-0.002
718	A_1	576		33347.108			9.132		
719	E	577	499	33352.556	33352.264	0.291	9.110	9.111	-0.001
720	A_1	578		33361.203			10.099		
721	E	579	500	33370.825	33371.148	-0.323	9.105	9.102	0.003
722	E	580	501	33386.634	33386.276	0.359	9.227	9.234	-0.007
723	A_1	581		33408.141			8.981		
724	A_2		502		33423.080			8.791	
725	E	582	503	33435.972	33435.319	0.653	9.520	9.537	-0.017
726	A_2		504		33439.955			8.852	
727	E	583	505	33451.419	33451.528	-0.109	9.112	9.105	0.006
728	E	584	506	33454.103	33453.672	0.431	8.956	8.956	0.000
729	A_1	585		33465.606			9.016		
730	E	586	507	33480.151	33480.225	-0.074	8.760	8.758	0.001
731	A_2		508		33493.204			8.457	
732	E	587	509	33507.421	33506.914	0.507	9.173	9.173	0.000
733	A_1	588		33513.046			9.017		
734	E	589	510	33520.417	33520.074	0.342	9.312	9.305	0.007
735	A_1	590		33536.546			9.354		
736	E	591	511	33548.771	33548.662	0.108	9.005	9.002	0.003
737	A_2		512		33578.056			8.601	
738	E	592	513	33585.695	33586.136	-0.440	8.713	8.711	0.003
739	A_2		514		33590.436			8.413	
740	A_1	593		33596.613			9.177		
741	E	594	515	33610.304	33610.742	-0.438	8.715	8.714	0.002
742	A_1	595		33643.759			8.737		
743	E	596	516	33644.016	33644.025	-0.009	8.580	8.566	0.014
744	A_2		517		33656.333			8.463	
745	E	597	518	33659.350	33659.003	0.347	8.922	8.920	0.002
746	A_1	598		33669.196			9.716		
747	E	599	519	33687.320	33687.161	0.159	8.536	8.530	0.006
748	E	600	520	33712.520	33712.255	0.265	8.928	8.938	-0.010
749	A_1	601		33717.896			8.550		
750	E	602	521	33738.878	33738.313	0.565	8.655	8.650	0.005
751	E	603	522	33766.443	33766.177	0.266	8.920	8.919	0.002
752	A_2		523		33774.187			8.787	
753	E	604	524	33791.538	33792.235	-0.697	8.440	8.442	-0.002
754	A_1	605		33801.342			9.100		
755	E	606	525	33807.817	33807.917	-0.100	8.719	8.719	0.000
756	A_2		526		33818.189			8.688	
757	E	607	527	33831.547	33831.385	0.162	8.870	8.865	0.005
758	A_1	608		33833.300			8.985		
759	E	609	528	33855.122	33854.478	0.644	9.352	9.375	-0.022
760	A_1	610		33861.541			9.193		
761	E	611	529	33866.532	33866.103	0.429	8.878	8.862	0.017
762	A_2		530		33889.648			8.307	
763	A_1	612		33892.770			8.622		
764	E	613	531	33913.401	33913.515	-0.114	9.138	9.090	0.048
765	A_2		532		33913.631			8.803	
766	E	614	533	33931.122	33931.283	-0.161	8.267	8.281	-0.014
767	A_2		534		33954.829			8.857	
768	A_1	615		33956.829			9.248		
769	E	616	535	33962.266	33961.269	0.997	8.553	8.558	-0.006
770	A_1	617		33992.400			8.509		
771	A_1	618		34009.164			8.508		
772	E	619	536	34016.883	34016.654	0.229	8.708	8.691	0.016
773	E	620	537	34029.507	34028.707	0.800	8.761	8.774	-0.012
774	A_1	621		34033.467			8.880		
775	A_2		538		34038.754			8.773	
776	E	622	539	34042.726	34042.571	0.155	8.889	8.894	-0.005
777	A_2		540		34058.184			9.044	
778	E	623	541	34065.946	34066.352	-0.406	8.562	8.560	0.002
779	E	624	542	34077.943	34078.154	-0.212	8.482	8.799	-0.317
780	E	625	543	34079.265	34078.937	0.328	8.858	8.541	0.318
781	A_2		544		34082.293			8.832	
782	E	626	545	34103.885	34103.639	0.246	9.369	9.368	0.001
783	E	627	546	34121.041	34121.179	-0.138	7.852	7.859	-0.008
784	A_1	628		34126.874			9.234		
785	A_2		547		34129.533			8.789	
786	A_1	629		34148.197			7.527		
787	E	630	548	34158.381	34157.974	0.407	9.044	9.042	0.002
788	A_1	631		34159.421			9.082		
789	A_1	632		34172.314			8.889		

continued...

Table A.1: *...continued*

N_s	Γ	N_e	N_o	E_e	E_o	$E_e - E_o$	C_e	C_o	$C_e - C_o$
790	E	633	549	34176.904	34176.872	0.033	8.865	8.853	0.012
791	A_2		550		34189.886			8.767	
792	E	634	551	34201.937	34201.897	0.040	8.790	8.789	0.001
793	E	635	552	34227.373	34227.365	0.008	8.870	8.867	0.003
794	E	636	553	34239.914	34239.410	0.504	8.857	8.860	-0.003
795	A_1	637		34263.257			9.554		
796	E	638	554	34274.618	34274.875	-0.257	8.342	8.341	0.001
797	A_2		555		34294.720			8.199	
798	E	639	556	34301.180	34300.556	0.624	8.994	9.001	-0.007
799	A_1	640		34313.672			8.385		
800	E	641	557	34321.640	34321.286	0.354	8.712	8.707	0.005
801	A_2		558		34326.376			6.976	
802	A_1	642		34334.312			7.175		
803	E	643	559	34356.618	34356.809	-0.191	8.249	8.262	-0.013
804	A_1	644		34371.402			8.398		
805	A_2		560		34377.121			8.583	
806	E	645	561	34383.147	34382.969	0.178	7.565	7.562	0.003
807	E	646	562	34412.583	34411.860	0.723	8.377	8.376	0.001
808	E	647	563	34425.624	34425.287	0.337	8.749	8.766	-0.017
809	E	648	564	34440.983	34440.495	0.489	7.946	7.933	0.013
810	A_1	649		34458.531			7.661		
811	A_2		565		34473.004			7.492	
812	E	650	566	34473.515	34473.589	-0.074	7.471	8.435	-0.964
813	A_2		567		34479.869			7.818	
814	E	651	568	34488.121	34487.642	0.479	8.265	8.248	0.016
815	A_1	652		34509.045			8.657		
816	E	653	569	34514.299	34514.257	0.041	7.878	7.873	0.005
817	E	654	570	34529.998	34530.019	-0.021	8.574	8.600	-0.026
818	A_1	655		34530.760			8.730		
819	E	656	571	34537.155	34537.276	-0.121	7.986	8.081	-0.094
820	A_2		572		34537.704			8.085	
821	E	657	573	34560.594	34560.576	0.018	7.971	7.974	-0.002
822	A_1	658		34578.624			8.561		
823	E	659	574	34596.011	34595.597	0.414	7.909	7.911	-0.002
824	A_2		575		34597.913			6.924	
825	E	660	576	34606.788	34606.887	-0.100	8.727	8.730	-0.003
826	A_1	661		34619.147			8.365		
827	E	662	577	34633.690	34634.262	-0.573	8.163	8.170	-0.007
828	A_2		578		34645.934			7.864	
829	A_1	663		34646.539			7.650		
830	A_1	664		34667.981			8.498		
831	E	665	579	34668.158	34668.009	0.148	8.515	8.253	0.263
832	E	666	580	34677.211	34677.667	-0.456	8.594	8.568	0.026
833	A_1	667		34685.077			7.562		
834	A_2		581		34694.164			6.875	
835	A_2		582		34711.831			8.461	
836	E	668	583	34716.850	34716.923	-0.073	5.704	5.684	0.019
837	E	669	584	34726.958	34727.178	-0.220	8.482	8.467	0.014
838	E	670	585	34744.139	34744.512	-0.373	6.572	6.505	0.067
839	A_1	671		34745.815			8.858		
840	E	672	586	34750.744	34751.210	-0.466	8.128	8.233	-0.105
841	E	673	587	34763.433	34762.543	0.891	8.679	8.700	-0.021
842	A_1	674		34769.659			6.759		
843	E	675	588	34790.860	34790.822	0.038	7.751	7.705	0.045
844	E	676	589	34795.457	34795.421	0.035	7.840	7.874	-0.034
845	A_2		590		34808.455			7.461	
846	A_1	677		34811.712			6.048		
847	A_2		591		34812.020			7.816	
848	E	678	592	34823.961	34823.928	0.033	7.227	7.239	-0.011
849	A_1	679		34825.222			7.343		
850	A_2		593		34834.888			8.548	
851	E	680	594	34836.529	34836.449	0.080	5.200	5.300	-0.099
852	A_1	681		34852.006			6.085		
853	E	682	595	34858.105	34857.931	0.174	6.825	6.832	-0.007
854	E	683	596	34865.425	34865.371	0.054	5.606	5.600	0.005
855	E	684	597	34882.977	34882.980	-0.002	6.483	6.540	-0.057
856	A_1	685		34891.348			1.941		
857	A_2		598		34897.104			8.405	
858	A_1	686		34897.999			7.423		
859	E	687	599	34901.023	34904.624	-3.601	2.371	3.042	-0.671

Appendix B

Wave functions of H_3^+

The probability amplitude of the vibrational wave functions of H_3^+ are plotted in Jacobi coordinates. For each state two cross-sections are taken, on the left θ and R are varied with r kept constant, on the right R and r are varied for constant θ. The cross-sections are chosen so as to pass through the maximum of the probability amplitude. The dashed vertical line on the other section indicates the position of the cut. The states were calculated in a Radau coordinate basis and therefore are transformed to Jacobi coordinates before plotting. The embedding that gives the Jacobi R splitting the two Radau radial coordinates is used. Contours are plotted for every ten percent of the probability amplitude relative to the maximum. The red contour indicates the classical turning point of the potential for the same energy. Each wavefunction is labelled as *even* or *odd* depending upon the vibrational basis parity s, the state number N_e (N_o) for even (odd) states, and the energy of the band origin. The basis extends to about 20 a_0 in the Jacobi R coordinate however this is only for the described embedding, the other two embeddings give a maximum for Jacobi R of about 15 a_0, therefore the plots are truncated at $R = 15\ a_0$.

Odd parity states 571 to 599 (figure B.43) are not plotted in exactly the same fashion. The cross-sections of these plots do not pass precisely through the maximum probability amplitude, they are taken at $r = 1.4a_0$ and $\theta = 90°$. This is to demonstrate their long range like nature as some of these states are the AVS states identified in chapter 7. Within the Jacobi coordinate embedding described above the odd parity states have a node at $\theta = 90°$. To demonstrate amplitude at long range the plots in figure B.43 are therefore obtained from an alternative embedding of the Jacobi coordinates.

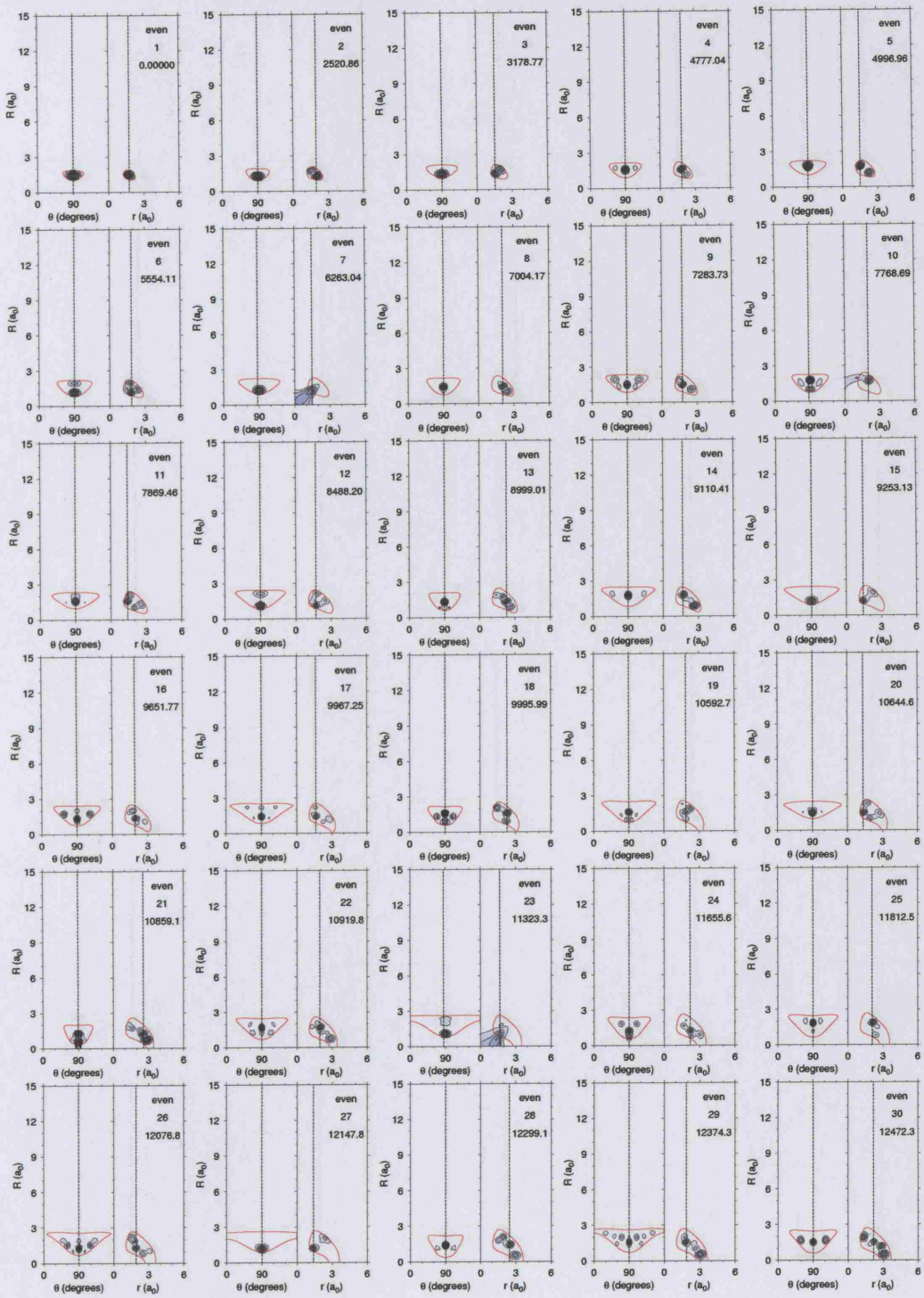

Figure B.1: Wave functions of H_3^+, even parity states 1 to 30.

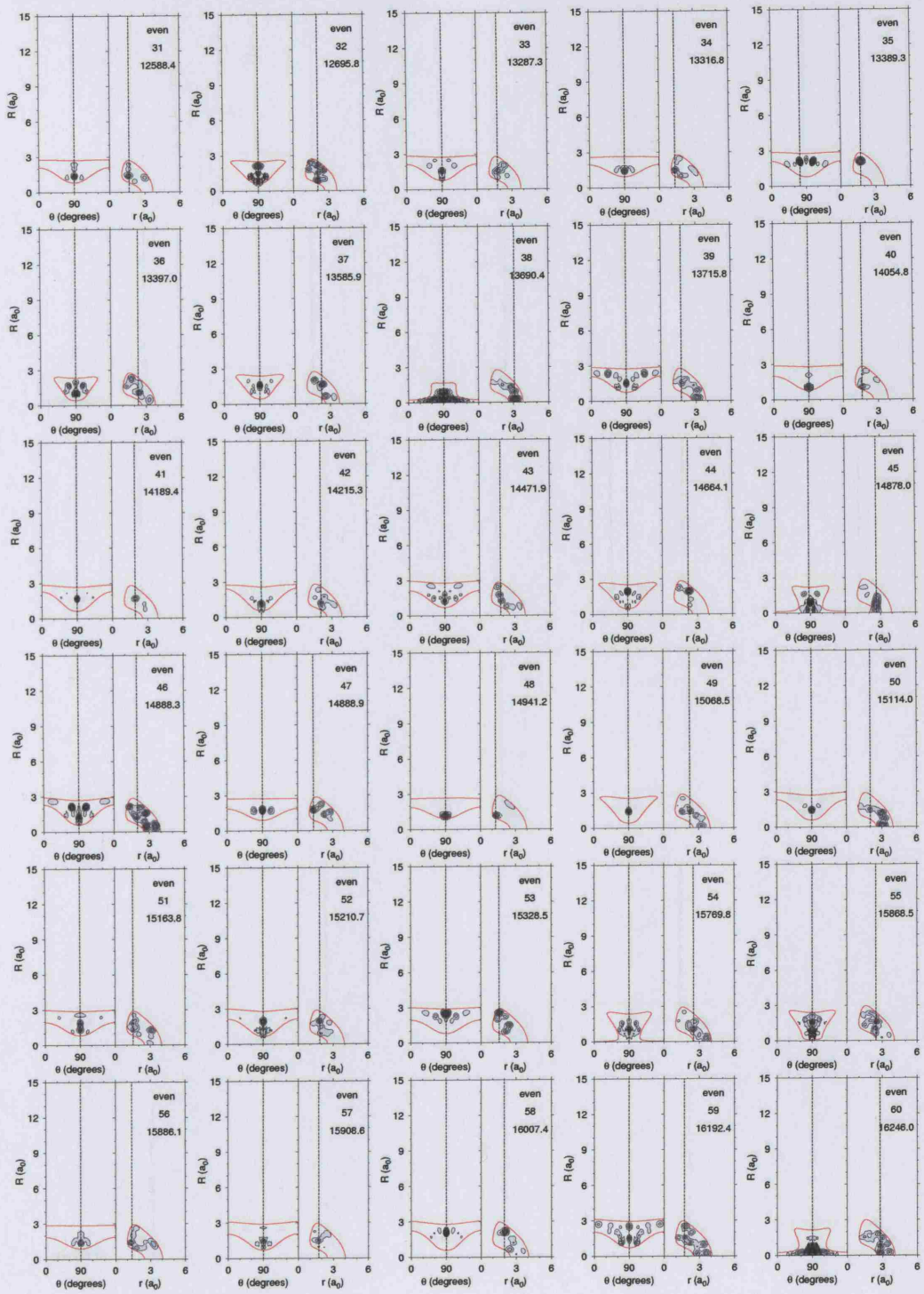

Figure B.2: Wave functions of H_3^+, even parity states 31 to 60.

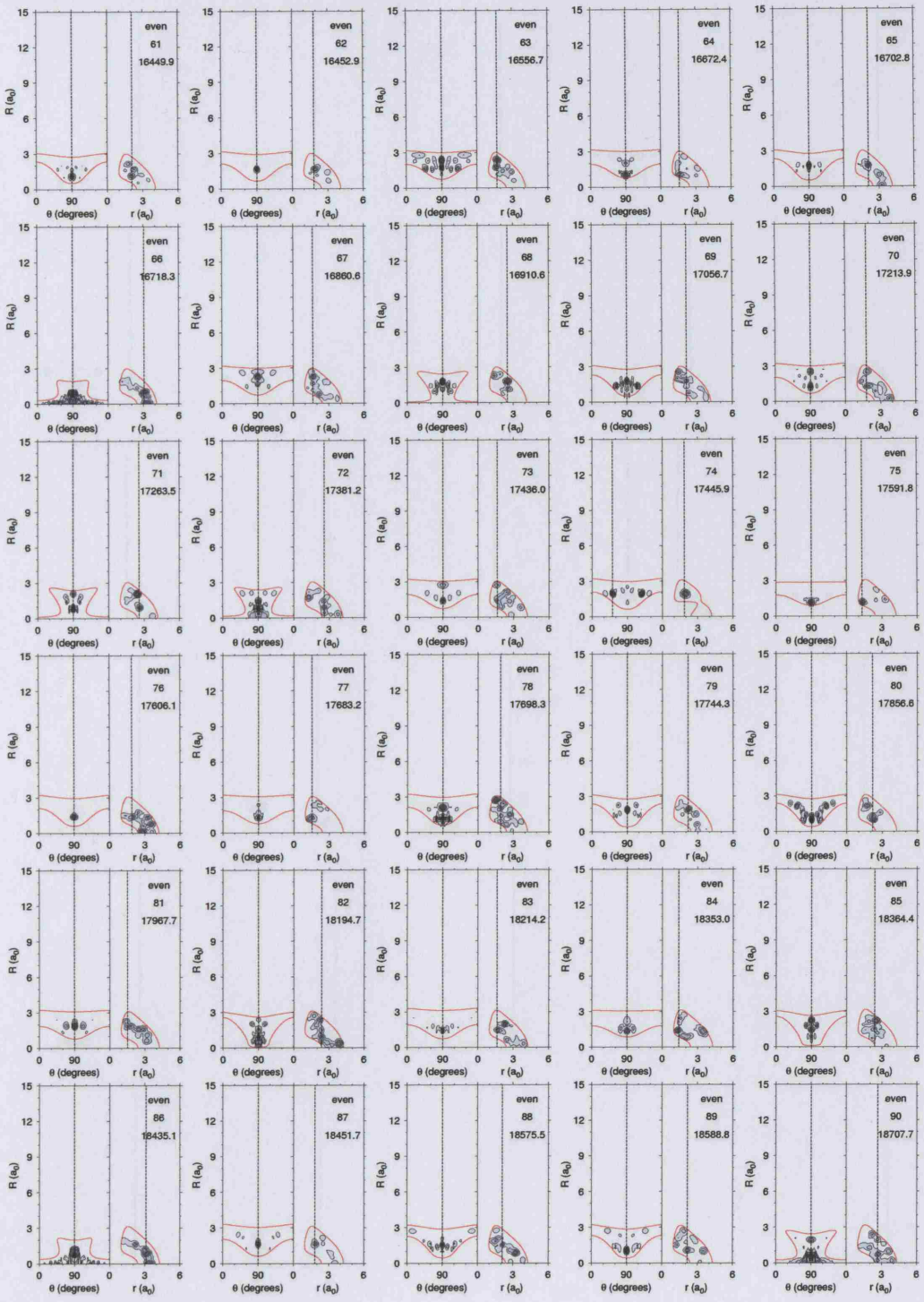

Figure B.3: Wave functions of H_3^+, even parity states 61 to 90.

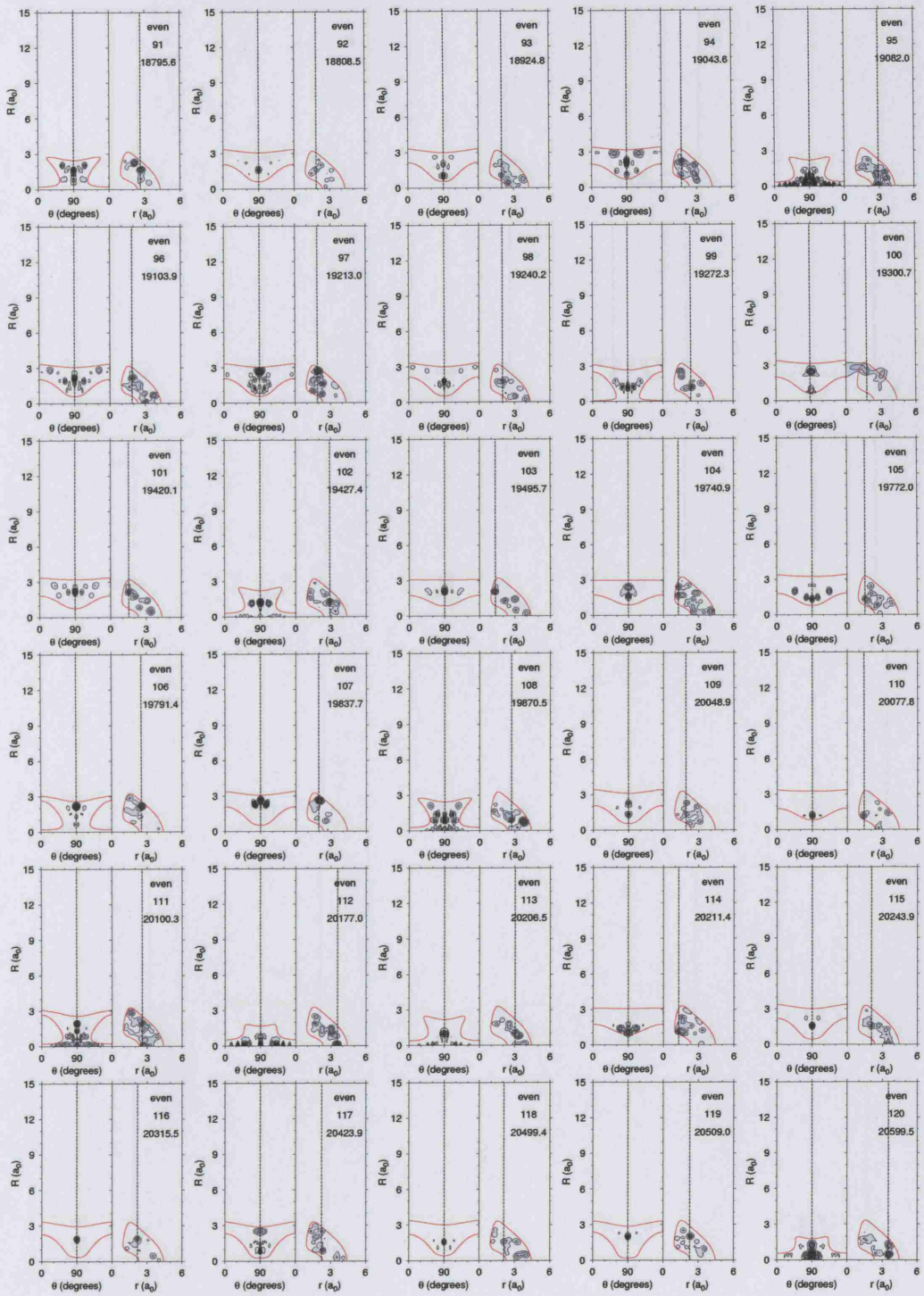

Figure B.4: Wave functions of H_3^+, even parity states 91 to 120.

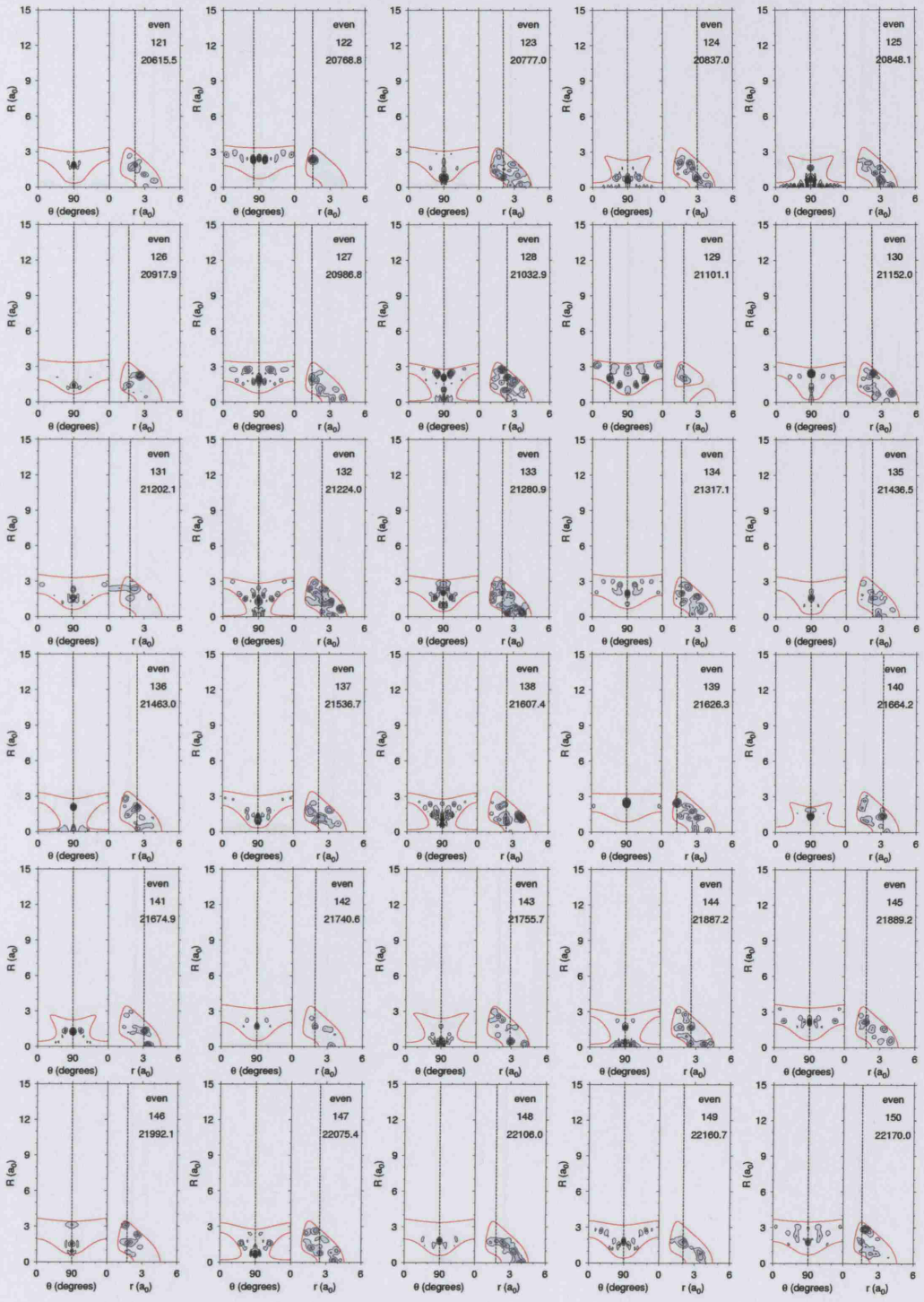

Figure B.5: Wave functions of H_3^+, even parity states 121 to 150.

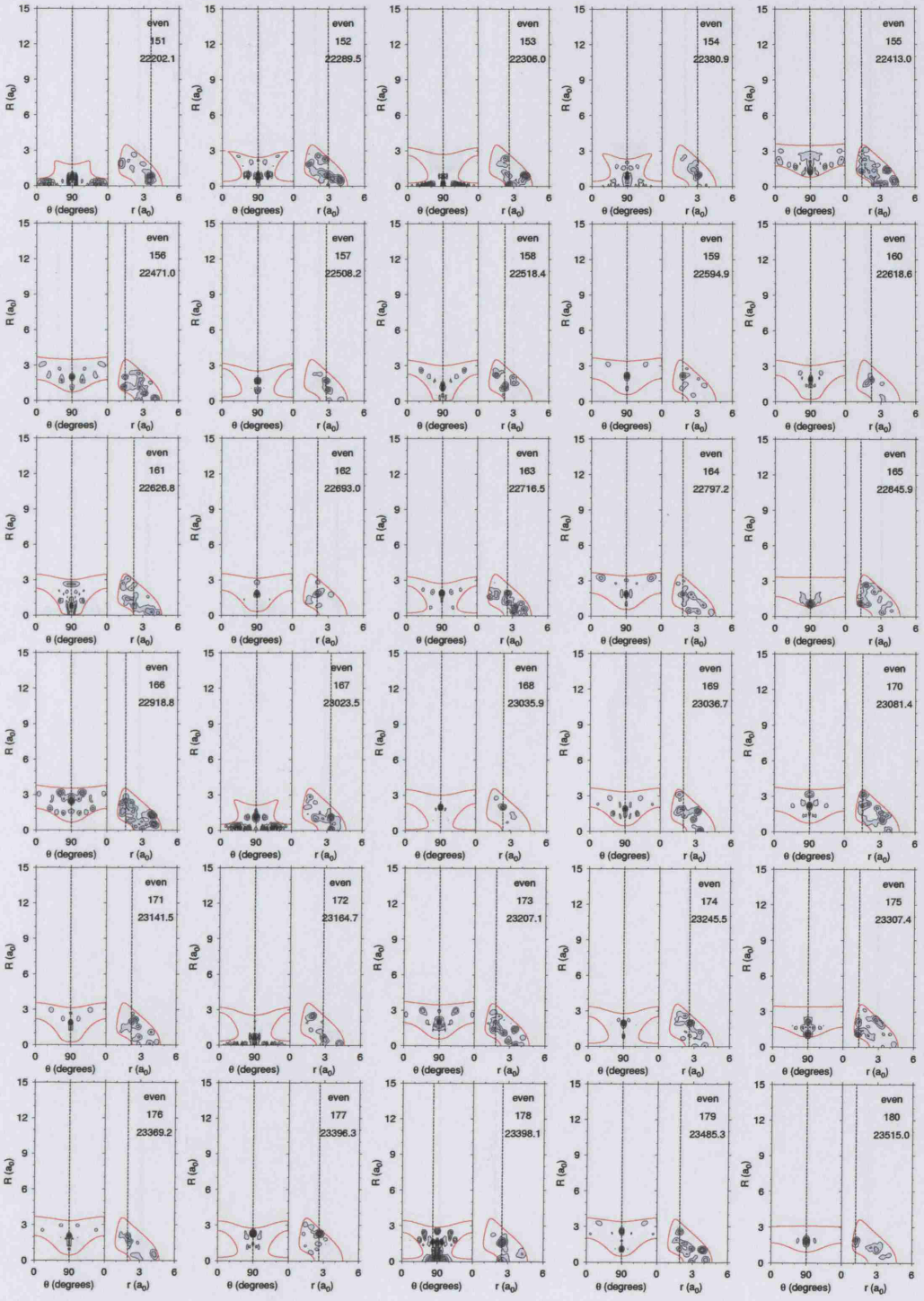

Figure B.6: Wave functions of H_3^+, even parity states 151 to 180.

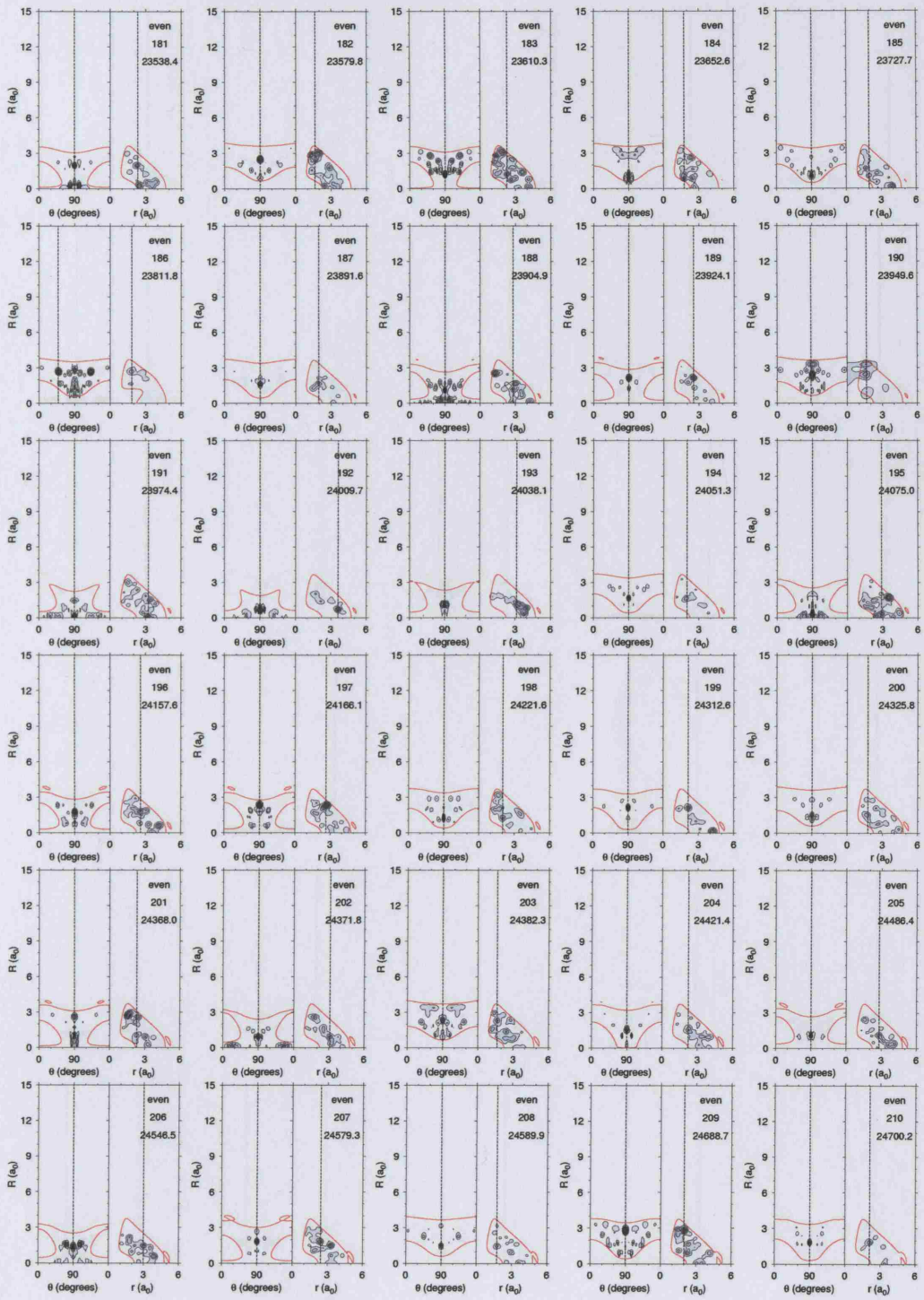

Figure B.7: Wave functions of H_3^+, even parity states 181 to 210.

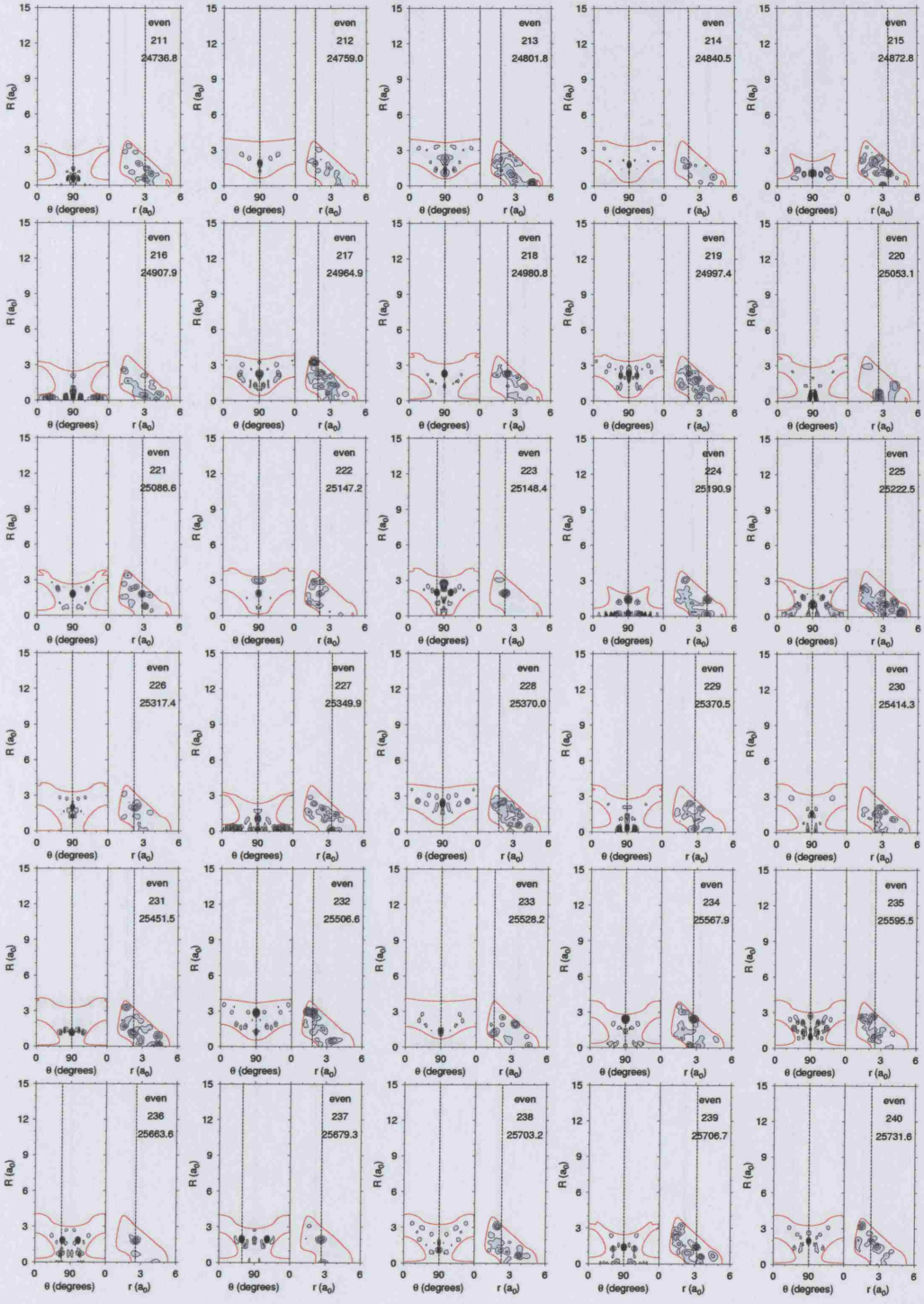

Figure B.8: Wave functions of H_3^+, even parity states 211 to 240.

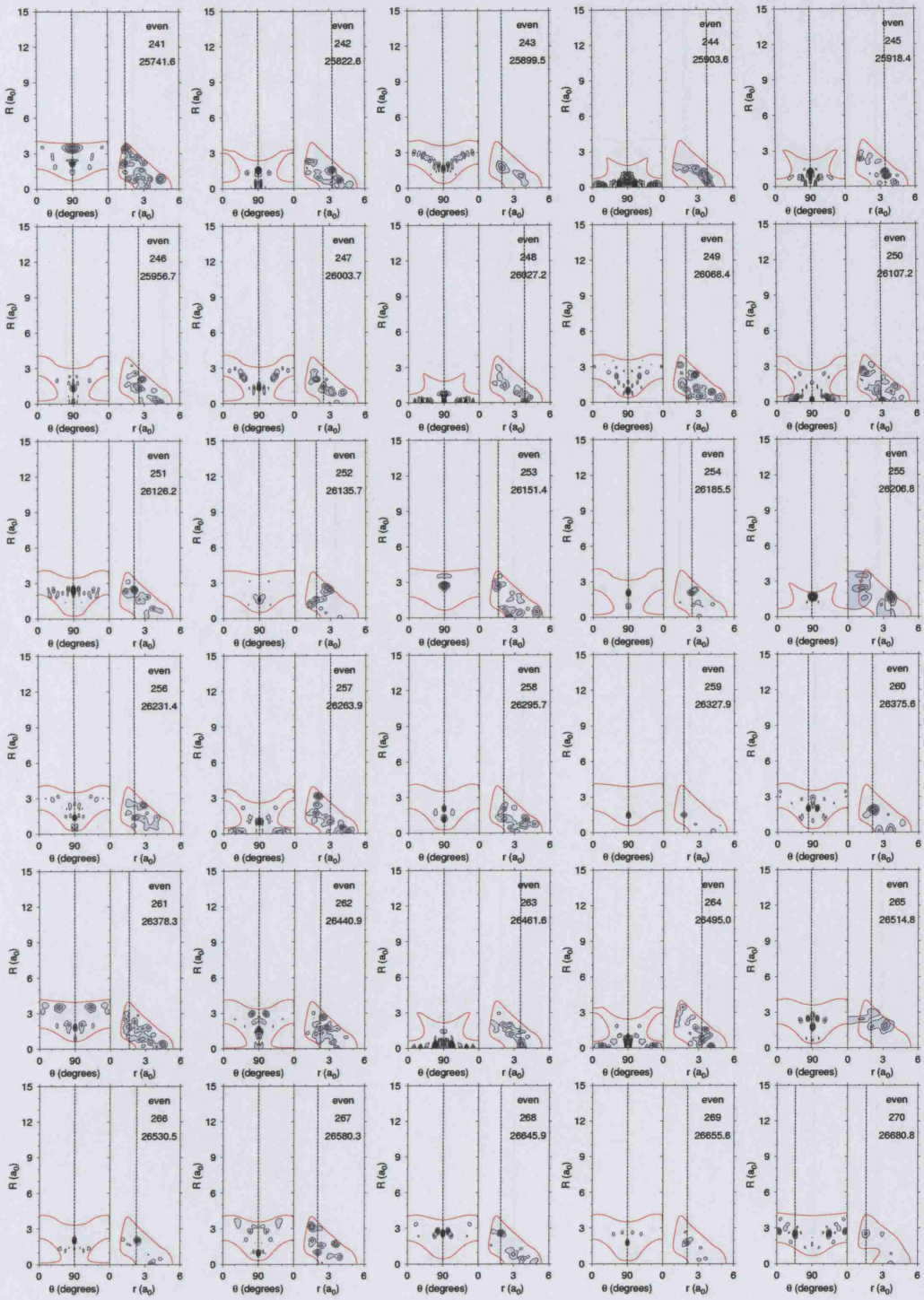

Figure B.9: Wave functions of H_3^+, even parity states 241 to 270.

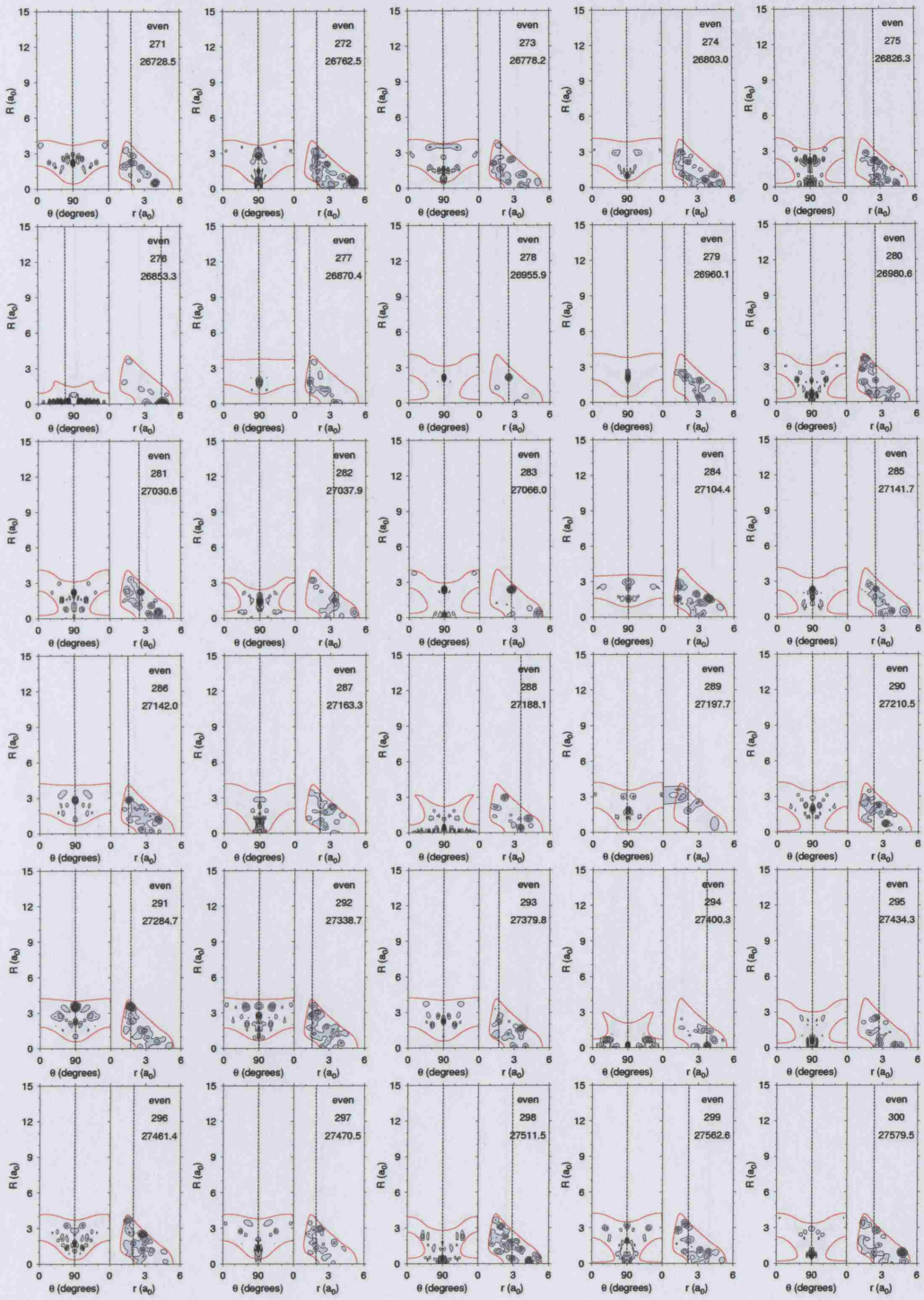

Figure B.10: Wave functions of H_3^+, even parity states 271 to 300.

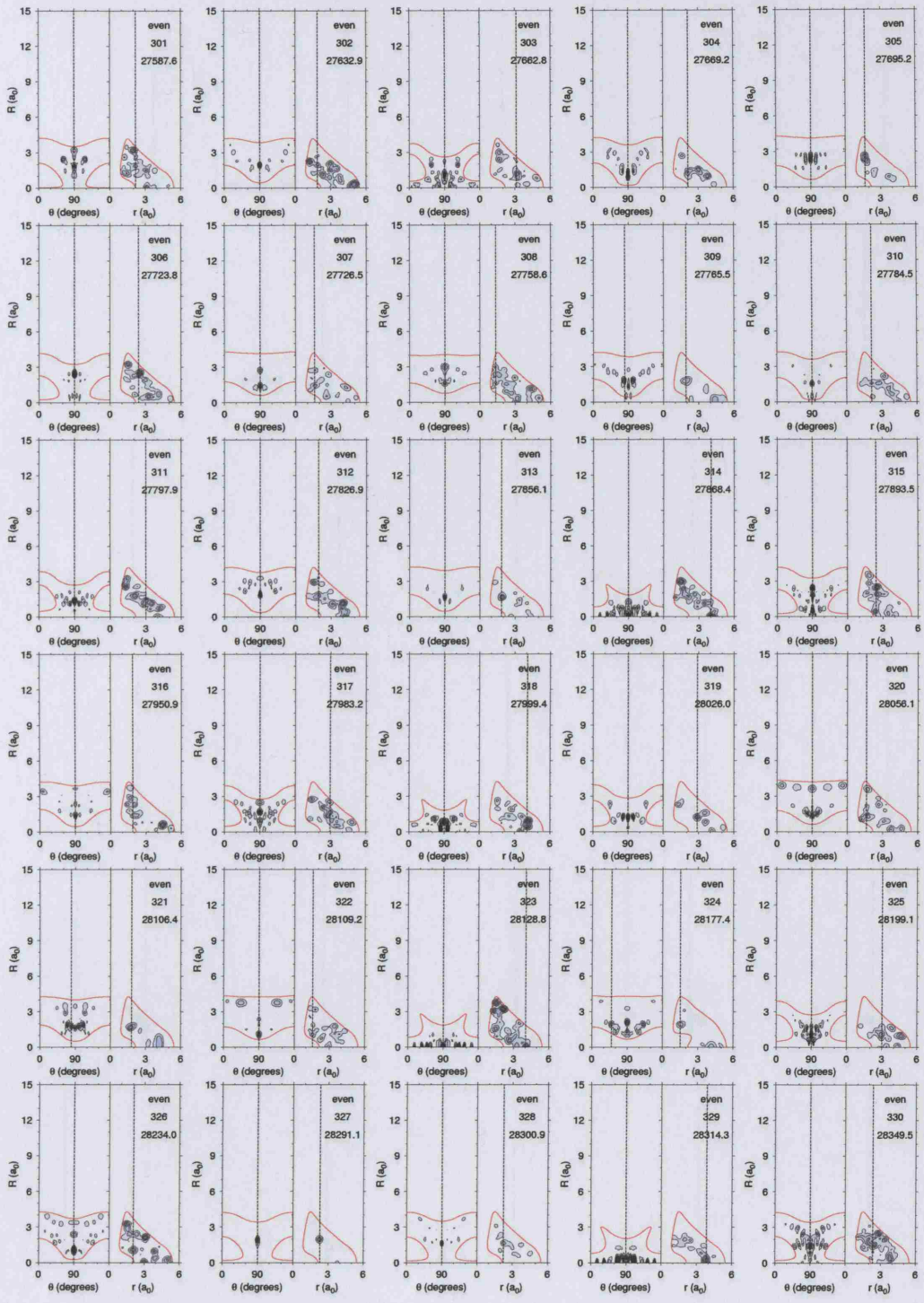

Figure B.11: Wave functions of H_3^+, even parity states 301 to 330.

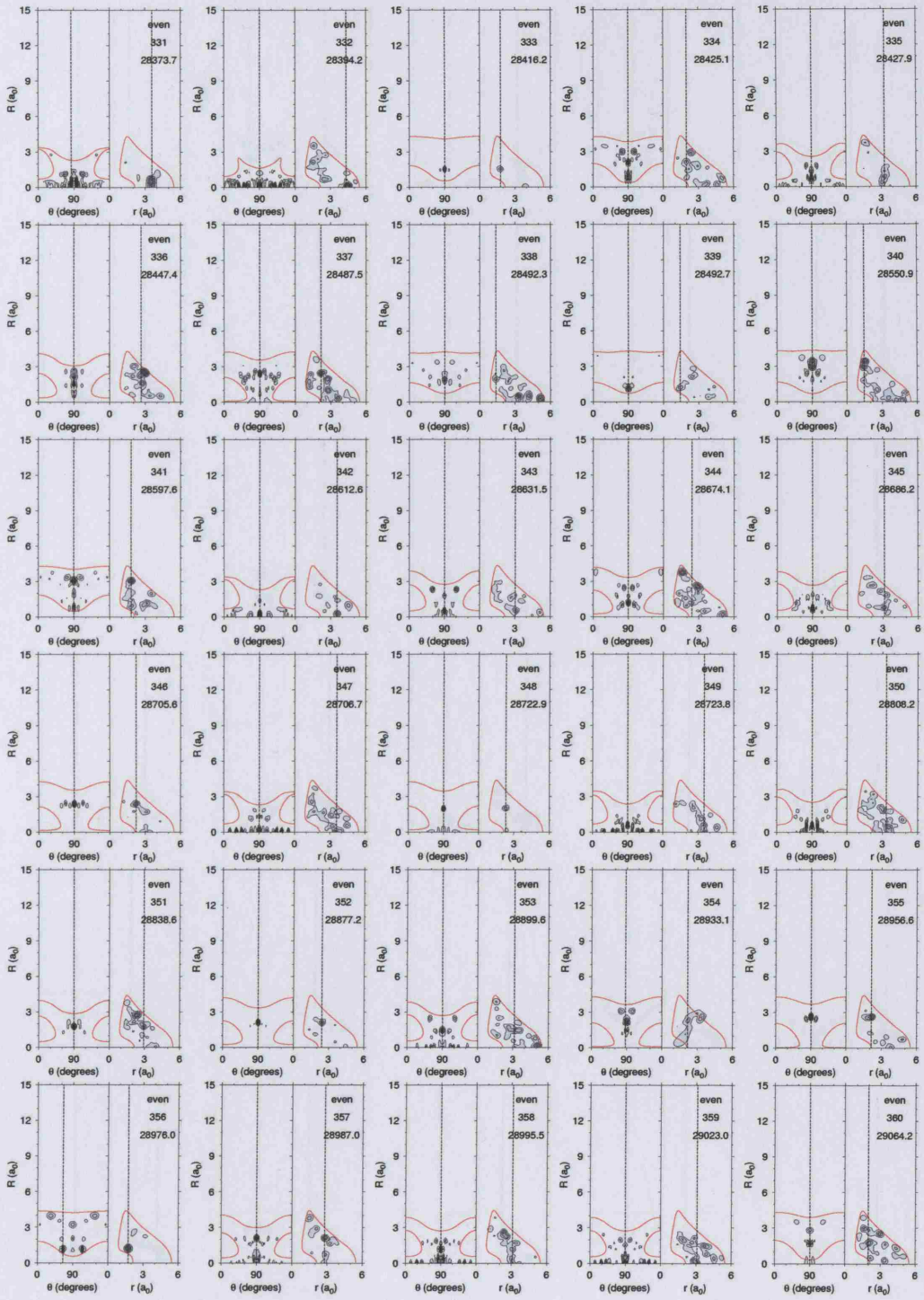

Figure B.12: Wave functions of H_3^+, even parity states 331 to 360.

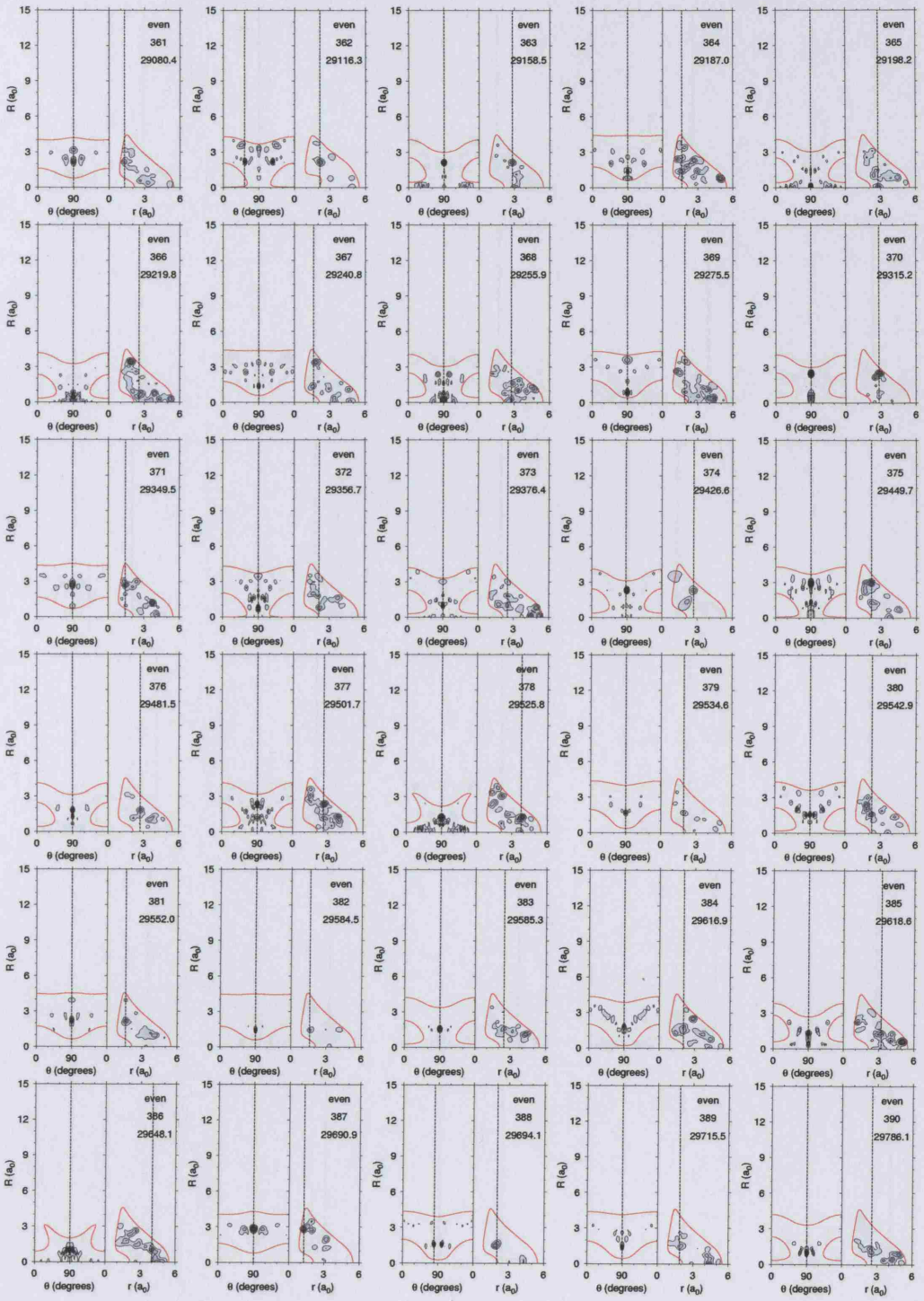

Figure B.13: Wave functions of H_3^+, even parity states 361 to 390.

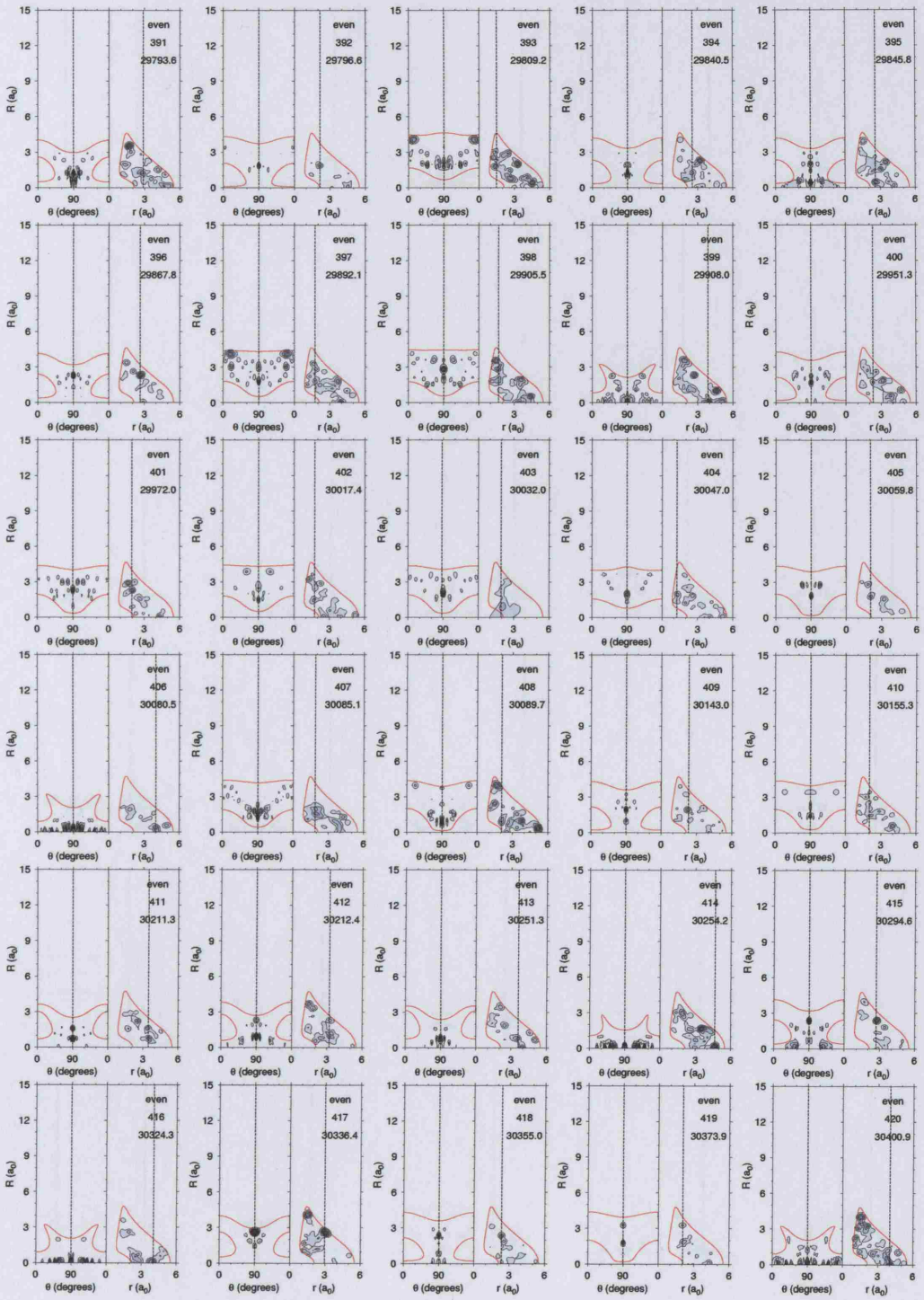

Figure B.14: Wave functions of H_3^+, even parity states 391 to 420.

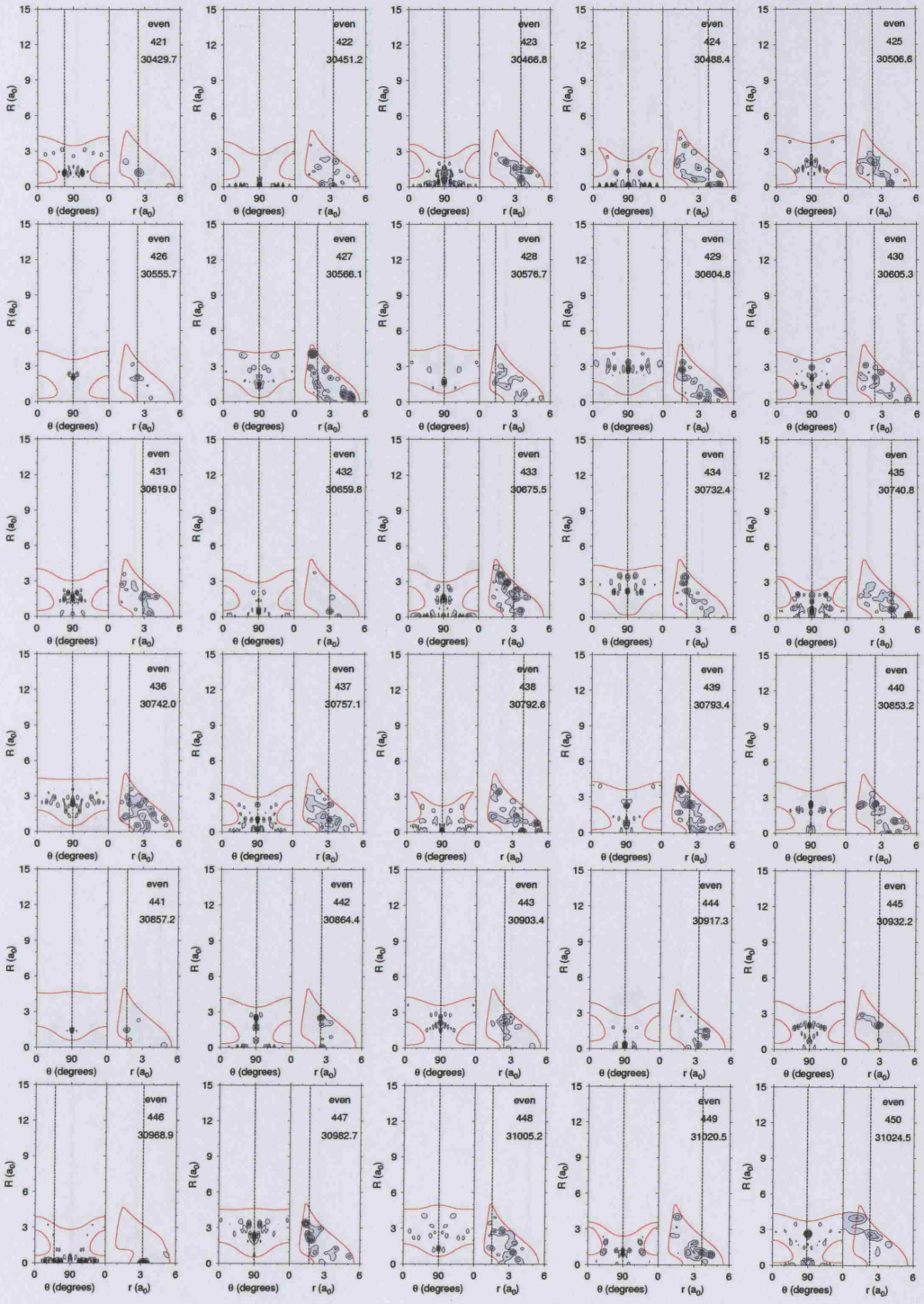

Figure B.15: Wave functions of H_3^+, even parity states 421 to 450.

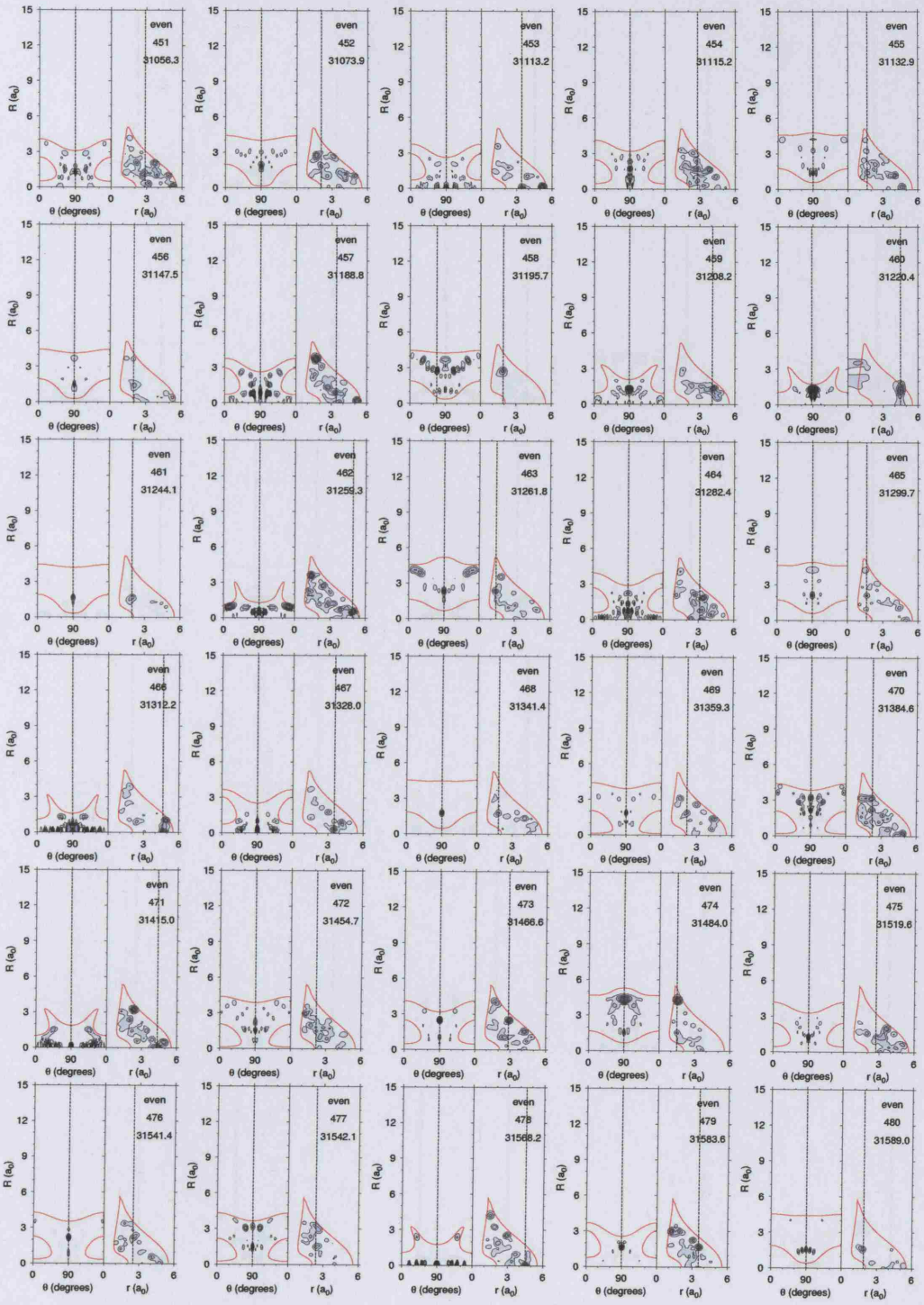

Figure B.16: Wave functions of H_3^+, even parity states 451 to 480.

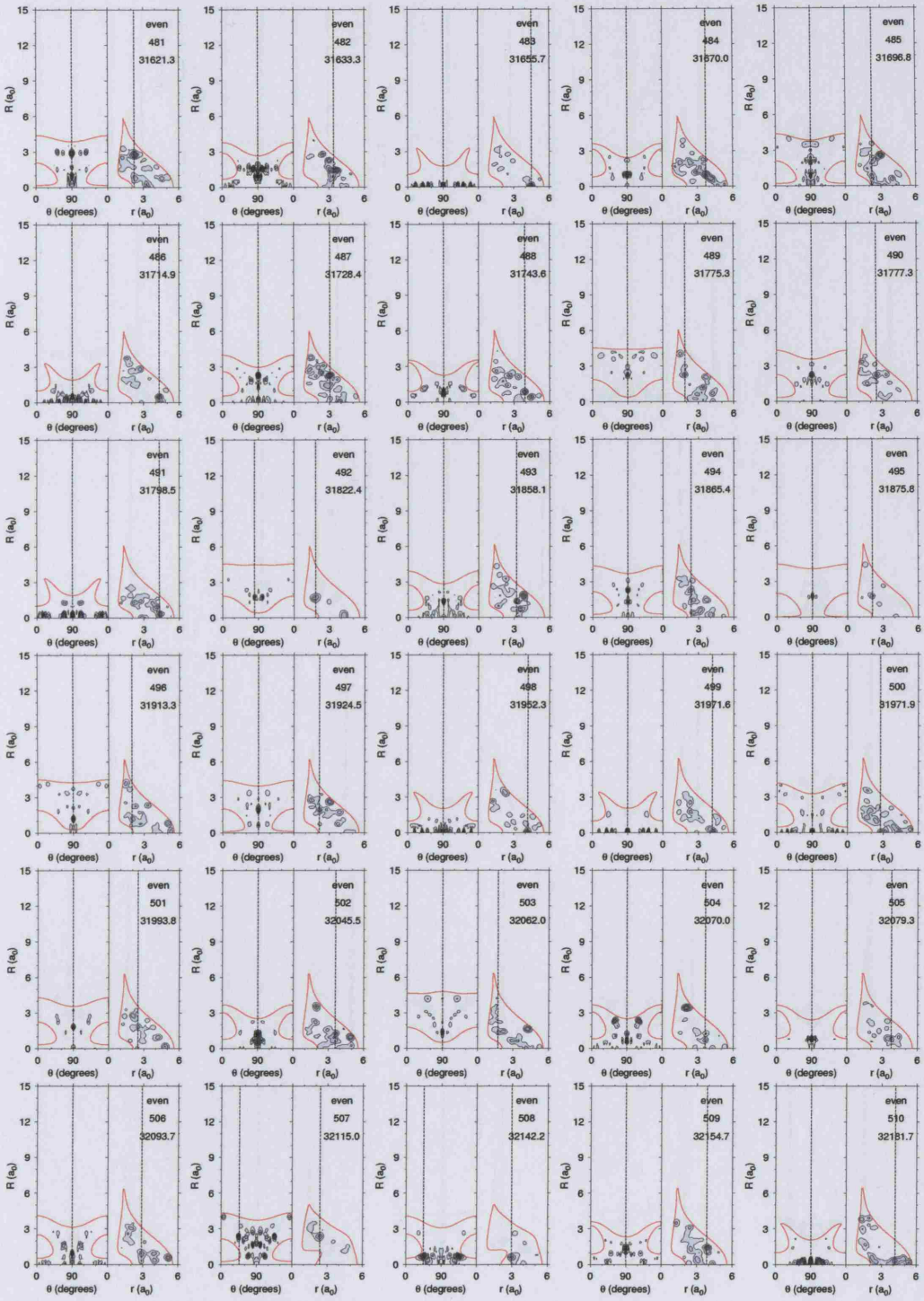

Figure B.17: Wave functions of H_3^+, even parity states 481 to 510.

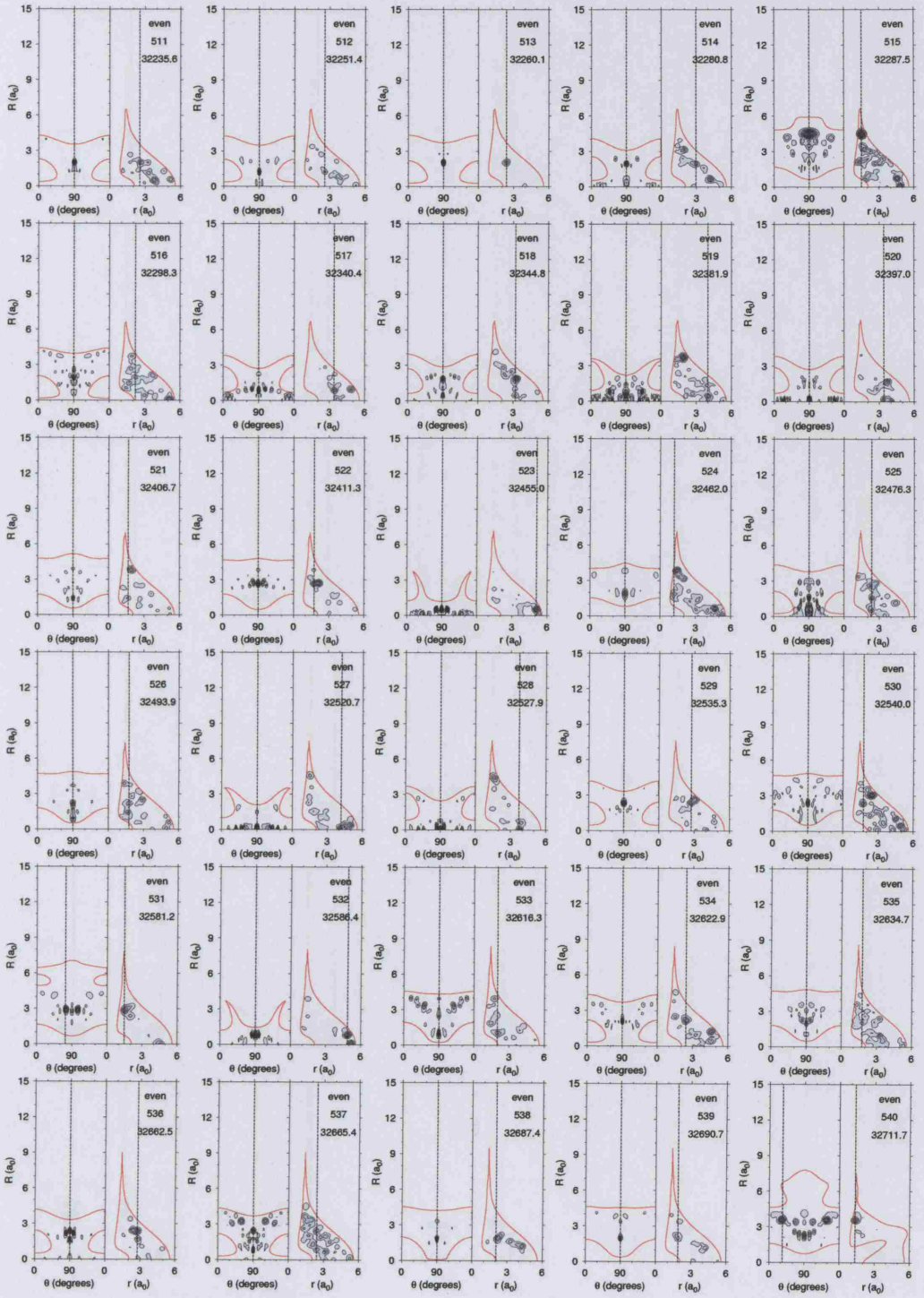

Figure B.18: Wave functions of H_3^+, even parity states 511 to 540.

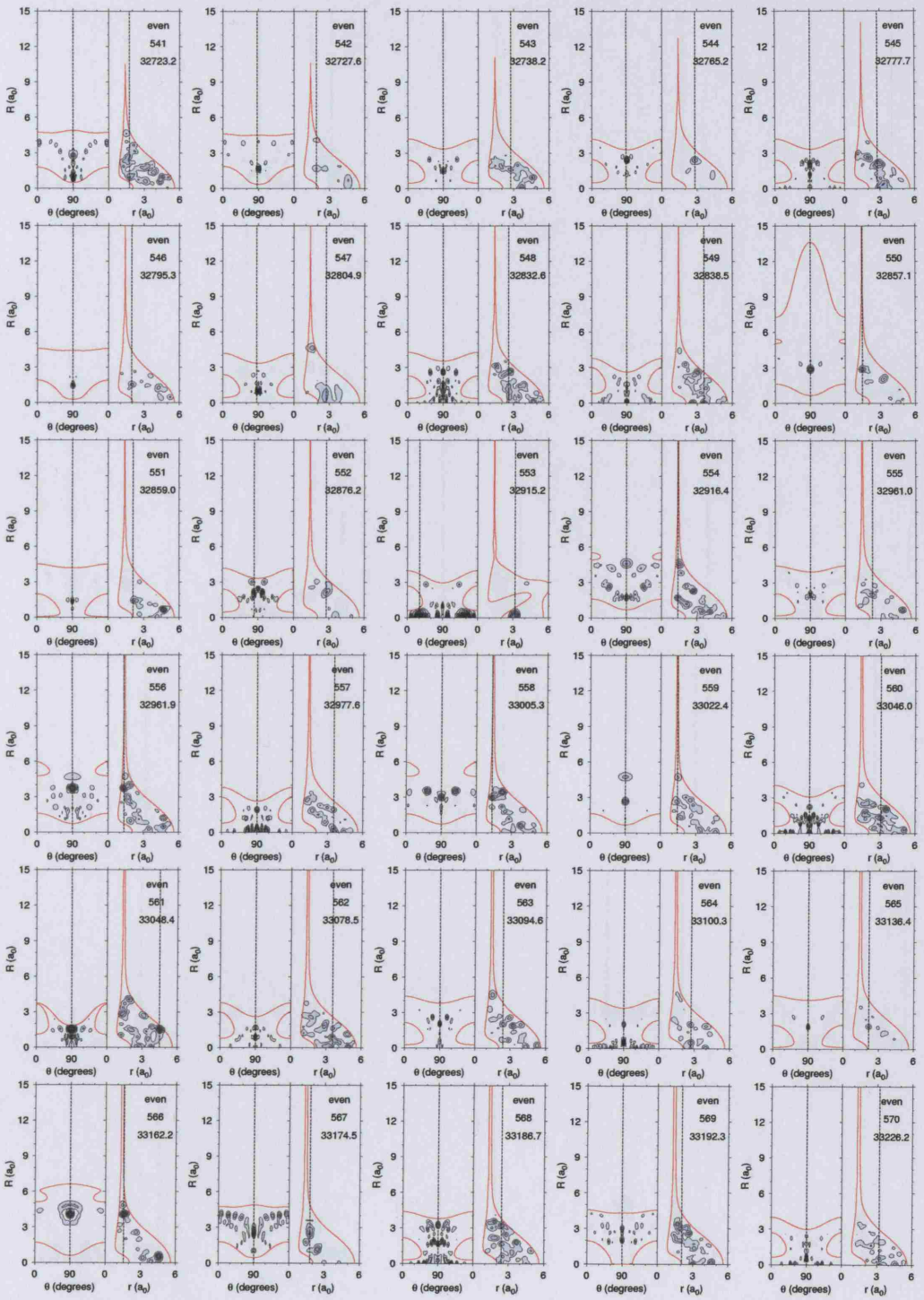

Figure B.19: Wave functions of H_3^+, even parity states 541 to 570.

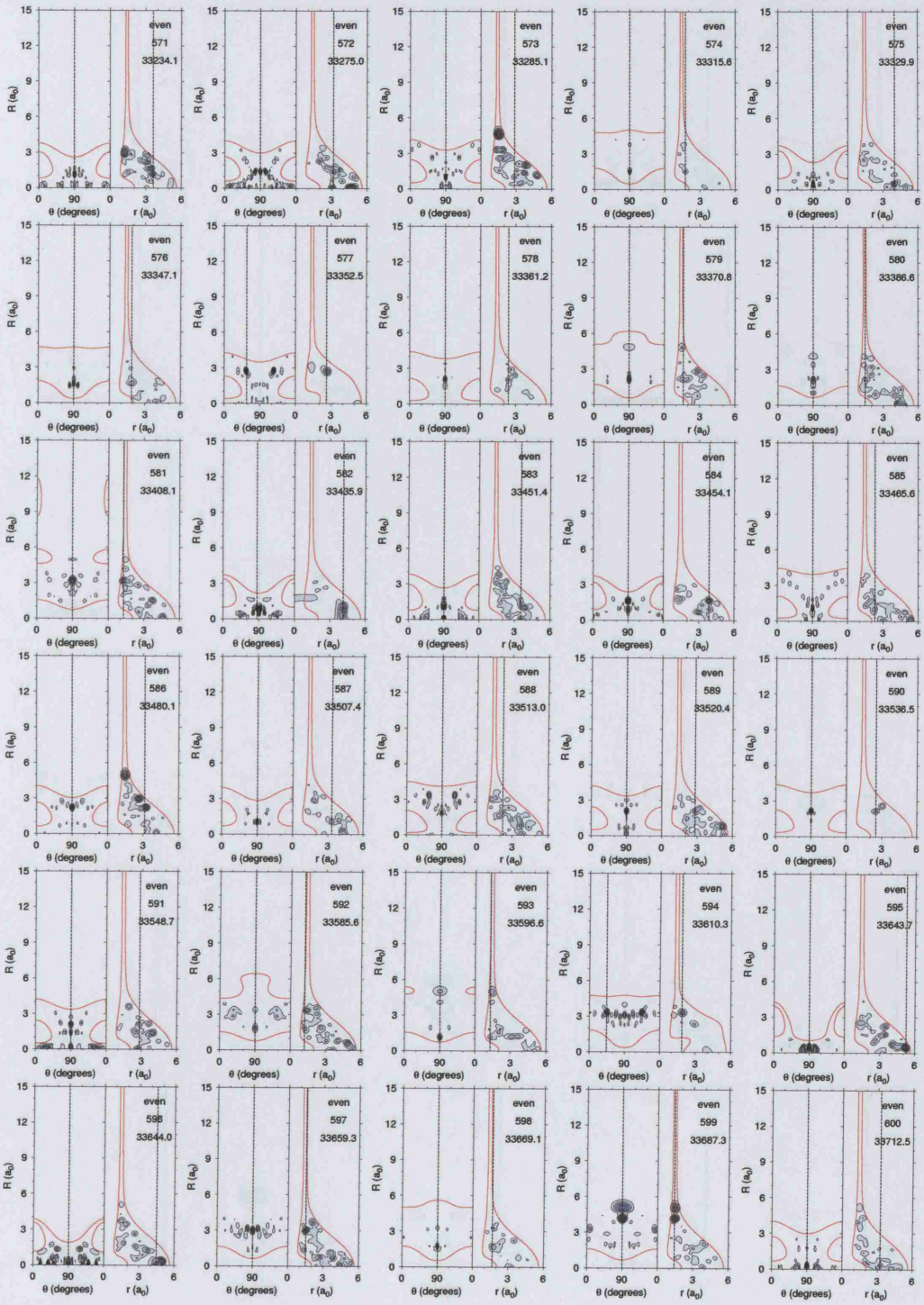

Figure B.20: Wave functions of H_3^+, even parity states 571 to 600.

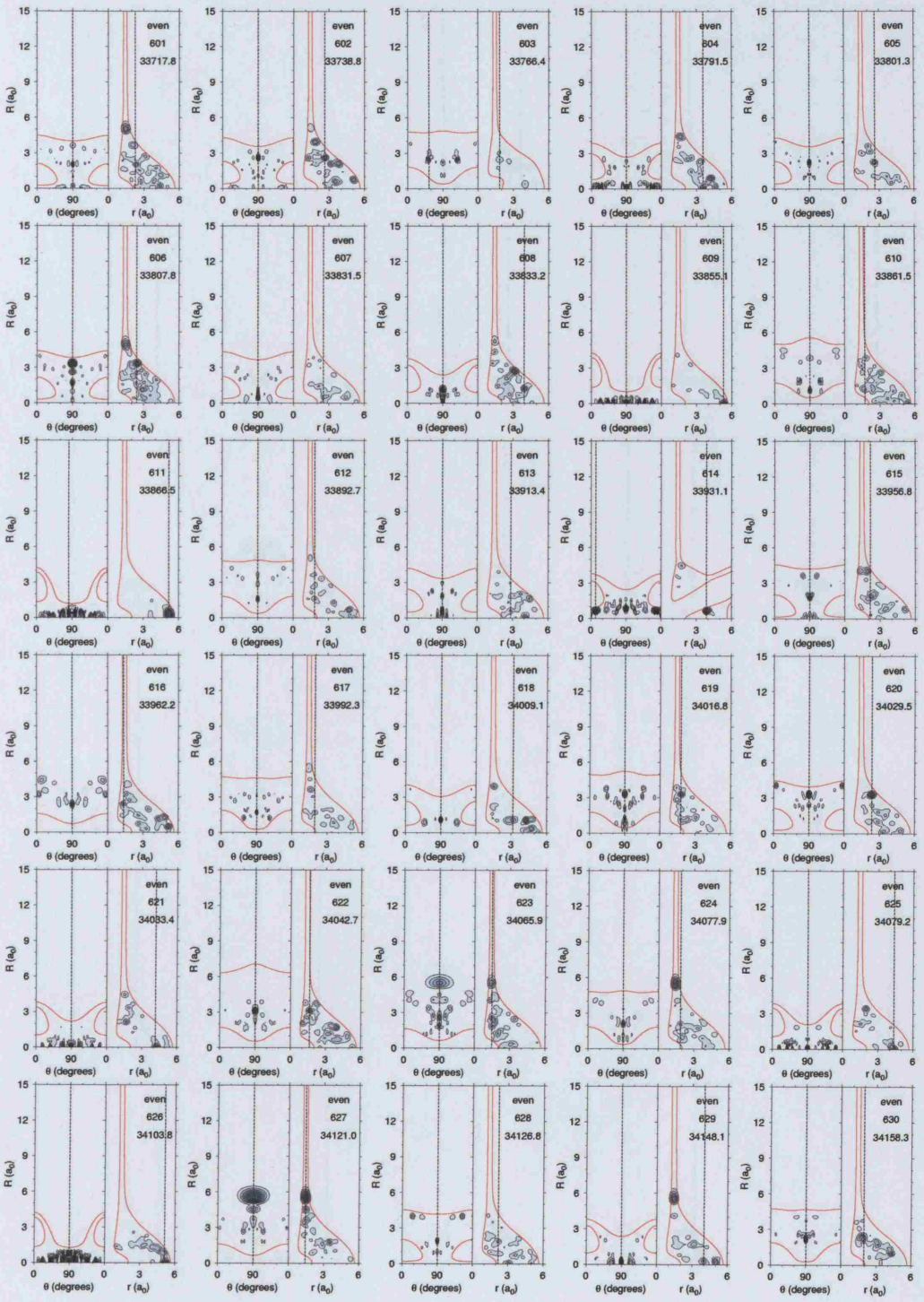

Figure B.21: Wave functions of H_3^+, even parity states 601 to 630.

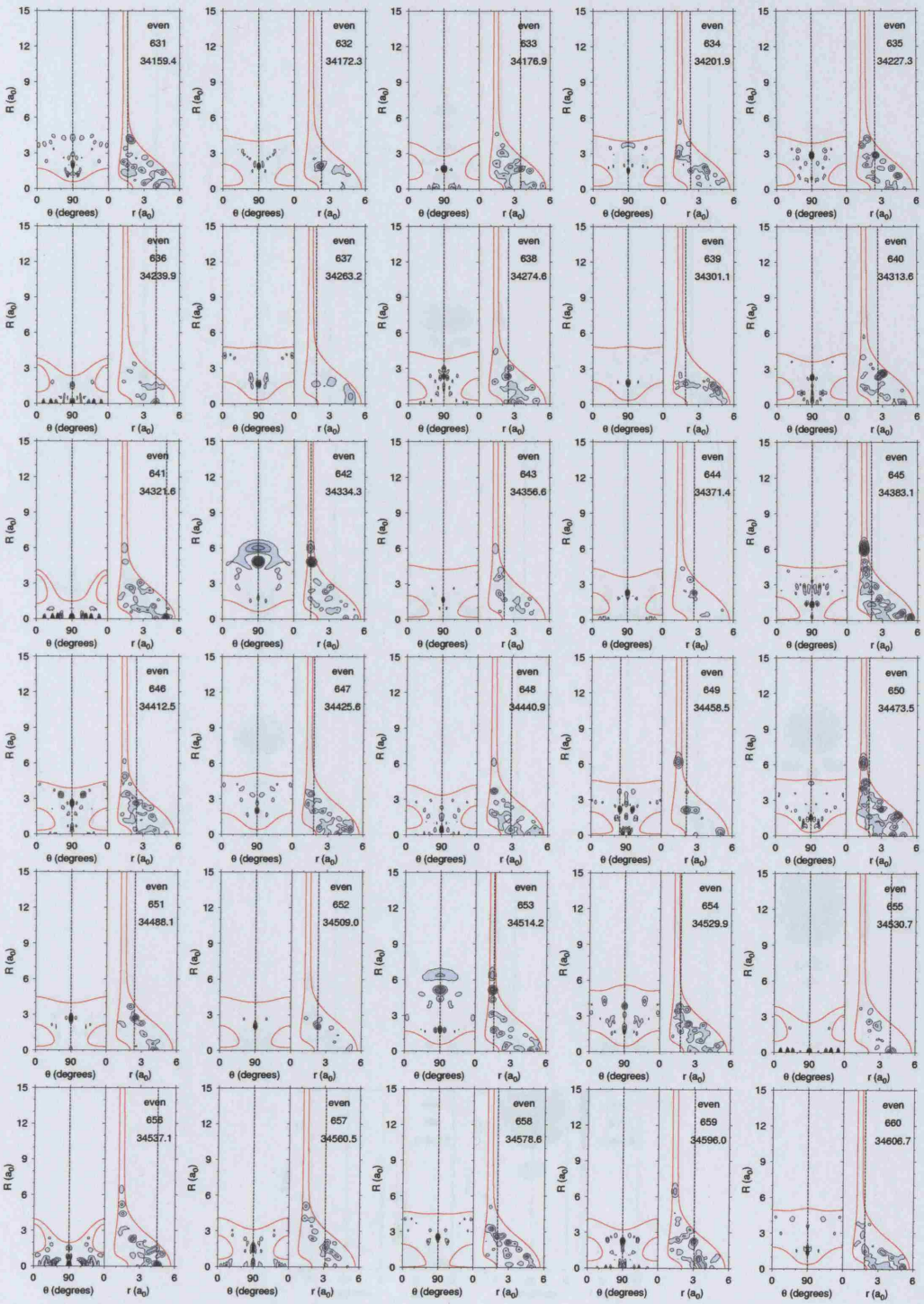

Figure B.22: Wave functions of H_3^+, even parity states 631 to 660.

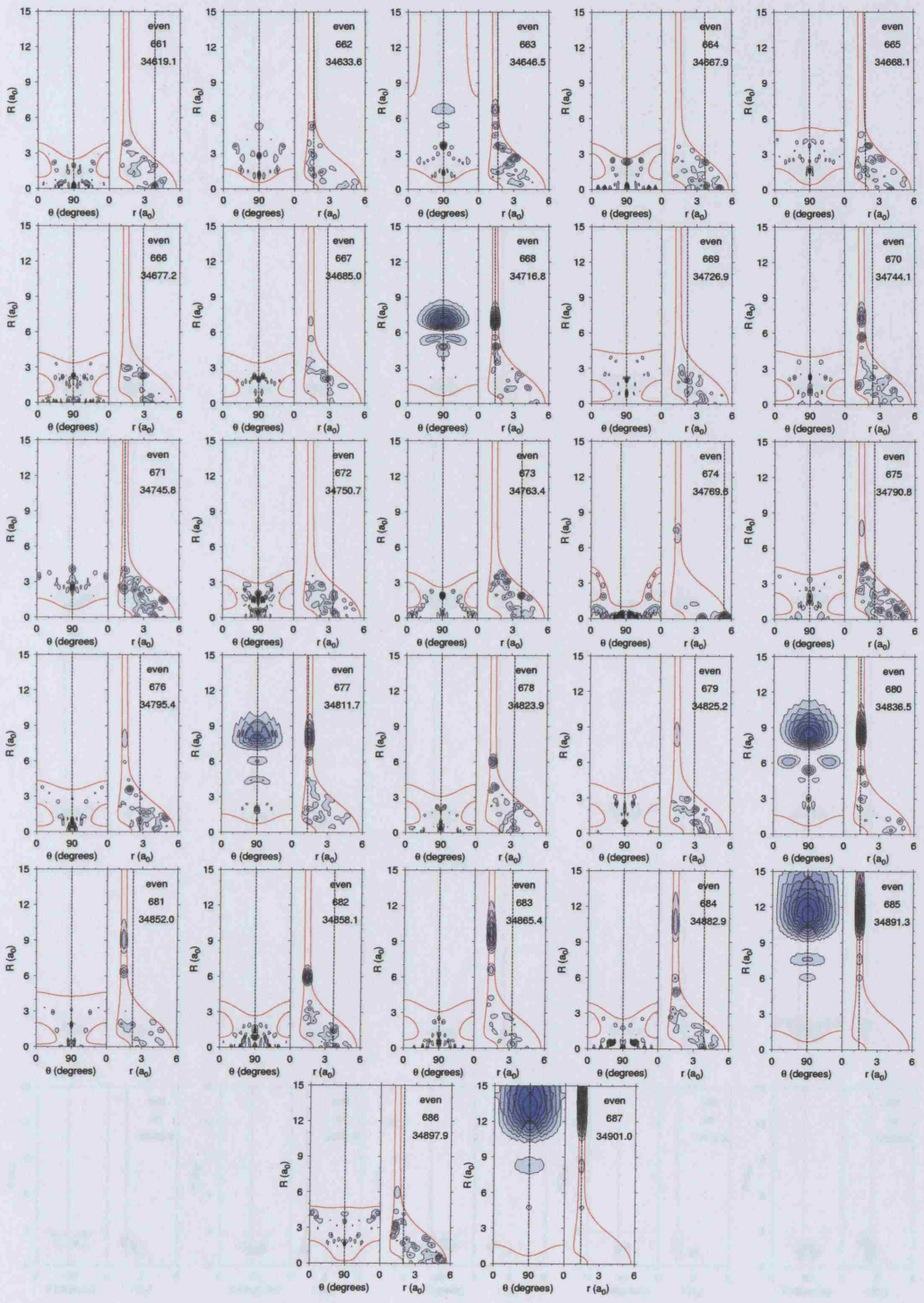

Figure B.23: Wave functions of H_3^+, even parity states 661 to 687.

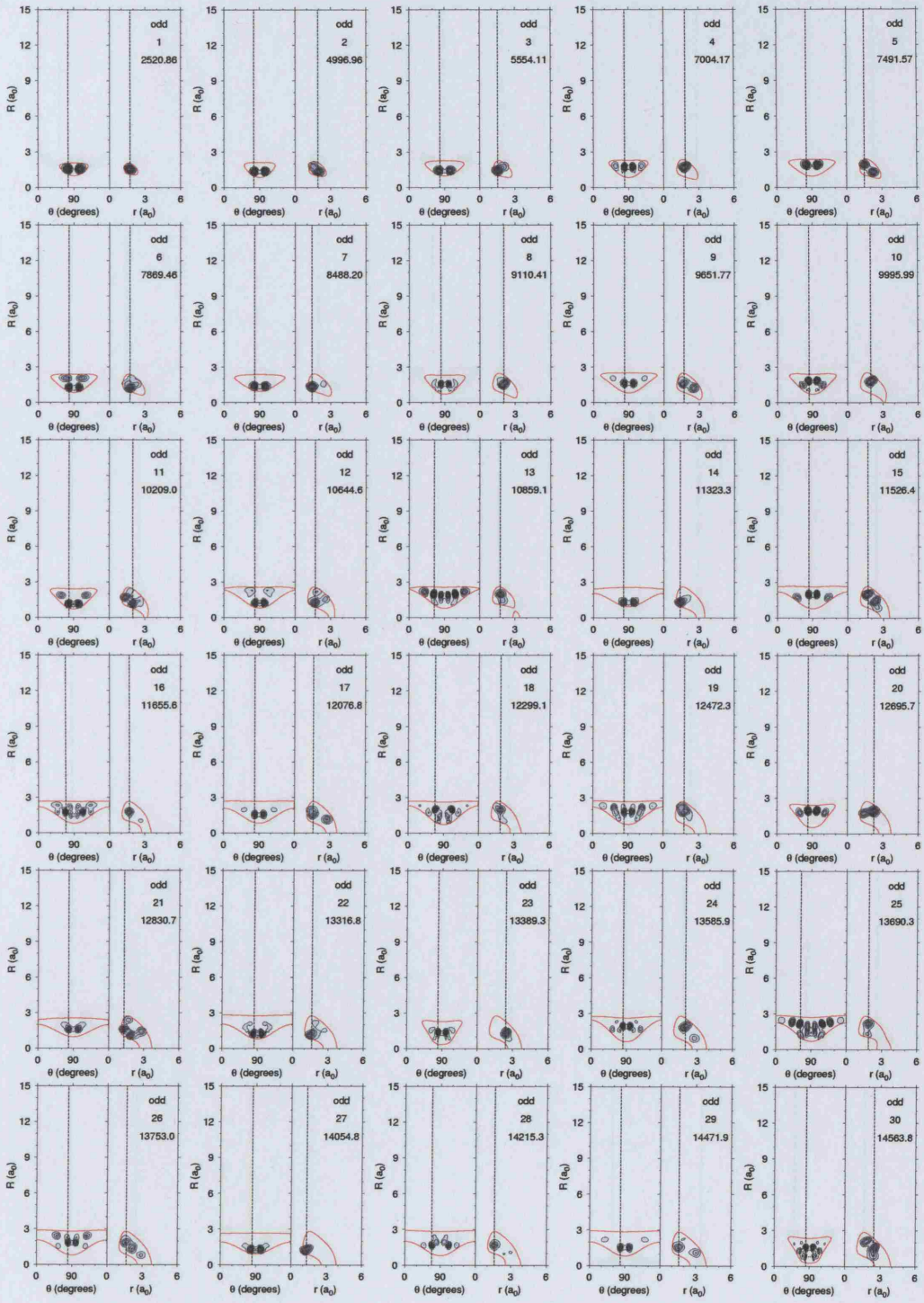

Figure B.24: Wave functions of H_3^+, odd parity states 1 to 30.

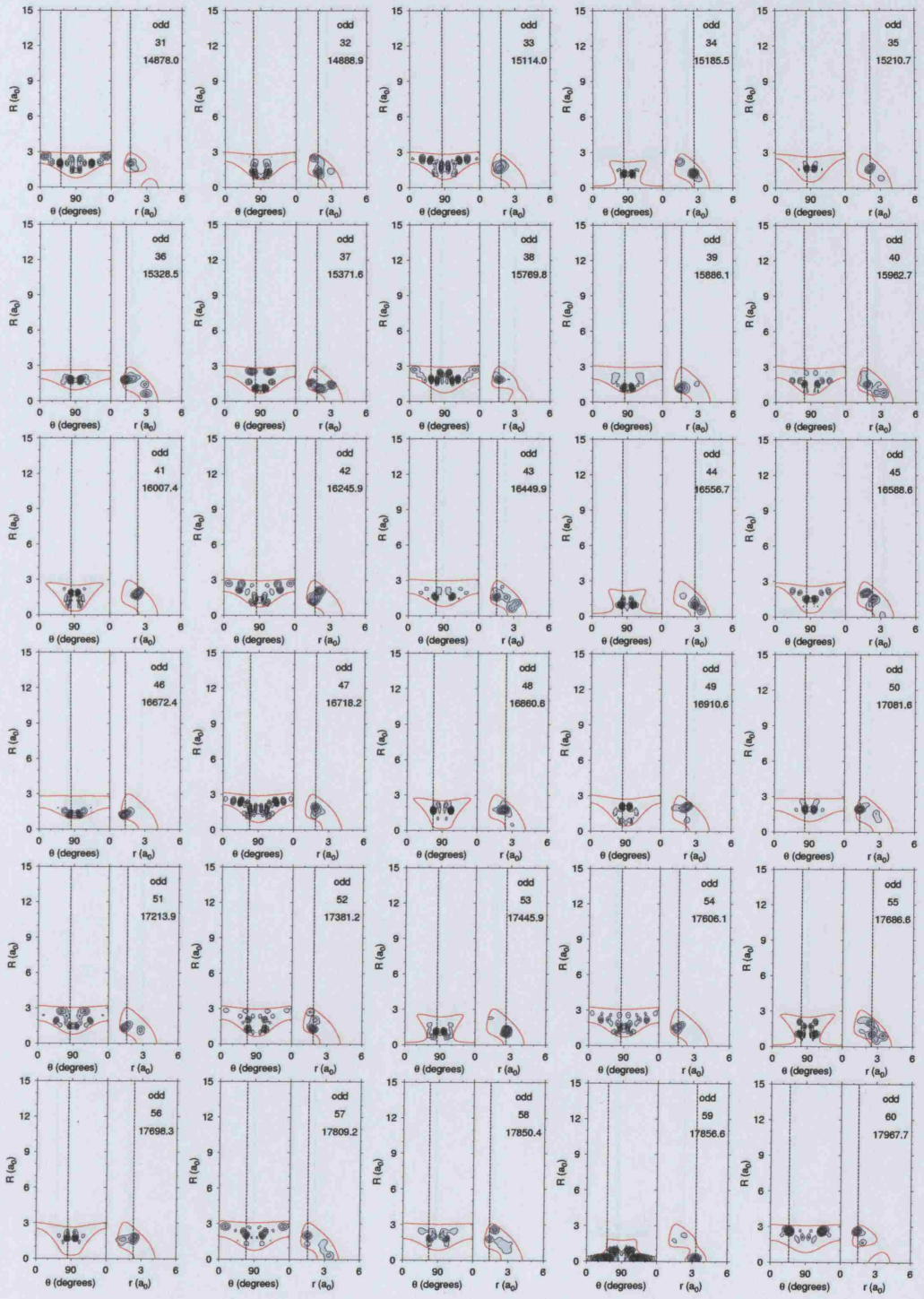

Figure B.25: Wave functions of H_3^+, odd parity states 31 to 60.

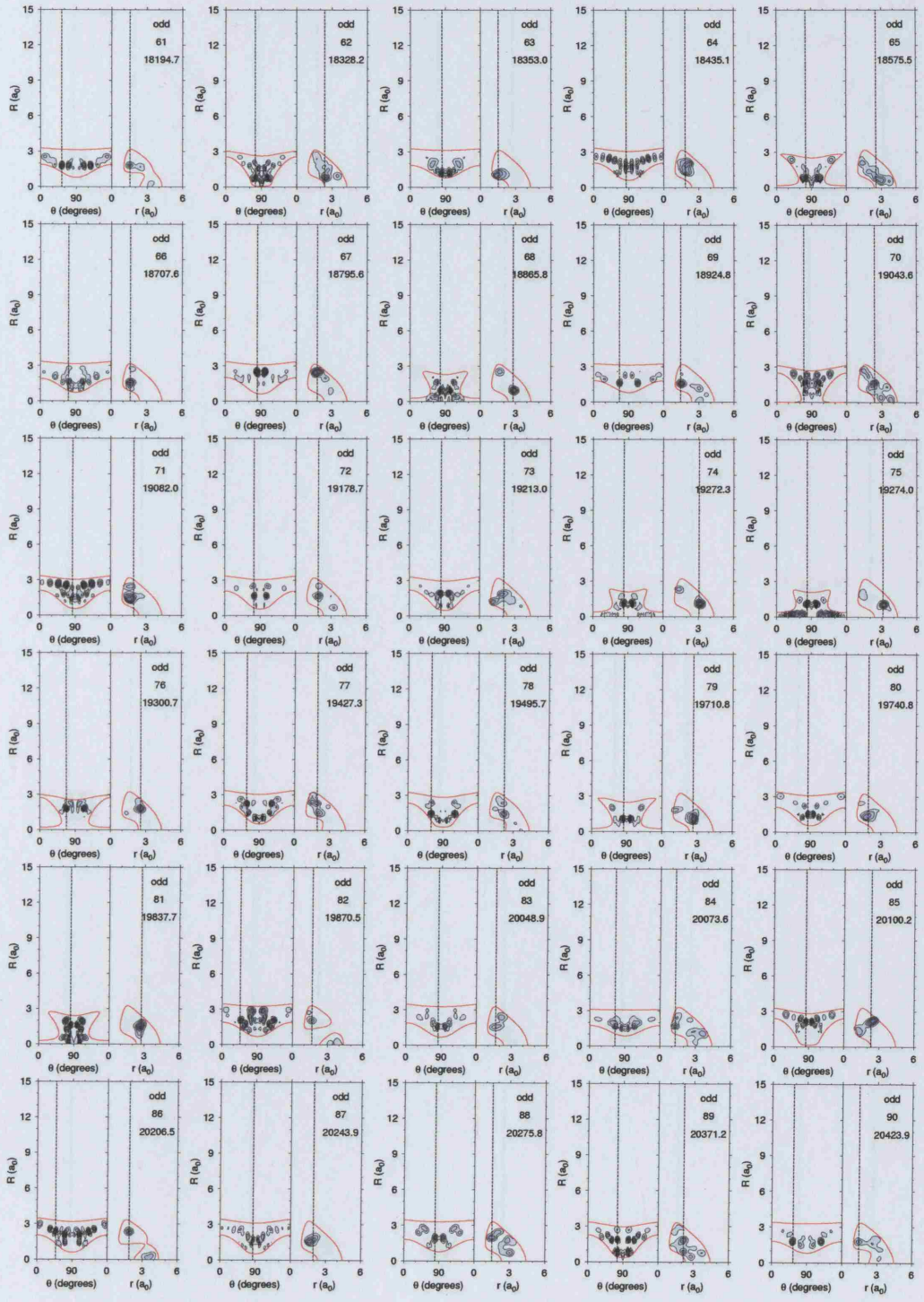

Figure B.26: Wave functions of H_3^+, odd parity states 61 to 90.

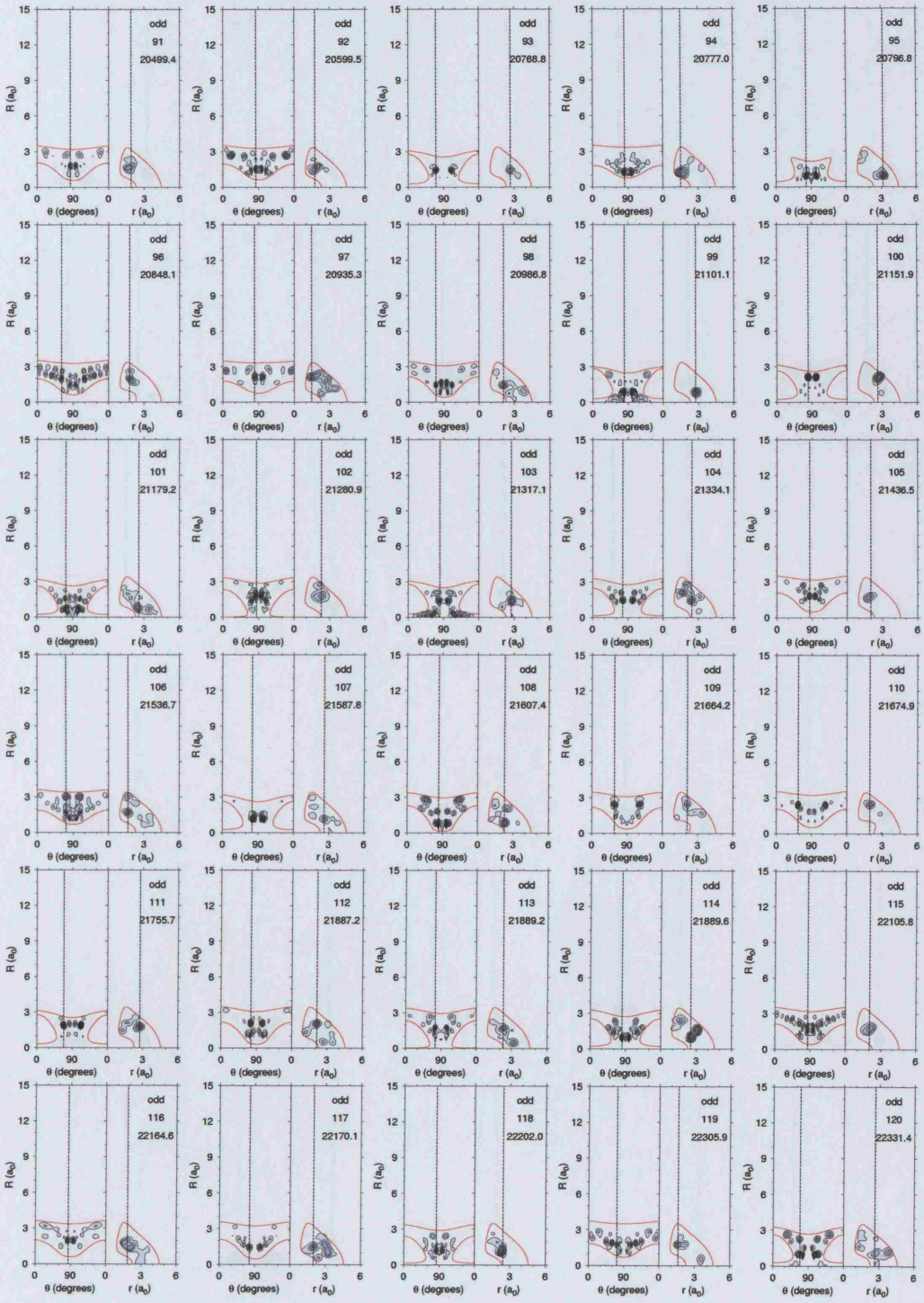

Figure B.27: Wave functions of H_3^+, odd parity states 91 to 120.

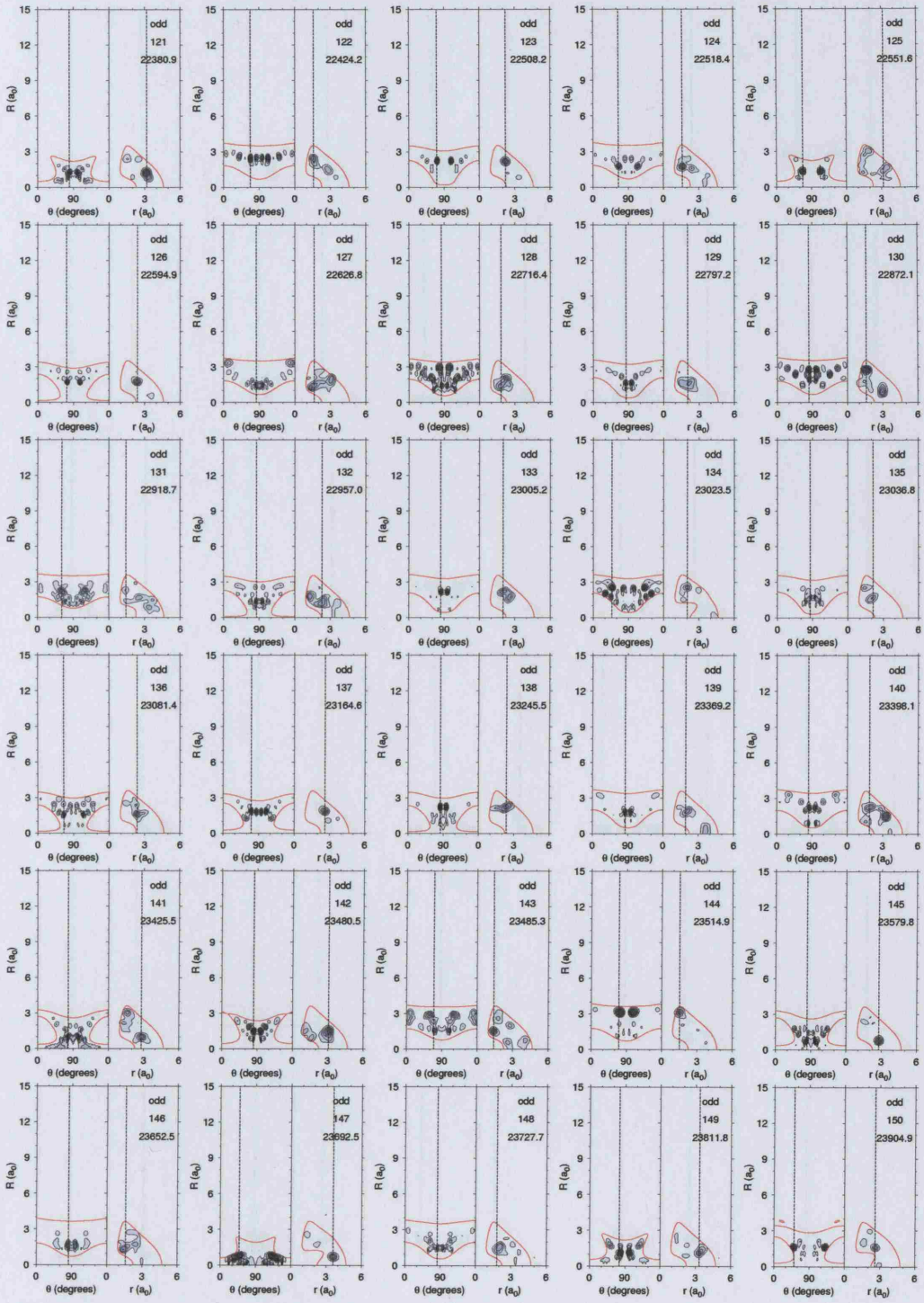

Figure B.28: Wave functions of H_3^+, odd parity states 121 to 150.

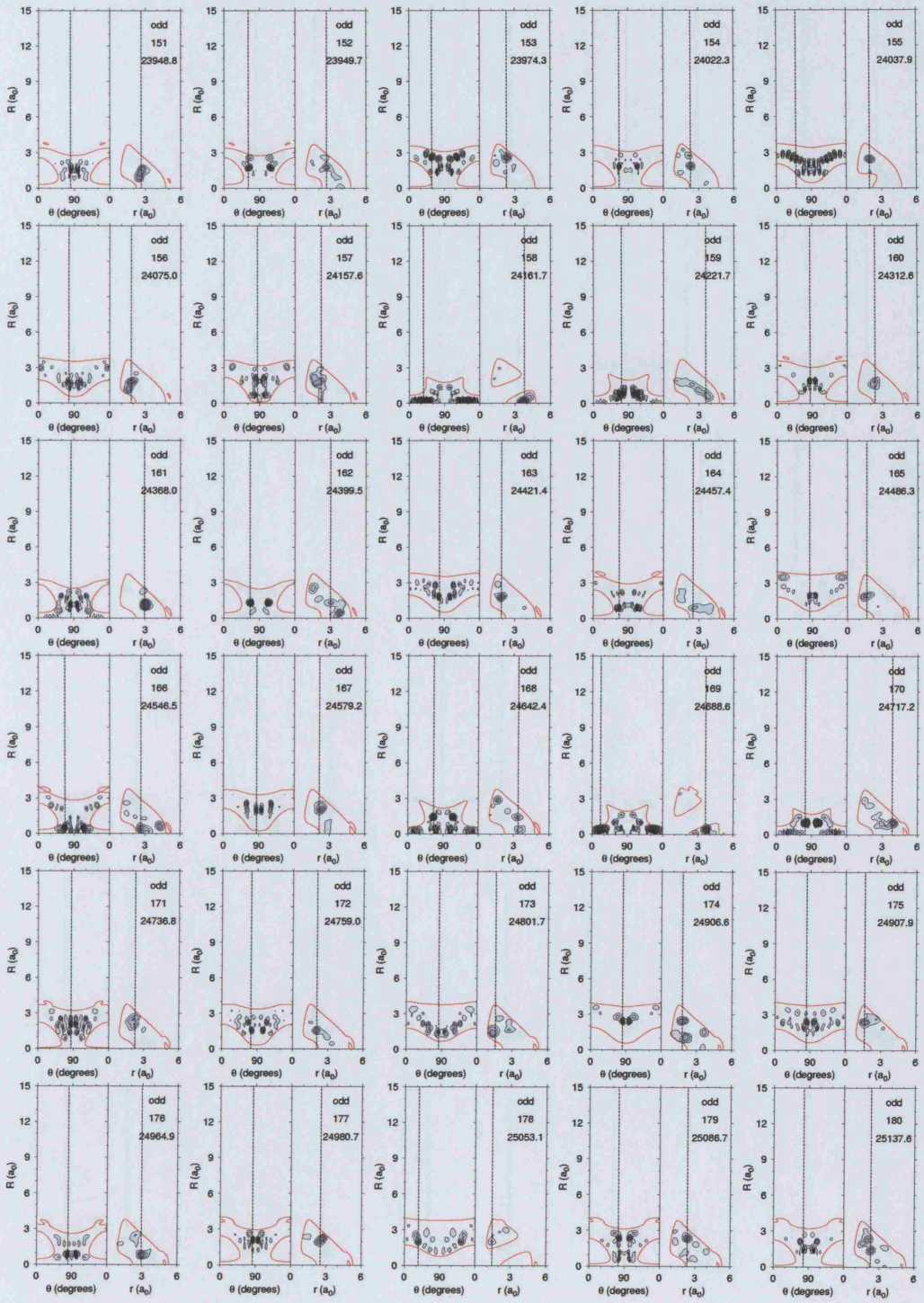

Figure B.29: Wave functions of H_3^+, odd parity states 151 to 180.

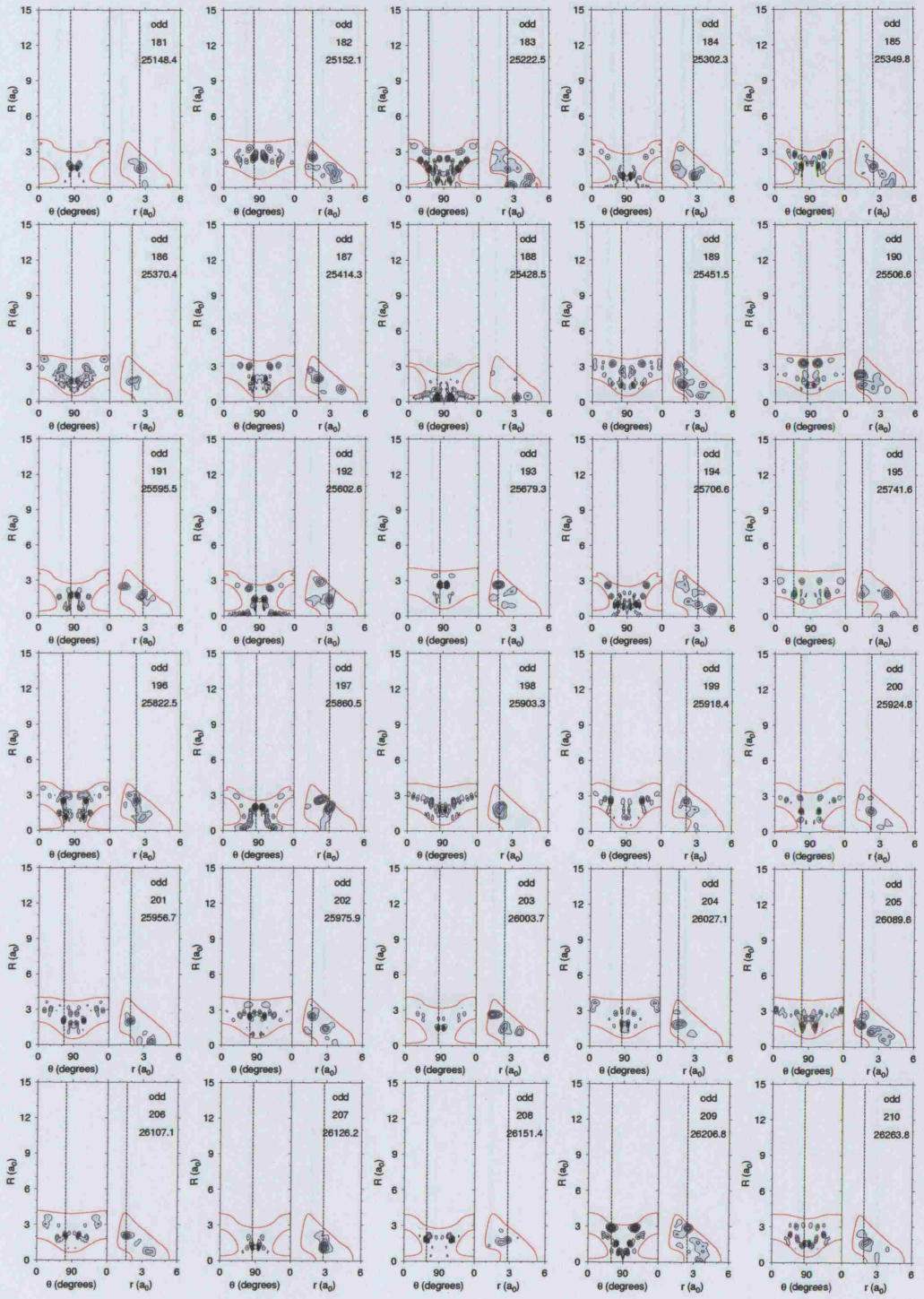

Figure B.30: Wave functions of H_3^+, odd parity states 181 to 210.

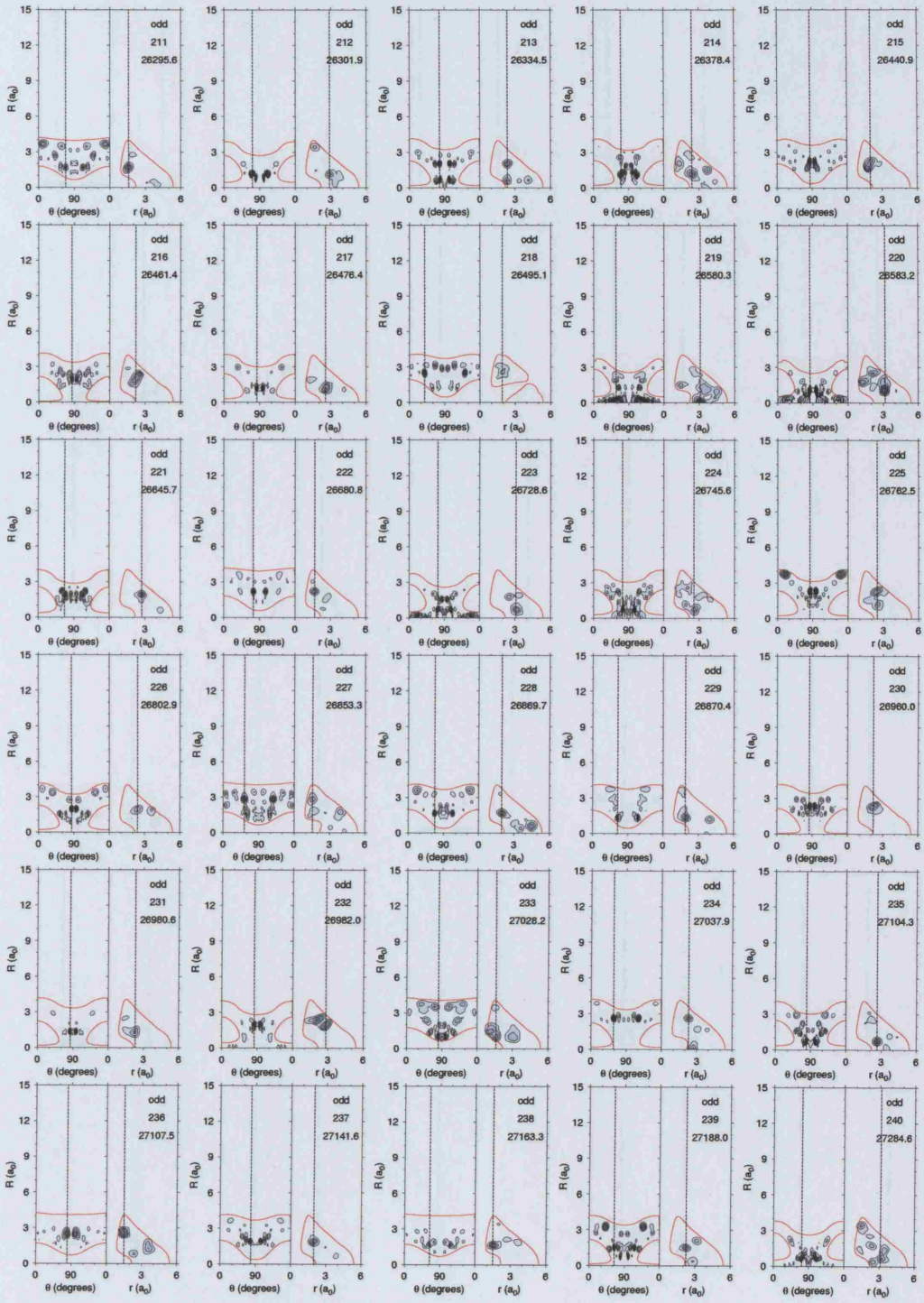

Figure B.31: Wave functions of H_3^+, odd parity states 211 to 240.

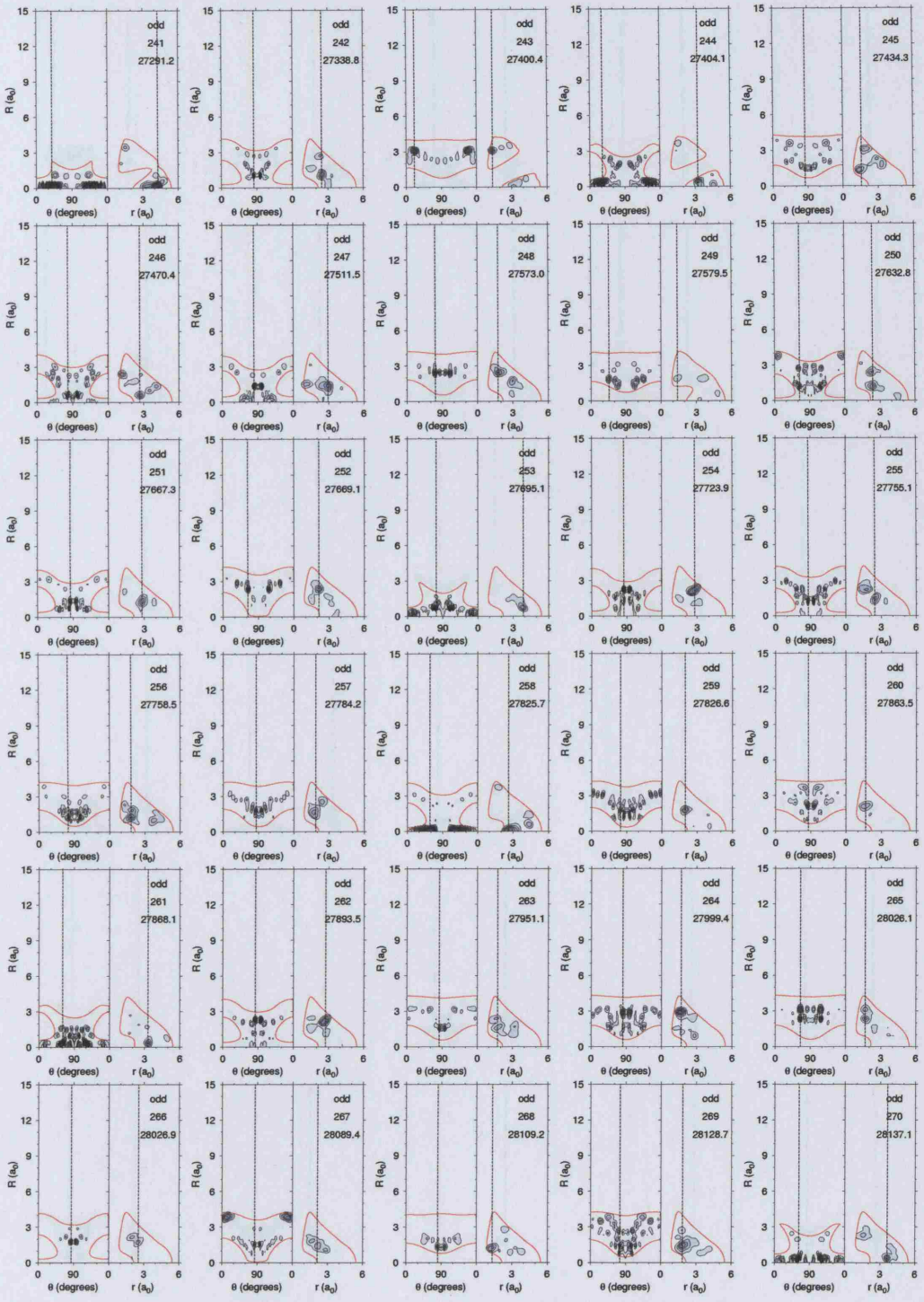

Figure B.32: Wave functions of H_3^+, odd parity states 241 to 270.

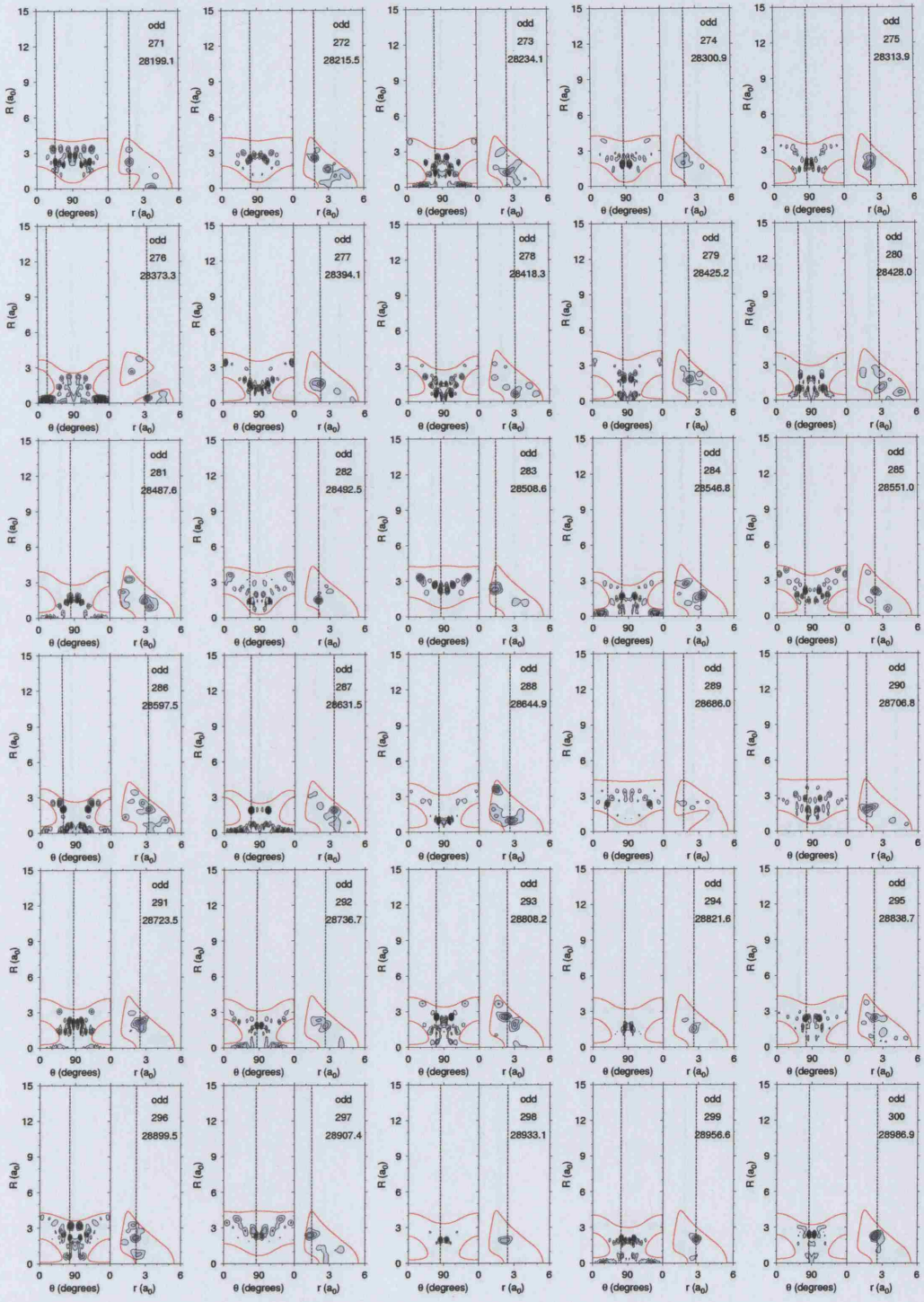

Figure B.33: Wave functions of H_3^+, odd parity states 271 to 300.

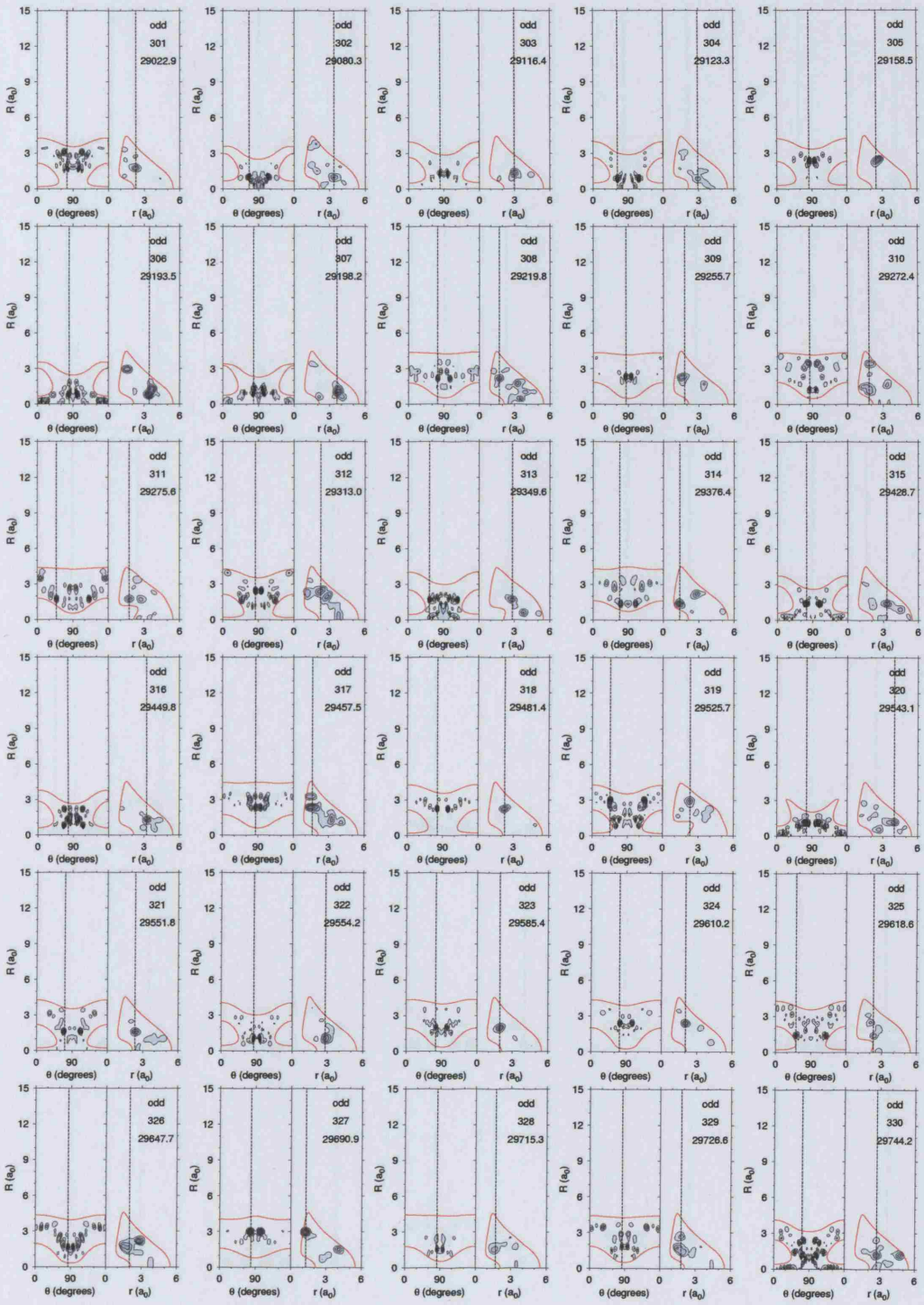

Figure B.34: Wave functions of H_3^+, odd parity states 301 to 330.

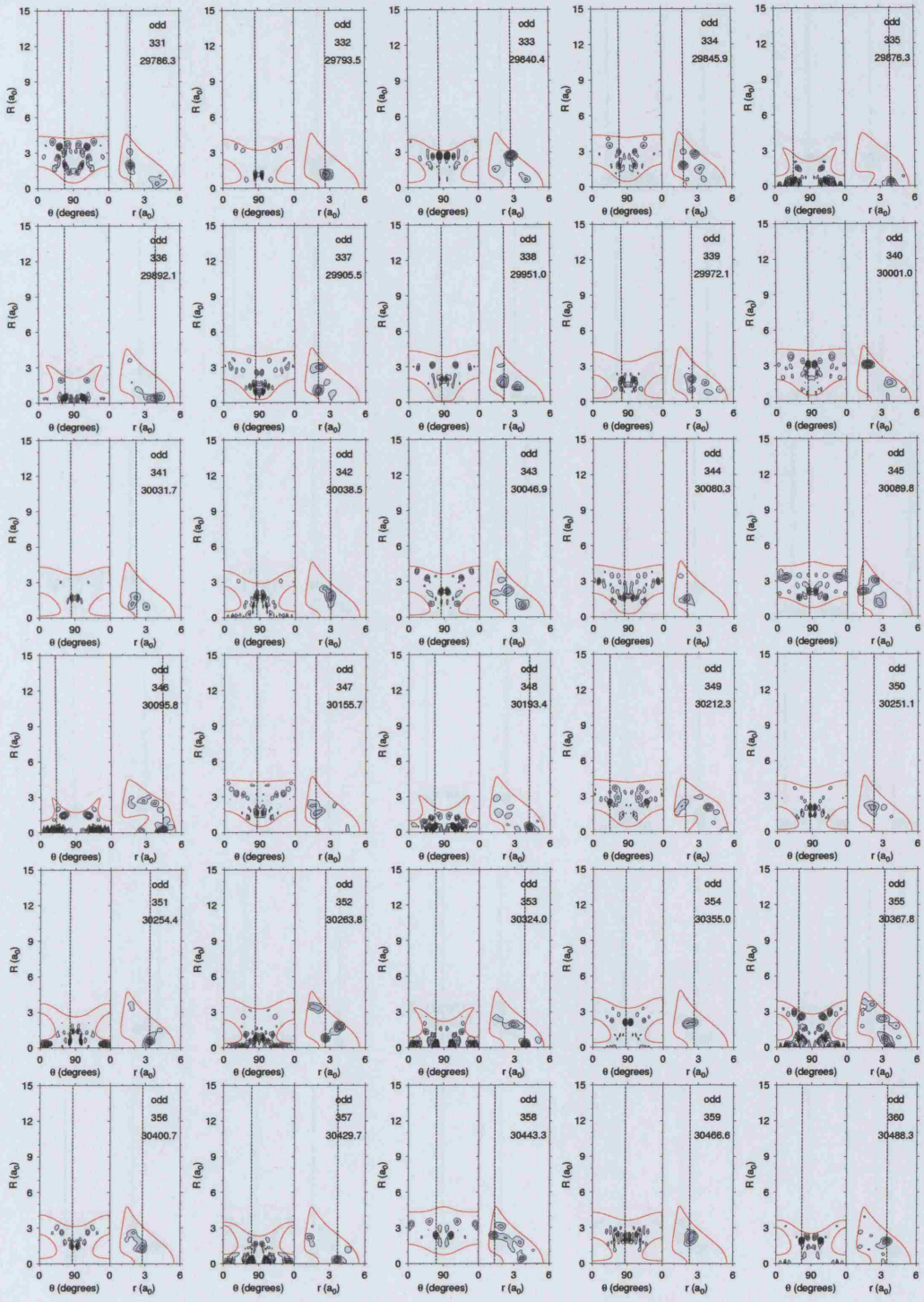

Figure B.35: Wave functions of H_3^+, odd parity states 331 to 360.

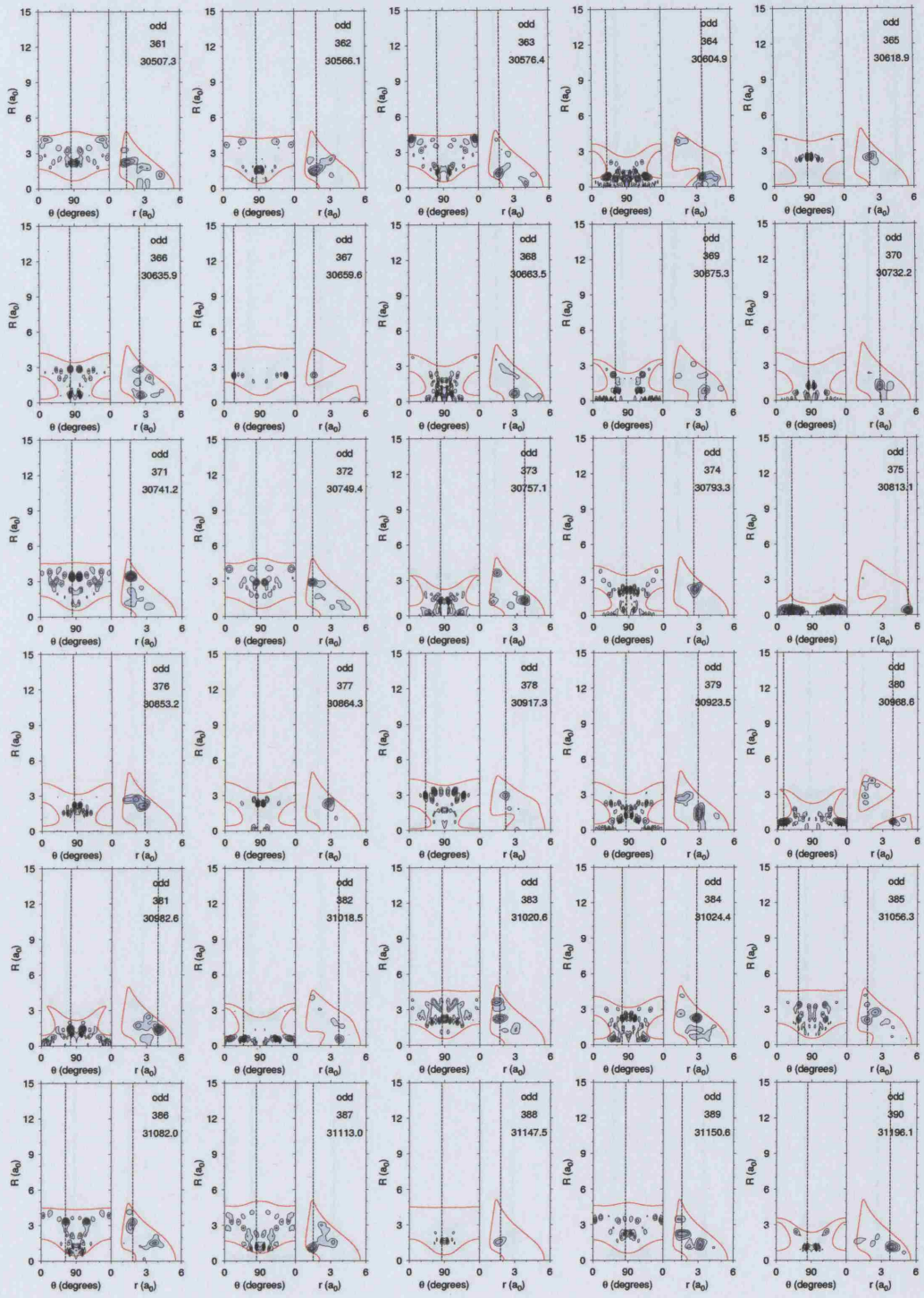

Figure B.36: Wave functions of H_3^+, odd parity states 361 to 390.

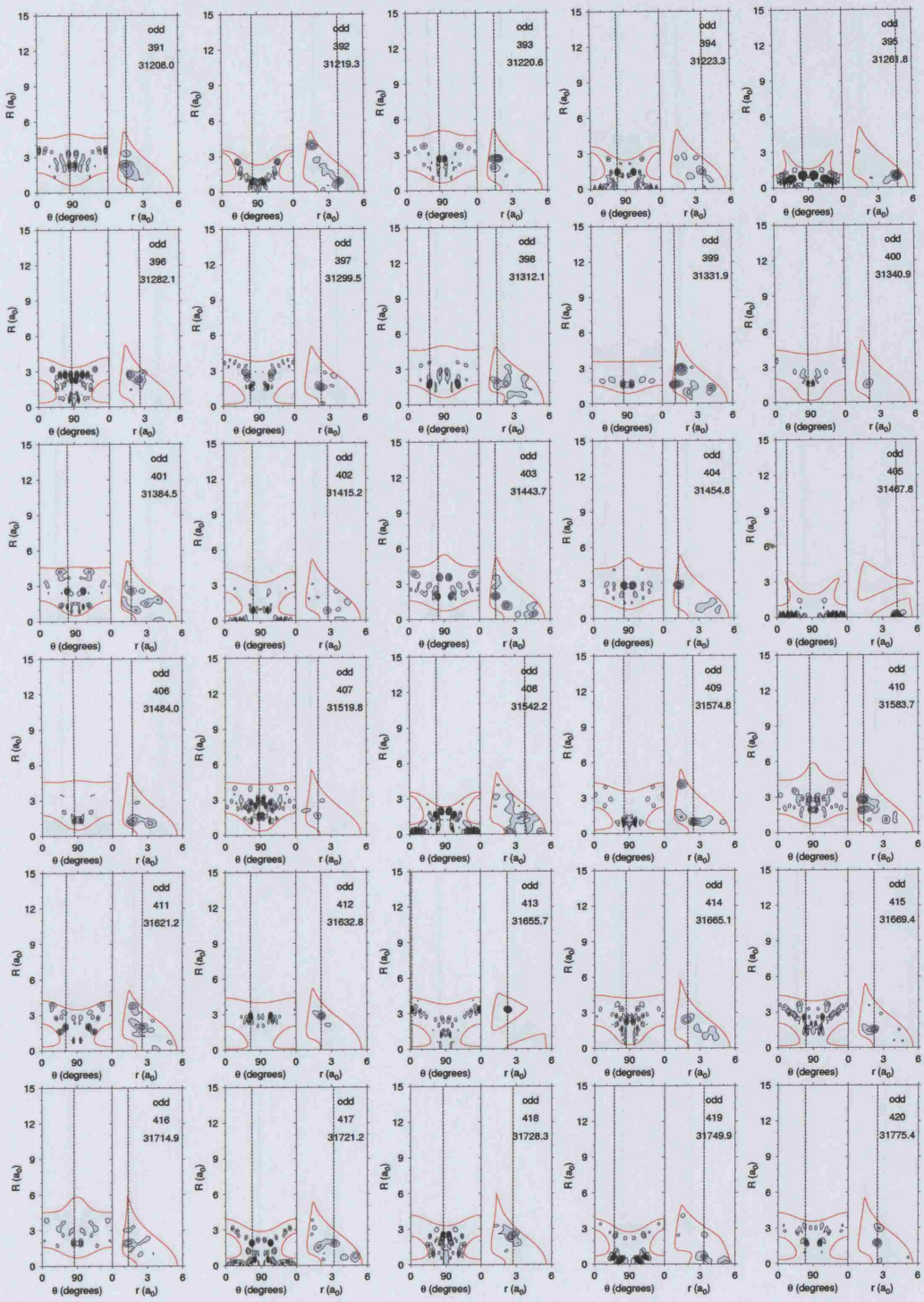

Figure B.37: Wave functions of H_3^+, odd parity states 391 to 420.

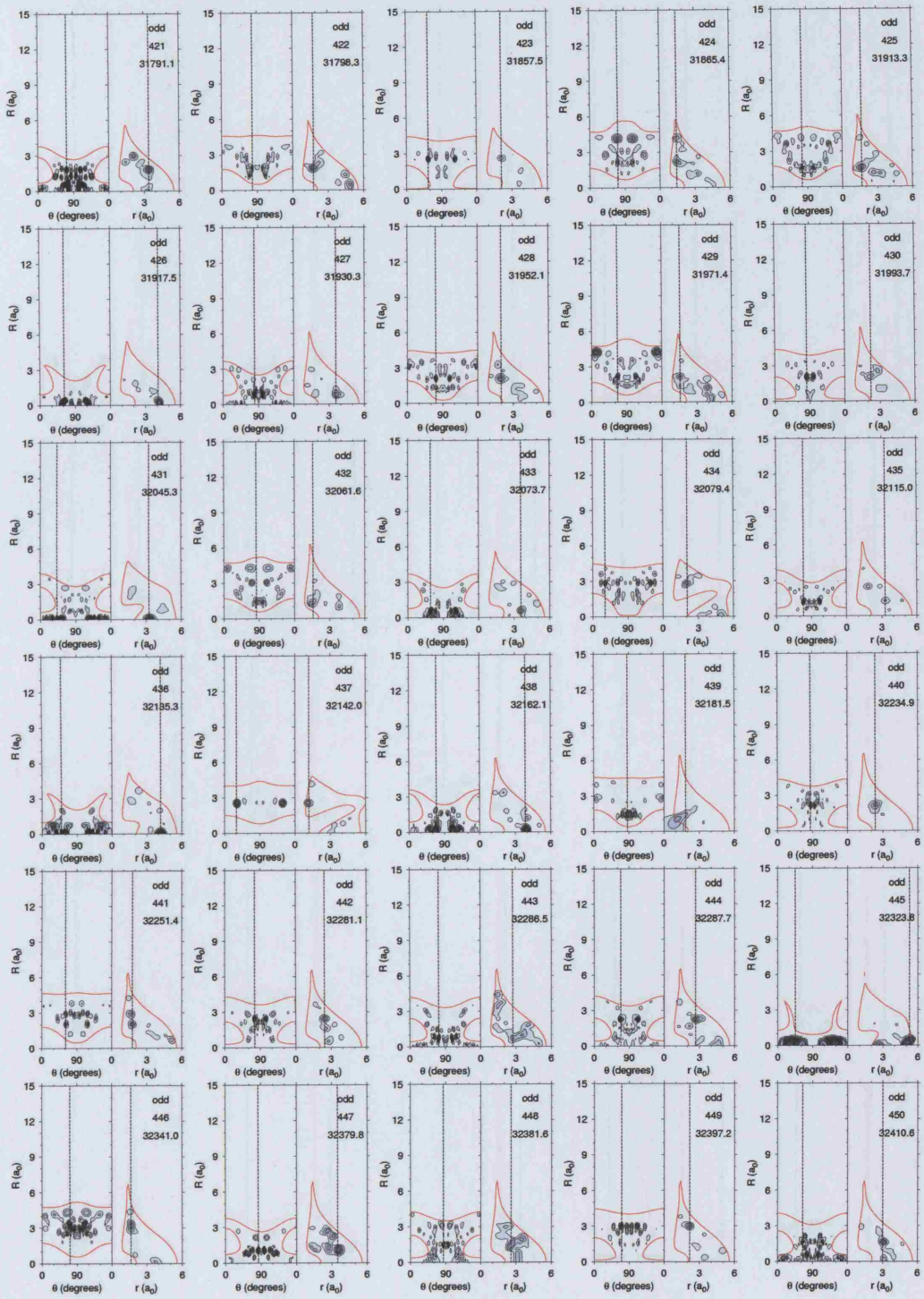

Figure B.38: Wave functions of H_3^+, odd parity states 421 to 450.

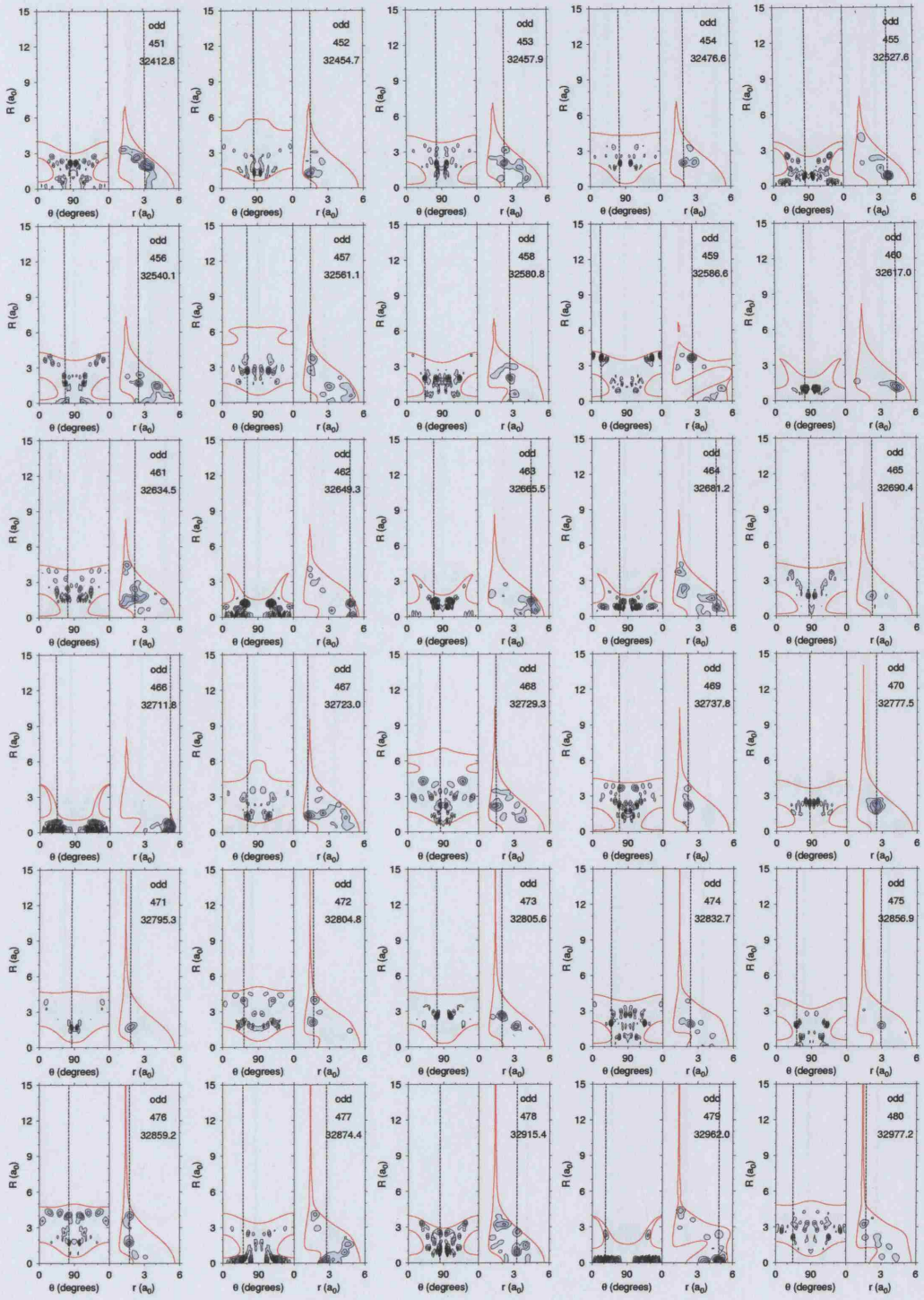

Figure B.39: Wave functions of H_3^+, odd parity states 451 to 480.

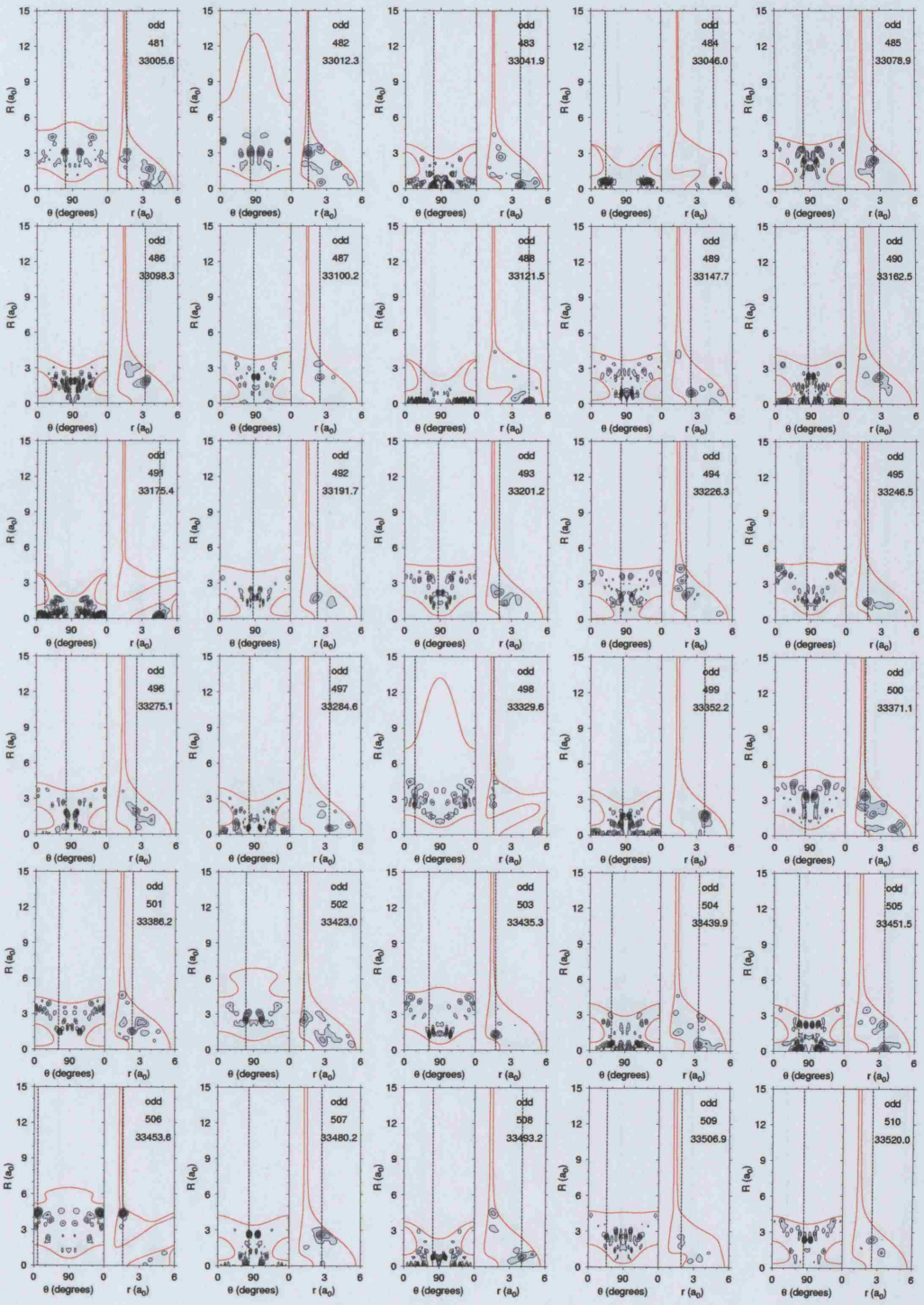

Figure B.40: Wave functions of H_3^+, odd parity states 481 to 510.

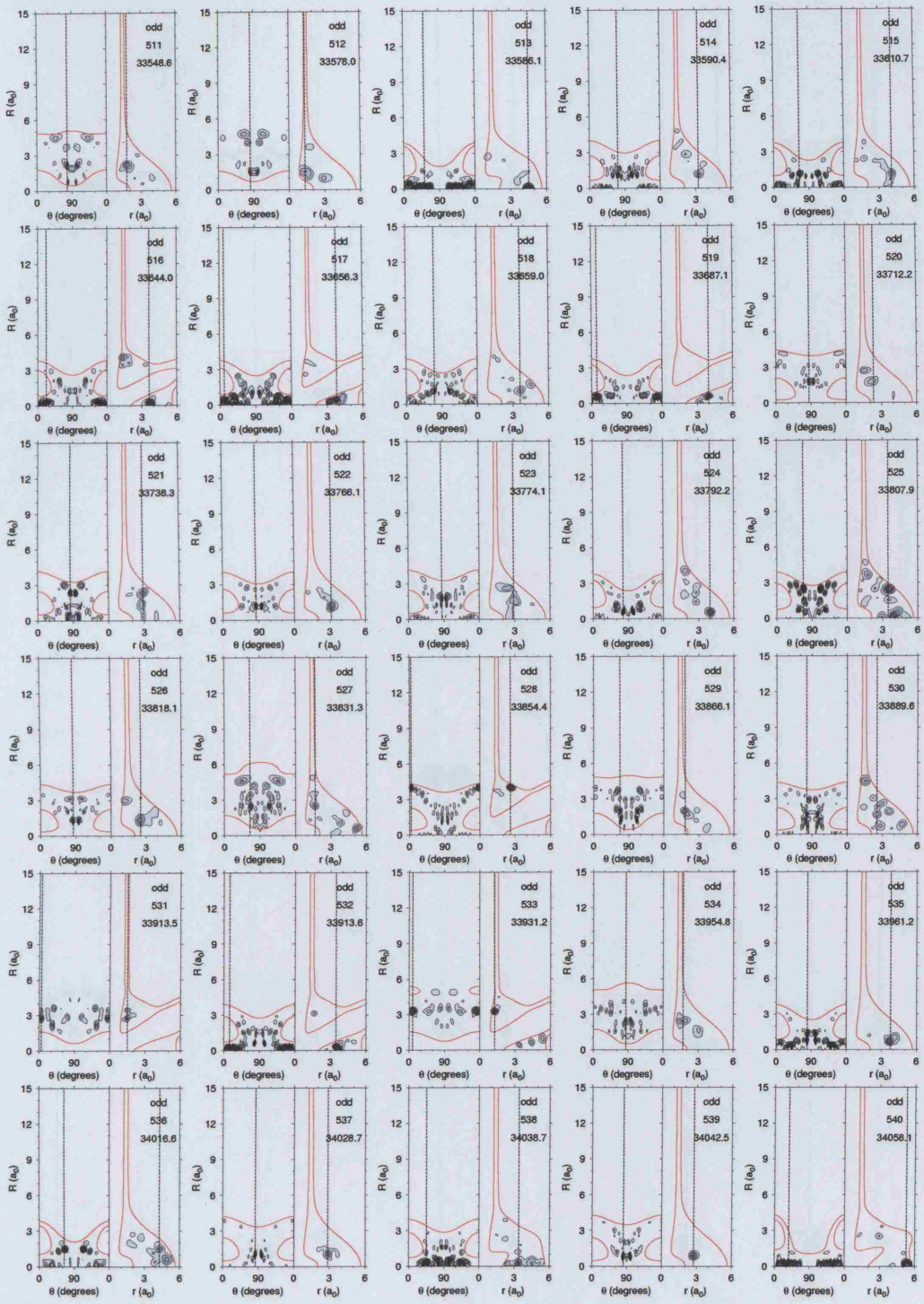

Figure B.41: Wave functions of H_3^+, odd parity states 511 to 540.

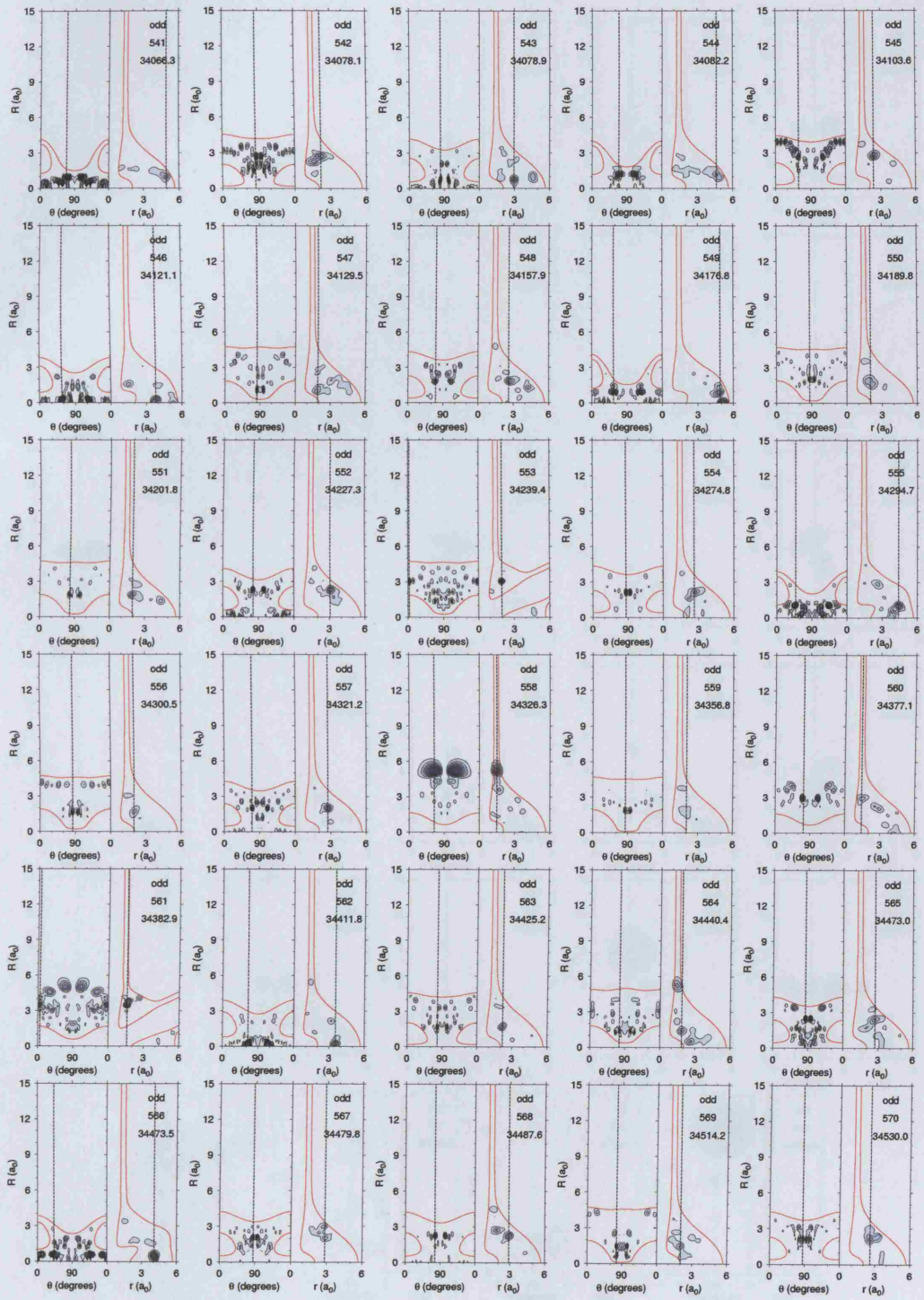

Figure B.42: Wave functions of H_3^+, odd parity states 541 to 570.

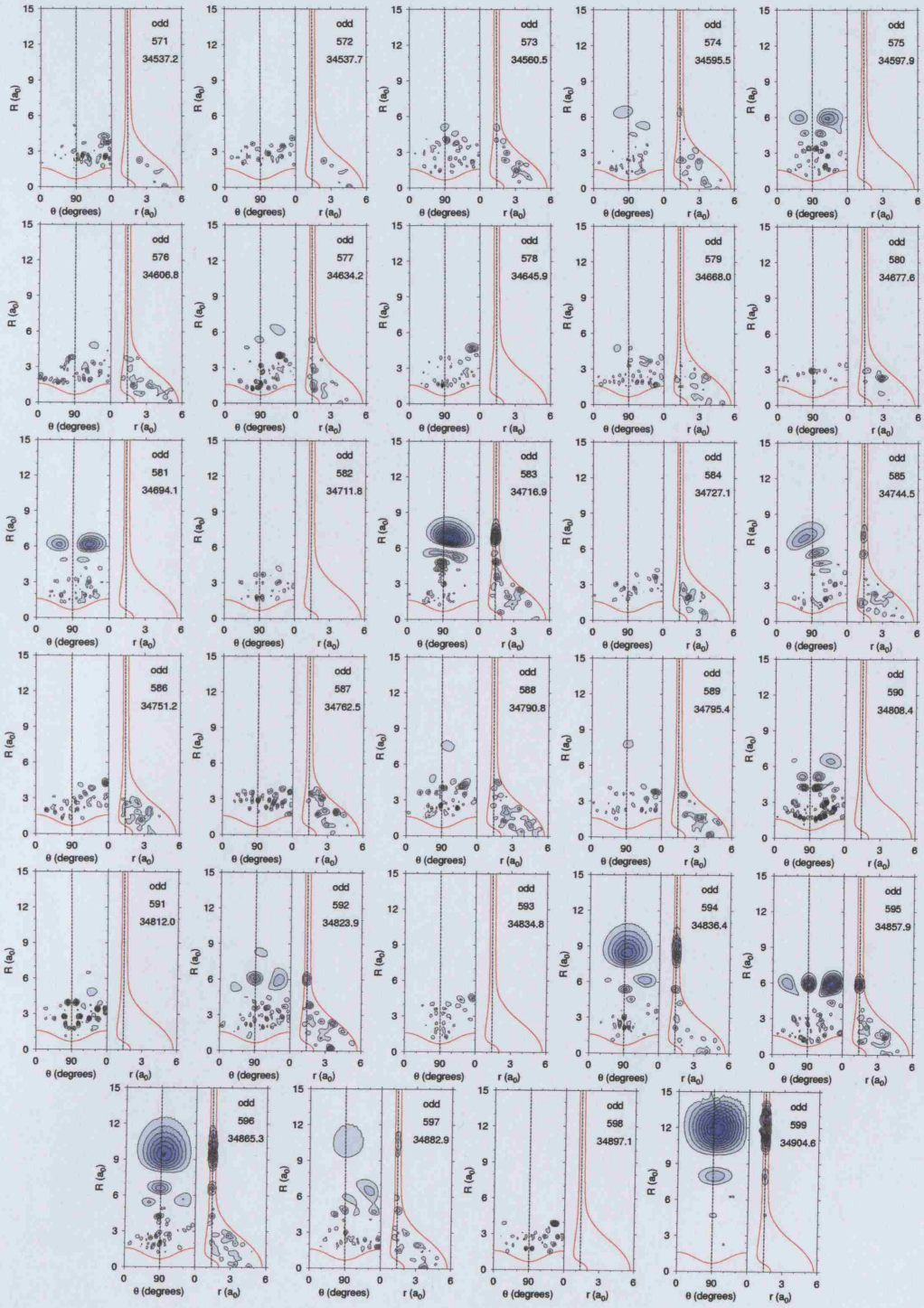

Figure B.43: Wave functions of H_3^+, odd parity states 571 to 599. These cross-sections do not pass through the maximum propability amplitude. The R and r cut is at $\theta = 90°$ and the R and θ cut is at $r = 1.4a_0$.